Tackling the Bottlenecks in Translational Nanomedicine: Towards Precision in Size Control and Facile Nanoformulation

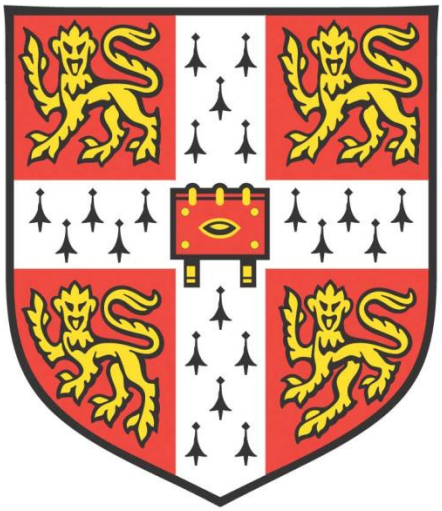

Geyunjian Zhu

Darwin College

Department of Chemical Engineering and Biotechnology

University of Cambridge

This dissertation is submitted for the degree of Doctor of Philosophy

September 2021

PREFACE

This thesis is submitted for the degree of Doctor of Philosophy in the Department of Chemical Engineering and Biotechnology at the University of Cambridge. The work described was undertaken with the supervision of Professor Nigel Slater and Dr. Hirak Patra at the Department of Chemical Engineering and Biotechnology, University of Cambridge between April 2018 and July 2021.

This thesis is the result of my own work and includes nothing which is the outcome of work done in collaboration except as declared in the Preface and specified in the text. I further state that no substantial part of my thesis has already been submitted, or, is being concurrently submitted for any such degree, diploma or other qualification at the University of Cambridge or any other University or similar institution except as declared in the Preface and specified in the text. It does not exceed the prescribed word limit for the relevant Degree Committee.

This thesis contains 63 figures/tables, and less than 65,000 words in total including appendices, tables, figure captions, and references. **Parts of the work in the thesis have been published or are under consideration for publication in the following journals:**

- **Zhu, G. H.**, Azharuddin, M., Islam, R., Rahmoune, H., Deb, S., Kanji, U., Das, J., Osterrieth, J., Aulakh, P., Ibrahim-Hashi, H., Manchanda, R., Nilsson, P. H., Mollnes, T. E., Bhattacharyya, M., Islam, M. M., Hinkula, J., Slater, H. K. H., & Patra, H. K. (2021). Innate Immune Invisible Ultrasmall Gold Nanoparticles—Framework for Synthesis and Evaluation. *ACS Applied Materials & Interfaces*.

- **Zhu, G.H.**, Azharuddin, M., Pramanik, B., Roberg, K., Biswas, S., D'arcy, P., Lu, M., Bhamra, A., Chen, A., Dhara, A. K., Zhuang, Y., Backer, A., Liu, X., Fairen-Jimenez, D., Mazumder, B., Chen, R., Kaminski, C. F., Kaminski, G., Hinkula, J., Slater, N. K. H., and Patra, H. K.* Feasibility of coacervate nanostructure for instant nanoformulation of drug. *Submitted.*

- Azharuddina, M., **Zhu, G. H.**, Dasc, D., Ozgur, E., Uzun, L., Turner, A. P. F.* & Patra, H. K.* (2019). A repertoire of biomedical applications of noble metal nanoparticles. *Chemical Communication*, 55.

- Banerjee, D., Cieslar-Pobuda, A., **Zhu, G. H.**, Wiechec, E., & Patra, H. P.* (2019). Adding nanotechnology to the metastasis treatment arsenal. *Trends in Pharmacological Sciences*, 40(6).

SUMMARY

Tackling the Bottlenecks in Translational Nanomedicine: Towards Precision in Size Control and Facile Nanoformulation – Geyunjian Zhu

Nanomedicine has been an intensive research area for decades. Despite the immense research output, the translation of nanoparticle-based formulations into clinics has been limited. The efficient clinical translation of nanomedicine is impeded by several bottlenecks that include low targeting efficiency, imprecise size control, lack of scalable fabrication, rigorous stability requirement, and complicated manufacturing process. The common focus of the studies here is to address these bottlenecks by developing novel nanoparticle systems which are better positioned for clinical translation. The dissertation specifically describes the experimental studies to develop i) a gold nanoparticle system with fine particle size tuning and superb biosafety and ii) a polymeric nanoparticle system with instant nanoformulation capability and enhanced intracellular delivery efficiency.

In the first system, a novel process-engineered fabrication method synthesizing sub-10 nm ultrasmall gold nanoparticles (uGNPs) with precise particle size control was achieved. The obtained uGNPs series exhibited size tunability at the nanometric resolution and well-defined physiochemical properties. A collection of *in vitro* and *ex vivo* analyses was performed to confirm their biosafety in cytotoxicity, immune compatibility, and blood compatibility. In the second system, an instantly formed polymeric nanoparticle delivery system using a polyelectrolyte coacervate system was created to achieve the facile fabrication of nanomedicine. Nanosized coacervates were successfully formulated with a pair of polyelectrolytes and a chemotherapeutic drug. With the intracellular trafficking properties provided by the assembly components, the coacervate system shows enhanced intracellular delivery.

The two novel nanoparticle systems contribute to the progression in tackling the bottlenecks by achieving precision in size control and facile fabrication. The uGNPs system with fine size tuning and excellent biosafety can be utilized to modulate pharmacokinetics and clearance profiles. The controlled stepwise synthesis also has great potential for the large-scale production of uGNPs. The nanocoacervate system, on the other hand, demonstrates the feasibility of instant nanoformulation of drugs using the complex coacervation process. This method can be employed to bypass the special requirement of large-scale production and elongated shelf life of nanomaterials for various applications. Both systems illustrate great potential in clinical translation and can serve as platforms for creating next-generation vaccines, chemotherapeutics, imaging agents, and theranostic agents.

ACKNOWLEDGEMENT

I would like to express my most sincere gratitude to my mentors Professor Nigel Slater and Dr. Hirak Patra, for their constant support, guidance, and inspiration throughout my PhD study. They are indeed the best supervisors one can ever ask for.

I would like to acknowledge present and previous members of the Bioscience and Engineering group, members of the Department of Chemical Engineering, and partners from external research institutions, who had contributed greatly to my studies and research. I would like to thank Dr. Ljiljana Fruk (my advisor), Dr. Mohammad Azharuddin, Selina Zhuang, Dr. Rongjun Chen, Dr. Bapan Pramanik, Dr. Hassan Rahmoune, Dr. Parminder Aulakh, Dr. Meng Lu, and Dr. Johannes Osterrieth for their valuable input and discussions. I would also like to thank all the technical staff members and all the administration staff members of the department for their support.

My studies would not have been possible without the love and support of my friends and family. I would like to thank my parents for always having faith in me and providing unconditional support throughout my life. I am forever in debt to them for their endless love and support. I am deeply grateful to my girlfriend, Yue, for her company, encouragement, and comfort through thick and thin during my PhD study. She has been the shining light in my life and enabled me to endure the two years of COVID-19 while staying sane and focusing on my study.

I would also like to thank my friends, Dr. Zhigang Hu, Aurelia, Dabwan, Ru, Qi, Runqiao, Qianyue, Yunhu, Drew, and Leander from the department for their thoughtful advice in research and beyond. I am also thankful for the invaluable friendship that I have developed during my time wtih the Chinese Students and Scholars Association with Weining, Daoming, Shengjun, Youchao, Jikai, Junfei, Yi Liu, Tong Guo, Sherry Deng, Shuyu, Zhuotong, Li Ding, Boyang, and so many others that I do not have the space list here. Last, I would like to express my appreciation to Dr. Zhi Chen, Jun Ma, Jason, Dr. Chris Schwall, Zihao, Paul, JJ, and Tom, for the happy memories that we created on the basketball court to keep me both fit and positive during the intense study.

TABLE OF CONTENT

LIST OF FIGURES

LIST OF TABLES

LIST OF ABBREVIATIONS

APTT	Activated partial thromboplastin time
ATP	Adenosine triphosphate
BSA	Bovine serum albumin
COVID	Corona virus disease
CT	Computed tomography
DNA	Deoxyribonucleic acid
Dox	Doxorubicin (hydrochloride)
DPBS	Dulbecco's phosphate-buffered saline
EMA	European Medicines Agency
EPR	Enhanced permeation and retention
FBS	Fetal bovine serum
FDA	Food and Drug Administration
GMP	Good manufacturing practices
GNP	Gold nanoparticle
GSH	Glutathione
LDH	Lactate dehydrogenase
LNP	Lipid nanoparticle
LSPR	Localized surface plasmon resonance
MDR	Multidrug resistance
MPS	Mononuclear phagocytic system
MRI	Magnetic resonance imaging
MSD	Meso Scale Discovery
MTS	3-(4,5-dimethylthiazol-2-yl)-5-(3-carboxymethoxyphenyl)-2-(4-sulfophenyl)-2H tetrazolium
NaCit	Sodium citrate
NIR	Near infrared
NM	Nanomaterial
NP	Nanoparticle
OCT	Optical coherence tomography
PAI	Photoacoustic imaging
PBS	Phosphate-buffered saline

PCA	Principal component analysis
PDT	Photodynamic therapy
PEG	Poly (ethylene glycol)
PET	Positron emission tomography
P-gp	P-glycoprotein
PP	Poly(L-lysine iso-phthalamide)-*g*-L-phenylalanine
PT	Prothrombin time
PTT	Photothermal therapy
PVP	Polyvinylpyrrolidone
RFA	Radiofrequency ablation
RNA	Ribonucleic acid
SARS-CoV-2	Severe acute respiratory syndrome coronavirus 2
siRNA	Small interference ribonucleic acid
SPECT	Single-photon emission computed tomography
TA	Tannic Acid
uGNP	Ultrasamll gold nanoparticle

1 Introduction – Use of nanoparticles in biomedical applications

Nanomedicine is a branch of biomedical application of nanotechnology in therapy, diagnosis, vaccination, and biosensing.[1] It is an interdisciplinary field that combines principles of material science, engineering, nanotechnology, biomedical, and pharmaceutical sciences. The advancement in all these fields of study allows scientists and engineers to create novel therapeutic formulations to achieve better efficacy, improve safety, enhance targeting ability, reduce systemic toxicity, and deliver multimodal therapy. Nanomaterials (NMs), generally defined as having sizes ranging from 1 to 100 nm, can have unique interactions with biological components and overcome biological barriers due to their extremely small size. Nano-sized therapeutic delivery systems can overcome many obstacles and afford multi-functionality, both of which are rather difficult to achieve with pure drugs alone. Nanomedicine is a fast-growing field, and it is destined to revolutionize numerous therapeutic and diagnostic regimes soon. This chapter explores state-of-the-art development in NP-based therapeutic and diagnostic agents. The chapter contains an overview of different types of NPs, interactions between NPs and biological systems, biomedical applications involving the use of nanosystems, and clinical translation of NP formulations. The section concludes with the research aims and an outline of this thesis.

1.1 Types of nanoparticles

Nanoparticles (NPs) can be categorized by the material and structure. Some of the major categories include metallic NPs, non-metallic/inorganic NPs, polymeric NPs, liposomes, micelles, and hybrid NPs (combination of different types) (Figure 1-1).[2] Metallic NPs, such as those made from gold, silver, copper, iron, zinc, titanium, and so forth, are known for their versatile synthesis methods and their physiochemical properties including optical and catalytic properties.[2] Non-metallic/inorganic NPs, such as carbon nanotube and mesoporous silica NPs, have also been extensively studied for potential applications in drug delivery and bioimaging.[2] Polymeric NPs are recognized by their biocompatibility, especially the ones which themselves (e.g., hyaluronic acid) or their metabolic by-products (e.g., poly(lactic-co-glycolic acid)) are already present in the human body.[3] Polymeric NPs can be prepared via the formation of emulsified systems followed by precipitation or polymerization. Nano gelation and polyelectrolyte complexation can also be utilized to form polymeric nanoparticles directly from solutions.[4] Liposomes are spherical vesicles composed of lipid bilayer membranes enclosing a liquid compartment where payloads can be encapsulated.[5]

The interior core space is suitable for encapsulating hydrophilic drugs while hydrophobic compounds can be entrapped within the lipid bilayers. Liposomes can be classified based on their size and the number of bilayer membranes (multilamellar liposomes).[5] Another class of nano-sized vesicles is the micelles, composed of a single layer of either lipid or block copolymer membrane. Because of the single-layered membrane structure, the core of a micelle is hydrophobic while the shell is hydrophilic, or vice versa in the case of a reverse micelle.[6] Therefore, micelles are especially suitable for encapsulation and delivery of hydrophobic drugs. In general, organic/polymer-based NPs possess better biocompatibility, whilst inorganic and metal-based NPs can be fabricated into more complex structures and afford unique physical properties for multimodality therapies.

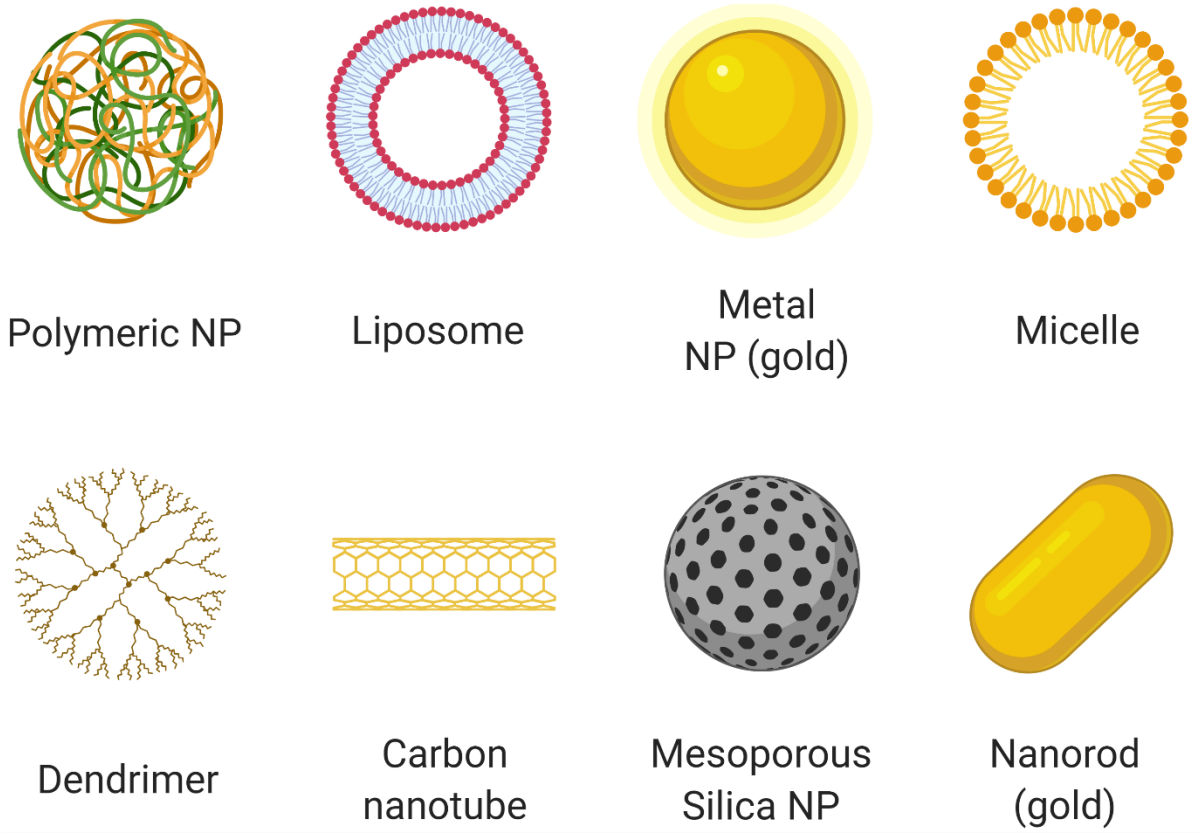

Figure 1-1. Schematic illustration of major types of NPs, including polymeric NP, liposome, metal NP (e.g., gold), micelle, dendrimer, carbon nanotube, nonmetal/inorganic NP (e.g., silica), nanorod. Created with BioRender.com.

1.2 Interaction between nanoparticles and biological systems

Interaction between NMs and biological components is a key factor to consider when it comes to material design. Surface protein adsorption, cellular uptake, and biodistribution of NMs are determined by various parameters including particle size, shape, surface charge,

hydrophobicity, etc. Particle size is one of the most important characteristics of nanosized systems. Studies have found that the size of NMs determines their clearance mechanism from the body, with smaller size particles (<10 nm) being cleared via urinal passage, and bigger size particles (>10 nm) being cleared through liver route. Therefore, the size of the NMs largely governs the circulation time, safety, and biodistribution. For example, fast urinal clearance is preferred for NPs used in imaging and diagnosis, whereas long circulation time is required for targeted drug delivery systems for better accumulation at diseased sites. In addition, particle size is crucial to achieving passive delivery, which takes the advantage of enhanced permeability and retention (EPR) effect of the tumor microenvironment.[7] For distinctive biomedical applications, the optimal particle size is likely to be different and should be carefully investigated.

Surface properties (charge, hydrophobicity, etc.) also play a vital role in the interactions between NPs and biological components (starting from small biomolecules to the assembled macromolecules such as the cell membrane, deoxyribonucleic acid (DNA), ribonucleic acid (RNA), proteins etc. to complex heterogeneous system such as blood components and organs). Interactions between NPs and the biological system *in vivo* usually start with the nonspecific protein adsorption and protein corona formation.[8] Adsorption of proteins onto the NP surface can lead to undesirable blood coagulation, complement activation, cell adhesion, and material degradation. Adsorption of protein onto synthetic surface often involves denaturing of the protein, leading to activation of signaling cascade of phagocytes clearance.[9] This will unfavorably alter the pharmacokinetics of therapeutics-loaded NPs and cripple their efficacy. Therefore, well-controlled protein adhesion is crucial for the success of delivering the drug to its designated sites. Protein adhesion and corona formation, however, cannot be fully eliminated, but they can be manipulated so that the functionalities of nanocarriers are preserved. Various strategies have been established over the years to control surface protein adhesion. Among all, low-fouling polymer coatings have been most widely utilized for their easy fabrication and low cost. The state-of-the-art poly (ethylene glycol) (PEG) has been discovered to possess excellent antifouling properties and has been proved by Federal Drug Administration (FDA) in a number of NM-related drug formulations.[10] PEG is a non-toxic and highly hydrophilic molecule that can firmly attract water molecules to form a hydration layer, which repels proteins from attaching to the surface. The polymers are usually chemically tethered to the surface of NPs, to not only reduce protein adsorption but also render high colloidal stability for NP during circulation. However,

repeated dosing of PEGylated NPs can lead to the production of anti-PEG antibodies.[11] Similarly, zwitterionic polymers, another class of super hydrophilic materials, can also achieve antifouling properties via the same mechanism.[12] Zwitterionic polymers are polymeric materials which contain equal numbers of positive and negative charges and are neutrally charged overall. The local polarity, however, attracts water molecules, therefore, making the macromolecules overall super hydrophilic. Although applying low-fouling polymer coatings to NP delivery systems helps to improve circulation time, safety, and colloidal stability, *in vivo* behavior of nanomedicines is collectively determined by multiple factors including the material, size, shape, surface charge, and special functionalization.

1.3 Biomedical application of nanoparticle-based formulations

Due to their nano-ranged sizes, NPs can have unique interactions with the biological components, overcome various biological barriers, and achieve special biodistribution within the body. Therefore, NPs are powerful tools in numerous biomedical applications, such as therapy, drug delivery, bioimaging, vaccination, diagnosis, gene editing, etc.

1.3.1 Nanoparticles as drug delivery system

The use of NPs as cargos to deliver therapeutic agents is one of the most explored applications, especially in cancer therapy. The use of NPs improves pharmacokinetics, bioavailability, cellular uptake, and targeting ability of the therapeutics.[2] The targeted delivery property of NPs is particularly attractive in cancer therapy because it can minimize systemic toxic effects of chemotherapeutic drugs on healthy tissues. NPs accomplish targeted delivery via either passive targeting, through the EPR effect,[7] or active targeting, via selective overexpressed receptors on cell membranes (Figure 1-2). Although research in NP-based drug delivery systems has mainly focused on cancer treatment, other unmet medical needs such as treatment of cardiovascular and neurodegenerative diseases have also been studied.[2]

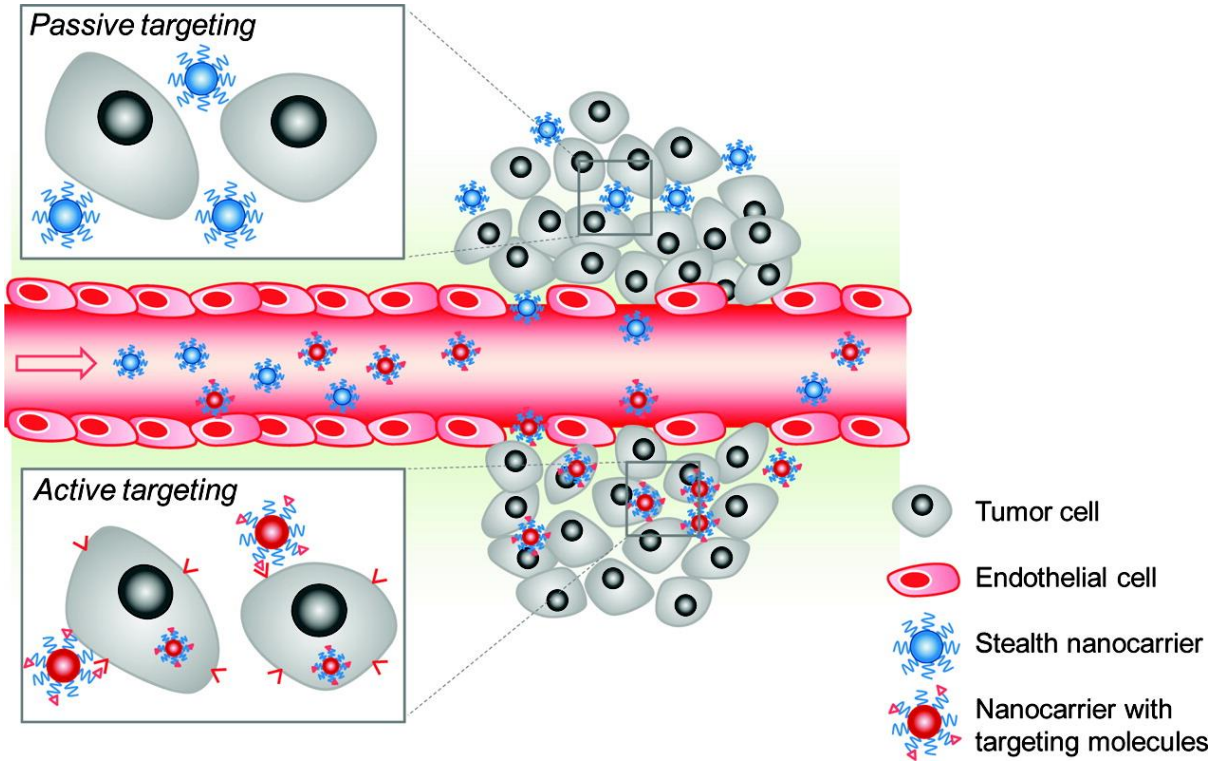

Figure 1-2. Schematic illustration showing the passive targeting (EPR) and the active targeting of nanocarriers against a tumor. In both cases, the nanocarriers reach the tumor through leaky vasculature. For active targeting, nanocarriers are decorated with targeting molecules capable of binding to the tumor cells. Reprinted (adapted) with permission from reference.[13] Copyright 2009 American Chemical Society.

1.3.2 Nanoparticles as imaging contrast agents

Using NPs as contrast agents in diagnosis and monitoring is another intensive field of study. This research area is mainly dominated by the inorganic NPs which possess unique physical properties, such as X-ray attenuation by gold NPs, magnetization of iron oxide NPs, and fluorescence of quantum dots.[14] Nanosystems have been explored as contrast agents in different imaging techniques such as computed tomography (CT), positron emission tomography (PET), single-photon emission computed tomography (SPECT), magnetic resonance imaging (MRI), near-infrared fluorescence imaging, etc.[15,16] With either passive or active targeting strategies, NP-based contrast agents can selectively accumulate in tumors for cancer diagnosis. In addition to conferring the contrast themselves, NPs can also serve as carriers of contrast agents, such as the Technetium-99m sulfur colloid, a nanosized sulfur colloid system containing the gamma-emitting ^{99m}Tc for liver-spleen scanning with SPECT.[16]

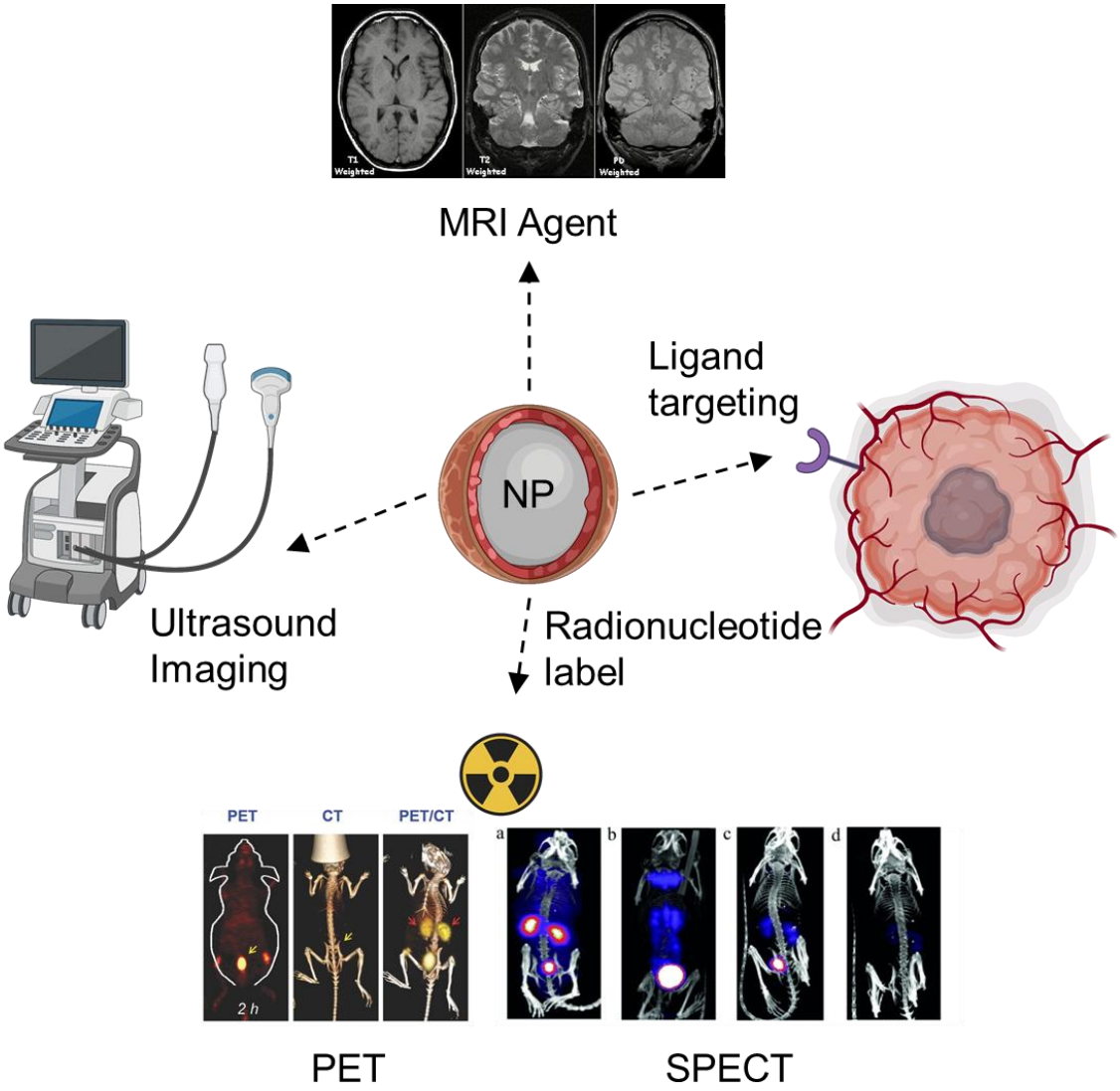

Figure 1-3. Schematic illustration of NP contrast agents in different types of imaging techniques.[17,18] Created with BioRender.com.

1.3.3 Nanoparticles in immunizations – Nanovaccine

NP-based vaccines (nanovaccines) have been formulated to not only overcome the drawbacks of traditional vaccines, but also confer higher levels of immunity modulation capability. Vaccines have been used in our healthcare systems for over two centuries, and they have changed human history for the better. The immune system consists of the innate and the adaptive immunity. The adaptive immunity is characterized by its ability to precisely identify a pathogen and to develop a long-term memory against the same type of pathogens that it had encountered. Vaccines train the adaptive immune system to either generate immunological memory prior to infections (prophylactic) or better recognize disguised ongoing disease (therapeutic). Superior efficacy can be accomplished by nanovaccines due to

(i) extended antigen stability, (ii) enhanced immunogenicity (e.g., via adjuvanticity), (iii) targeted delivery, and (iv) sustained release. NPs provide strong protection to both the antigens and adjuvants against enzymatic and proteolytic degradation.[19] Nanovaccines can evoke both humoral and cell-mediated immune responses due to their unique physicochemical characteristics. They also aid in targeted delivery and can load multiple components on a single platform.[20] Lastly, fine tuning the physical properties of the NMs can result in a substantial extension of the duration of antigen presentation and enhancement of dendritic cells (DCs)-mediated antigen uptake, leading to matured DCs and promotion of cell-mediated immunity.[21]

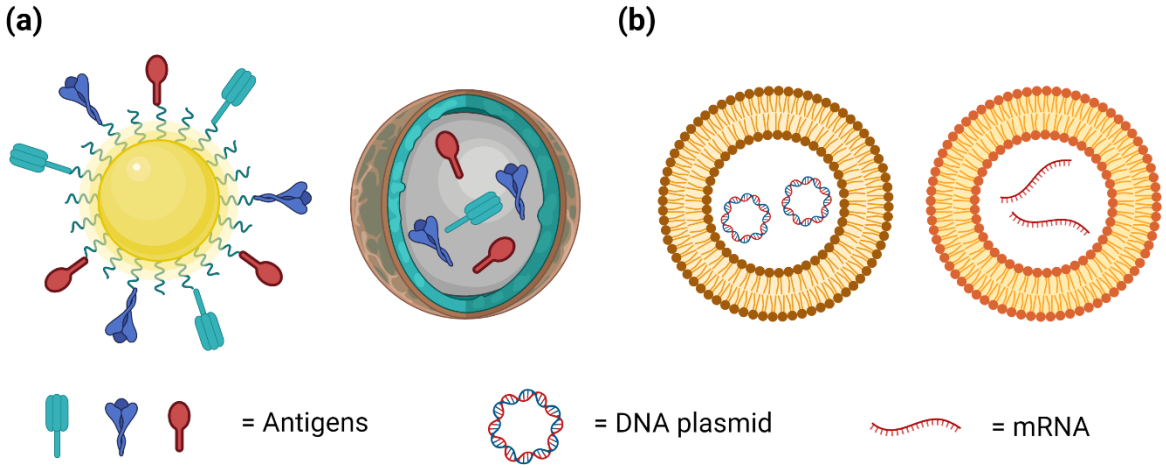

Figure 1-4. Schematic illustration of the two types of delivery strategies in nanovaccines. (a) Direct delivery of antigens conjugated on the surface of NPs and encapsulated inside NPs. (b) Delivery of nucleic acids encoding the antigens using liposomes as examples. Icons not drawn to scale. Created with BioRender.com.

There are two main strategies to create nanovaccines, (i) delivering the antigens directly and (ii) delivering nucleic acids which encode the antigens. The former allows antigen-presenting cells to directly recognize, process, and present the antigens, whilst the latter utilizes the intrinsic protein production machinery of the cells to generate the antigens for immune recognition. Both strategies have shown some clinical success in the past (Table 1-1). It is worth highlighting that the COVID-19 pandemic probably expedited the clinical translation of messenger RNA (mRNA)-based nanovaccine. The two lipid nanoparticle (LNP) vaccines developed by BioNTech and Moderna in the combat against COVID-19 not only became the first two clinically approved mRNA vaccines, but also were the first two clinically approved COVID-19 vaccines.

Table 1-1. List of clinically approved nanovaccines

Product	Nanovaccine type	Indication	Company	Agency
Comirnaty® (Tozinameran)	LNP-mRNA	SARS-CoV-2	BioNTech	FDA
mRNA-1273	LNP-mRNA	SARS-CoV-2	Moderna	FDA
Inflexal®V	Virosome with Influenza virus surface antigens (hemagglutinin and neuraminidase)	Influenza	Crucell	EMA
Epaxal®	Virosome with inactivated virus particles	Hepatitis A	Crucell	EMA
Gardasil®9	Capsomere (made with major capsid protein L1)	HPV	Merck & Corp.	FDA EMA
Cervarix®	Capsomere (made with major capsid protein L1)	HPV	GSK	FDA EMA

1.3.4 Other biomedical applications

In addition to the aforementioned biomedical applications, NPs were also used in biosensing, *in vitro* diagnosis, non-viral vectors in gene transfection, and theranostic applications (combination of therapeutics and diagnostics). For example, GNPs functionalized with thiol modified single-stranded DNA (ssDNA) probes have been used to detect a single mismatch through a cross-linking approach in the presence of a complementary ssDNA.[22] Several comprehensive review articles have been published covering these topics and therefore will not be discussed in detail here.[23–25]

1.4 Nanomedicines in clinics

Since the mid-1990s, approximately 13 nanomedicine formulations have been approved for clinical use every 5 years by the U.S. Food and Drug Administration (FDA). A summary of different types of nanomedicines which had been approved by the FDA or had entered clinical trials by 2015 is shown in Figure 1-5 (excluding bone regeneration or dental implants, immunotherapies, vaccines, adjuvants, and antibody-drug conjugates).[26] Liposomal and polymeric NPs account for over 70% of approved nanomedicines excluding nanocrystals (pure drug). This is likely due to their excellent biocompatibility and high loading capacity. At the same time, the proportions of metallic and protein-based NP formulations in the clinical trials are considerably larger than the makeups of these two categories in FDA-approved nanomedicines. Therefore, more formulations from these categories will likely be approved by FDA in the near future.

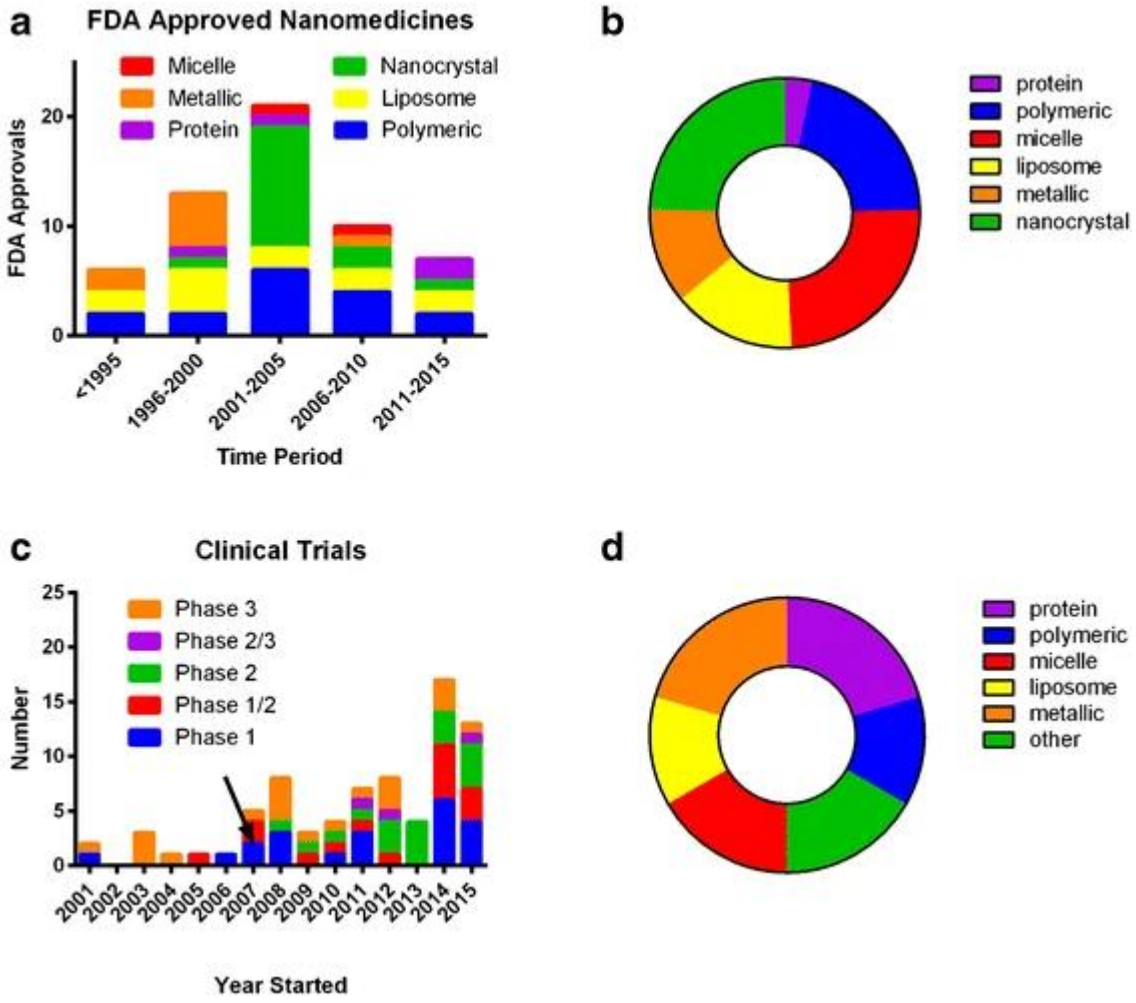

Figure 1-5. Trends in the development of nanomedicines. (a) FDA-approved nanomedicines grouped by NP types; (b) FDA-approved nanomedicines grouped by NP type; (c) clinical trials obtained from clinicaltrials.gov from 2001 to 2015 with the arrow indicating the implement date of US law (FDAAA 801) requiring reporting to FDA database; (d) nanomedicines under clinical trial investigation by category. Reprinted with permission from reference.[26]

In terms of the therapeutic areas of focus, an analysis on 409 clinical trials involving nanomedicines from 2008 to 2020 revealed a shift of focus from oncology to other applications, especially in vaccine and pain management (Figure 1-6). In addition, new therapeutic areas including neural science, eye disease, and genetic disease also emerged, demonstrating the expansion of nanomedicines into non-cancer clinical applications.

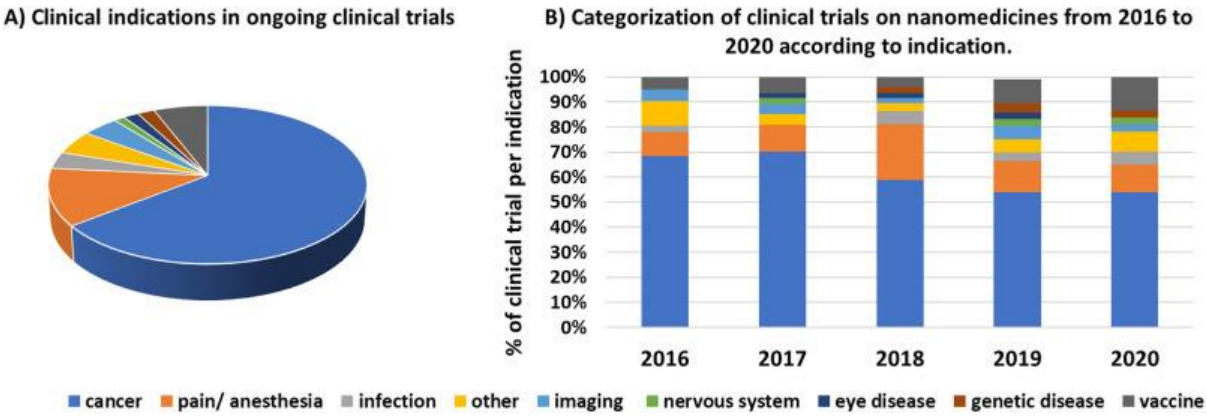

Figure 1-6. Categorization of clinical trials based on nanomedicine formulation per indication: A) analysis of all the 409 trials and b) repartition per year in the 2016- May 2020 period (333 trials). The analysis was performed on 409 clinical trials (active, ongoing, or recruiting), identified in the clinicaltrials.gov database in May 2020. Reprinted from reference.[27]

A summary of the evolution of some landmark nanomedicines which have been approved for clinical use or have entered clinical trials in cancer therapy in recent years is presented in Figure 1-7. Nanomedicines initially began with simple nanoarchitectures as delivering cargos and have later evolved to contain a wider range of materials and an increasing level of complexity to accommodate various therapeutic needs. Early approved nanomedicines were made with micellar (e.g., Genexol-PM) and liposomal (e.g., Doxil® and Marqibo®) formulations. Later, inorganic materials were investigated (NanoTherm®) towards utilizing their unique physical properties (e.g., PTT) to treat cancer. Furthermore, biomaterials, such as albumin, were also used to formulate nanomedicine (e.g., Abraxane®), and then systems that can deliver multiple therapeutics emerged (e.g., VyxeosTM). In more recent efforts, NPs with more complicated structures, including multilayered liposomes (e.g., Stimuvax® and Atu027) and NPs composed of multiple polymers (e.g., Livatag®) was developed. In terms of the payload, the therapeutics of interest in nanomedicines have expanded from small-molecule anticancer drugs to peptides (e.g., Stimuvax®) and small interference RNA (siRNA) (e.g., Atu027). The evolution of the structure and architecture of nanomedicines has enabled them to accommodate multiple functions in a single delivery platform.[28]

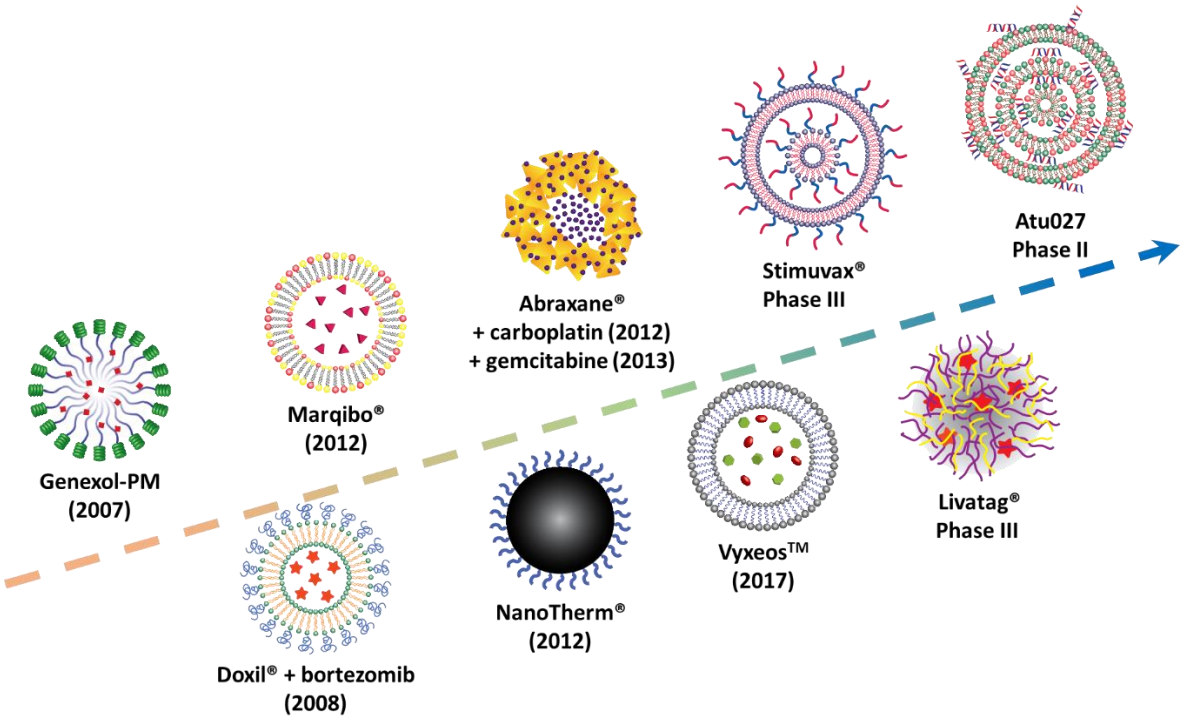

Figure 1-7. Evolution of nanoarchitectures towards custom-fit uses in cancer therapy. The early generations of nanomedicines had simple structures, such as micellar (e.g., Genexol-PM) and liposomal (e.g., Doxil® and Marqibo®) formulations. As the field progressed, more advanced nanoparticles (NPs) were prepared, beginning with NanoTherm® and Abraxane®, and systems that can deliver multiple therapeutics emerged (VyxeosTM). More recently, multilayered liposomal (Stimuvax® and Atu027) and multipolymer (Livatag®) NPs were developed. Furthermore, the payloads (drugs) being delivered have expanded from small-molecule anticancer drugs to peptides (Stimuvax®) and siRNA (Atu027).[28]

1.5 Challenges in translation of nanomedicine

Despite the immense research effort that has been spent in the field of nanomedicine, the translation of the NP-based formulations has been relatively limited. According to Huang et al., close to 60,000 peer-reviewed articles on the topic of nanomedicine were published from 1986 to March of 2020, and over 9000 articles on the topic were published alone in 2018.[29] In contrast, there were only 235 clinical trials enrolled in 2019, among which most were new indications of approved products, such as Doxil® and Abraxane®.[29] The discrepancy between the number of scientific reports and the number of NPs that have been clinically approved or entered into clinical trials reveals the big gap between fundamental studies and the clinical translation in the field of nanomedicine.

Overall challenges involved in the clinical translation of nanomedicine include a lack of batch-to-batch reproducibility, the absence of standard comparison frameworks, the

requirement of long-term stability, difficulties and complexity in scale-up production, good manufacturing practices (GMP) production, and uncertainty and fragmentation in the regulatory framework.[27,30,31] The following sections dissect some of the root causes of the bottlenecks in nanomedicine translation, including NP targeting efficiency, NPs clearance, and industry-level fabrication.

1.5.1 Targeting efficiency of nanoparticles

The enthusiasm for nanomedicines has largely been predicated on their expected targeting properties through either passive or active targeting. However, it seems that the expectation is yet to be reached. An analysis of the *in vivo* tumor targeting efficiency of NPs from 2005 to 2015 concludes that a median of less than 1% of injected dose (ID) reaches the tumors.[32] The fact that about 99%ID of the NPs ended up off target imposes multiple practical hurdles for the translation of NP in tumor targeting. Firstly, the therapeutic dosage level would require a large number of NPs to be injected; therefore, reliable large-scale and reproducible production would be needed. Secondly, because of the limited targeting efficiency, the cost of NP formulations can be unnecessarily high. Thirdly, concentrated NP suspensions would be needed to deliver the required number of NPs with a reasonable injection volume, and the concentrating process can impair the NPs' colloidal stability and reduce the shelf-life. Fourthly, the 99%ID off-targeted NPs will cause systemic toxicity and long-term safety issues, especially when the formulations are not quickly cleared. Lastly, taking into the account drug release rate, cellular uptake efficiency, and subcellular distribution, the dosage requirement can be even higher.[32]

In order to improve the translation of NPs in biomedicine, more research should focus on (i) improving the targeting efficiency, (ii) creating scalable and cost-effective fabrication methods, (iii) engineering nanosystems with high colloidal stability and long shelf-life, (iv) developing nanomedicines with efficient clearance and high biocompatibility, (v) formulating NPs with effective cellular uptake and drug release.

1.5.2 Clearance pathways of nanoparticles

The accumulation and clearance mechanism collectively determine the targeting efficiency and safety of NMs applied *in vivo*. Premature clearance shortens the circulation time of NPs, limiting their opportunity to pass through the diseased area. In addition, with most injected NPs *in vivo* not being able to reach the therapeutic target, the safety of the NPs could become a big concern if they cannot be cleared efficiently from the body. Non-

biodegradable NPs, usually made of inorganic materials, can result in long-term and undesired accumulation. For example, citrate-capped gold NPs are found to almost exclusively accumulate in the liver and with only less than 10% cleared over six months.[33] Lasting presence of NPs in organisms can cause unpredictable adverse effects. A study has found that most of the administrated quantum dots (QDs) accumulate in the liver, spleen, and kidney 90 days post injection in a rhesus macaque model.[34] Long-term retention of QDs can result in leaking of toxic heavy metal ions including Cd^{2+}, Cu^{2+}, Pd^{2+}, and Hg^{2+}.[35] The accumulation of NPs in organs such as the liver and spleen occurs when NMs/clusters of NMs are captured by the mononuclear phagocytic system (MPS) or tissue-resident phagocytes.[36] MPS clearance can lead to both shortened circulation time and unfavorable buildup of NMs in the liver and spleen. This process is initiated by the formation of protein corona and activation of the complement system. The adsorbed protein tags can increase the hydrodynamic diameters (H_D) of the NPs and allow MPS to recognize and scavenge the NPs as alien substances.[37] The formation of protein corona and its characteristics determine the fate of NPs. For instance, receptor-mediated cellular uptake of NPs can be triggered by the recognition of either specific proteins (e.g., complement system proteins) or new epitopes presented by common proteins with conformational changes upon adsorption onto the NP surface.

In addition to the MPS pathway, NPs can also be excreted via the renal clearance pathway similar to small molecule drugs.[38] Renal pathway allows NMs to be eliminated directly through renal filtration while staying intact, thus avoiding extended and unintentional interaction with the biological system.[39] A general agreement within the field on kidney filtration threshold (KFT) is around 6-8nm.[40] However, the renal clearance efficiency is not solely determined by the size only, as other factors such as aspect ratio and surface chemistry are also important. A summary of reported *in vivo* renal clearable nanosystems and their renal clearance efficiencies is presented in Figure 1-8. The renal clearance efficiency is interestingly not always correlated to the size of the NPs. Larger NPs could achieve higher renal clearance efficiency than smaller ones because renal clearance can be modulated by proper tuning of both NP size and surface chemistry.[41] Renal-clearable NP has been the main focus for the imaging agents application because (i) they require fast body elimination as per requirement by FDA;[42] (ii) they are usually within ultra-small size range (sub-10 nm) to possess special optical properties, so are under the KFT; and (iii) they are often made of inorganic materials with special optical and photoelectric properties and are non-

biodegradable. Controlled and effective renal clearance is the preferable elimination route to the hepatobiliary metabolism, as the latter is more likely to cause long-term unforeseeable adverse effects.[43] However, rapid renal clearance might be a drawback for targeted applications as it shortens their circulation time. Therefore, the ideal NPs should have slow and controlled renal clearance to allow a long circulation time but can also achieve high final renal clearance efficiency in a reasonable timeframe, so that most of the NPs go through renal excretion than accumulate in the MPS system. In order to achieve this, the NPs must be invisible to the MPS cells and the size of the nanosystem must be close to the renal clearance cut-off size, so that the NPs can get cleared via the renal pathway slowly but also efficiently (Figure 1-8).

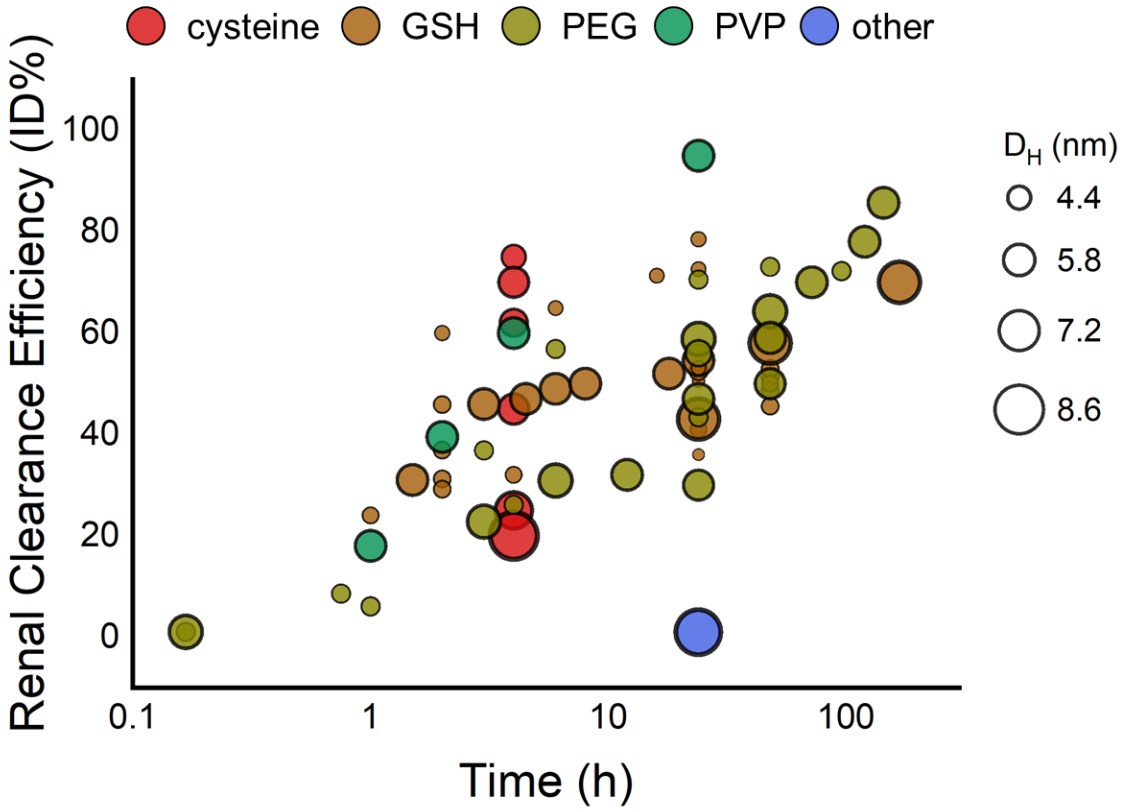

Figure 1-8. Renal clearance efficiency (%ID) of NPs with various H_D, capping agents, and sampling time. Plot generated from data reported in the references.[17,18,50–58,41,42,44–49] GSH = glutathione, PVP = polyvinylpyrrolidone.

1.5.3 Fabrication and formulation

Reliable, scalable, and cost-effective fabrication methods are essential for the translation of nanomedicine for both GMP and financial considerations. Various synthesis methods have been developed in effort to fabricate NPs with controlled size, shape, and

purity. The preparation of nanoparticles fundamentally follows two distinctly different approaches, top-down and bottom-up.[59] The top-down processes involve bulk materials being reduced to particles with nano-dimension using various physical and chemical methodologies. On the contrary, in the bottom-up approach, nanoparticles are formed through the assembly of the atoms, the molecules, or the clusters and thus this is generically termed self-assembly.

Based on the condition, NP synthesis methods can be categorized into dry(physical) methods, wet (chemical) methods, high-temperature (thermal) methods, biosynthesis, and hybrid methods.[60] Some representative dry methods include solid-state synthesis, mechanochemical synthesis, and inert gas condensation synthesis. In solid-state synthesis, NPs are generated directly from solid material assisted by heat and pressure without the involvement of any solvents. It can be easily utilized for mass production but suffers from the large particle size and wide size distribution. In mechanochemical synthesis, raw materials are mechanically activated (e.g., ball milling) to create NPs.[60] Nanocrystalline alloys and ceramics are among the materials commonly produced with this method for electronics, food packing, and biosensing applications. The limitations associated with the mechanochemical synthesis method include low purity and aggregation in large-scale production. The third method under the dry method category is the inert gas condensation, where metal vapor is formed in ultrahigh vacuum chamber filled with inert gas and then condensated into NPs.[60] Although the inert gas condensation can produce NP with well-controlled particle size, its production rate might be too slow for industrial application.

In contrast to dry methods where the size and shape of NPs are inadequately controlled, wet chemical methods involving the use of solvents (including water) are better at producing NPs with more defined size and shape. Wet methods include chemical precipitation, sol-gel, hydrothermal, and emulsion-based synthesis. Chemical precipitation refers to the production of NPs directly from solution, such as metal salt reduction and solvent displacement. It is suitable for large-scale production and has a relatively low cost within the wet method group. The sol-gel methods are based on the hydrolysis polymerization of inorganic alkoxides. The sol can be created with the assistance of surfactant and converted to a gel phase with condensation or gelation reactions. The gel can then be dried and calcinated to form the final nano powder product. The technique offers good control over particle size, shape, morphology, and crystallinity, but has relatively high costs and is limited to certain reagents.[60,61] Emulsion-based synthesis fabricates NPs from a preformed emulsion (water-in-oil or oil-in-water) followed by emulsion polymerization,

emulsion solvent-evaporation, and emulsion precipitation.[62] This method usually shows good control over particle size but can be costly due to the use of surfactants and organic solvent during the process.

The high-temperature method involves the use of high-temperature processing and is thus energy-intensive. Three major subtypes of the high-temperature methods are combustion method, spray pyrolysis, and spray drying synthesis method. In combustion or solution combustion synthesis, an exothermic redox reaction between a fuel and an oxidant takes place in the presence of metal cations. Usually, the metal precursor also serves as the oxidant and the fuel is an organic material that can form complexes with metal ions.[63] Although it does not produce NPs with narrow size distribution and well-defined morphology, it has found its fair share of utilization in industrial settings especially with ceramic and metallic materials, due to the low cost and simple process.[60] The spray pyrolysis synthesis involves spraying NP precursor solutions onto a flame to generate vapors and gases, followed by nucleation and growth of NPs in the gas phase.[60] Like the combustion synthesis, it suffers from wide size distribution, severe aggregation, and high energy consumption. The spray drying synthesis produces NPs by drying the atomized precursor solution droplets (usually in micron size) with hot air in an insulated chamber.[60] The temperature requirement for spray drying is relatively lower than the previous two methods, as long as it is above the vaporization temperature of the solvent. The characteristics of each of the above-mentioned NP manufacturing methods are summarized in Table 1-2.

Other methods for making NPs include biosynthesis, which involves the use of microorganisms including bacteria or fungi.[64] Biosynthesis methods can render NPs with less toxicity, higher biocompatibility, and are eco-friendly in nature. Current research is focusing on improving particle fabrication efficiency and exploring biomedical applications for industrial implementation and commercial adoption.[64] Although each kind of synthesis method has its own advantages and limitations, wet chemical methods with narrow size distribution, well-controlled shape, and satisfactory scalability are more suitable for manufacturing NPs for biomedical applications.

Table 1-2. Features of common NP synthesis methods. Reproduced based on reference with permission.[60] (temp. = temperature, distribu. = distribution, rel. = relative, crystal. = crystallinity)

Synthesis methods	Advantages	Disadvantages	Charateristics of particles				
			Size	Size distrib.	Shape	Crystal. degree	Phase Purity

Dry Methods							
Solid-state synthesis	Low cost, large scale, simple to produce, eco-friendly	Severe aggregation, high temp., slow reaction	Usually micron	Wide	Diverse (usually irregular)	Very high	Low
Mechano chemical synthesis	Low cost, large scale, simple & efficient	Severe aggregation, high energy consump., long milling time, potential contamin. of NP due to metal balls	Micro to nano	Wide	Diverse	Very high	Low
Inert gas condensa-tion synthesis	Precies control of particle size and size distribution	High cost due to equipment, extremely slow rate, lab-scale only	Nano	Narrow	Diverse	Various	Various
Wet Methods							
Chemical precipi-tation synthesis method	Low cost, large scale, low temp., energy saving, solvent-free, simple, rapid preparation	Aggregation, product size not easy to control, time-consuming, may use harsh chemical & cause residual toxicity	Micron to nano	Wide	Diverse	Low	Various
Sol-gel synthesis method	Narrow size distribution, precise size & morphology control, degree of porosity control, high purity	High cost, special reagents, time-consuming, small scale, solvents may be harmful, particle agglomeration at certain cases	Nano	Narrow	Diverse	Usually low	High
Hydro-thermal synthesis method	High crystallinity, precise control of size & shape, most materials are soluble at high temp.	High cost (autoclaves), impossible to observe the reaction process, potential safety issues, difficult to control the process, low reliability	Micron to nano	Narrow	Needle, rod, octa-hedral	Usually low	Various
Emulsion synthesis	Narrow size distribution, easy preparation, minimal agglomera-tion, precise control of size & shape, thermo-dynamically stable	High cost, time-consuming, requires a large amount of surfactant, external factors (pH or temp.) affect the stability of the process	Nano	Narrow	Needle, rod	Usually low	Various
High-temperature Methods							
Combus-tion synthesis	Simple preparation process, homo-geneity of products, low cost	High energy consump., severe aggregation	Micron to nano	Wide	Diverse (usually irregular)	Various	Usually high
Spray	Low cost (wide	High energy	Micron	Rel.	Diverse	High	Various

pyrolysis synthesis	variety of possible low-cost precursors), high crystallinity, high purity of materials, size control	consumption, severe aggregation	to nano	narrow			
Spray drying synthesis	Large scale, high purity	High energy consumption	Micron to nano	Wide	Diverse (can be cubic)	Various	High

Although multiple challenges currently hinder the efficient translation of nanomedicine, it still remains a high-value and low-cost solution to address unmet medical needs according to European Technology Platform on Nanomedicine (ETPN).[27] Effective integration of knowledge, communication, and cooperation among different stakeholders, such as research institutions, industry, healthcare providers, patients, and regulatory bodies, is required to accelerate the transition from academic development to proven clinical value.

1.6 Research aims

The aims of the research in this thesis are to tackle the current translational bottleneck problems in nanomedicine, specifically developing nanosystems with precise size control and facile fabrication. A novel process-engineered synthesis method was developed to achieve fine tuning of particle size at a single nanometer resolution for making ultrasmall gold NPs (uGNPs). The produced uGNPs were subjected to various *in vitro* biocompatibility tests to establish the basic safety profile and verify their potential as nanoplatforms in biomedical applications. The feasibility of making instant nanoformulation of drug delivery systems was explored using complex coacervation. As a proof-of-concept study, the model nanocoacervate delivery system was further investigated for potential applications in future cancer therapy against multidrug resistance.

1.7 Outline of the thesis

Chapter 1 summarizes the state-of-the-art development in the field of nanomedicine. The chapter reviews the different types of NPs, the interaction between NPs and biological components, various biomedical applications of NPs, NPs in clinics (both approved and under clinical trials), and major challenges in the translation of nanomedicines.

Chapter 2 describes the development of the process-engineered synthesis of uGNPs and an effort to understand the mechanism of gold seed formation by a combination of tannic

acid and sodium citrate through kinetic studies. A comprehensive set of characterization of uGNPs is covered in the chapter as well.

Chapter 3 investigates the safety and the biocompatibility of the uGNPs manufactured with the novel process-engineered synthesis method. Specifically, the colloidal stability, cytotoxicity, immunotoxicity, complement system compatibility, influence on cytokine release profile, and blood compatibility of the uGNPs were examined.

Chapter 4 depicts the fabrication of a nanocoacervate drug delivery system as a way to create instant nanoformulation of a drug for bedside preparation. The chapter covers the assembly mechanism of the nanosystem, optimization of fabrication conditions, characterization, and pH-responsive drug release.

Chapter 5 demonstrates the delivery of a therapeutic agent, doxorubicin, using the nanocoacervate to various cell lines in both 2D and 3D models *in vitro*. The endocytosis mechanism, cytotoxic effect, and drug penetration and retention were carefully studied. The system shows great potential as a therapeutic agent against multidrug-resistant cancers.

Chapter 6 presents the main findings of this work and outlines future studies that can bridge the gaps that are not closed by this study as well as possible future research areas that can be built upon this work.

2 Process-engineered synthesis of ultra-small gold nanoparticle with nanometer tunability

2.1 Introduction

This chapter depicts the strategy to develop a process-engineered synthesis of ultra-small gold nanoparticles (uGNPs). The fabrication process is based on a stepwise seed-templated growth strategy. A series of uGNPs with sizes ranging from 3 to 15 nm were fabricated with an engineered synthesis method that comprises an initial seed template formation step and multiple discrete growth steps to achieve nanometer-by-nanometer tunability. The initial seeding reaction was achieved by using competing reducing agents, sodium citrate (NaCit) and tannic acid (TA), and a careful kinetic study was conducted. Both NaCit and TA can reduce gold precursors to NPs individually. The TA, a much stronger reducing agent than the NaCit, can reduce the gold precursor at a much faster rate but produce NPs with wider size distribution. In contrast, the NaCit, as a milder reducing agent, can reduce gold precursor in a more controlled manner and result in more narrow size distribution. By exploiting the combination of these two reducing agents, an initial burst generation of a large number of seed particles and a consequential controlled growth step can be accomplished. The TA-NaCit method was then utilized to produce uGNP seed templates. With the help of recent advances in the seeded growth method, a process-engineered synthesis method for making size-tunable uGNPs is devised. The obtained uGNPs were characterized for their size, geometry, localized surface plasma, ζ-potential, and potential for surface modification.

2.1.1 Biomedical application of gold nanoparticles

Gold nanoparticles (GNPs) have taken the center stage of nanoparticle (NP)-based biomedical application for years, owing to their well-established synthesis routes, relatively higher content in the earth crust, desirable safety profile, superb processability, and diverse physical properties.[65] The unique characteristics of GNPs, such as high surface-to-volume ratio, broad optical properties, and ease of surface functionalization, provide important advantages in drug delivery, bio-diagnostics, biophysical studies, biosensing, and medical therapy.[66]

Table 2-1. Summary of biomedical applications involving the use of GNPs.

Types of Application	Properties of GNPs utilized to achieve action

Therapeutic applications	
Drug Delivery	GNPs allow loading of drugs via covalent and non-covalent linkage, while their nano size allows targeting through both passive and active targeting strategies.
Photodynamic Therapy (photosensitizer delivery)	Loading of hydrophobic photosensitizers (PS) with colloidal gold increases the solubility & bioavailability and achieves targeted delivery.
Photothermal Therapy	Localized surface plasmon resonance (LSPR) of GNPs enhances absorption and scattering of near-infrared light and conversion of photon energy to heat.
Radiofrequency (RF) Ablation	GNPs can quickly absorb RF energy and release heat to surrounding regions due to their metal nature and quantum characteristics.
Radiotherapy	GNPs with high atomic numbers can absorb x-rays efficiently and deposit this energy locally, mostly by the emission of photoelectrons, Compton scattering and Auger electrons.
Contrast agents for imaging	
X-ray Imaging & Computed Tomography	GNPs with high atomic numbers have high x-ray absorption coefficients.
Photoacoustic Imaging	LSPR of GNPs enhances electric field coupling and optical absorption.
Optical Coherence Tomography	LSPR of GNPs enhances backscattering at specific wavelengths.
NIR Fluorescence Imaging	GNPs with the size of a few nanometers can be luminescent and visible under NIR fluorescence imaging.
Biosensing/In vitro diagnosis	
Detection of proteins, oligonucleotides, small molecules, pathogens, etc.	Colorimetric sensing, fluorescence-based sensor, electric & electrochemical sensor, surface plasmon resonance sensor, bio-barcode assay sensor etc.

2.1.1.1 GNPs as drug delivery systems

GNPs have been the subject of intensive studies in carrying therapeutic agents. GNP-based drug delivery systems can passively or actively target tumor sites, where gold colloids can extravasate into the tumor stroma because of the defective vasculature and increased lymphatic drainage leading to its accumulation at the target site (Figure 2-1).[67] Active targeting relies on the surface tuneability of GNPs specifically designed for the target molecules to provide high specificity and selectivity.[68] Loading of drugs onto GNPs can be achieved with both covalent and non-covalent linkages. Drugs covalently conjugated to GNPs through gold-thiol chemistry can be released through glutathione (GSH) displacement, while other linker cleavages can be accomplished with changes in pH and presence of enzymes.[69] Targeted delivery of drugs can also be carried out efficiently using gold colloids by loading drugs onto GNPs through non-covalent interactions. For example, polymer encapsulated GNPs provide an amphiphilic surrounding for the entrapment of hydrophobic silicon phthalocyanine 4, a photodynamic therapeutic (PDT) agent.[70] PDT treatment is mainly achieved by focusing the light source on the diseased area of the body. The spectrum of light used here is in the range of 630-900 nm, or near infrared region (NIR) to generate reactive singlet oxygen of the reactive oxygen species (ROS) for cancer cells destruction.[71] This range of wavelength minimizes the light extinction by intrinsic chromophores in the

normal or healthy tissue.[72] Loading hydrophobic photosensitizer onto colloidal gold increases the bioavailability and shortens the time to reach maximum accumulation of these drugs in tumors.

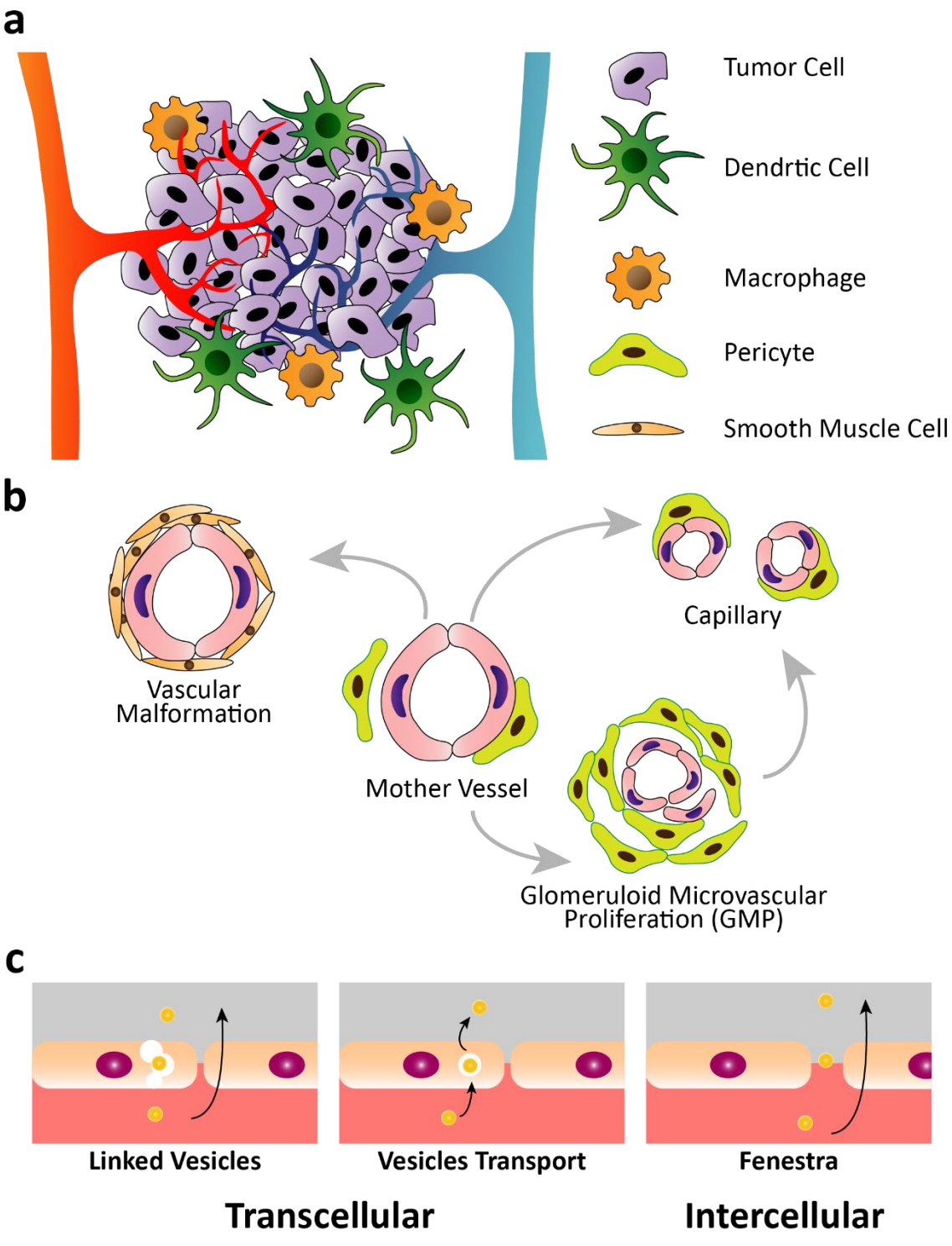

Figure 2-1. Schematic illustration of the tumor microenvironment, vascular characteristics, and NP leaking mechanism; (a) Schematic illustration of the tumor microenvironment. (b) Mother vessels with thinned or compressed endothelial cells, degraded basement membranes,

and pericyte detachment are highly permeable to both small molecules and proteins. Mother vessels can further differentiate into glomeruloid microvascular proliferation, vascular malformations, and capillaries. (c) Schematic representation of transcellular and intercellular transport of NPs from across vessel wall.

2.1.1.2 GNPs as therapeutic agents

In addition to acting as chaperones,[73] GNPs can serve as therapeutic agents themselves, thanks to their unique optical properties. Currently, regional hyperthermia, radiofrequency ablation (RFA), and radiotherapy are actively being exploited for localized cancer treatment.[74] In regional hyperthermic tumor therapy or photothermal therapy (PTT), the cancerous cells are damaged upon exposure to elevated temperatures, where membrane integrity, DNA damage, and induction of apoptosis, and necrosis within a few hours can be achieved.[75] In one study, it has been shown that GNPs can act as PTT agents and selectively destroy cancerous cells at very low laser frequency.[76] Citrate capped GNPs (15 nm) have also been deployed as PTT agents against A431 cells. This study shows combined PTT and PDT effect upon exposure to low levels of laser light, as GNPs induce the destruction of the malignant cells through ROS mediated apoptosis.[77] RFA in conjunction with GNPs has proved to be an effective treatment strategy for liver cancer cell (HepG2) lines.[78] GNPs offer an attractive advantage in radiotherapy owing to their excellent optical properties, surface plasmon resonance, and surface modalities. Upon X-ray irradiation, GNPs have been shown to induce cellular apoptosis by the generation of ROS.[79] This therapeutic treatment strategy has effectively increased the percentage of cancer cells killed without harming the nearby surrounding healthy tissue.[80]

2.1.1.3 GNPs as imaging agents

Due to their unique physicochemical properties, especially the interactions with electromagnetic waves, GNPs have been exploited as imaging agents in multiple clinically relevant techniques. Possessing higher X-ray absorption coefficients, less bone and tissue interference, and a wider imaging window than conventional iodine-based contrast agents, GNPs have been investigated as contrast agents for both X-ray imaging and computed tomography (CT).[81] In addition, The ability of GNPs to absorb and scatter light in the NIR region makes them one of the most potent candidates as contrast agents in other biomedical imaging applications, such as photoacoustic imaging (PAI), and optical coherence tomography (OCT).[82] In addition, uGNPs with small enough sizes can provide luminescence with NIR-emitting properties and can thus serve as contrast agents for NIR fluorescence

imaging.[18] The application of gold nanostructures in *in vivo* imaging techniques allows certain advantages over conventional NIR organic dyes, such as avoiding rapid photobleaching, better detection sensitivity, improved stability in biological systems, and possible multimodality.[83]

2.1.1.4 Applications of GNPs in biosensing and *in vitro* diagnosis

GNPs are also widely exploited in biosensing and *in vitro* diagnosis applications. The phenomenon of Localized Surface Plasmon Resonance (LSPR) of GNPs has been most widely used for the development of new biosensors. Upon excitation by an external light source, GNPs produce an intense absorption and scattering as a result of the collective oscillation of the conductive electrons present at their surface and conduction bands. The sensing efficiency of GNPs depends upon their intrinsic LSPR, with wavelengths around 510-530 nm for gold nanoformulations of around 4-40 nm, which can be used for biosensing.[84] The binding of molecules onto the particle surface changes the LSPR. This attribute of GNPs has been utilized, for example, for the detection of DNA, by taking advantage of the binding affinity of ssDNA and dsDNA onto their surface.[85] Fluorescence-based GNP biosensors have been developed by utilizing the quenching property of the NMs. Molecular nano-beacons have been used to detect single-base mismatches in DNA with higher sensitivity as compared to conventional molecular beacons.[86]

2.1.1.5 GNPs in clinical trials

Although, GNPs are yet to be used in clinics, a few of them have been made it to the clinical trials. These nanodrugs harness the light-absorbing ability of GNPs and are being currently explored for treating solid tumors and acne. One such gold colloid nanodrug approved for clinical trials is AuroLase, developed by Nanospectra, which comprises silica-gold nanoshells coated with polyethylene glycol (PEG) designed for the treatment of solid tumors by thermal ablation using a NIR source.[87] In another example, Sebashells developed by Sebacia Inc., which are similar to AuroLase, have been applied to treat acne by disrupting overactive sebaceous glands in the skin.[88] These Sebashells are topically administered to the site of acne, delivered deep into the sebaceous glands by low-frequency ultrasound, and ultimately stimulated via a NIR laser, utilizing the heating capacity of the gold nanoshells for effective acne treatment. Some other GNPs that have entered the clinical trials are summarized below.

Table 2-2. GNPs in clinical trials.

Condition or disease	Properties of noble metal NPs	NCT number	Phase	Status
Coronary Artery Disease Atherosclerosis	GNPs with silica-iron oxide shells with photothermic burning or melting effect onto the lesion	NCT01436123	Phase I	Terminated (under political pressure)
Type 1 Diabetes	GNPs with attached peptide fragment related to insulin	NCT02837094	Phase I	Recruiting
Gliosarcoma Recurrent Glioblastoma	Small GNPs with nucleic acid arranged on the surface (NU-0129)	NCT03020017	Phase I	Active, not recruiting
Stable Angina, Heart Failure, Atherosclerosis, Multivessel Coronary, Artery Disease	GNPs with silica-iron oxide shells with photothermic burning or melting effect onto the lesion	NCT01270139	N/A	Completed
Caries Class II	AgNPs & GNPs suspended in 70 % isopropyl alcohol used for cavity pre-treatment	NCT03669224	N/A	Not yet recruiting
Pulmonary Hypertension	GNPs coated with organic ligands as sensor array for detecting volatile organic compounds in exhaled breath in patients	NCT02782026	N/A	Unknown
Stomach Diseases	Functionalized GNPs & carbon nanotubes nanosensors array identifying gastric diseases	NCT01420588	N/A	Unknown
Parkinson's Disease	Functionalized GNPs & carbon nanotubes nanosensors array identifying Parkinson's diseases	NCT01246336	N/A	Completed

2.1.2 Parameters affecting interactions between GNPs and biological systems

Surface functionalized gold colloids have been extensively studied for interaction with the cell membrane to achieve efficient and improved drug delivery.[89] The cellular uptake efficiency depends on the physicochemical parameters of the GNPs including shape, size, surface charge, and surface chemistry. For instance, spherical GNPs exhibit greater cellular uptake than rod nanostructures with comparable size and surface chemistry.[90] In terms of size, it has been reported that 40-50 nm particles have the most effective cellular internalization.[91] Similar result was obtained in a separate study where 50 nm GNPs exhibit a relatively faster internalization rate than other sizes.[90] Surface charge also plays an important role in cellular internalization. The exterior of the cell is mostly anionic; hence, positively charged noble metal NPs can easily traverse through the cell membrane via electrostatic interaction.[92] Surface chemistry of GNPs is also critical in regulating cellular uptake. It was observed that surface ligand rearrangement on GNPs can regulate cell membrane permeability.[93] GNPs functionalized with an ordered arrangement of amphiphilic molecules were able to penetrate the cell membrane more efficiently than particles with a disordered arrangement of the same

molecules that were entrapped in vesicular bodies.[93] Cell type also affects the interaction between GNPs and cells due to the difference in cellular uptake mechanisms. It was found in one study that MDA-MB-435 cells were able to internalize more GNPs in the aggregation form than in the monodisperse form, the opposite of Hela and A549 cells.[94]

2.1.3 Need for systematic approaches to making ultra-small GNPs with fine size tunability

As mentioned above, particle size is one of the determining factors for GNPs to bypass biological barriers, possess unique physical properties, and undergo favorable clearance pathways. In general, smaller size particles are favorable as a consequence of their higher stability in colloidal form, as well in efficiently avoiding detection by the immune system and premature clearance.[95] Scientists have also shown that smaller size has led to better tumor penetration,[8] less macrophage uptake,[96] longer blood circulation time,[97] and higher renal clearance.[43] Other advantages of having smaller particle sizes include larger specific surface area and unique physical properties, many of which are only possible when the particle size reaches sub-10 nm and are extremely useful for diagnostic purposes.[98] Although it seems that smaller particles should be beneficial in biomedical applications, optimal particle size is believed to be application-specific.[99] For example a recent report showed that among 3, 15, and 200 nm GNPs, the 15 nm GNPs have the best delivery rate in focused ultrasound-induced blood-brain barrier opening delivery, even better than their smaller counterparts due to longer blood circulation time.[100] Therefore, the abilities to fabricate ultrasmall NPs and to finely tune the particle size are both highly desirable. In addition to biomedical applications, sub-10 nm GNPs possess unique and appealing intrinsic properties which are absent in their larger counterparts. Within this ultrasmall range, the composition of the surface atoms starts to outweigh the interior atoms. Due to the decreasing atomic coordination number at the surface, the GNPs exhibit enhanced reactivity leading to catalytic properties, plasmon shifts, corrosion, stability etc.[101,102]

A big arsenal of fabrication methods for making GNPs of a wide range of sizes and geometries has been reported since Faraday discovered the very first GNPs synthesis method via the reduction of tetrachloroaurate with phosphorus.[103] One of the most frequently used GNPs synthesis is the wet chemical reduction of tetrachloroauric acid ($HAuCl_4$) using NaCit pioneered by Turkevich.[104] However, the Turkevich method fails to prepare sub-10 nm uGNPs. To prepare uGNPs, strong reducing agents, such as $NaBH_4$, are usually used with

strong capping ligands to limit particle growth.[105] This can be performed in either two-phase (Brust method) or single-phase systems to render hydrophobic and hydrophilic uGNPs. Hydrophobic capping agents include phosphines,[106] amines,[107] and alkanethiols,[108] while hydrophilic capping agents include polymeric stabilizers,[109] strong binding cationic surfactants,[110] and thiols.[111] These methods result in passivated particle surfaces which can be difficult to further modify. In addition, such methods frequently result in polydispersed particle size, and the use of strong and toxic capping agents makes it difficult for future surface modification and requires detoxification steps for use in biological settings.[112] Mühlpfordt, and later Slot and Geuze, proposed the use of TA and NaCit as combined reducing agents, which led to the synthesis of sub-10 nm uGNPs.[113,114] However, the reaction mechanism of this TA-NaCit method is poorly understood, and although the method has some tunability over particle size, it does not show systematic control at a nanometer-by-nanometer level.

Several fabrication methods have been devised to prepare GNPs with tunable size. Brinas *et al*. fabricated GNPs with sizes between 2 to 6 nm by varying the pH of the reaction mixture with a $NaBH_4$ method,[115] while Ohyama *et al*. prepared GNPs in the similar size range to a sulfur-based ligand system by adjusting the thiol/$HAuCl_4$ ratio.[116] Song *et al*. synthesized GNPs with diameters between 1 and 6 nm using the reduction of triphenylphosphine gold chloride by *tert*-butylamine borane, and the size control was achieved by changing the fraction of $CHCl_3$ in a mixture with benzene.[117] In another study, Jun *et al*. used milli- and micro-fluidic flow systems to make 7 to 25-nm GNPs, where the particle size was tuned by modifying the ratio between the reducing agent, ascorbic acid, and the gold precursor as well as the flow rate of the solutions.[118] Although these mentioned methods all achieved size control, they involve the use of strong capping agents, organic solvents, or complicated apparatus; therefore, are not suitable for mass production of GNPs for biomedical applications.

An alternative method to fabricate GNPs of controllable sizes is to utilize the process engineering method that splits the growth of GNPs into discrete steps by limiting the reagents.[119,120] In the current report, a series of uGNPs with well-predicted size were fabricated in a systematic way by using the TA-NaCit method as the seed formation step followed by sequential stepwise addition of Au precursor to the reaction mixture. Such a system is of great interest for biomedical applications, since ultra-small NPs tend to be more biocompatible and the size tunability is valuable for tailoring disease-specific delivery

requirements. In addition, a careful kinetic study of the TA-NaCit method is conducted to provide new insight into the reaction mechanism.

2.2 Materials and Methods

2.2.1 Synthesis of Au seed

Chloroauric acid, tannic acid, potassium carbonate, and sodium citrate were purchased from Sigma Aldrich, United Kingdom. All materials were used as received without further purification. A custom lab-made apparatus setup as depicted in Figure 2-2, was used to synthesize uGNPs of various sizes in a one-pot fashion. In a typical synthetic procedure, 25 mL aqueous solution containing 2.2 mM sodium citrate (NaCit, Sigma Aldrich), 6 mM potassium carbonate (K_2CO_3, Sigma Aldrich), and 1.7 µM tannic acid (TA, Sigma Aldrich) was brought to boil under reflux for 5 minutes and then kept at 80°C under N_2 purge and reflux. Chloroauric acid stock solution (20 mM) was added to the reaction solution using a syringe to achieve a final Au^{3+} concentration at 125 µM. The reaction mixture was then stirred for 15 minutes.

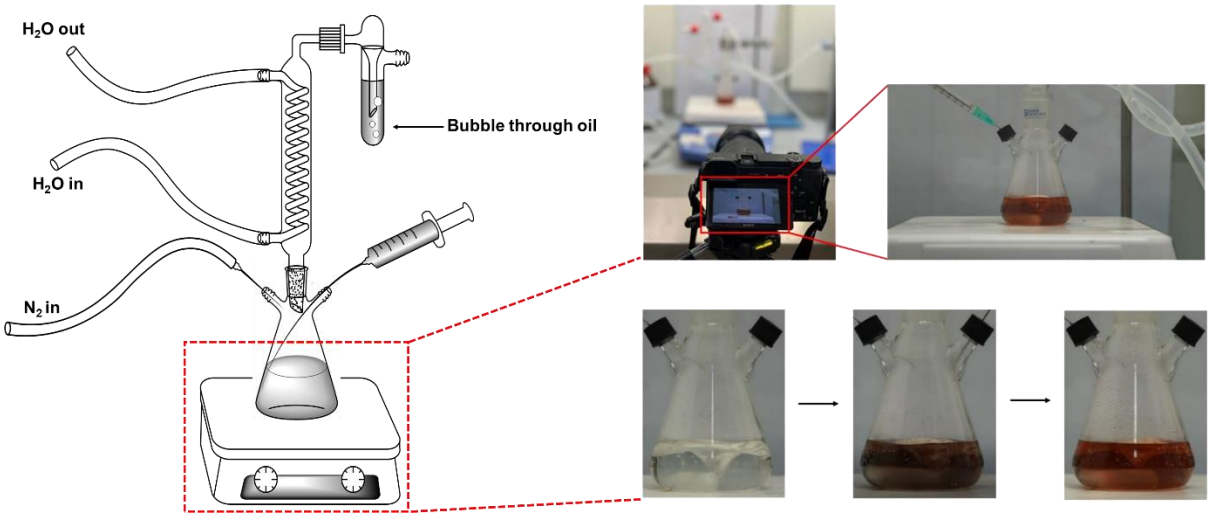

Figure 2-2. Schematic illustration of one-pot synthesis set-up for seeded growth of uGNPs, and photographs showing the set-up to studying the reaction kinetics by recording the color change of the reaction mixture over the synthesis course.

2.2.2 Seed-templated growth of uGNPs

After the color of the seed solution was persistent, 10 mL of solution was extracted from the flask and replaced by 10 mL of 2.2 mM sodium citrate. The reaction mixture was heated up to 80°C, before adding an aliquot of chloroauric acid (20 mM). The reaction was again allowed to proceed for at least 25 minutes until the color of the solution stayed constant.

This process was repeated several times to obtain the uGNPs products with increasing diameters. The final [Au^{3+}] in each synthetic round are listed in Table 2-3.

Table 2-3 Au^{3+} Concentration (mM) of each round of uGNPs synthesis

$uGNP_3$	$uGNP_5$	$uGNP_6$	$uGNP_7$	$uGNP_8$	$uGNP_{10}$	$uGNP_{12}$	$uGNP_{15}$
0.125	0.15	0.175	0.2	0.225	0.25	0.275	0.3

2.2.3 Investigating the role of tannic acid and sodium citrate in uGNPs synthesis

To understand the role of TA and NaCit in the synthesis of uGNPs, kinetic studies were performed using the same reaction setup. One set of experiments were conducted by varying TA concentration and keeping NaCit concentration fixed at 2.2 mM, and in the second set of experiments, NaCit concentration was varied at a fixed TA concentration of 0.1 mM. The reaction was recorded using a Sony Alpha A6000 camera (Figure 2-2). The red color component as a fraction of the total red, blue, and green components was extracted using MATLAB's Image Processing Toolbox™. The red component extraction was performed by H. Ibrahim-Hashi and R. Manchanda, who were Part IIb students in the group. The evolution of the red component fraction as a function of time was used as the basis for the calculation of reaction rates. The reaction profiles and the rates were used to investigate and propose the underpinning reaction mechanism and determine the corresponding kinetics.

2.2.4 uGNPs characterization

The hydrodynamic diameter (D_H) and Zeta (ζ)-potential of the as-synthesized uGNPs were characterized with Dynamic Light Scattering (DLS) and Electrophoretic Light Scattering (ELS) using Zetasizer Nano ZS (Malvern PANalytical Products, United Kingdom) with at least 90 scans for each sample. Transmission Electron Microscopy (TEM, FEI Tecnai F20) was used to confirm the size and shape of the GNPs. The particles were first subjected to ligand exchange with oleylamine and phase transferred to hexane. It was accomplished by mixing 0.5 mL as prepared uGNPs solution with 0.5 mL/1.5 mM oleylamine/hexane solution. The uGNPs/hexane solutions (10 µL) were then drop cast onto carbon-coated grid and allowed to air-dry overnight. The particle size distributions were analyzed using ImageJ by counting at least 100 particles. The LSPR of uGNPs was measured by UV-Vis spectroscopy from 210 to 1000 nm. The LSPR was determined as the absorbance peak wavelength for each sample.

2.2.5 Theoretical calculation of particle numbers and surface area

The uGNPs concentration or number of particles per unit volume was calculated based on particle size obtained from TEM imaging using the following equation:

$$[\#particles] = \frac{3 \cdot [Au^{3+}] \cdot m_{a,Au}}{4 \cdot \rho_{Au} \cdot \pi \cdot \left(\frac{d}{2}\right)^3}$$

where $[Au^{3+}]$ is the molar concentration of gold ion added in each synthesis step as summarized in Table 2; $m_{a,Au}$ is the atomic mass of gold, ρ_{Au} is the density of elemental gold, and d is the particle size obtained with TEM image. The total surface area of each uGNPs sample is calculated according to the equation:

$$A_{surface} = 4\pi \left(\frac{d}{2}\right)^2 \cdot [\#particles] \cdot v_{sample}$$

The theoretical particle sizes of each uGNPs sample were also calculated based on the #particles and particle size of the seed ($uGNP_3$) using the equation:

$$Diametre\ (uGNP_{n+1}) = 2 \cdot \sqrt[3]{\frac{3 \cdot [Au^{3+}] \cdot m_{a,Au}}{4 \cdot \rho_{Au} \cdot \pi \cdot 0.6 \cdot [\#particles(uGNP_n)]}}$$

2.2.6 uGNPs PEGylation

The 8-arm PEG-SH (Biochempeg Scientific, Massachusetts, USA) was conjugated to uGNPs through gold-thiol linkage. The as-synthesized uGNPs samples were first diluted to reach the identical surface area. The dilution factors (DF) are summarized in Table 2. In a typical reaction, 2 mL of uGNPs was mixed with the desired amount of PEG solution and stirred for 1 hour in 60°C water bath. The change in hydrodynamic diameter, LSPR, and ζ-potential were measured using the same method as for bare uGNPs. The PEGylated uGNPs were purified using Amicon® centrifuge tube 3 times right before the next modification step.

Table 2-4. Dilution factor (DF) of each uGNPs sample to reach the same surface area

uGNPs	3 nm	5 nm	6 nm	7 nm	8 nm	10 nm	12 nm	15 nm
DF	2.18	2.42	1.86	1.47	1.27	1.22	1.02	1.00

2.2.7 Flocculation test of PEGylated uGNPs

Flocculation tests with NaCl were conducted on both bare uGNPs and PEGylated uGNPs. NaCl (1 M) was added stepwise to both as-prepared uGNPs and PEGylated samples. The samples were measured by UV-Vis spectroscopy after each addition of NaCl. The shift in peak position indicates the aggregation of NPs.

2.3 Results and Discussion

2.3.1 The seed-templated synthesis for size tunable uGNP fabrication

The objective of the study is to develop a process-engineered synthesis procedure to obtain sub-10 nm uGNPs of different sizes and to tune the particle size accurately for biomedical applications. The synthesis process was created based on the concept of controlled stepwise seed-templated growth with suppressed secondary nucleation.[119] The synthetic procedure can be divided into two parts, namely the seed template formation step and the sequential controlled growth step (Figure 2-3). The initial seed template formation was based on the TA-NaCit synthesis method with reaction conditions established in previous reports, including reaction temperature, pH, and reagent addition sequence.[121,122] Additionally, a controlled reducing environment was created by pre-boiling the reaction solution and implementing a nitrogen purge throughout the reaction to exclude the effect of oxygen level variation as much as possible.

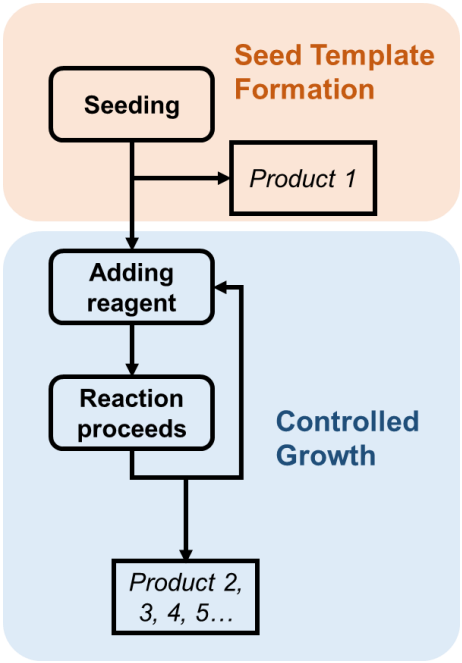

Figure 2-3. Flowchart showing the engineered uGNPs synthesis procedure containing seed formation step and controlled growth step.

2.3.2 Synthesis of seed template uGNP using TA-NaCit reaction

The TA-NaCit GNP synthesis method, discovered by Mühlpfordt in 1982, can successfully produce sub-10 nm uGNPs with just a trace of TA added to the original Turkevich reaction but has been relatively underinvestigated compared to its predecessor.[104,113] It is thus selected as the first reaction in the synthesis process to produce templates for further growth of uGNPs. However, the reaction mechanism to render monodispersed uGNPs with facile wet chemistry reaction conditions and easily modifiable surfaces remains unclear. In an effort to better understand the factors affecting the size of particles and the reaction mechanism, the roles of TA and NaCit as reducing agents on the final particle size of uGNPs, and the reaction kinetics were studied.

2.3.3 Investigation on the impact of reagent stoichiometry on particle size

First, the impacts of TA/Au and NaCit/Au ratios on the final uGNPs particle size are shown in Figure 2-4. The particle size of obtained uGNPs is unaffected within the TA concentration range between 0.25 μM and 17 μM and becomes relatively large with a very low TA concentration. This is expected because at negligible TA concentration, the TA-NaCit method essentially turns into the Turkevich method. The NaCit concentration, on the other hand, seems to have a smaller impact on the size between 0.75 mM to 3.75 mM. The observation suggests that TA acts as a dominant regent determining the uGNP particle size in the TA-NaCit method. Although the concentrations of neither TA nor NaCit alter the particle size within the respective range, higher concentrations of both reagents led to a noticeably faster reaction rate. Therefore, the reaction kinetics were investigated with various TA and NaCit concentrations.

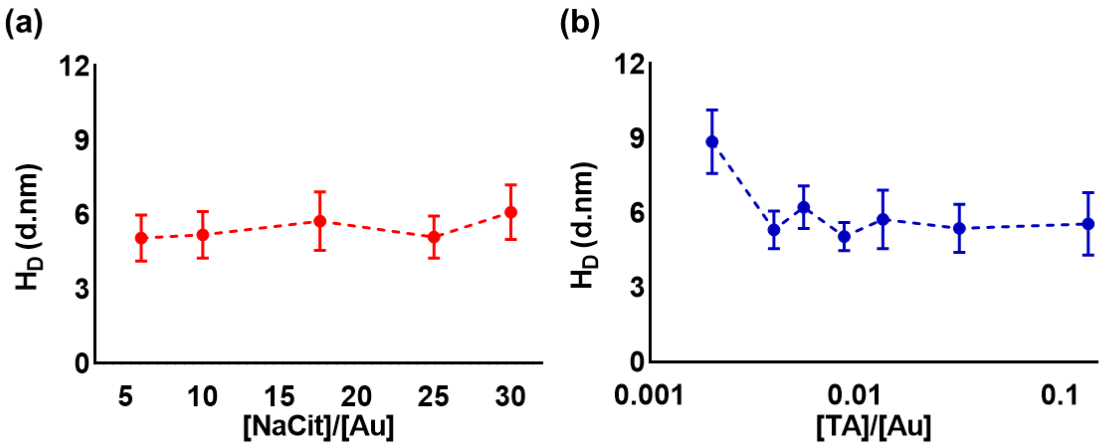

Figure 2-4. Impact of NaCit and TA concentrations on particle size; Hydrodynamic diameter (H_D) of GNPs produced at various (a) NaCit and (b) TA to gold precursor ratios using the TA-NaCit method.

2.3.4 Investigation on the impact of reagent stoichiometry on reaction kinetics

To study the reaction kinetics, the reaction progression was recorded using a video camera and the change in color of the reaction mixture was analyzed with MATLAB's Image Processing Toolbox™ in a Red-Green-Blue (RGB) mode. The red component (R/RGB) was taken in substitution for peak absorbance in the UV-Vis spectrum due to the fast reaction rate and a lack of in-situ UV-Vis apparatus.[123] In this fashion, real-time monitoring of the reaction profile was achieved. A side-by-side comparison of reaction profiles between Turkevich reaction and TA-NaCit is exhibited in Figure 2-5. Although the overall curve shapes of the two types of reaction are similar, the TA-NaCit reaction profile has an initial "jump" which is not shown in the Turkevich reaction. The reaction rate of TA-NaCit is also much faster than Turkevich reaction with a similar NaCit/Au ratio (both around 17.5 in Figure 2-5). It can be inferred that the addition of the small amount of TA is responsible for the initial burst of reaction and the increase in the overall reaction rate.

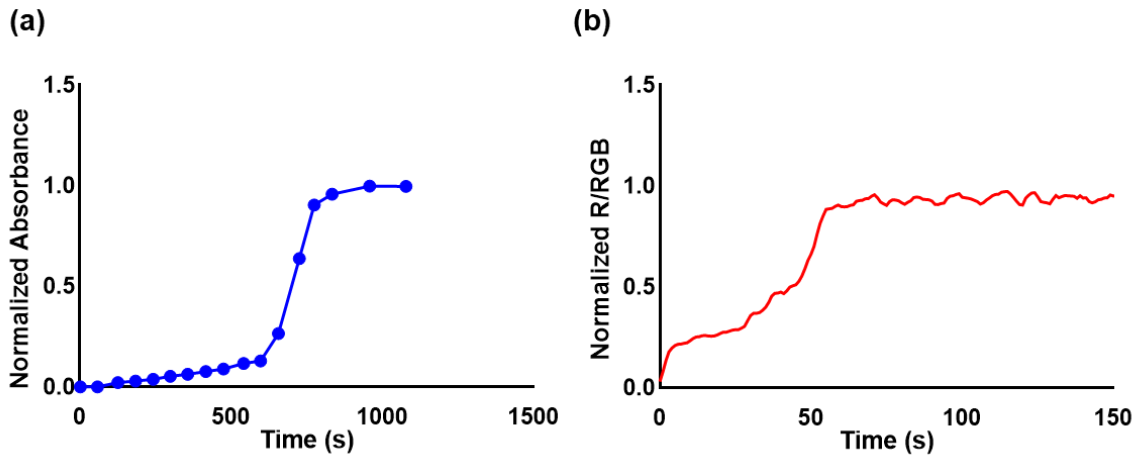

Figure 2-5. Reaction profile comparison between Turkevich and TA-NaCit methods; (a) Turkevich reaction profile replot based on peak absorbance, replotted from reference[124] (b) TA-NaCit reaction profile based on R/(RGB).

It was previously reported that in both Turkevich and TA-NaCit methods, the formation of GNPs follows a seed-mediated reaction pathway, where the reaction consists of two steps, seed formation and particle growth steps.[124,125] The seed formation step is the reduction of precursor to form small nuclei, or seeds, and is the first step in the reaction. Here the 'seed-mediated reaction pathway' of the TA-NaCit method is not to be confused with the overall 'seed-templated controlled growth' synthesis; the former is the reaction mechanism of the producing solid GNPs from chloroauric acid, and the latter is the engineered process of making size-tunable uGNPs in multiple reaction steps. It is thus proposed that the initial eruption in the reaction profile corresponds to the initial reduction of gold precursor to small particles predominantly by the stronger reducing agent, TA, while the growth of the seeds is controlled by NaCit.

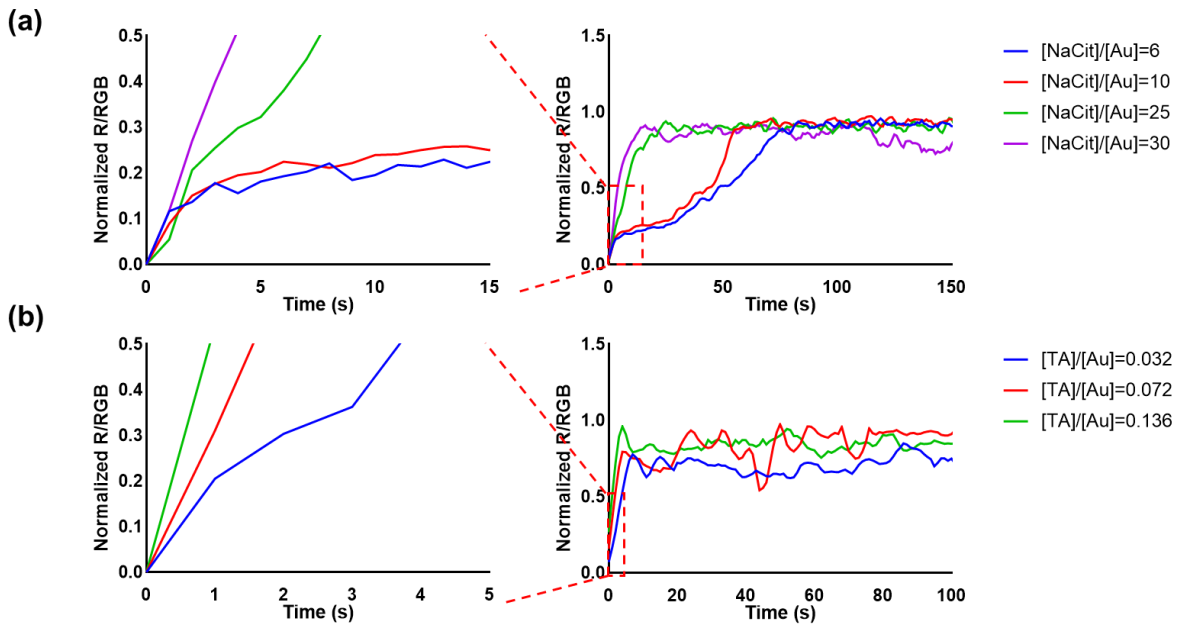

Figure 2-6. Kinetic study of TA-NaCit reaction with various TA and NaCit concentrations. Normalized red component (R/RGB) as functions of time for different ratios of (A) NaCit/Au (B) TA/Au.

The role of TA and NaCit in the initial reduction was explored further by checking the reaction profiles as a function of time at (a) different ratios of NaCit/Au while fixing TA concentration and (b) varying TA/Au ratio at a constant NaCit concentration. The increase in the NaCit/Au ratio expedites the reaction, thereby, leading to faster attainment of final sizes of uGNPs, while the rate of the initial seed formation process is unaffected with TA holding constant (Figure 2-6a). An increase in TA/Au however led to an increase in the initial reaction rate (Figure 2-6b). This indicated that both NaCit and TA might play a joint role in the reduction; however, TA is the dominant reducing agent. The rate law of the initial seed formation reaction can be written as follows:

$$r_{r,0} = k_{r,0} \cdot [AuCl_4^-] \cdot [TA]^l \cdot [NaCit]^m \quad (1)$$

where $[AuCl_4^+]$, [TA] and [NaCit] stand for the concentration of respective reagents. It is assumed that chloroauric acid follows a first-order reaction law in excess NaCit as reported previously.[126] TA-mediated reduction of Au^{3+} ions to form Au^0 involves each phenolic group of TA donating two electrons to form quinone. Therefore, TA is assumed to be the reacting species. NaCit undergoes speciation in the solution forming Ct^{3-}, CtH^{2-}, CtH_2^-, CtH_3 or a combination thereof. Ojea-Jimenez and Campanera reported that the reducing agent in the case of sodium citrated mediated synthesis is CtH_2^- while Kettemann et al. and Agunloye et al.

found that it is CtH^{2-}.[124,127,128] The concentrations of CtH^{2-} and CtH_2^- were calculated as described in the previous report and both the species were tested.[124] The initial reaction rate was calculated as follows:

$$\frac{r_{r,0}}{c_{AuCl_4^-,0}} = \frac{\frac{dC_{Au^0}}{dt_{t\to 0}}}{c_{AuCl_4^-,0}} = \frac{d(red\%)}{dt_{t\to 0}} \tag{2}$$

where red% is the normalized (R/RGB). The relationship between reducing agents and initial reduction rate was summarized as functions of [TA], [CtH_2^-] and [CtH^{2-}] (Figure 2-7).

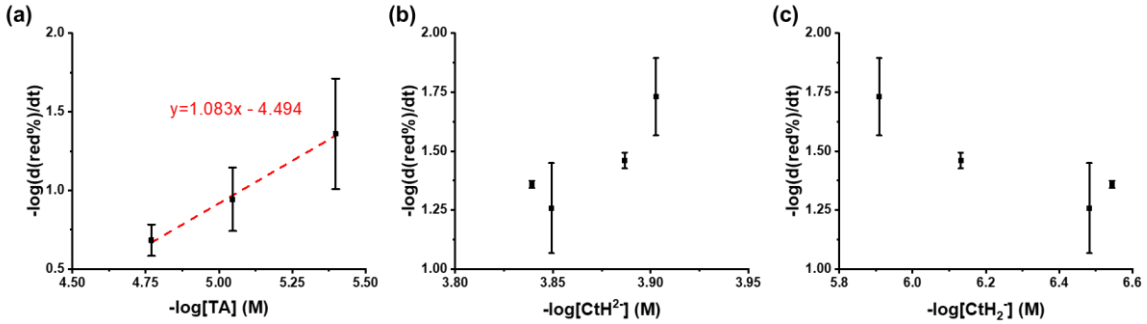

Figure 2-7. Correlations between reaction rate and concentration of different reactive species. Log-log plot correlating (A) TA, (B) CtH^{2-}, and (C) CtH_2^- concentrations to the d(red%)/dt.

A linear correlation between log(d(red%)/dt) and log [TA] is obtained and the value *l* is estimated, whereas neither [CtH_2^-] nor [CtH^{2-}] demonstrate clear correlations with reaction rate. Based on results from Figure 2-6 and Figure 2-7, it can be confirmed that TA is the dominant reducing agent in the initial reduction process when the influence of NaCit can be ignored. Thus Equation 1 can be rewritten as follows:

$$\log\left(\frac{d(red\%)}{dt}\right) = \log(k_{r,0}) + 1.08\log([TA]) \tag{3}$$

$$k_{r,0} = 10^{4.50}(m^3 mol^{-1})^{1.08} s^{-1}$$

2.3.5 Potential reaction mechanism for TA-NaCit

Multiple mechanisms have been proposed to describe the formation of monodispersed NPs. The LaMer model or classical nucleation theory is among the oldest and viewed as a basic model.[129] In this original model, the formation of colloidal particles is separated into three phases. Phase I is the pre-nucleation phase, in which the soluble solid monomers continue to build up to a supersaturated level. Once the concentration of the monomer reaches a critical supersaturation level, the reaction enters the second phase which is an

instantaneous nucleation step to form the nuclei. Phase II is then followed by phase III, during which it is postulated that the free energy of the system drives the attachment of monomers to the preformed nuclei. Polte later brought new perspectives in the growth of colloidal metal NPs based on the relative rates of monomer generation and particle growth.[130] There exist two scenarios under the theory. The first scenario, where the supply of monomer is much faster than the growth of particles usually takes place with strong reducing agents, such as $NaBH_4$. In this case, the precursor is instantaneously reduced to monomers and the growth of particles is almost exclusively driven by the aggregation and coalescence of the monomers. This scenario does not conform to the LaMer model. In Scenario 2, the monomer generating reaction is the limiting step of particle growth. The Turkevich reaction is believed to fall into this category, while it is unclear which scenario the mechanism of the TA reaction follows.

One interesting observation worth mentioning here is the independence of particle size on [TA] or [NaCit] within the range explored (Figure 2-4). With overall gold precursor concentration held constant, same particle size equates same particle number for different batches of product (assuming nearly 100% conversion). In the seed-mediated growth mechanism, the number of final particles should be the same as the number of seed particles generated at the beginning of the reaction. That means the number of seed particles is independent of the [TA] and [NaCit] with the range investigated. As the seed formation step is dominantly driven by TA, it is understandable why change [NaCit] does not have a noticeable impact on the number of seeds formed. Interestingly, an increase in [TA] for more than 10 times does not result in seed number changes either. That means with more Au^{3+} ions being reduced to Au^0, available for forming the seed particles, there is an increase in seed particle size rather than an increase in seed particle number. This observation is in contrast with the recently proposed colloidal stability driven seed-mediated growth mechanism for NPs, where seed size is determined by colloidal stability.[130] In the case of varying [TA], the changes in ionic strength and pH are negligible with increasing TA, as NaCit is in large excess and kept constant. According to the theory, when more Au^0 is available for seed formation, more seeds will be produced.[131] However, the data suggest otherwise.

In the above discussion, it is assumed that all TA reduces gold precursor at once followed by the rearrangement and coalescence of Au^0 to form seed particles and ‘seeds’ have been defined as particles formed from all Au^0 reduced by TA, corresponding to Scenario 1 as mentioned above. However, this might not be the actual case. To better

rationalize the seed formation mechanism, we can simplify the overall reaction by assuming NaCit reduction only happens after TA reduction and focusing only on the TA reduction part (in reality both happen simultaneously but the TA reduction rate is a lot faster). The reaction between gold precursor and stoichiometric TA itself could involve a seed-mediated growth, especially those with higher [TA]. Just like in the Turkevich reaction (NaCit reduction), where the seed particles are generated with a small amount of firstly reduced Au^0 at the beginning of the reaction in a very short period of time followed by attachment of more monomers onto these preformed nuclei. This is Scenario 2 as discussed above and the TA reduction could follow this pattern. If this holds true, the reduction of the gold precursor by TA can be separated into seed formation and subsequent growth steps. Here the 'seed particles' are the few first colloidally stable Au^0 particles generated during the initial stage of the TA reaction with a very small amount of TA. Because parameters affecting colloidal stability, such as ionic strength, pH, and temperature are held constant, the seed particles, in terms of size and number, created within the investigating [TA] range are indistinguishable. Any Au^0 atoms produced by extra TA beyond seed formation stoichiometry thus only participate in increasing the size of the seed particles rather than forming new seeds. For this to happen, the formation of initial seeds by the aggregation and coalescence of Au^0 must happen almost instantaneous and much faster than the reduction of the gold precursor by the remaining TA. Advanced in-situ monitoring techniques of the particle formation process at relevant timescale are required to test this seed formation mechanism.

Based on the previous reports on seed-mediated growth and the evidence set out above on the mechanism of seed-mediated synthesis, a reaction mechanism of TA + NaCit is proposed (Figure 2-8). In the proposed mechanism, the gold precursor firstly undergoes reduction almost exclusively by some of the TA to form small Au^0 atoms. The Au^0 atoms then quickly rearrange and aggregate into gold seeds, followed by the growth of GNP with the reduction of precursor by the remaining TA and NaCit. In the previously reported mechanism for the Turkevich reaction, most of the growth step is believed to be achieved by passivation of gold precursor, and it was found that passivation happens in a time scale of tens of seconds under similar gold and NaCit concentrations.[124,131] Depending on the [TA] and [NaCit], the reaction time spans from a couple of seconds to around 80 seconds. Therefore, growth through the passivation path takes place at very different degrees under different conditions.

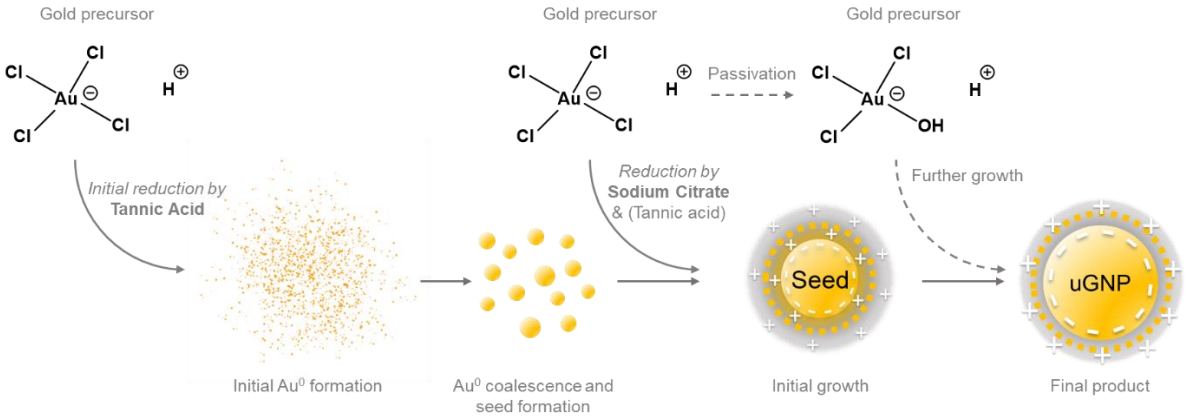

Figure 2-8. Proposed seed-mediated growth mechanism consists of the initial reduction of chloroauric acid to form small clusters which later coalesce into seed particles, followed by further growth leading to final products.

2.3.6 Synthesis and characterization of uGNPs

The TA-NaCit method was utilized to synthesize small uGNP seeds as templates for further seed-templated growth reactions to obtain a series of uGNPs using the setup in Figure 2-2 and procedure in Figure 2-3. The obtained uGNPs are characterized for their size and geometry using TEM and DLS (Figure 2-9), as well as LSPR and ζ-potentials using UV-VIS spectroscopy and ELS (Figure 2-10). As mentioned previously, the LSPR is the result of the collective oscillation of the conductive electrons confined at the surface of metal NPs upon irradiation of electromagnetic waves. The level of the oscillatory energy depends on the curvature of NP and would result in strong absorption of the electromagnetic wave at a specific wavelength. Therefore, LSPR can be used to indicate particle size given the geometry. The ζ-potential is the electrical potential between the bulk fluid and the stationary liquid layer surrounding the NPs. It can be measured by ELS, where the direction and speed of the NPs' movement are determined by the ζ-potential. For charged NPs, the absolute value of ζ-potential, positive or negative, is correlated with the colloidal stability of the system, as a larger charge can provide stronger inter-particle repulsion and prevent aggregation. Spherical uGNPs with a gradual nanometer-by-nanometer increase from ~3 nm to ~15 nm in particle size with the progression of synthesis were observed with TEM. The hydrodynamic size of uGNPs was measured with DLS as shown in Figure 2-10c, which also exhibits a continuous increase in particle size with the progression of synthesis. It is noticeable that there is some discrepancy between particle sizes evaluated by DLS and by TEM. In general, for smaller particles, their hydrodynamic diameters (H_D) obtained from DLS is about 1 nm larger than

the diameter assessed by TEM. This is expected as a hydration layer forms as the uGNPs surfaces are covered with citrate and tannate groups.

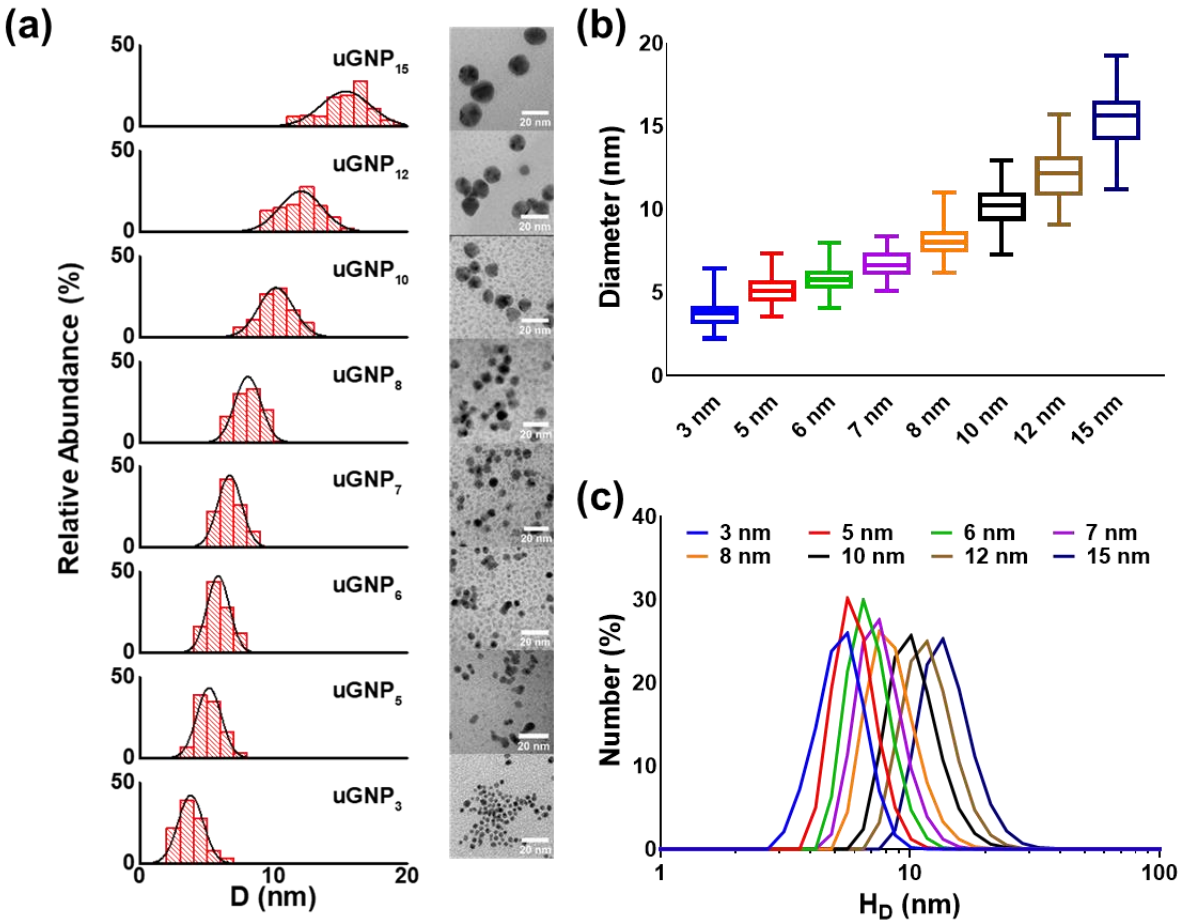

Figure 2-9. Size and geometry characterization of uGNP series. (a)-(b) Particle size distribution and respective TEM imaging of each uGNP batch. The particle size distributions were analyzed using ImageJ with 100 particles. Error bars represent standard deviations. (c) The hydrodynamic size of each uGNP batch.

LSPR is recorded for as-synthesized uGNPs (Figure 2-10b & c). The maximum absorption wavelength (λ_{max}) in UV-VIS spectra shifts from 497 to 520 nm for $uGNP_3$ to $uGNP_{15}$, which indicates that increasingly larger particles are successfully obtained as the reaction progresses. The ζ-potentials of freshly made uGNPs were also measured (Figure 2-10d). Largely negative ζ-potentials (~-60mV) are observed for all uGNPs of different sizes. The negative surface charge is due to the citrate and tannate groups as capping agents and the large absolute ζ-potential values indicate high colloidal stability.

(a)

(b)

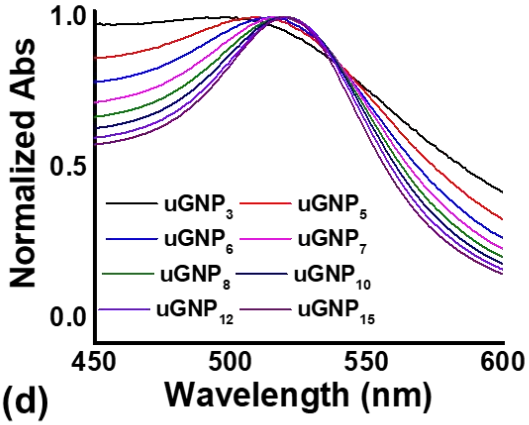

(c)

uGNPs	λ_{max}
$uGNP_3$	497
$uGNP_5$	508
$uGNP_6$	513
$uGNP_7$	519
$uGNP_8$	519
$uGNP_{10}$	519
$uGNP_{12}$	520
$uGNP_{15}$	520

(d)

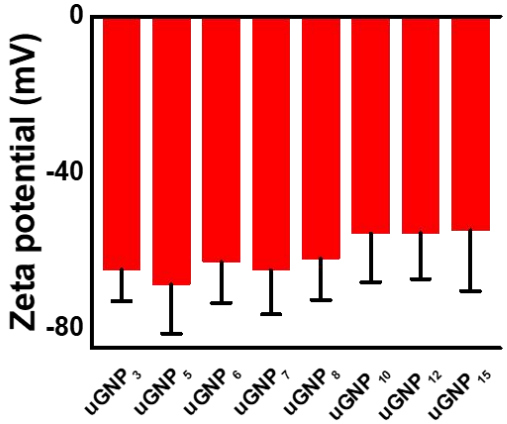

Figure 2-10. Optical and surface charge characterization of uGNPs; (a) Photograph of as-prepared $uGNP_3$ to $uGNP_{15}$; (b) Normalized UV-Vis spectra of the uGNP series with peak absorbance position summarized in (c); (d) ζ-potentials of as-prepared uGNPs.

The theoretical size of each uGNP sample was calculated based on the measured seed size and the amount of Au precursor injected at each reaction step, assuming 100% yield (Figure 2-11a). The results showed that the theoretically calculated particle sizes fall well within the standard deviation of measured particle sizes. It is notable that the theoretical particle sizes are slightly larger than the measured particle size. This could likely be due to the fact that the extent of the reaction is slightly lower than 100% and the loss of material during experimental operation. A correlation between LSPR and particle size (based on TEM) was obtained and consistent with findings in the literature (Figure 2-11b).[125] The LSPR initially increases dramatically as the size of uGNPs gets larger, but the slope levels out once the size of uGNPs exceeds 6 nm. This is because the change of particle surface curvature is much more prominent when the size of the NP is small.

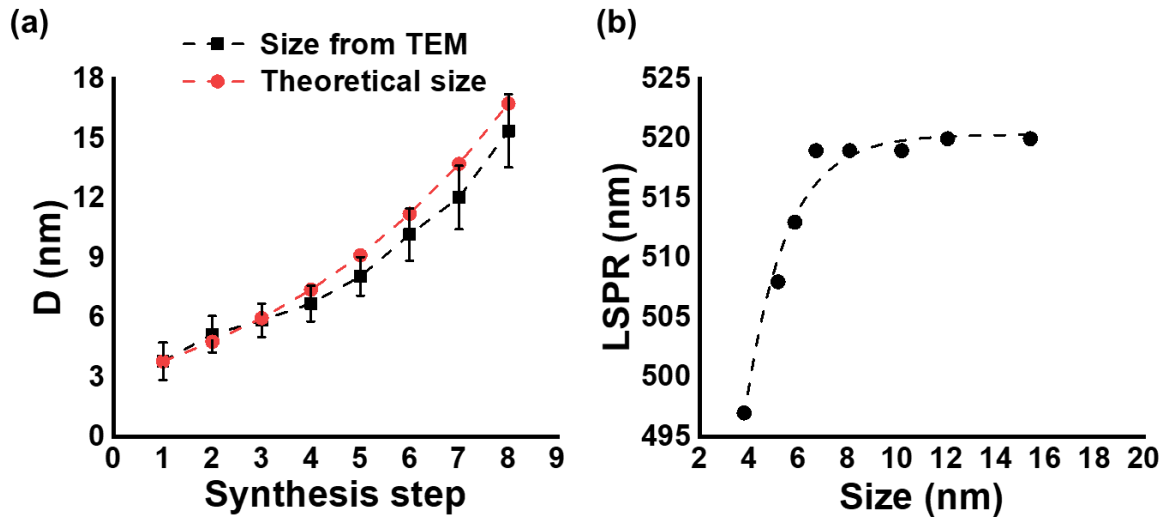

Figure 2-11. (a) Theoretical size and measured size of different uGNPs samples and (b) LSPR vs size of different uGNPs samples.

2.3.7 Surface modification of freshly prepared uGNPs with PEG

One of the biggest advantages of synthesizing NaCit capped GNPs is the ease of replacing them with other functional molecules. Coating the nanosurface with an antifouling molecule that can resist unwanted interactions with blood components and impart "stealth" properties is a common practice in nanomedicine. It is widely acknowledged that antifouling materials such as PEG and zwitterionic coatings can provide the stealth effect to reduce or alter protein adsorption onto NP surface leading to longer circulating time and improved targeting efficiency.[132,133] PEGylation is the most extensively used "stealth" in biomedical applications. PEG as stabilizing and protective agent has been utilized in several clinically approved nanoformulations (e.g., Doxil®, Oncaspar®, and Onivyde®), and thus remains the gold standard for NP coating. To demonstrate the potential of uGNPs to be surface functionalized and the ease of functionalization their surface, 8-arm PEG-SH (M.W.=10kDa) was used to coat uGNPs. The gold-thiol linkage was widely used for gold surface modification to form self-assembled monolayer. The PEGylation reaction in this study was conducted by simple incubation of 8-arm PEG-SH with as-prepared uGNPs at an elevated temperature for 1 hour. The minimum PEG:uGNPs ratios needed to fully cover the uGNPs was studied with changes in HD, LSPR, and ζ-potential (Figure 2-12). It was estimated that between 3 to 4 8arm-PEG molecules per nm2 (stoichiometry ratio) are needed to fully cover the uGNP surface.

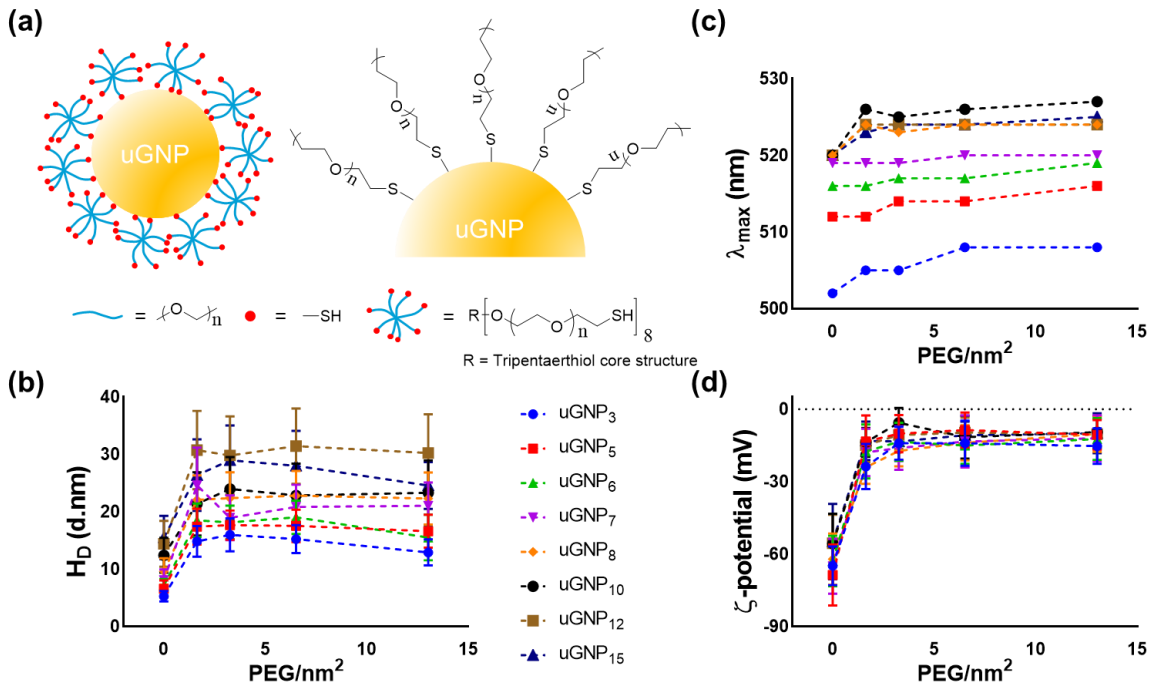

Figure 2-12. uGNP PEGylation with 8-arm PEG thiol. (a) Schematic illustration of PEGylation of uGNPs through gold-thiol chemistry. Changes in (b) H_D, (c) ζ-potentials, and (d) λ_{max} of uGNPs functionalized with various amounts of 8-arm PEG. Error bars represent standard deviations generated from the fitted distribution curves by the Malvern software.

To further prove the success in functionalizing uGNPs with PEG and exhibit the increased colloidal stability with PEGylation, a flocculation test was carried out in a high ionic strength solution (mimicking physiological condition). Both bare and PEGylated uGNPs were initially suspended in aqueous media, and aliquots of 1M NaCl were added to the NP solution. After thorough mixing, the LSPR was measured by UV-Vis spectroscopy (Figure 2-13). The shift of absorbance peak position (λ_{max}) to a larger wavelength indicated aggregation of uGNPs. Both bare uGNPs and uGNP-PEG demonstrated good colloidal stability up to ~50 mM of NaCl, but the λ_{max} of bare uGNPs shifts to a larger wavelength when the ionic strength of the suspension increased to close to 100 mM. The only exception is $uGNP_3$ which exhibited extraordinarily high colloidal stability. This was likely due to the extremely small size of $uGNP_3$. As the size of the uGNPs increased, the shift of λ_{max} became larger and larger, indicating less stability. In contrast, uGNP-PEG-SH with all sizes did not show any shift in λ_{max}. The result shows that the uGNPs are easily modified with simple gold-thiol chemistry and stabilized with PEG coating.

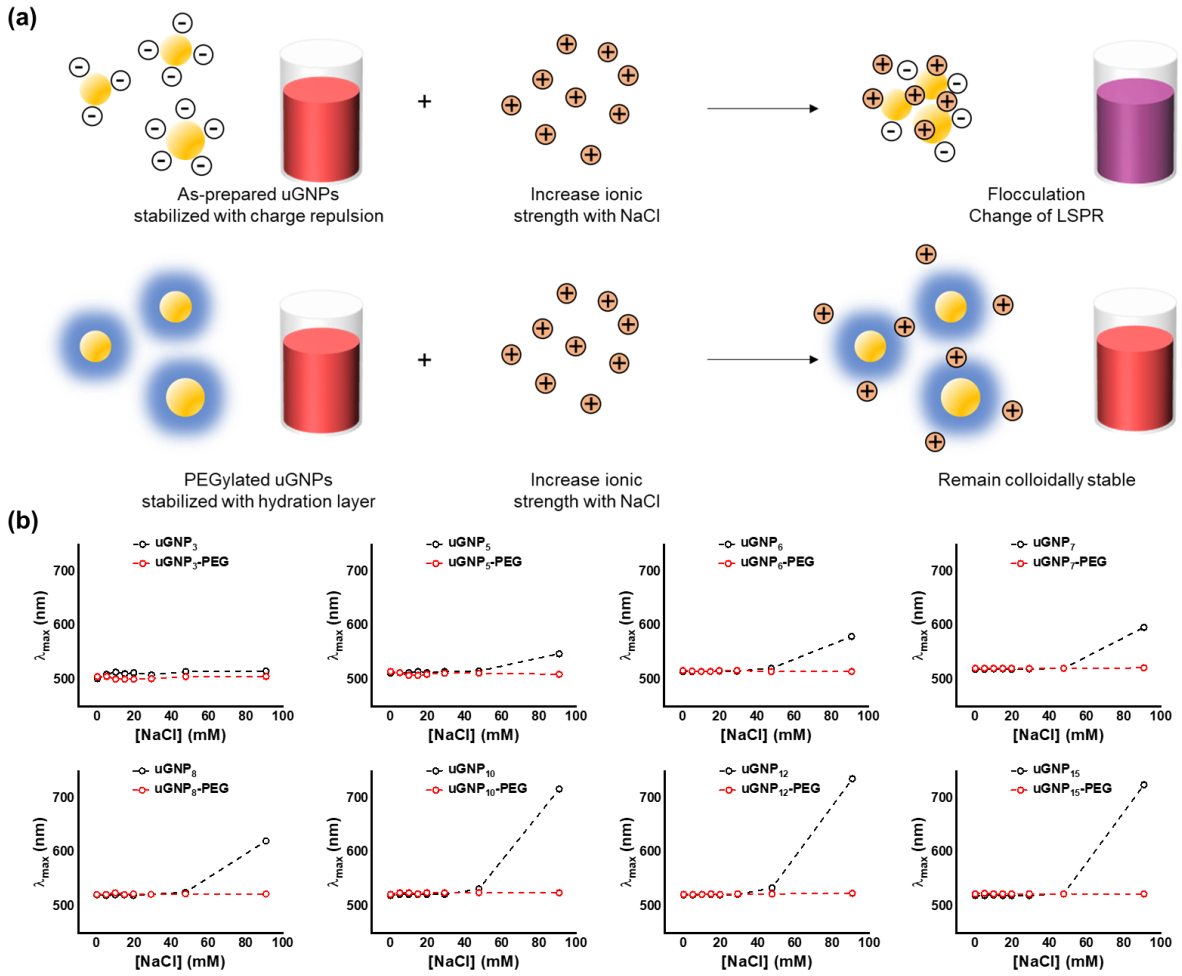

Figure 2-13. Flocculation test with freshly prepared and PEGylated uGNPs. (a) Schematic illustration of flocculation test with charge stabilized uGNPs and PEG stabilized uGNPs; (b) flocculation experiments of bare uGNPs and PEG-uGNPs as shown by λmax changes with the addition of NaCl.

2.4 Conclusions

To overcome the challenge of producing sub-10 nm uGNPs with readily modifiable surfaces and systematic fine tuning the NP size, a one-pot and process-engineered synthesis method is devised to successfully make uGNP with precise size tunability at single nanometer resolution. The process takes advantage of both strong (TA) and weak (NaCit) reducing agents to achieve small seed templates formation and multistep controlled growth. Kinetic studies of the seeding reaction using both TA and NaCit as reducing agents provided new insights into the reaction mechanism. A series of spherical uGNPs of sizes ranging from 3 to 15 nm was successfully synthesized. The uGNPs are colloidal stable, within the range of renal clearable size, and can be easily functionalized; therefore, they possess high potential in biomedical applications especially those with special size requirements. This engineered

process is a great candidate for large-scale production of size-tunable uGNPs with minimum batch variability.

The ability to consistently produce ultrasmall NPs with precise control over the particle size is highly desirable in biomedical applications. On the one hand, ultrasmall NPs have been associated with better toxicity profile, pharmacokinetics, protein corona formation, clearance pathway, cellular uptake, targeting ability, specific surface area (loading capacity of solid NPs) in many studies. On the other hand, the optimal particle size for each individual application can be different. Therefore, the seed-templated growth synthesis method can benefit a wide array of GNP related biomedical applications, in which small and tunable particle size of the nanosystems is required. However, in order to confirm their potential in biomedical settings, especially for *in vivo* applications, the safety and biocompatibility of uGNPs have to be carefully studied. The next chapter investigates the interaction between uGNPs and various biological components to reveal more details on their potential in biomedical applications.

3 Safety evaluation and biocompatibility of uGNPs – cytotoxicity, immune compatibility, and blood compatibility

3.1 Introduction

Despite the tremendous progress, a recent study summarizing *in vivo* tumor targeting efficiency from 2005 to 2015 has cast a shadow on the field of nanoparticle (NP) drug delivery.[32] The study has found a median tumor targeting efficiency of only 0.7% injected dose (ID), and with active targeting strategies, this value just reaches 0.9%ID.[32] That means in most cases, about 99%ID NPs end up being off-target. Off-target NPs either get cleared from the body prematurely before their desired functions or end up within healthy tissues which can potentially lead to critical safety concerns. Therefore, achieving immune tolerable, blood compatible, and biofriendly NPs remains a critical prerequisite for NP translation. The translational success of nanoformulations from bench to bedside involves a thorough assessment of their compatibility beyond cytotoxicities such as immune-toxicity, immune-safety, immune-mediated destruction/rejection, and clearance profile. This chapter focuses on the safety and biocompatibility evaluation of the uGNPs series synthesized using the seed-templated growth method as depicted in Chapter II to further assess their potential as delivery, diagnostic, and therapeutic agents in clinical applications. This framework of *in vitro* analyses outlined in this chapter is suitable for evaluating biosafety and biocompatibility for any newly developed nanomedicine before *in vivo* model studies.

3.1.1 Mechanism of Nanotoxicity

The extraordinary properties of NMs can be a double-edged sword providing both favorable functions and potential safety concerns. Upon encountering biological systems, NPs can have unique interactions with various components due to their exceptional physiochemical properties. The terminology ‘nanotoxicity’ was created to exclusively describe the toxicology of nanosized materials. Material type, composition, size, shape, and surface chemistry are key factors determining the toxicology of NPs. Some of the most common mechanisms by which NMs can exert toxic effects on the molecular and cellular level include creating oxidative stress, evoking protein conformational changes, and causing DNA damage.[134]

Oxidative stress caused by the generation of reactive oxygen species (ROS) is one of the most common toxic effects of NPs.[135] Transition metal NPs can cause elevated ROS

levels by catalyzing the ROS generating reactions (e.g., Fenton type reaction).[136] After entering cells, certain types of NPs are capable of damaging the mitochondria through morphological damage and mitochondrial membrane potential disruption.[137] In addition to oxidative stress, NPs can induce protein conformation change. Irreversible conformation distortion of human transferrin upon interacting with iron oxide NPs was observed, leading to a loss of protein function.[138] Another study shows that complexes of polyampholyte and dodecanoic acid induce β-sheet formation in amyloid-β peptide, which is directly related to fibrillogenesis commonly observed in Alzheimer's disease.[139] NPs can cause DNA damages therefore can potentially have genotoxic effect. Impairment of DNA may result from ROS production and interaction with heavy metal ions (Ag^{+}, Pt^{2+}) released from the respective metallic NPs.[140] DNA damage can also take place in cells not in direct contact with NPs but through intercellular interaction. It was demonstrated that DNA damage without significant cell death can be elicited via transmission of adenosine triphosphate (ATP) from a cellular barrier which is subject to direct exposure to cobalt-chromium NPs.[141]

3.1.2 Immune compatibility

The immune system collectively works round the clock to maintain a stronghold of tissue homeostasis in order to protect the host from detrimental environmental agents such as microbes or foreign chemicals, thus conserves the integrity of the host body. Avoiding immune recognition is highly favorable when the desired nanosystems are not intended to stimulate or inhibit any immunological responses. Immune compatibility is a critical characteristic of an NP-based system, as it not only affects the safety of the system (e.g., inflammatory reaction, allergic reaction), but also plays a critical role in the delivery efficiency (e.g., premature scavenging by immune system).

3.1.2.1 Pro- and anti-inflammatory cytokine secretion

Cytokines are a group of small soluble proteins that helps regulate the immune response, facilitate intercellular signaling among immune and non-immune cells, and maintain homeostasis. Cytokines work as a complicated but well-orchestrated network. Their functions are described as pleiotropic, as different cytokines have multiple yet overlapping functions and can synergize or counteract each other.[142] Cytokines are primarily secreted by immune cells, but can also be produced by non-immune cells, such as endothelial and epithelial cells.[143] Cytokines can be paracrine (affecting only the vicinity of the secretion sites), autocrine (acting on the same cells secreting the cytokines), and occasionally endocrine

(reaching and acting on distant parts of the body).[144] Cytokine release is correlated with physiological reactions including fever, hypertension, nausea, and headache. Imbalance and deregulation in cytokine release can be harmful and lead to severe diseases, such as rheumatoid arthritis and multi-organ failure.[145] Infusion reaction, immunosuppression, and autoimmunity are possible cytokine-related adverse effects caused by intravenous administration of pharmaceutical products, including NPs.[146] Therefore evaluation of NPs' influence on cytokine profiles is of critical importance for checking their immunotoxicity.

One of the major functions of cytokines is to regulate inflammation upon stimuli through pro- and anti-inflammatory cytokines typically secreted by monocytes and macrophages.[143] Monocytes and macrophages belong to the mononuclear phagocytic system (MPS) as a part of innate immunity. Monocytes are the largest leukocytes derived from bone marrow, circulating in the bloodstream with a half-life of around 70 hours in healthy adults.[143] Monocytes are able to recognize alien invaders, including pathogens, drugs, exogenous proteins, and NPs, and, in response, they can participate in phagocytosis, present antigens, enhance proliferation, and produce cytokines.[147] Monocytes can differentiate into macrophages once enter the connective tissues, resulting in increased size, organelle number and complexity, and phagocytic ability.[143] Macrophages are in charge of engulfing and eliminating alien objects, recruiting other immune system components through chemical signaling such as cytokines, and processing and presenting antigens to lymphocytes.[143,147]

Proinflammatory cytokines, such as tumor necrosis factor α (TNF-α), Interleukin-1β (IL-1β), IL-6, IL-8, and IL-12, are released by macrophages.[143] TNF-α plays an important role in induced necrosis in tumors and is one of the first cytokines produced in the body reacting to a pathogen invasion.[148] TNF-α leads to vasodilation and increased vessel permeability the for recruitment of lymphocytes, neutrophils, and monocytes to the inflammation site.[149] Extra TNF-α release has been related to inflammatory bowel disease, psoriasis, rheumatoid arthritis, asthma, cancer, infectious diseases, and autoimmune disorders.[143] IL-1β can be produced not only by monocytes and macrophages but also by natural killer (NK) cells, B cells, dendritic cells, fibroblasts, and epithelial cells and is among the earliest released pyrogenic cytokines in response to infections and injury.[143] It mediates fever, enhances acute-phase protein production, and initiates an inflammation cascade.[150] Excess release of IL-1β is related to autoinflammatory disease,[151] metabolic syndromes,[152] acute and chronic inflammation.[150] IL-8 or chemokine ligand 8 is a chemokine, a signaling cytokine capable of inducing chemotaxis, which specifically attracts neutrophils.[153]

Abnormal IL-8 level in blood has been associated with chronic obstructive pulmonary disease,[154] cardiovascular diseases,[155] and psychiatric disorders.[156] IL-12p70 is a bioactive and heterodimeric form of the IL-12 cytokine formed by the fusion of its p35 and p40 subunits.[157] Mainly synthesized in monocytes, macrophages, and other antigen-presenting cells, IL-12 facilitates T helper (Th) 1 cell differentiation and subsequent interferon gamma (IFNγ) production, as well as enhances cytotoxicity of NK and CD8+ T cells.[158] Deregulation of IL-12 has been associated with autoimmune disease and cancer development.[159]

Anti-inflammatory cytokines are immunoregulatory cytokines that modulate the release and response of proinflammatory cytokines. IL-4 and IL-13 are a pair of anti-inflammatory cytokines that share 25% homology and certain functions, such as inhibitory effect on proinflammatory cytokine release[160] and are key players in type 2 immunity.[161] They can be secreted by CD4+ T cells, basophils, eosinophils, mast cells, and NK T cells.[162] Other than their similar functions in regulating antibody production and inflammation response, only IL-4 is capable of regulating T cell differentiation due to the absence of IL-13 receptors on T lymphocytes.[163] IL-10 acts on macrophages to suppress their antigen presentation,[164] dials down their proinflammatory cytokines secretion,[165] and desensitize their responsiveness to IFNγ.[166] IL-10 is mainly produced by activated macrophages, B cells, and T cells, and has been shown to be related to inflammatory bowel disease.[143,167]

As mentioned above, ILs are characterized by their pleiotropic nature, meaning they often participate in multiple, and sometimes opposing, functions. IL-2 is one of the cytokines that can perform in both pro- and anti-inflammatory roles. IL-2 facilitates the proliferation of CD8+ T cells and NK cells and promotes the differentiation of Th1 (cell-mediated response) and Th2 cells (humoral response).[168] On the other hand, it hinders the differentiation of Th17 cells, a subset of T cells that produce the proinflammatory cytokine IL-17.[169] IL-2 plays a critical role in preventing autoimmune reactions.[168] IL-6 is another cytokine that has both pro- and anti-inflammatory effects. IL-6 mediates inflammation, immune response, and hematopoiesis,[170] but also exerts anti-inflammatory activity through inhibitory effects on TNF and IL-1 production.[171] Uncontrolled release of IL-6 can lead to chronic inflammation, autoimmunity, as well as immune-suppression.[170]

3.1.2.2 Activation of complement system

In order to achieve the desired clinical output, nanocarriers are usually injected intravenously, with an eye to reaching specific and targeted drug delivery.[95] Intravenously

administered NMs encounter a huge protein load when it enters the bloodstream.[172] A natural phenomenon, termed 'opsonization', usually takes place when a foreign body enters and this determines the alien object's fate, which predominantly depends on the amount and type of proteins adsorbed onto the particle's surface.[173] Serum albumin being the most abundant protein present in the blood is readily adsorbed onto the surface of the NP. Following the adsorption, a cascade of reactions occurs, such as binding or displacement of the adsorbed albumin with fibrinogen. The immune system gets activated on recognizing the adsorbed protein on the NP, which sequentially causes activation of the complement cascade.[172] Complement activation can cause premature clearance of NPs before they can reach the designated sites. It can also enhance the immunogenicity of NPs leading to immunorecognition with repeating injections.[174] Uncontrolled complement activation might also lead to complement activation related pseudo-allergy (CARPA), a potentially life-threatening condition caused by certain types of drugs and NP-based combination products.[175]

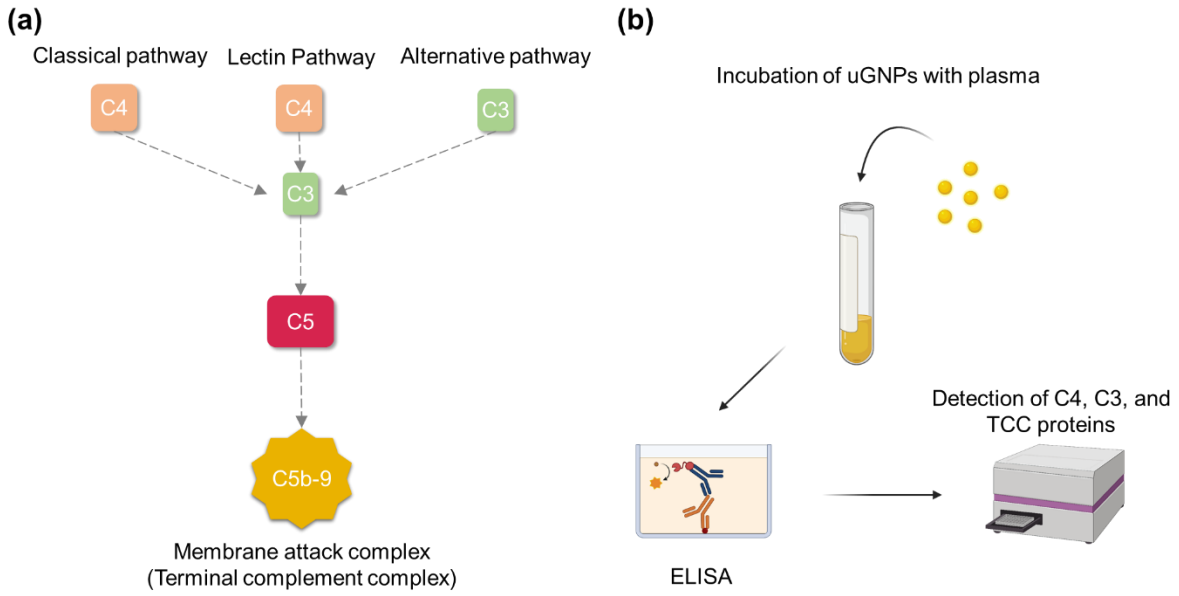

Figure 3-1. Schematic illustration of the relevant pathways to trigger complement activation and the experimental procedures for detecting the relevant biomarkers. (a) Complement activation can be triggered with three different pathways, the classical pathway, the lectin pathway, and the alternative pathway. The important proteins C4, C3, and TCC are involved in respective pathways as shown.[176] (b) To evaluate the possibility of uGNPs eliciting the complement activation, uGNPs were incubated with plasma and the levels of corresponding biomarkers were then measured through ELISA. Created with BioRender.com.

The complement system is a part of the innate immune system that helps to clear pathogens and alien objects. Different signals involving different proteins can trigger

activation of the complement cascade. The schematic illustration of the three pathways, the classical pathway, the lectin pathway, and the alternative pathway is shown in Figure 3-1. NPs trigger the complement activation through all three pathways.[9] The cleavage of C3 is a key event, which ultimately opsonizes the NP with C3b for phagocytosis.[172] NPs with low protein binding capacity can remain longer in the blood circulation since they have a low potential to activate the complement system.[177,178]

3.1.3 Blood coagulation pathway

Blood coagulation is an important mechanism to maintain hemostasis especially facing injuries. Blood clotting is achieved by the activation of thrombin which cleaves fibrinogen to form a fibrin network. The coagulation cascade can be activated via two pathways, namely the intrinsic (contact activation) pathway and the extrinsic (tissue factor) pathway. The intrinsic pathway is activated by negatively charged surfaces or molecules, such as endothelial collagen, and the extrinsic pathway is triggered by vessel damage.[179] Various clotting factors are involved in the process as shown in Figure 3-2.

The functioning of the intrinsic pathway response can be evaluated by the activated partial thromboplastin time (APTT), while the functioning of the extrinsic pathway response is estimated by prothrombin time (PT). Both screening tests measure the approximate time it takes for blood to clot. A blood-compatible and coagulation-safe nanoparticle is expected to have no effect on the coagulation time. A shorter coagulation time could lead to blood clotting risk by the formation of a thrombus, while a longer coagulation time would cause hemorrhage.[178]

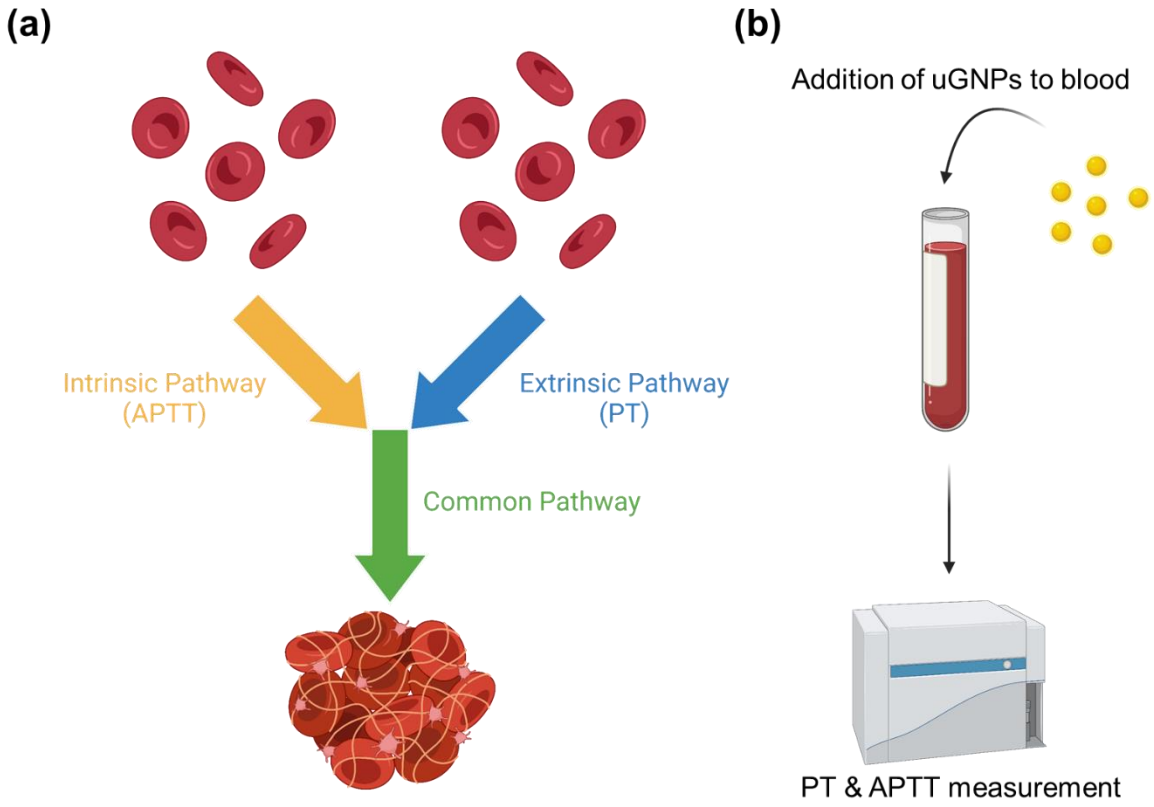

Figure 3-2. The blood coagulation cascade and experiment to measure PT and APTT. (a) The intrinsic pathway is activated by a negatively charged surface while the extrinsic pathway is activated by vascular trauma and the exposure of tissue factors to the blood. Both pathways end up activating the common pathway where fibrinogen is transformed into fibrin leading to blood coagulation. (b) To investigate the influence of the uGNPs on blood coagulation, uGNPs were mixed with blood before the PT and APTT were measured by the instrument using a chronometry measurement. Created with BioRender.com.

Thrombogenicity of NPs has been studied for a wide range of NPs. It was found that the positively charged polystyrene NPs (amine surface modification) reduced thrombin formation, while negatively charged polystyrene NPs (carboxyl surface modification) activated blood coagulation in plasma via the intrinsic pathway.[180] In another study, it was found that at low concentration (100µg/ml), metallic oxide NPs activated blood coagulation regardless of their surface charge, but at high concentration (1mg/ml) only the negatively charge metallic oxide NPs promoted blood coagulation and positively charged metallic NPs impeded blood clotting.[181] Size of the NPs plays a critical role in their thrombogenicity as it was demonstrated that 60 – 220nm carboxyl modified polystyrene NPs were capable of initiation thrombin production while their smaller counterparts (24 and 26 nm) had little effects.[182]

3.1.4 Systematic *in vitro* safety check of uGNPs

Although GNPs are usually applied with biocompatible coating materials such as PEG and zwitterionic molecules, which are capable of greatly affecting the protein adsorption onto NPs, dissociation and incomplete surface coverage can happen inadvertently. Therefore, direct interactions between unmodified NPs and the biological components need to be investigated. Interactions between biological components and NPs might be inferred based on NP properties, such as material, size, shape, and surface chemistries. However, this propensity cannot always be extrapolated. Ethnic concerns aside, animal models are best at capturing the complexity of the human body in preclinical studies, although the development in the 'organs-on-chips' technology could change this status quo.[183] Before taking things *in vivo*, however, systematic *in vitro* biocompatibility tests can serve as a checklist to rule out a number of potential acute adverse effects and help to establish a concentration threshold for *in vivo* studies. Such a framework should cover a wide range of potential safety concerns and can become a standard practice to evaluate newly developed NMs. To achieve this goal, a complete set of *in vitro* analyses of the cytotoxicity, immunotoxicity, immunogenicity, and blood compatibility of uGNPs with different biological components was conducted.

3.2 Materials and methods

3.2.1 In vitro stability of uGNPs in physiologically relevant media

The stability of as-prepared and unmodified uGNPs was studied in Dulbecco's phosphate-buffered saline (DPBS, Gibco, Thermo Fisher Scientific, Waltham, Massachusetts, USA), 10% fetal bovine serum (FBS, Gibco), and colorless Dubelco's modified essential medium (DMEM, Gibco) supplemented with FBS (10%), penicillin (50 IU/mL) and streptomycin (50 µg/mL). The uGNPs were incubated with various media at a 1 to 2 volume ratio for different times and the localized surface plasmon resonance (LSPR) was measured through UV-Vis spectroscopy.

3.2.2 Cytotoxic study on MCF7, 293A, and SW480 cell lines

The effect of uGNPs on the viability of MCF-7, 293A, and SW480 was determined by MTS [3-(4,5-dimethylthiazol-2-yl)-5-(3-carboxymethoxyphenyl)-2-(4-sulfophenyl)-2H tetrazolium] assay. Cells were cultured in DEME (Gibco) with 10% FBS containing penicillin (50 IU/mL) and streptomycin (50 µg/mL) (Thermo Fisher Scientific). In all the experiments, cells were maintained at 37°C in a humidified 5% CO_2 incubator. MCF7, 293A,

and SW480, were treated with uGNPs of 8 sizes and at varying concentrations (0-125 µM). The cells were seeded in 96-well plates at 10,000/well with the final volume (growth media + uGNPs solution) to be 200 µL/well. The cells were then cultured for 24, 48, and 72 hours, respectively. A positive control of cells with DMEM only and a negative control of cells with DMEM/MTS assay reagent were also seeded in triplicate. At the end of treatment, 20 µL of CelTiter 96® AQ_{ueous} One Solution (Promega, Wisconsin, USA) MTS reagent was added to each well, and the cells were then incubated at 37°C, 5% CO_2 for 0.5 – 4 hours. The absorbance of each well was measured at 490 nm (650 as reference wavelength) using a plate reader (VersaMax™, Molecular Devices, California, USA). All experiments were conducted in at least triplicates. The percentage viability of cells was calculated according to the following equation: Cell viability (%) = (Absorbance of treated cells-blank)/(Absorbance of control cells-blank)×100. Blank= No cell, only media with MTS reagent.

3.2.3 Compatibility test of uGNPs to acute monocyte leukemia cell line (THP-1) and THP-1 differentiated macrophage

The cell lines were maintained in RPMI 1640 medium (Gibco), supplemented with 10% FBS (Gibco), 1% penicillin-streptomycin (Thermo Fisher Scientific), 1% L-glutamate and 1 mM sodium pyruvate (Gibco). THP-1 cells were cultured in a humidified chamber at 37°C, 5% CO_2. MTS assay as described previously was performed to evaluate the cytotoxicity of uGNPs on the THP-1 cell line. Briefly, cells (100,000 cells/mL) were seeded into a 96-well plate in triplicate and incubated for 72 h (37°C, 5% CO_2) with varying concentrations of uGNPs (0 – 125 µM). A positive control of THP-1 with RPMI only and a negative control with RPMI/MTS assay reagent were also seeded in triplicate. After the incubation period with the particles, an MTS assay was performed as described previously.

Simultaneously, membrane integrity assay, lactate dehydrogenase (LDH) assay, using the CytoTox-ONE™ homogenous reagent (Promega) was also carried out on the THP-1 differentiated macrophage induced by phorbol-12-myristate 13-acetate, 100 nM (PMA, Sigma-Aldrich, Saint Luis, MO, USA) for 48 h. After this differentiation window, the cells were replenished with fresh complete RPMI medium without PMA for an additional 48 h to allow for cell recovery. Cell differentiation was determined by evaluating cell adhesion and spreading using a bright field microscope (Axio, Carl Zeiss AG, Oberkochen, Germany). The differentiated macrophage was incubated for 72 h (37°C, 5% CO_2) with varying concentrations of uGNPs (0-125 µM). As a positive control for maximum LDH release, 2 µL

of lysis solution (provided in the kit) was added to the untreated or control wells followed by the addition of 100 µL of CytoTox-ONE™ homogenous reagent to all the wells. The plate was then incubated at 22°C for 10 minutes, this step was followed by the addition of 50 µL of stop solution (provided in the kit) and the plate was shaken for 10 seconds. The final step involves fluorescence measurement at an excitation and emission wavelength of 560 and 590 nm respectively, Spark™ 10M multimode microplate reader (TECAN, Switzerland). The studies with the THP-1 cell line were performed in collaboration with Dr. Hassan Rahmoune.

3.2.4 Complement activation of uGNPs by *ex vivo* plasma incubation

To prepare plasma, whole blood was collected from six healthy donors in 4.5 mL sterile tubes (Nunc, Roskilde, Denmark) containing the thrombin inhibitor lepirudin (Refludan; Pharmion ApS, Copenhagen, Denmark) at a final concentration of 50 µg/mL to prevent blood clotting.[184] Blood was immediately centrifuged at 3000 x g for 15 minutes at 4°C to obtain plasma, which was pooled. Complement activation was studied by incubating 100 µL of pooled plasma with uGNPs for 30 minutes at 37°C in 1.8 mL round-bottom sterile polypropylene NUNC cryotubes (Nunc). After incubation, activation was stopped by adding EDTA (20 mM) and the plasma was stored at -80°C until further analysis. The levels of activation markers C4 (C4bc), C3 (C3bc) and the soluble C5b-9 (sC5b-9), terminal complement complex (TCC), were analyzed in the plasma samples using ELISA as described previously.[185] Briefly, the assays were based on monoclonal antibodies detecting neo-epitopes exposed after activation hence, specifically measuring only activation specific fragments (C4bc, C3bc), and complexes (sC5b-9). Zymosan (100 µg/ml) was used as the positive control. The complement activation study was carried out in collaboration with Dr. Rakibul Islam from Oslo University Hospital, Norway.

3.2.5 Cytokine analysis in THP-1 and THP-1 differentiated macrophage

Differentiated (Macrophage-like) and undifferentiated (Monocyte-like) THP-1 cells ($1x10^5$ cells/mL) were treated with increasing concentrations of uGNPs, with and without Lipopolysaccharide (LPS, 10 ng/mL) for 24 h. The addition of LPS is primarily used for the following: (1) as a positive control, and (2) to mimic endotoxins contamination which leads to proinflammatory responses. At the end of the uGNPs treatment window, 1 mL of cells from individual wells were aliquoted and centrifuged at 1000 rpm for 5 minutes. The supernatant was collected and kept at -80°C for cytokine analysis. Meso Scale Discovery (MSD) multiplex assay platform was used here to allow quantitation of multiple cytokines in

the same sample. THP-1 monocytic and macrophage-like cell culture media were collected, and the corresponding cytokines levels were measured using ultrasensitive electrochemiluminescence immunoassay on the MSD assay platform. The luminescent readout was performed on the Meso Scale Diagnostics Sector Imager 6000. All reagents and calibrators were supplied by Meso Scale Discovery and the samples were analyzed at the Core Biochemical Assay Laboratory (NHS Cambridge University Hospitals; UK).

3.2.6 Coagulation test with uGNPs

Blood was collected from healthy individuals with their due consent and then mixed with anticoagulant (3.2% NaCit) in a 9:1 ratio (by volume). To obtain the platelet-poor plasma, blood was centrifuged at 1000× g for 15 minutes at room temperature. The plasma obtained after centrifugation was then incubated with uGNPs for 10 minutes at 37°C in a water bath. The samples were then taken for coagulation analysis, namely APTT to study the intrinsic pathway and PT for the extrinsic pathway using Stago Compact Max (USA) an automatic coagulation analyzer. The study is performed with the help of Dr Suryyani Deb (Maulana Abul Kalam Azad University of Technology [MAKAUT], India) and her clinical collaborators.

For the control sets, DPBS was used as the volume controller, and unfractionated heparin (UFH, 1000 U/mL, Sigma Aldrich) was used as the negative control for the APTT experiment. Briefly, in Stago Compact Max, to evaluate PT value, a 50 µL of each sample (uGNPs treated or control) was taken automatically to the reaction chamber (cuvette) followed by the addition of 100 µL of thromboplastin (STA Neoplastie R15) phospholipid and then 50 µL $CaCl_2$ (0.025 M). Within 3-5 seconds, PT value was measured and shown in the machine. The normal range of PT is 11 to 16 seconds, which depends on the analytical technique and source of thromboplastin. According to Stago Compact Max, the standard PT is between 11 to 14.5 sec. To measure the APTT, a 50 µL sample was taken to the reaction chamber (cuvette) same as mentioned for PT measurement. Each sample was then treated with 50 µL of a phospholipid, kaolin activator (STA c.k. Prest 5), and then lastly 50 µL $CaCl_2$ (0.025 M). APTT value was then measured. The time required for this measurement was ~3-5secs. The normal range of APTT is 24 to 37 sec. According to Stago Compact Max the standard time for APTT is from 24 to 37 sec (Table 3).

Table 3-1. Blood coagulation test sample preparation.

Control 1	Control 2	Control 3	Set 1	Set 2	Set 3	Set 4

1 mL plasma	999 µL plasma + 1 µL heparin	900 µL plasma + 100 µL PBS	900 µL plasma + 25 – 100 µL $uGNP_5$	900 µL plasma + 25 – 100 µL $uGNP_7$	900 µL plasma + 25 – 100 µL $uGNP_{10}$	900 µL plasma + 25 – 100 µL $uGNP_{15}$

3.2.7 Principal Component Analysis (PCA)

Principal Component Analysis (PCA) was performed on the uGNPs and cytokines data using R (v3.5.3) and FactomineR[186] and factoextra packages.[187] To compute the quantitative variables and factors, the PCA was calculated by normalizing the same weight from the first eigenvalue of the same variance. Briefly, the measurements of each of the ten cytokines were first standardized. Next, the covariance matrix was calculated and corresponding eigen decomposition was performed. The obtained eigenvectors were ordered in decreasing order and the first two eigenvectors were taken as the first two principal components for PCA. The representation of the variables was used to describe the dimensions in the plot.

3.2.8 Statistical Analysis

All the experiments were conducted independently twice with different batches of NPs and the subsequent analysis was performed in triplicate. Statistical analysis was performed using the ANOVA in GraphPad Prism 8.0 (GraphPad Software, San Diego, USA), followed by Bonferroni t-test for comparison with the untreated/control group. Statistical significance was determined at a *$p \leq 0.05$, **$p \leq 0.01$ and***$P \leq 0.001$.

3.3 Results and Discussion

3.3.1 uGNPs stability in PBS, FBS, and cell culture medium

The stability in the biological complex milieu of as-prepared uGNPs was investigated in 3 different media. The λ_{max} and Abs_{max} reflecting the changes in LSPR were measured by UV-Vis spectra and summarized in Figure 3-3. The stability of citrate-capped uGNPs in various dispersing media was studied. As-prepared uGNPs were dispersed in DI-water, PBS (1X, pH 7.4), fetal bovine serum (FBS, 10% in PBS), and cell culture medium at a 1:2 volume ratio for 24 hours and the respective UV-Vis spectra were recorded. It can be seen that uGNPs became colloidally unstable in PBS as evidenced by the complete flattening of the LSRP peak. Surprisingly the uGNPs stayed relatively stable in FBS and culture medium as the overall shape of UV-Vis spectra remained unchanged. The absorbance of uGNPs increased in FBS solution and remained at the same level in the culture medium, compared

with DI-water. In terms of the shift in λ_{max}, upshifts in peak position were observed with uGNPs dispersed in both FBS and culture medium. A larger degree of shift was resulted in FBS than in culture medium. Changes in peak positions were more prominent for intermediate sizes (uGNP5 to uGNP8).

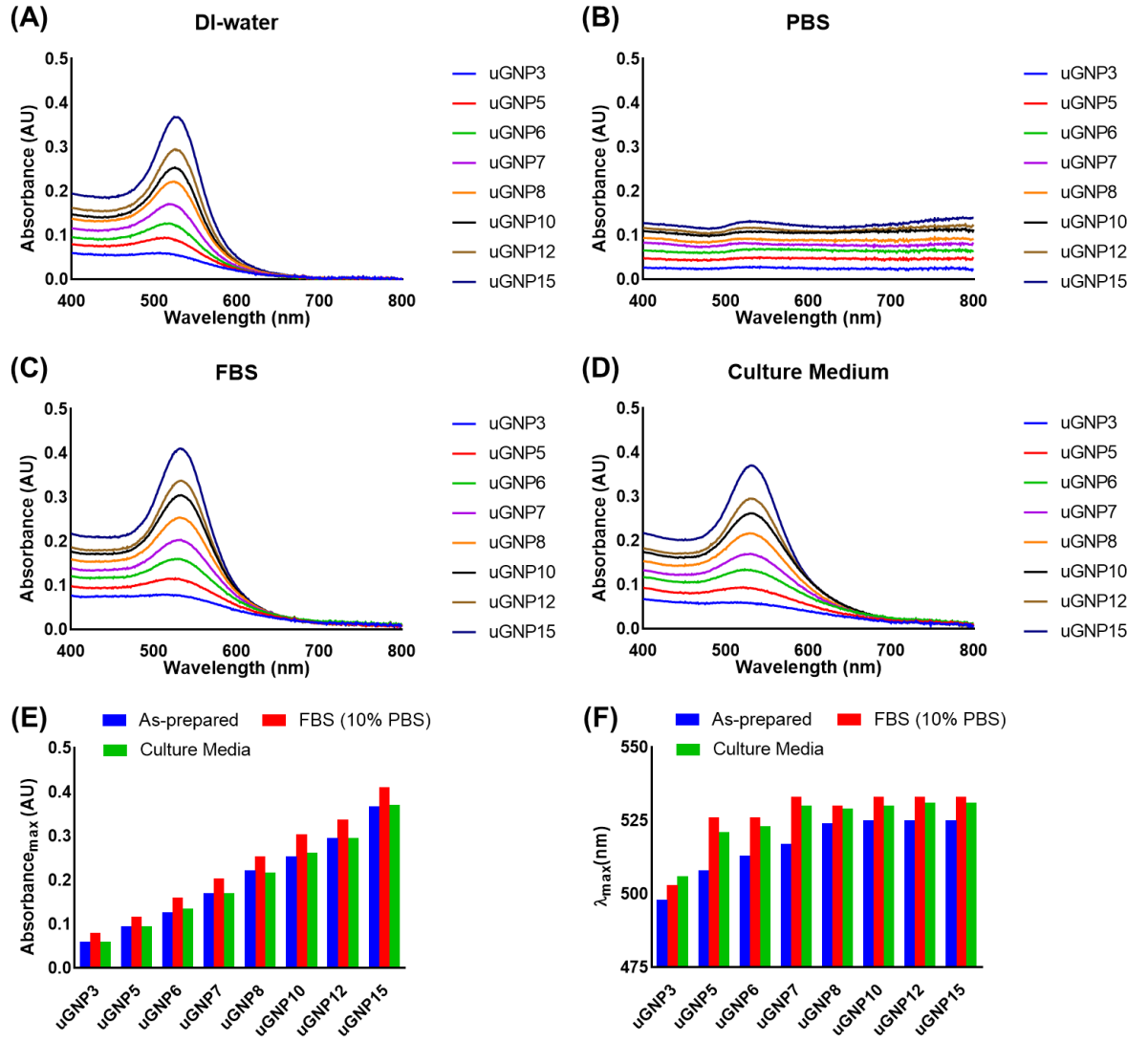

Figure 3-3. Stability of uGNPs in various dispersing media. UV-Vis spectra of uGNPs dispersed in (A) DI-water (control), (B) PBS (1X, pH 7.4), (C) fetal bovine serum (10% in PBS), and (D) colorless Dulbecco's Modified Eagle Medium supplemented with 10% FBS. Summary of maximum absorbance and λmax in DI-water, FBS solution, and culture medium. Measurements were performed after 24 h of incubation.

3.3.2 Cytotoxicity analysis with various cell lines

Although the cytotoxicity of gold nanoparticles has been extensively reported in the literature, conclusive agreement on their biosafety and biocompatibility has not been reached.[188] The *in vitro* cytotoxicity of uGNPs was assessed in human embryonic kidney cells

(HEK 293A), breast cancer cells (MCF7), and colon adenocarcinoma cells (SW480), after exposure for 24, 48, and 72 h respectively (Figure 3-4). The cytotoxicity assay used was the MTS assay, in which the MTS tetrazolium compound is bio-reduced by mitochondria into a colored formazan product that is soluble in cell culture media. The extent to which the tetrazolium compound is reduced is proportional to the number of viable cells, assuming mitochondrial activity is directly related to cell viability. The absorbance of the final color change is measured and converted to cellular viability.

Overall, uGNPs of all sizes exhibit low cytotoxicity for all three cell lines with a few sizes and doses causing noticeable low cell viability that does not fall into the general trends. In the case of 293A cell line, strong promotion of proliferation is observed at 24 hours up to 10 nm size. The boosted proliferations by GNPs were consistently reported in the literature.[189] Relative low cell viabilities were observed with 12 and 15 nm uGNPs at intermediate doses. At 48 hours, time point, the 12-nm uGNPs continued to exhibit some cytotoxicity effect at all doses investigated; however, interestingly this trend was reversed after 72 hours and promoted proliferation was observed. Further study is required to confirm whether there is an acute short-term suppressing effect followed by enhancing effect in proliferation caused by the treatment with the 12-nm uGNPs. An unexpectedly low cell viability has resulted from a low dose of 10 nm uGNPs at 72 hours; yet, the higher dose of the same treatment led to cell viability close to the control group. This could be due to the conflicting effects between cytotoxic and proliferation promoting effects, but the exact dose- and time-dependencies require more thorough investigation.

For MCF7, limited inhibitory effects in proliferation were observed for most of the treatment at 24 hours; although the differences were statistically significant for some groups, the cell viability stayed above 90%. The MCF7 treated with 12-nm uGNPs at intermediate dose exhibited more noticeably lower cell viability, which was also observed in the 293A cell line. After 48-hour treatment, the 8-nm and 12-nm uGNPs treated groups at a high dose resulted in an obvious decrease in cell viability while the rest of the groups either showed enhanced proliferation or had negligible influence on the cell viability. At the 72-hour time point, all treated groups had similar cell viability close to the control group, with 12-nm uGNPs at low dose displaying the lowest cell viability at 91.8%. For SW480 cells, all uGNP-treated groups exhibited close to 100% cell viability for 24 and 48 hours of treatment. Only the 10-nm uGNPs at low dose caused smaller than 90% cell viability at 82.1%.

To sum up, the actuate cytotoxicity of different sized uGNPs was investigated with three different cell lines. In general, smaller uGNPs promoted proliferation while medium-sized uGNPs around 8 to 12 nm resulted in some limited cytotoxic effects at specific time points and doses. Overall, the uGNPs fabricated with the process-engineered seed templated growth strategy showed no significant sign of acute cytotoxicity against three different cell lines at up to 125μM (gold element concentration) and 72 hours.

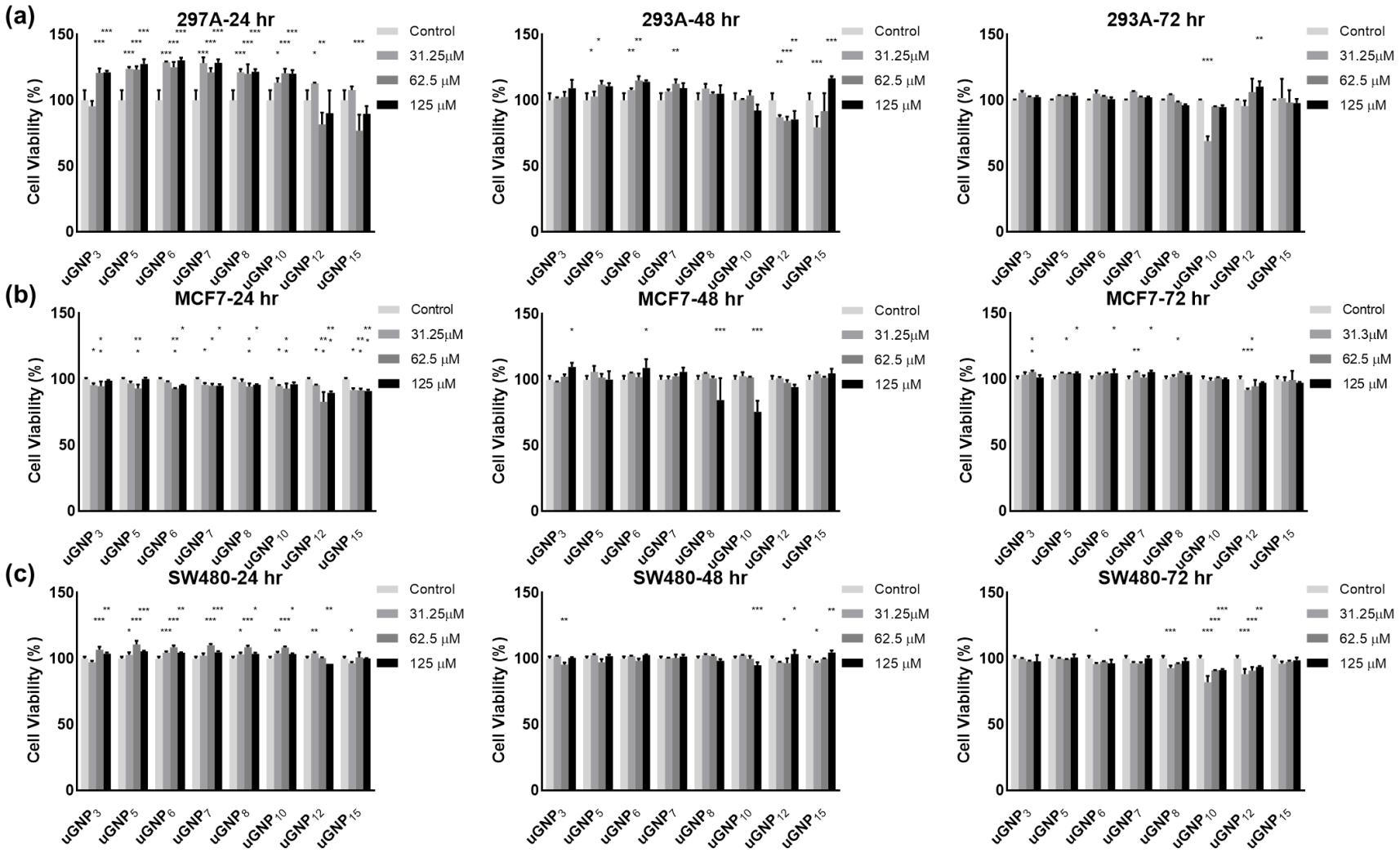

Figure 3-4. Cytotoxicity of uGNPs. Cell viability measured by MTS assays with (a) 293A, (b) MCF7, and (c) SW480 cell lines with the treatment of uGNPs for 24, 48, and 72 hours. Statistical analysis was performed between each treatment condition and the control set respectively. ($p \leq 0.05$*, 0.01**, 0.001***).

3.3.3 Compatibility analysis with THP-1 and THP-1 differentiated macrophages

In addition to non-connective cells, the cytotoxicity of uGNPs against connective tissue (blood) cells, monocytes and macrophages, was also examined as a part of immunotoxicity evaluation. The cytotoxicity of uGNPs (3, 6, 8, and 12 nm) was also assessed in THP-1 and THP-1 differentiated macrophages using MTS and LDH assay respectively over an incubation window of 72 h. As mentioned above, the MTS assay is an intracellular indicator evaluating the activity of mitochondrial dehydrogenase. In contrast, the LDH assay is an extracellular indicator that measures the leaked cytoplasmic contents from cells with compromised cell membranes. Specifically, the assay is a rapid fluorescent measurement of the released LDH from cells with compromised membranes. Evaluation of the leakage of components from the cytoplasm into the surrounding medium is taken as a measurement to determine the number of non-viable cells.

The schematic illustration of the experimental procedures as well as the respective morphologies of monocytes and macrophages are shown in Figure 3-5. Even after exposure at a high dose (125 μM) for 72 hours, both monocyte-like and macrophage-like THP-1 cells showed no significant reduction in viability when compared to the control group (Figure 3-5). Monocyte-like THP-1 cells exhibited strong promoted proliferation with the treatment of $uGNP_8$ at 62.5 μM and $uGNP_{12}$ at 31.25 μM. The enhanced proliferation was again observed with specific particle sizes and concentrations.[190] The unusual large extent of promotion close to 200% in viability, however, indicated potentially special interactions between uGNPs and monocytes, and can be further investigated in future work. It is interesting that the enhanced proliferation was not observed at a higher dose. These decreases in cell viability in the $uGNP_8$ and $uGNP_{12}$ groups at higher doses could be the results of cells entering the decline phase after being possibly overconfluent at shorter treatment periods. The exact mechanism for the enhancement in proliferation is unclear but should be further investigated in the future.

The cell membrane integrity assay (LDH assay) was performed on THP-1 macrophages to assess their viability after uGNPs exposure. As macrophages tend to execute phagocytosis on alien objects, the use of a membrane integrity assay to assay their viability is more relevant than the mitochondrial activity activity-based assay. The results from the LDH assay exhibited no observable leakage of cytoplasmic contents into the cell culture medium (Figure 3-5). The fluorescence intensities of uGNPs treated groups are at the same level as the negative control group and are statistically significantly different from the positive control

group (lysis solution treated). These results suggest that uGNPs are highly compatible with THP-1 differentiated macrophages and do not cause acute toxicity. The data obtained on macrophages showed that there were no significant effects on the viability after 72 hours of exposure to various uGNPs concentrations. The results are consistent with other studies previously reported in macrophages and human leukemia cells.[191] The results of cytotoxicity studies with uGNPs on various cell lines are in agreement with previously published reports on GNPs cytotoxicity.[192] It was found that spherical and negatively charged NPs, same as the uGNPs, often display less toxicity than rod-shaped and positively charged ones.[193]

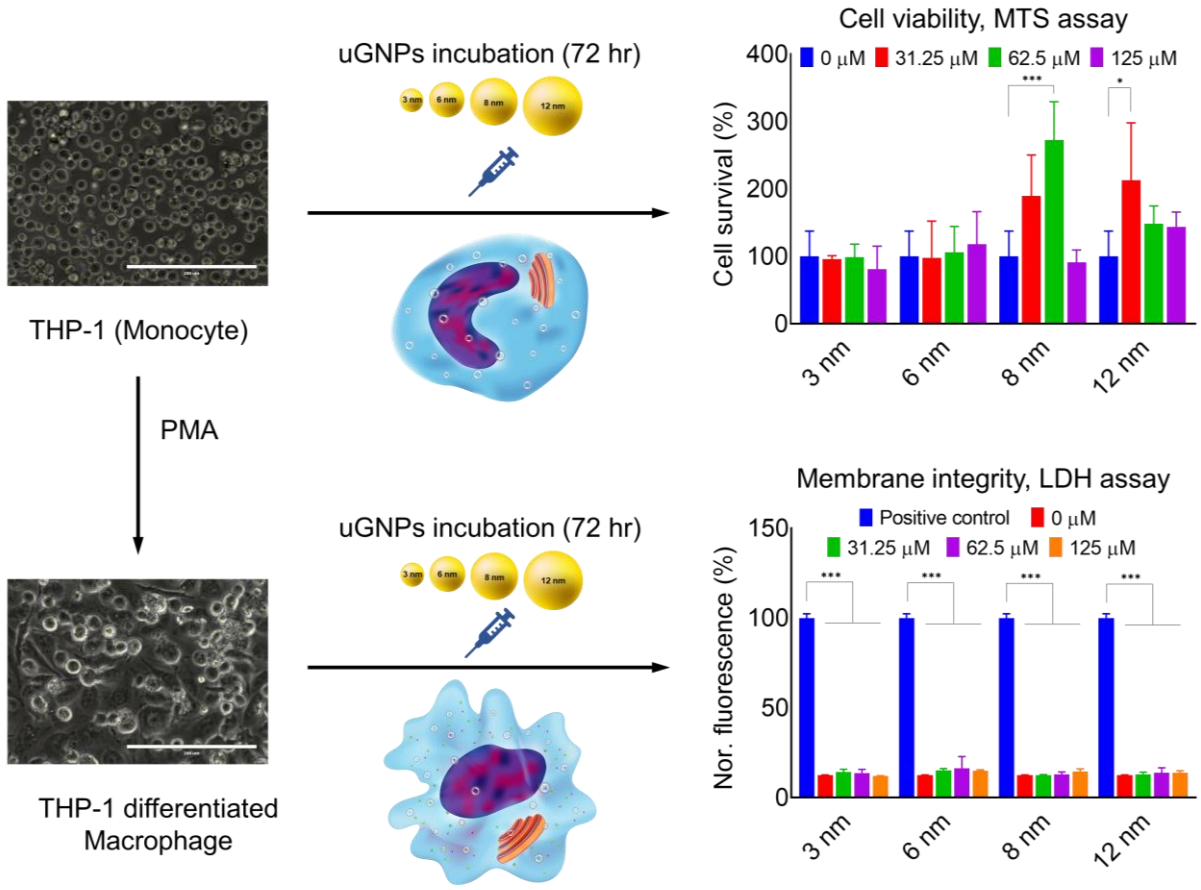

Figure 3-5. Cytotoxic effects of uGNPs on undifferentiated THP-1 monocyte cell line as measured with MTS assay (upper) and on differentiated THP-1 macrophage cell line as measured with LDH assay (lower) over a 72-hr period at various uGNPs doses. Data are expressed as mean ± SD. (***$p < 0.001$ and *$p < 0.05$).

3.3.4 Evaluation of uGNPs compatibility with the complement system

For NMs to be used *in vivo*, it is crucial to check their immune compatibility, especially for vaccination applications, where the immunogenicity of the NMs has a direct impact on the success in eliciting a desired immune response. The ability of uGNPs to induce

complement activation was investigated. In general, the complement system acts in immune surveillance by instantly responding to eliminate pathogens, other foreign substances, or damaged substrates.[194] To evaluate the immune safety of uGNPs, activations of specific markers C4bc (C4b/C4c), C3bc (C3b/C3c), and sC5b-9 (or terminal complement complex, TCC) by uGNPs were assessed after incubation in plasma for 30 minutes. The three markers represent three nodes of the complement system. The C4bc is the early stage of the complement cascade and is involved only with the classical and lectin pathway.[194,195] The C3bc is the common junction of the three complement activation pathways.[194,195] The terminal C5b-9 complement complex is the terminal product of activation as shown in Figure 3-1.[194,195] Complement was activated spontaneously (PBS-treated, negative control) during the incubation as measured by C4bc (18 ± 5.34 CAU/mL), C3bc (29 ± 5.7 CAU/mL), and C5b-9 (0.86 ± 0.25 CAU/mL), and no additional activation was seen by the presence of uGNPs for any size (Figure 3-6). It can be concluded that the treatment of uGNPs of any size did not elicit any stronger activation than the negative group and caused much less complement activation than the positive (zymosan) group.

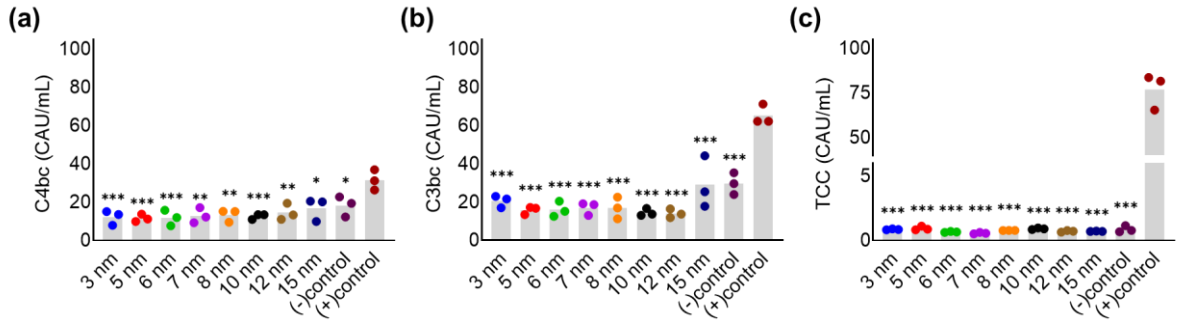

Figure 3-6. Complement activation in ex vivo human plasma by uGNPs of different sizes. (a) C4bc, (b) C3bc, and (c) TCC levels respectively at the end of incubation treated with uGNPs of all sizes at a gold elemental concentration of 125μM. The (-) control represents PBS-treated plasma and the (+) control represents zymosan-treated plasma. Statistical significance was determined between each group and the (+) control group at *$p \leq 0.05$, **$p \leq 0.01$ and***$P \leq 0.001$.

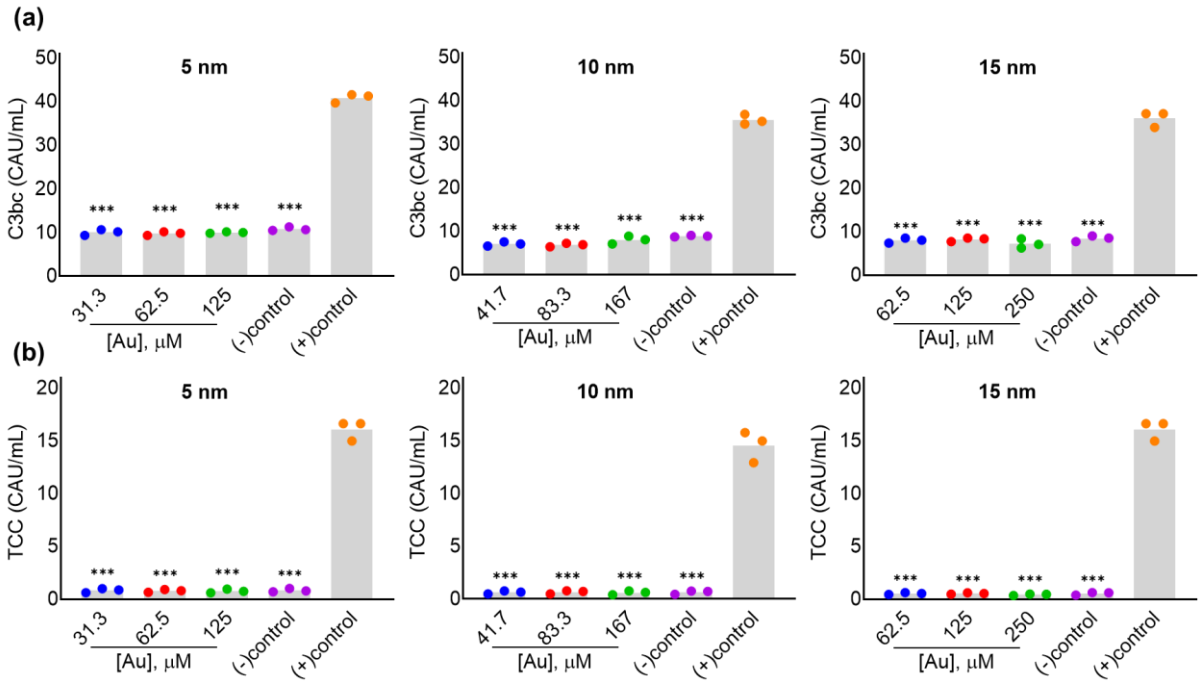

Figure 3-7. Complement activation in ex vivo human plasma by $uGNP_5$, $uGNP_{10}$, and $uGNP_{15}$ at different concentrations. (a) C3bc, and (b) TCC levels respectively at the end of incubation treated with $uGNP_5$, $uGNP_{10}$, and $uGNP_{15}$ at different concentrations. The (-) control represents PBS-treated plasma and the (+) control represents zymosan-treated plasma. Statistical significance was determined between each group and the (+) control group at *$p \leq 0.05$, **$p \leq 0.01$ and***$P \leq 0.001$.

The complement activation levels provoked by $uGNP_5$, $uGNP_9$, and $uGNP_{15}$ at various concentrations were also evaluated (Figure 3-7). The result showed that for these three NPs, their immunogenicity was substantially lower than the zymosan control within the concentrations examined. The result suggests that even without biocompatible surface coatings, the bare uGNPs fabricated using the seed-templated growth strategy do not elicit elevated complement activation.

3.3.5 uGNPs induced pro- and anti-inflammatory cytokines secretion

The influence of uGNPs on cytokine release by monocytes and macrophages was investigated using electrochemiluminescence immunoassay. For each treating condition, ten different cytokines were measured and compared to both the negative control (no treatment) and the positive control (LPS treated). Due to the large number of variables, PCA was employed to reduce the dimensionality of the data and enable the analysis of the cytokine release pattern. Figure 3-8 shows the PCA biplot of the cytokines release profile, showing both PC scores of different samples and loadings of the variances (cytokines). PC1 and PC2 are both linear combinations of all ten variables. The projected values of the cytokine vectors

onto each PC axis are proportional to their weight on the PC. Therefore, the IL-4 and IFNγ have small influence on both PC1 and PC2 as their loadings are very small. The rest of the cytokines all point in the positive direction of the PC1. The IL-6 and IL-12 have strong positive contributions to PC2, while IL-1β has strong negative contributions to PC2. It is interesting that all monocyte data points fall into the positive direction of PC2, and all macrophage data points are in the negative direction of PC2. This means monocytes in general produce more IL-6 and IL-12, whereas macrophages release more IL-1β.

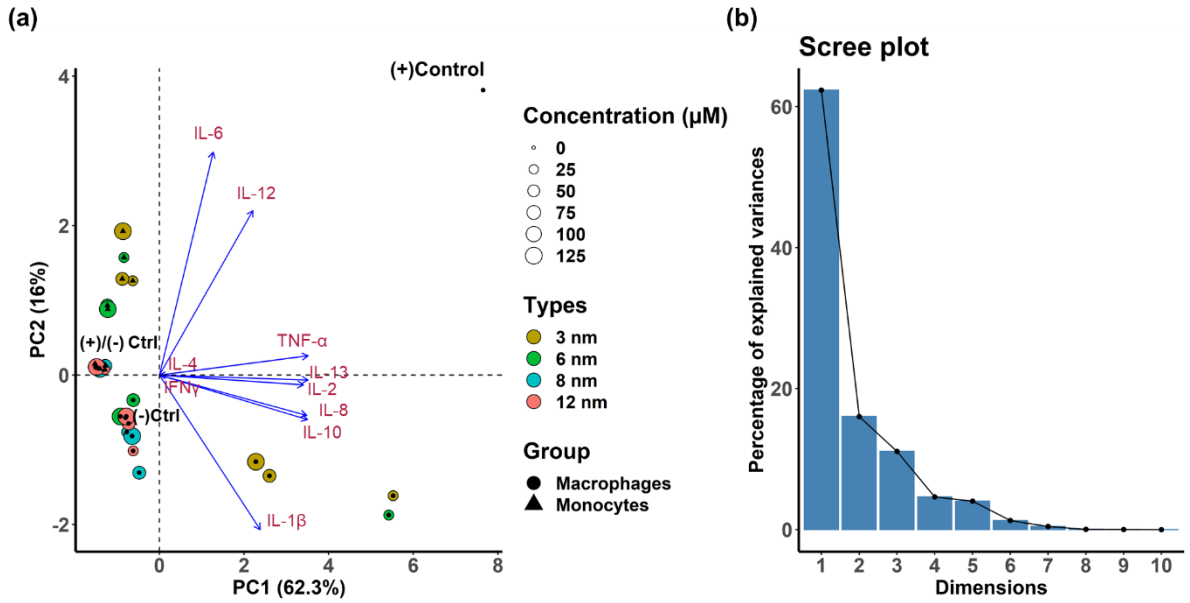

Figure 3-8. Cytokines and uGNPs illustrating sources of variance in the data following principal component analysis (PCA). (a) Both PCA scores and loadings were displayed in the biplot, representing their effective tendency on the data. Different uGNPs were marked with different colors (uGNP3: brown, uGNP6: green, uGNP8: cyan and uGNP12: red); the concentrations are represented by the circle size (lower concentration to higher concentration defines as smaller to larger circle). The negative and positive controls of the monocyte group locate closely with the 8 nm- and 12 nm-uGNP-treated monocytes in the upper left quadrant. The negative control of the macrophage group locates closely with 12nm-uGNP-treated macrophages in the lower left quadrant and the positive control locates by itself high up in the upper right quadrant. (b) The corresponding scree plot showing the proportion of variance of the first 10 principal components.

Each data point on the PCA plot can also be viewed as a vector with the starting point at the origin. Similar to the case with PCs, the projected values of variable vectors on data vectors are proportional to the weight of the variables on the data points. If two data points are located close to each other, it means they exhibit similar cytokine release profiles, and vice versa. The negative and positive controls of monocytes both lie closely with the cluster

composed of $uGNP_8$-treated and $uGNP_{12}$-treated monocytes close to the PC2 = 0. This indicates that neither the endotoxin LPS nor the larger uGNPs elicit significant changes in the cytokine release profile by monocytes. The treatment of $uGNP_3$ and $uGNP_6$, however, promoted the secretion of IL-6 and IL-12 and suppressed that of IL-1β as compared to the control groups. It shows that smaller uGNPs alter the cytokine release pattern to more extent than larger uGNPs in monocyte.

A similar trend was also observed with macrophages. The negative control for macrophages falls closely with the cluster consisting of $uGNP_6$ (intermediate and high concentration), $uGNP_8$ and $uGNP_{12}$ groups, while the positive control is positioned all by itself in the upper right quadrant. This means that treatments by larger-sized uGNPs do not skew the cytokine release prominently away from the negative control. In contrast, it was discovered that $uGNP_3$-treated and $uGNP_6$-treated (lowest concentration) groups were placed in the lower right quadrant, away from the negative control. Based on the relative displacement, it can be inferred that elevated release of IL-1β, IL-2, IL-8, IL-10, IL-13, and TNF-α was resulted by $uGNP_3$ and $uGNP_6$, suggesting proinflammatory effects.

In summary, larger particle size had less effect on cytokine release profile in both monocytes and macrophages. The locations of all uGNPs-treated macrophages on the PCA plot are far from that of the endotoxin-treated group (positive control), suggesting that uGNPs are relatively nontoxic when benchmarked against LPS. The smaller uGNPs seemed to direct cytokine release towards proinflammatory reactions, because the releases of more proinflammatory than anti-inflammatory cytokines were promoted; however, the exact implication of the changes in cytokine profiles needs further investigation. The results suggest that the uGNPs are immune compatible in general with larger uGNPs being immune invisible to monocytes and macrophages, and the smaller uGNPs possessing some proinflammatory effects and thus having the potential of being utilized in nanovaccine applications.

3.3.6 Effect of uGNPs on blood coagulation

For a successful translation of nanoparticles into a clinical setting, it is imperative to understand their interaction with blood and its components. Blood clotting is a relevant test which can be extremely useful in assessing the reaction of coagulation factors upon exposure to nanoparticles. There have been many recent investigations of NP interactions with blood and blood components.[173,196–198] Mostly, the hemolytic effect is quantitatively estimated for

understanding nanoparticle interactions.[199] In this study, the influence of uGNPs on blood coagulation was estimated using APTT and PT tests. These are the standard tests generically used for investigating the functions of the intrinsic and extrinsic pathways of coagulation. The APTT evaluates the time required to form fibrin following the activation of factor XII via the intrinsic pathway, while the PT estimates the time needed to form fibrin following the activation of factor VII via the extrinsic pathway.

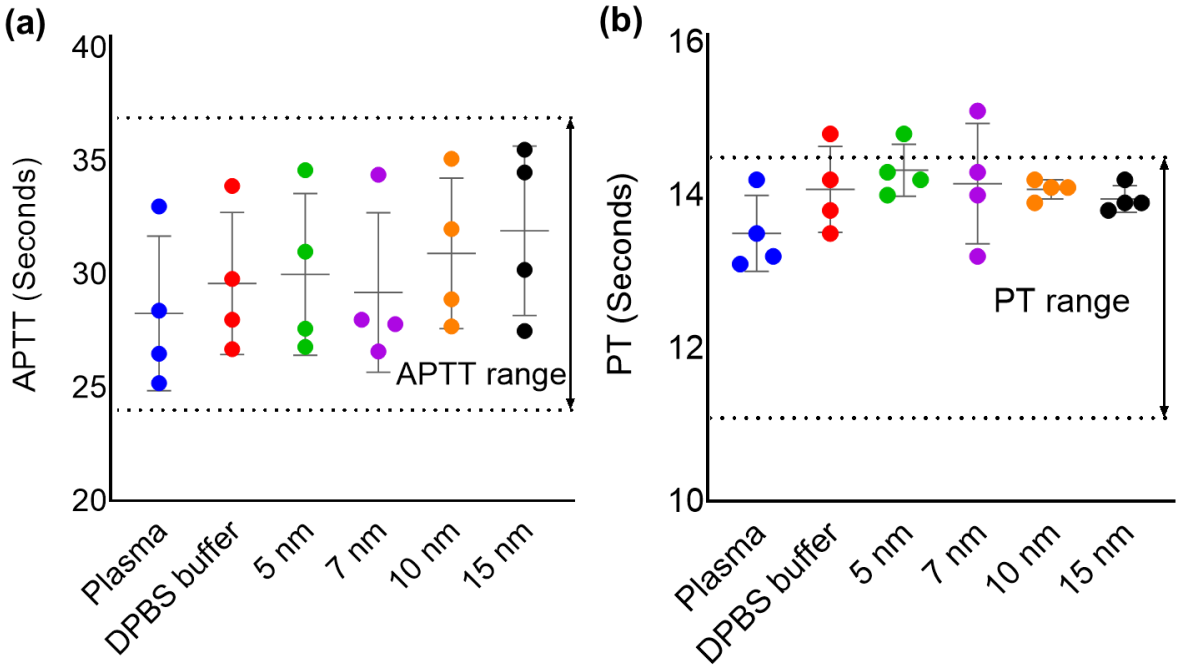

Figure 3-9. Effect of uGNPs (5, 7, 10, and 15nm) on blood coagulation. Effect of uGNPs on (a) intrinsic pathway (APTT) and on (b) extrinsic pathway (PT), due to the exposure of uGNPs in each of their size. Data are expressed as individual points and mean ± SD.

The APTT is generally used to assess coagulation disorders in patients with bleeding abnormalities owing to deficiencies within the intrinsic factors which leads to induced prolonged APTT. Additionally, it also reflects the effect a biomaterial can have on coagulation. It has been known that the normal physiological levels for APTT and PT are 25.1 ~ 36.5 s and 9.4 ~ 12.5 s, respectively.[200,201] After incubating plasma with increasing volume of uGNPs for 10 minutes, the solution was mixed with different reagents for testing clotting time. The results showed that there was no significant effect of uGNPs on plasma coagulation time (APTT and PT) from low concentration to high concentration of uGNPs for both the pathways (Figure 3-9). The results indicate that uGNPs exert no significant influence on blood coagulation in *ex vivo* tests with human plasma. This observation further validates

the biocompatibility of the as-synthesized particles. Hence, the uGNPs can be an exceptionally valuable asset for nanomedicine translational studies.

3.4 Conclusions

In this chapter, the biocompatibility of uGNPs, fabricated using the seed-templated synthesis method described in Chapter II, was investigated in terms of cytotoxicity, immune compatibility, and blood compatibility. The as-synthesized uGNPs displayed negligible cytotoxicity against multiple cell lines and, in some cases, they even enhanced the proliferation of cells. The uGNPs induced no additional level of complement activation in human plasma samples. They also showed high biocompatibility and immune compatible profile with no toxicity towards monocyte and macrophage. It was found that larger uGNPs had no impact on cytokine release profiles by monocyte or macrophage, whereas smaller uGNPs had slight promotional effects on proinflammatory cytokine release. Even with the proinflammatory effects, smaller uGNPs steers the cytokine release profile in a manner far different that that caused by the endotoxin-treated positive control group, implying the nontoxic nature of uGNPs. The proinflammatory effects of smaller uGNPs could make them suitable candidates for nanovaccine applications. Lastly, the uGNPs also showed negligible thrombogenicity.

In conclusion, the uGNPs exhibited superb biocompatibility in a framework of *in vitro* and *ex vivo* check-ups. With nanometric size control and superior biocompatibility, the uGNPs can serve as versatile platforms to benefit a wide array of biomedical applications including vaccines, cancer therapies, and imaging contrast enhancer in translational settings. In addition, the all-around safety check framework established in the chapter can be extended in the future for any newly synthesized NMs for systematic biocompatibility examination before *in vivo* studies.

4 Nanocoacervate systems for rapid nanoformulation

4.1 Introduction

As mentioned in Chapter 1, facile and cost-effective fabrication of NPs remains a bottleneck in nanomedicine translation. Complicated manufacturing procedures and energy intensity synthesis routes of many NP systems inevitably increase the cost and hinder their clinical application from an economic perspective. In addition, the rigorous requirement in storage conditions to maintain the colloidal stability during transportation also exerts difficulties for efficient translation. For example, the low sub-freezing temperature requirement for LNP-mRNA vaccines against COVID-19 (for both BioNTech and Moderna vaccines) prohibited them from being more readily available worldwide. Therefore, instant nanoformulation systems that can be fabricated bedside in a mix-and-go fashion, with the minimum amount of operative intervention requirement, are highly desirable. One method that can achieve such features is the complex coacervation-driven self-assembly process.

This chapter describes the development and characterization of a rapid nano-formulation system via coacervation of two oppositely charged and intracellular trafficking polyelectrolytes together with a chemotherapeutic drug doxorubicin (Dox). The fabrication conditions were optimized with mixing ratios and sequence to achieve colloidally stable nanocoacervate systems which were then characterized for their particle size, charge, morphology, drug encapsulation, and payload release. The nanocoacervate system allows *in situ* formation of nanosystems for biomedical applications. It helps to bypass the obstacles of the complicated fabrication process and long-term storage requirement, and can become a platform technology for many applications in different clinical settings.

4.1.1 The benefits of facile and rapid nanoformulation

Nanosized materials can have unique interactions with biological systems which enable researchers to design special delivery, diagnostic, and biosensing systems.[1] However, large-scale manufacturing and storage requirements for nanoformulation impose difficulties in their translation and commercialization. Readily scalable NPs fabrication methods, such as laser ablation and lithography-based processes, require complex equipment and facilities and are energy-consuming.[202] Other more cost-effective fabrication methods, such as wet chemical synthesis, are routinely utilized to make colloidally stable NP in laboratory settings, but can be difficult to scale up to the industrial level.[32] In addition to high fabrication costs

and difficult size control, the shelf-life of nanomedicines is also a big concern, as long-term storage of NP can compromise the morphology, stability, and functionality.[203]

One approach to overcome the manufacturing and storage issues of NPs is to develop instant nanomedicine formulations which can be prepared bedside right before administration from the precursor ingredients in a "mix-and-go" fashion. Inorganic NPs are usually synthesized using special apparatus or via chemical reactions with strict conditions, so they are not suitable for the instant formulation of NPs as they need to undergo several more steps in drug loading and purification. Polymeric NPs on the other hand can be fabricated using spontaneous or self-assembly processes, such as nanoprecipitation, micelle formation, and hydrophobic association, so are more promising candidates of instant nanoformulations.[204–206]

4.1.2 Rapid nanoformulation by complex coacervation

One such method is the complexation of oppositely charged polyelectrolytes. Polyelectrolyte complexation can lead to the formation of liquid-liquid separation called coacervate at right charge ratios in nanometer to sub-micron sizes.[207] Coacervate has been recognized as an effective way to compartmentalize macromolecules in aqueous systems without the presence of membranes.[208] It is also believed in the Oparin-Haldane hypothesis that it could be an important mechanism to form protocells as a step in the origination of life.[209] Coacervates can be formed either by polyelectrolyte pairs or by polyelectrolyte and charged small molecules, as long as they can provide multivalent interaction. Charged payloads, such as protein, small molecule drugs, and nucleic acid, can thus either directly participate in coacervate formation with a polyelectrolyte as the second component, or be incorporated into a polyelectrolyte pair to compose a tertiary (or higher order) system. Coacervate systems have previously been utilized in hydrophobic drug dissolution, protein delivery, wound healing, angiogenesis enhancement, antibiotics delivery, and heart repair.[210]

4.1.3 Polyelectrolyte complex systems with stimuli-responsive properties

Many complex and coacervate systems possess intrinsic stimuli-responsive dissociation properties. Complexation and coacervation are driven primarily by electrostatic interaction between charged groups. These interactions can be influenced by multiple factors, such as polyelectrolyte charge density, molecular weight, and screening effect.[211] Therefore, changes in such conditions could result in disruption of the coacervate structure and discharge of the loaded agents. Polyelectrolytes containing ionizable groups (-NH_2, -COOH) and those composed of biodegradable components (disulfide, gelatin, hyaluronic acid) can

respond to changes in pH,[212] redox potential,[213] and enzyme.[214] Many of these stimuli are present in different biological environments and can be employed by coacervate delivery systems for desired release schemes. For example, the slightly acidic pH can be found in endosomes/lysosomes and in cancer cells, while redox potential difference changes dramatically across cell membranes.

4.1.4 Nanocoacervate with facilitated intracellular trafficking

The polyelectrolytes incorporated in the coacervate can not only provide protection and stability to the payloads but also bring favorable functionalities such as targeting and intracellular trafficking. For instance, cationic polyelectrolytes, including polyethylenimine (PEI) and polyallylamine, are widely used as non-viral gene vectors.[215] Because cationic polyelectrolytes can efficiently condense negatively charged nucleic acids and bind to negatively charged cellular membrane components, they are widely used in gene transfection applications.[216] Once internalized through endocytosis, the "proton sponge" effect of polyamines can enhance endosomal escape by causing the influx of proton leading to the bursting of endosomes.[217] However, the cytotoxicity of cationic polyelectrolytes cannot be neglected.[218] Therefore, synthetic polyelectrolytes with high intracellular delivery efficiency and low cytotoxicity are highly desirable replacements for cationic polyamines.

Bioinspired polymers mimicking the structure and pH-responsive endosomolytic activity of viral peptides have been previously synthesized and studied.[219] Polyelectrolyte with ionizable carboxylic acid groups can undergo charge density change with decreasing pH leading to the reduction of intramolecular repulsion and the transition from extended to coiled chain conformation.[220] The conformation change results in the emergence of hydrophobic domains which enhance hydrophobic interaction between the polymer and the lipid bilayer membrane and finally disrupt the intracellular vesicles. Anionic pseudo-peptide poly(L-lysine iso-phthalamide) grafted with L-phenylalanine (PP) and other polymers is among this class of polymers. The transition pH of the polymer series has been discovered to depend on the type and degree of grafted side chains.[221,222] In this study, PP50 and PP75, which are PP polymers synthesized with 50% and 75% L-phenylalanine stoichiometric substitution ratio, were used to form coacervate with Dox. In the nanocoacervate system described in the following sections, the PP polymer and PEI were selected to form a nanosized coacervate delivery system to sequester a payload. Despite the potential cytotoxicity, PEI is selected as an assembly component due to its cationic nature and wide exploitation in delivery applications.

4.2 Materials and methods

4.2.1 Materials

Polyethylenimine (PEI), branched (M_w ~25,000 M_n ~10,000) was purchased from Sigma-Aldrich (Merk) and used without further purification. Doxorubicin Hydrochloride (Dox) (>95%) was purchased from Tokyo Chemical Industry and used as received. All solvents were procured from Sigma-Aldrich of Merk. To prepare the samples for the experiments, Milli-Q water with a conductivity of less than 2 μS cm^{-1} was used.

4.2.2 Synthesis of PP polymer

PP50 was synthesized by our previous group member Dr. Alex Chen and PP75 was kindly provided by Dr. Rongjun Chen's group from Imperial College London. PP polymers were synthesized in-house according to a previously established procedure.[219,221] Poly (L-Lysine Iso-phthalamide) (PLP) (Mw = 35,700, Mn = 17,900, polydispersity =1.99) was grafted with different amounts of L- phenylalanine (Phe) to prepare the PP polymers. The numbers 50 and 75 represent the stoichiometric molar percentages of Phe relative to pendant carboxylic acid groups on the backbone of PLP. The actual degrees of grafting of PP50, and PP75 were determined from ^{1}H-NMR spectra, and it was found to be 41.4 and 63.4 mol % respectively.

4.2.3 Fabrication and optimization of coacervate

PP polymers and PEI were first dissolved in DPBS at a concentration of 5 mM with respect to the repeating unit. Dox was dissolved separately in DI-water at 1mg/ml. To make the coacervate, a predetermined volume of Dox stock solution was added to the PP polymer solution. The mixture was vortexed (Vortex-Genie 2) at 3200 RPM for at least 5 seconds. The PEI stock solution was added to the mixture and the mixture was again vortexed for about 10 seconds. Similar procedures were used to make PP-Dox and PEI-Dox with respective components. The coacervate can be used directly as prepared. However, to strictly compared the loaded and free Dox, coacervates were dialyzed (Slide-A-Lyzer™ MINI Dialysis Devices) against DPBS overnight. The exact amount of Dox remaining in the system was calculated with quantification of Dox in the dialysis solution by measuring the fluorescence intensity with emission signal at 590 nm and excitation at 470 nm (Tecan Spark Multimode Microplate Reader).

4.2.4 ^{1}H-NMR spectroscopy measurement

^{1}H-NMR spectra were recorded on a Bruker Ascend 500 MHz (Bruker, Coventry, UK) for at least 1200 scans (due to solubility limitation). Samples were prepared in D_2O or deuterated DMSO solvent (DMSO-d_6).

4.2.5 Dynamic Light Scattering (DLS)/ζ-potential measurement

Hydrodynamic diameter and ζ-potential were measured at 25°C with Zetasizer Nano ZS (Malvern PANalytical Products, UK) with at least 90 scans for each sample. For coacervate samples, measurements were taken directly with the emulsion, and measurements were taken on the supernatant solution for samples with visible precipitate.

4.2.6 Transmission electron microscopy (TEM) imaging

The TEM study was carried out in collaboration with Andrew Backer. The TEM images were captured with an FEI TECNAI F20 instrument with an acceleration voltage of 200 kV. Samples were prepared by drop-casting coacervate onto a 300 mesh Cu grid grit followed by air-drying overnight.

4.2.7 Scanning electron microscopy (SEM) imaging

The acquisition of the SEM images was performed by Xiewen Liu. SEM images were taken on a Nova nanoSEM instrument at 10kV and a working distance of 6.3 mm. The nanocoacervate samples were drop cast onto the substrate and allowed to air-dry overnight. The dried samples were then coated with Platinum before imaging.

4.2.8 Evaluation of Loading Capacity and Encapsulation efficiency

Samples were centrifuged at 14,000 g for 30 minutes before the Dox content in the supernatant was measured by fluorescence intensity with emission signal at 590 nm and excitation at 470 nm (Tecan Spark Multimode Microplate Reader). Loading Capacity and Encapsulation efficiency are defined as followed:

$$LC\% = \frac{Weight\ of\ Dox\ encapsulated}{Weight\ of\ Polymers + Weight\ of\ Dox} \times 100\%$$

$$EE = \frac{Amount\ of\ Dox\ encapsulated}{Amount\ of\ Dox\ in\ feed} \times 100\%$$

4.2.9 Investigation on the pH-dependent release profile

As-prepared coacervate systems (0.5 mL) were pipetted into the Slide-A-Lyzer™ MINI Dialysis Devices against DPBS (14 mL) with adjusted pH. The dialysis devices were placed on a shaker for the entirety of the release experiment. At different time points, 1mL of dialysate was taken from the device and replaced with 1 mL of DPBS with the corresponding pH. The released Dox content in the dialysate was measured by fluorescence intensity.

4.2.10 Stability assessment of coacervate in aqueous and BSA solutions

Coacervates made with different compositions were compared for their relative colloidal stability in both DPBS and in presence of Bovine Serum Albumin (BSA). Freshly made coacervates were diluted by 2 times with DPBS or BSA-containing DPBS and allowed to stand for 24 hours. The absorbance of the samples right after the fabrication and at 24 hours were both measured. In the case of samples with precipitate, measurements were taken with supernatant. The relative absorbance was taken as a metric for colloidal stability.

4.3 Results and Discussion

4.3.1 Formation of the PP-PEI-Dox nanocoacervate system

Two polymers, PP50 and PP75, were used to create the nanocoacervate, where the numbers (50 and 75) denote the stoichiometric substitution percentages of the L-phenylalanine relative to pendant carboxylic acid groups along the backbone. The ^{1}H- NMR spectra of PP50 and PP75 revealed the actual degrees of substitution were 41.4 and 63.4mol%, respectively (Figure 4-1). The chemical structures of PP and PEI, the schematic illustrations of coacervate assembly and the fabrication process are shown in Figure 4-2. The complex coacervation was achieved by simple mixing of PP, PEI, and Dox in PBS. PBS was used to mimic the physiological condition and prevent premature release of Dox due to pH and ionic strength shock once applied to culture media. The PP was first mixed with Dox, and PEI was then added to form the nanocoacervate system.

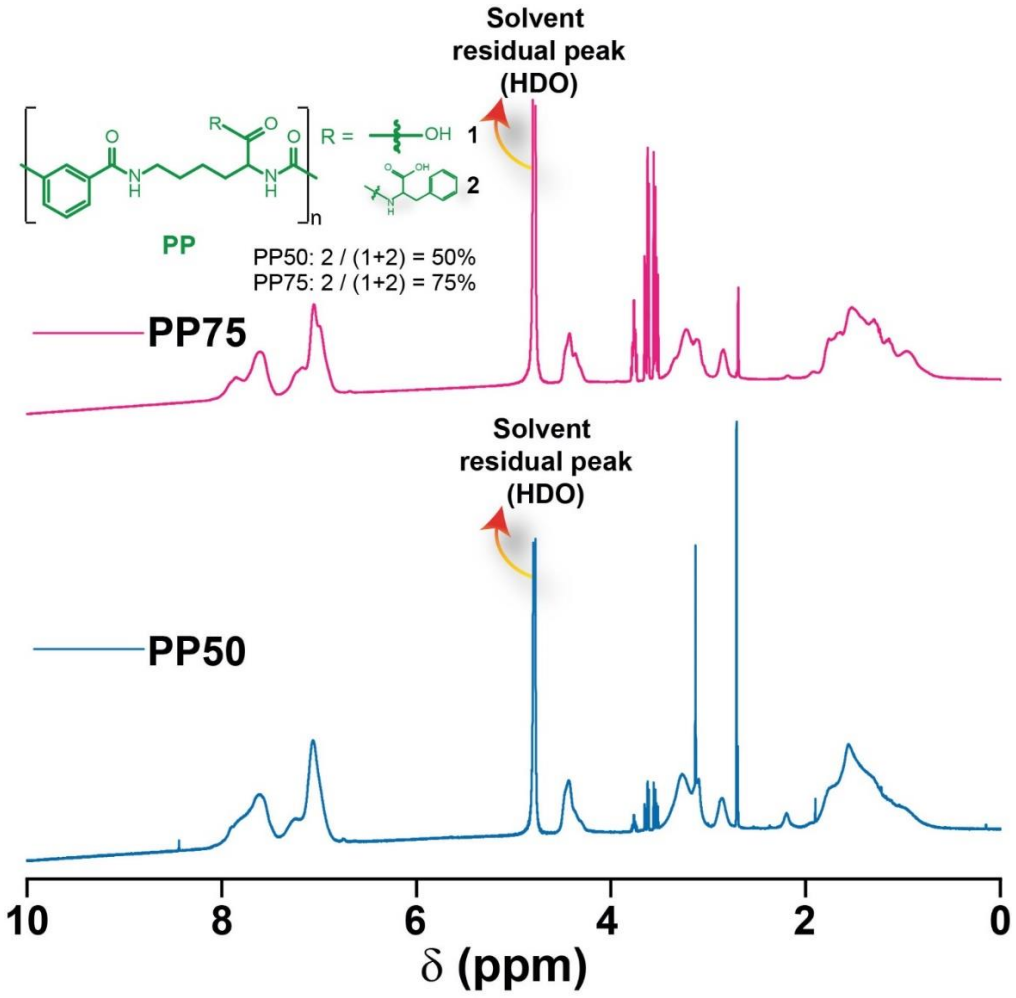

Figure 4-1. 1H-NMR spectra of PP50 and PP75 measured in D2O.

Electrostatic interaction between the cationic and anionic polymers, π–π interaction between phenylalanine and doxorubicin, and H-bonding are the probable driving forces contributing to the coacervate formation.[223] To check the H-bonding and π–π stacking, the ^{1}H-NMR spectral peak shifts were investigated. In the PP75-Dox mixture, a prominent upfield shift of Dox -phe protons as well as broadening of PP75 -phe protons were observed, indicating probable π–π stacking between phenyl rings of PP75 and Dox during the self-assembly process (Figure 4-2C).[224,225] In the case of the PP50, the upfield shift of -Phe protons was less prominent than that of PP75 (Figure 4-3). This distinction could be due to the difference in the degree of L-phenylalanine substitution and thus the hydrophobicity between PP75 and PP50.[221,226]

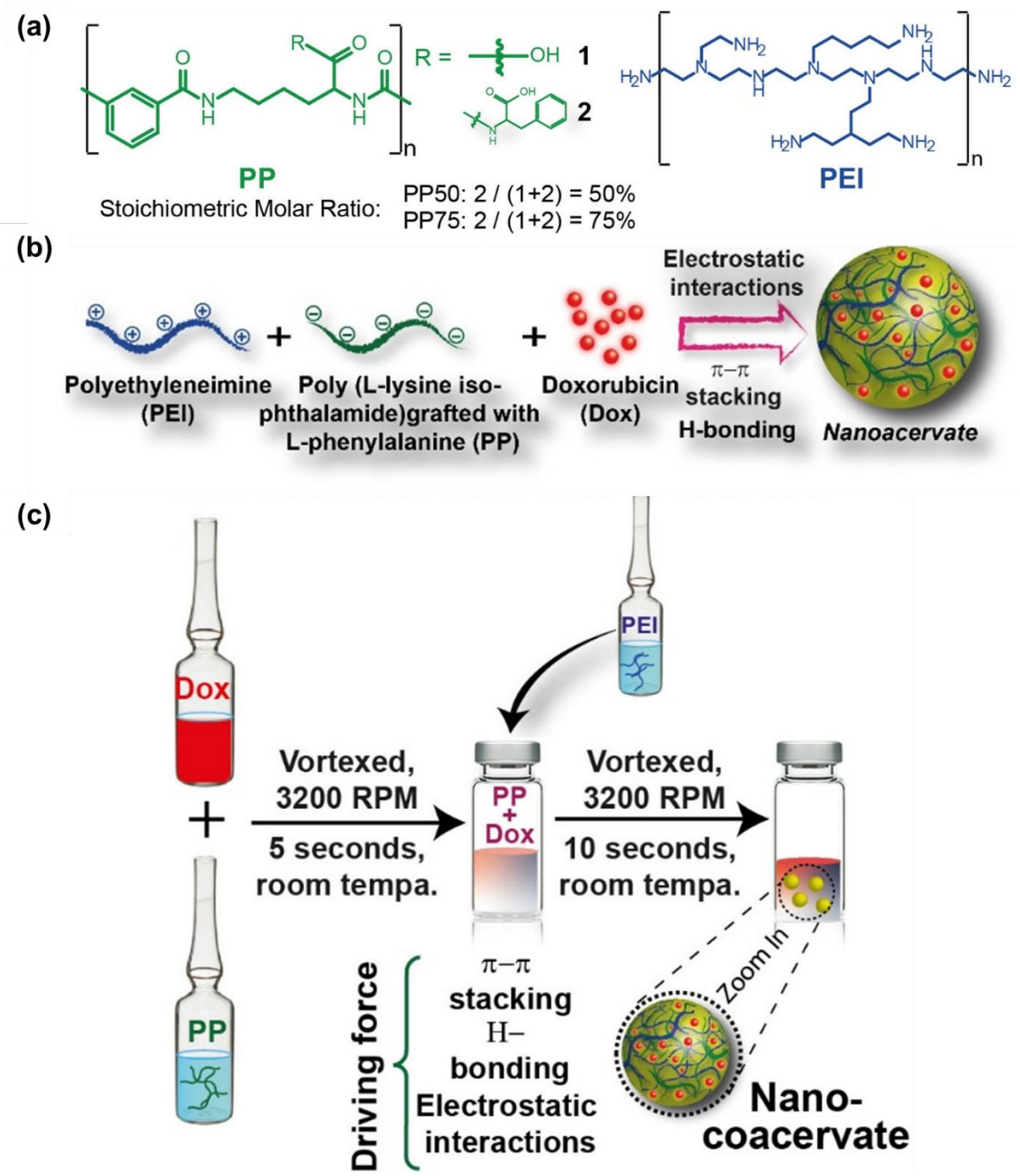

Figure 4-2. (a) Chemical structures of PP polymers (PP50 and PP75) and PEI used in this study; (b) Schematic representation of the encapsulation of Dox during coacervate formation. The scheme only shows the inter-molecular interactions with mixing time and mixing sequence not being reflected. (c) Pictorial presentation of coacervate preparation by simple mixing of anionic polymer (PP), cationic polymer (PEI), and chemotherapeutic drug, doxorubicin (Dox) in DPBS buffer (pH 7.4).

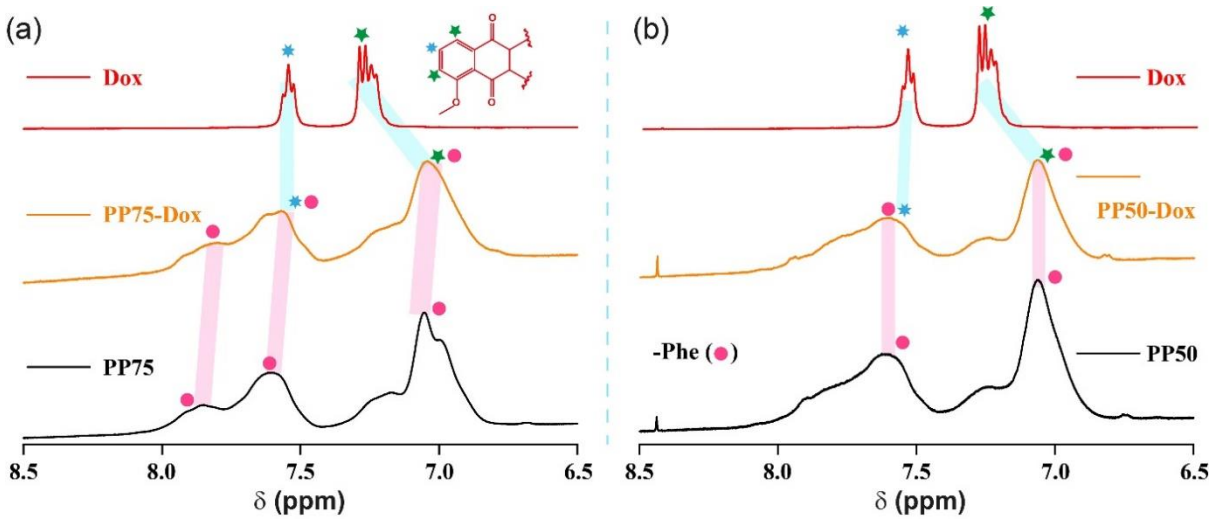

Figure 4-3. Aromatic region of ^{1}H NMR spectra of (a) PP75 and (b) PP50, Dox and their mixture in D_2O displaying the upfield shifts as well as broadening of aromatic protons because of π–π stacking in the aromatic region.

Because of the low solubility as well as -OH peak intensification of PP in D_2O, ^{1}H-NMR was measured in DMSO-d_6 to check the role of -OH group present in PP during coacervate formation (Figure 4-4). In the presence of PP50, the -OH signals of Dox diminished confirming the participation of -OH in the assembly process (Figure 4-4b). The generation of dark red or deep brown color from bright red Dox solution also indicated the complex formation between PP and Dox (Figure 4-4a). The continuous decrease of absorbance at 482 nm with the concomitant enhancement of a new peak at a higher wavelength of 602 nm in UV-Vis spectroscopy indicates the active participation of -OH group as well as complexation with Dox in the coacervate.[227] The evidence from ^{1}H-NMR, the color change of the mixture, and UV-Vis spectroscopy together indicate the active participation of -OH group in complexation with Dox.

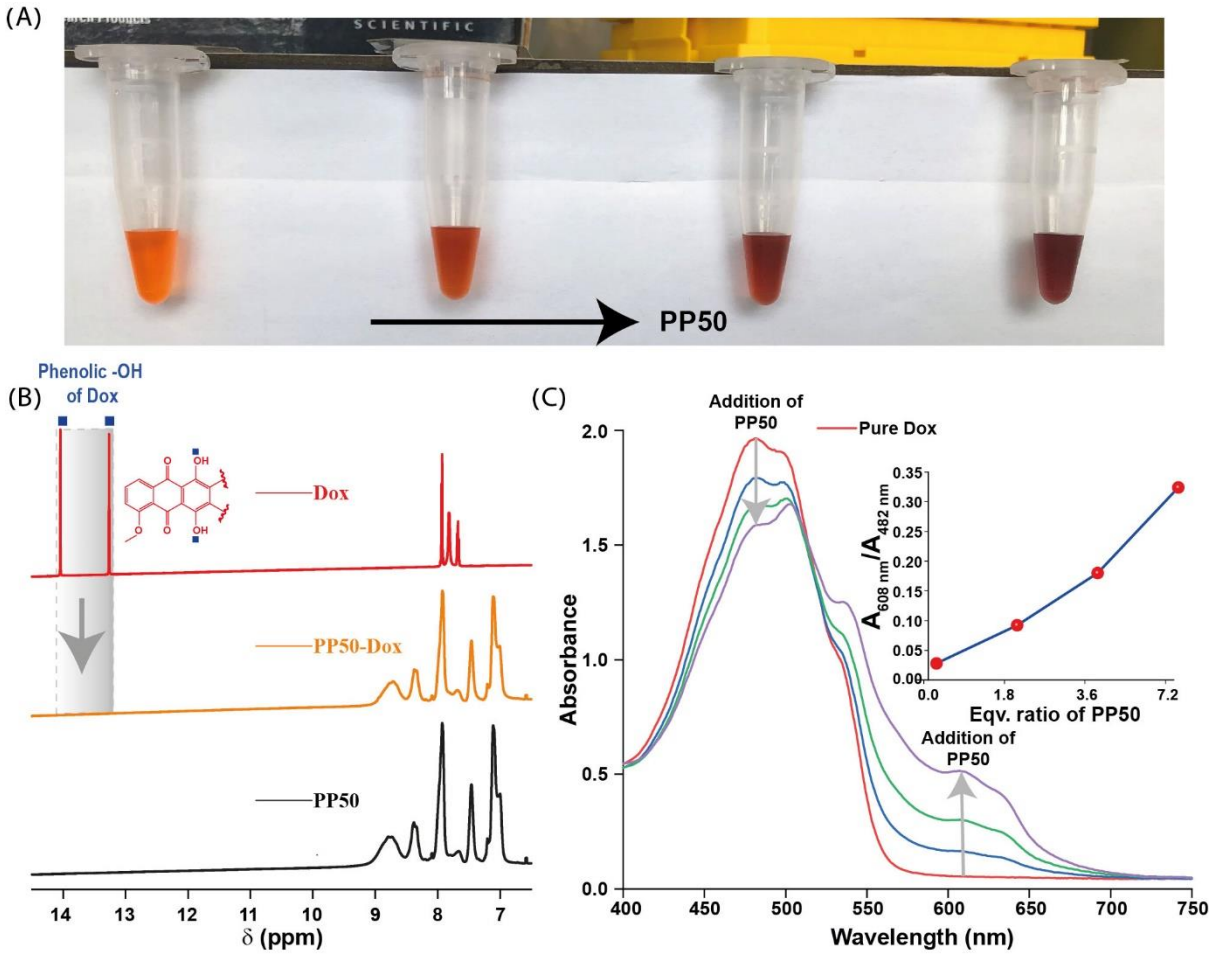

Figure 4-4. (a) Photographs of microcentrifuge tubes containing Dox solutions in DMSO mixing with different amounts of PP50 showing the color change at room temperature; (b) Partial region of ^{1}H NMR spectra of PP50, Dox, and their mixture in DMSO-d_6; (c) UV-Vis spectra of Dox in the presence of different amounts of PP50. Inset of (c): variation of absorption ratio ($A_{608\ nm}/A_{482\ nm}$) as a function of PP50 equivalence, obtained from Figure (c).

4.3.2 Optimization of conditions for the formation of nanocoacervate

Complex coacervate systems formulated with various mixing ratios between PP50 and PEI were investigated, with combined polymer concentration held constant at 4.5 mM with respect to the repeating units, while the Dox concentration was kept at 172 μM (Figure 4-5). When the PP50 composition ($\frac{PP50}{PP50+PEI}$) in the system was greater than 0.75, turbid coacervates were formed. The ζ-potentials and hydrodynamic diameters of complexes or coacervates with various mixing ratios were measured. The ζ-potential of complexes decreases with an increasing amount of PP50. The large negative values in the three formulations with the highest PP50 compositions (0.75, 0.8, and 1) provided the strong repulsion necessary for colloidal stability. It is worth mentioning that measurements of

samples with visible precipitates were conducted with supernatant. The formulation of PP50 composition at 0.8 was used for further investigation. The hydrodynamic diameters of the two coacervates (PP50 composition 0.75 and 0.8) exhibit two-peak distribution patterns, with one close to 100 nm and the second approaching 1μm. This wide particle size distribution is well-established in the literature for coacervate systems, where small droplets can coalesce to form larger droplets over time and finally reach bulk phase separation.[228]

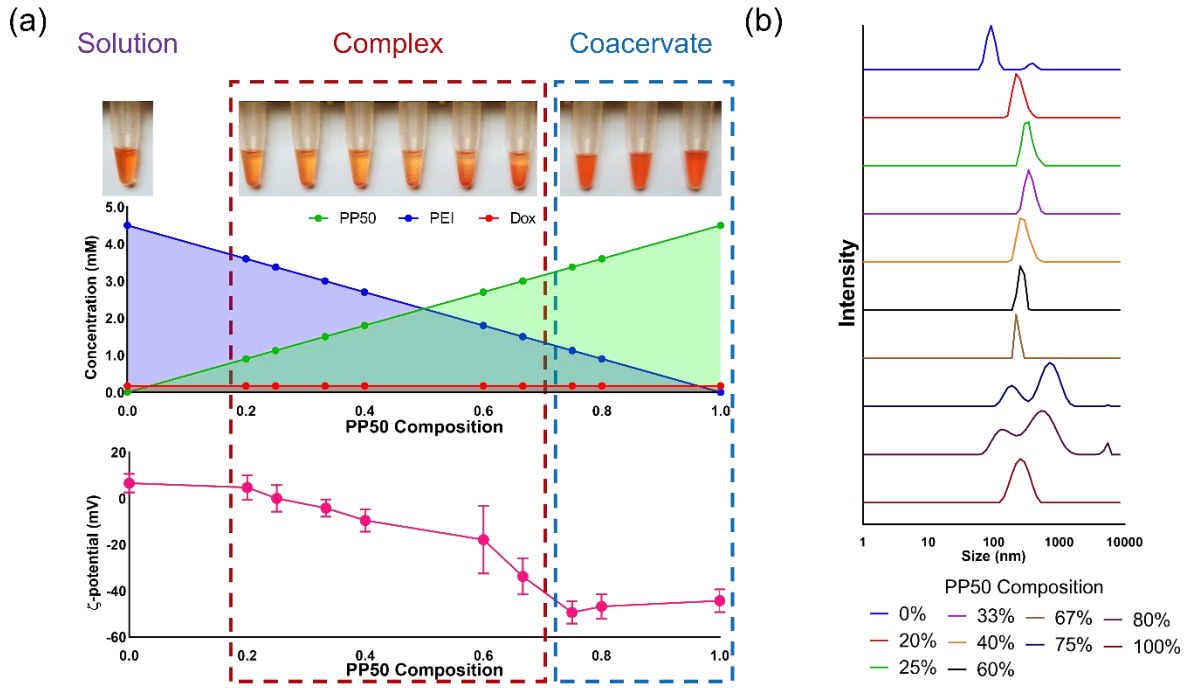

Figure 4-5. (a) Photographs of different formulas made with various PP50 to PEI ratios are listed in the top panel. A solution was obtained with only PEI + Dox, precipitations were obtained with PP50 composition from 0.2 to 0.67, and coacervates were obtained with PP50 composition greater than 0.75. Detailed concentrations of components in different formulas are shown in the middle panel. Respective ζ-potential of complexes/coacervates with different formulations are exhibited in the bottom panel. Error bars represent standard deviations. (b) Hydrodynamic diameters of complexes/coacervates measured by DLS with different samples (PP50 composition is defined as [PP50] / ([PP50] + [PEI])).

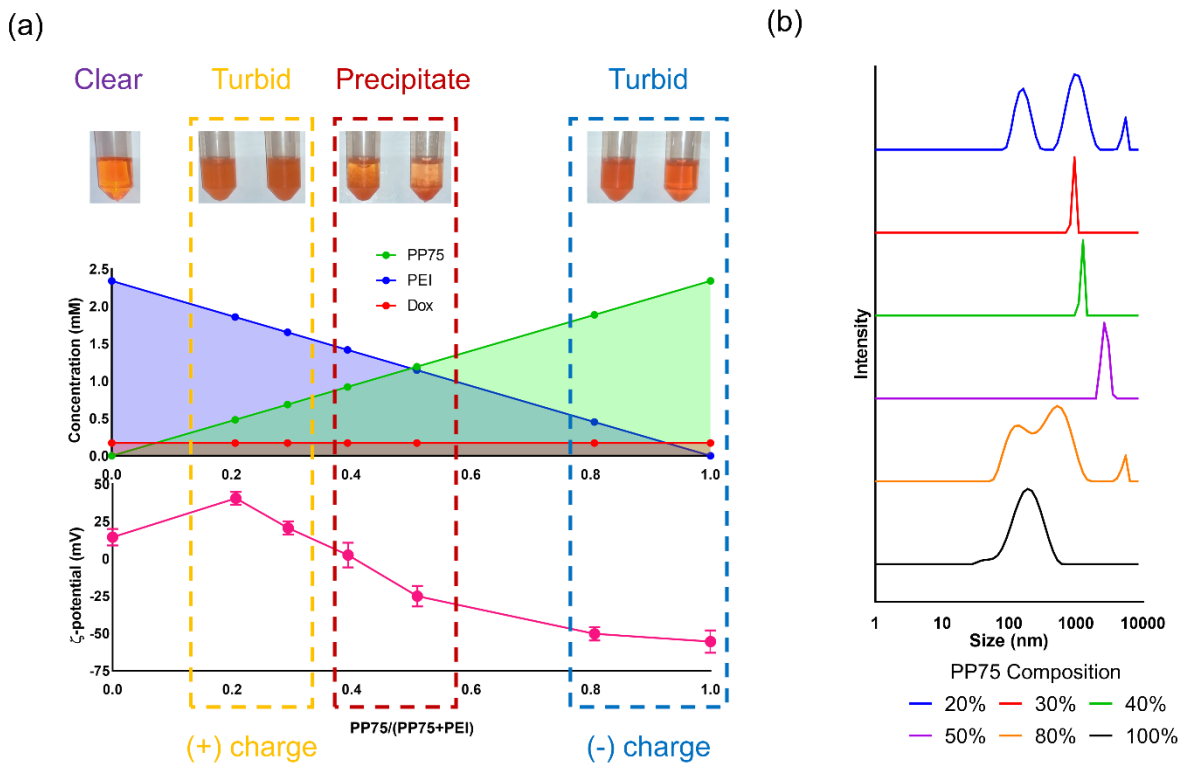

Figure 4-6. (a) Photographs of different formulas made with various PP75 to PEI ratios are listed in the top panel. A clear solution was obtained with only PEI + Dox, precipitations were obtained with mixing ratio close to 1, and turbid mixtures were obtained with the overload of both PP75 and PEI. Respective ζ-potential of complexes/coacervates with different formulations are exhibited in the bottom panel. Error bars represent standard deviations. (b) Hydrodynamic diameters of complex coacervate system measured by DLS (PP75 composition is defined as [PP75] / ([PP75] + [PEI])).

A parallel optimization with PP75 was also conducted (Figure 4-6). Turbid mixtures were obtained with both high composition of PP75 and high composition of PEI (Figure 2A), where the polymer composition is defined as $(\frac{PP75}{PP75+PEI})$ for PP75. The ζ-potentials and hydrodynamic diameters with various mixing ratios were again monitored. The ζ-potential of complexes decreases with an increasing amount of PP75. The change in the charge ratio between the anionic carboxylate group of PP polymers and the cationic amine groups of PEI is responsible for the decrease in the overall charge of the system. The large negative values in the two samples with the highest PP75 compositions (0.8 & 1) provide a strong repulsion necessary for high colloidal stability and vice versa for the overall positively charged samples with low PP75 compositions (0.2 & 0.3). Since excess PP75 in the system will allow more complexation with Dox through both electrostatic attraction and π–π stacking; therefore, formulations with an overload of PEI, or positively charged samples, were not subject to

further investigation. The mixing ratio of PP75 composition at 0.8 was selected for further investigation. The hydrodynamic diameter of the coacervate with PP75 composition of 0.8 exhibits a two-peak distribution pattern, with one close to 100nm and the second approaching 1µm, similar to those observed with PP50 coacervate.

4.3.3 Comparison of PP50 and PP75 coacervate system

Next, the encapsulation efficiency and loading capacity of PP50 and PP75 were compared. The encapsulation efficiency and loading capacity were evaluated by estimating the non-encapsulated Dox in the supernatant via fluorescence measurement after centrifugation. A typical standard curve that was used to convert fluorescence intensity to concentration is shown in Figure 4-7a. At their respective optimal mixing ratios as shown in the above two figures, PP50-PEI at a mixing ratio of 4:1 can sequester 55.3 ± 5.7% of Dox to achieve a final loading capacity of 3.93 ± 0.40%. The PP75-PEI at a mixing ratio of 4:1 was able to encapsulate 84.2 ± 5.0% Dox reaching a loading capacity of 9.14 ± 0.55% (Figure 4-7b). As was shown in Figure 4-5 and Figure 4-6, PP polymers can complex with Dox without PEI, and the ability to complex Dox mainly depends on the PP, because it is the source of aromatic rings and negative charges. Therefore, to compare their ability to form complexation with Dox, the encapsulation efficiency and loading capacity were measured with various Dox to PP polymer ratios in absence of PEI (Figure 4-8).

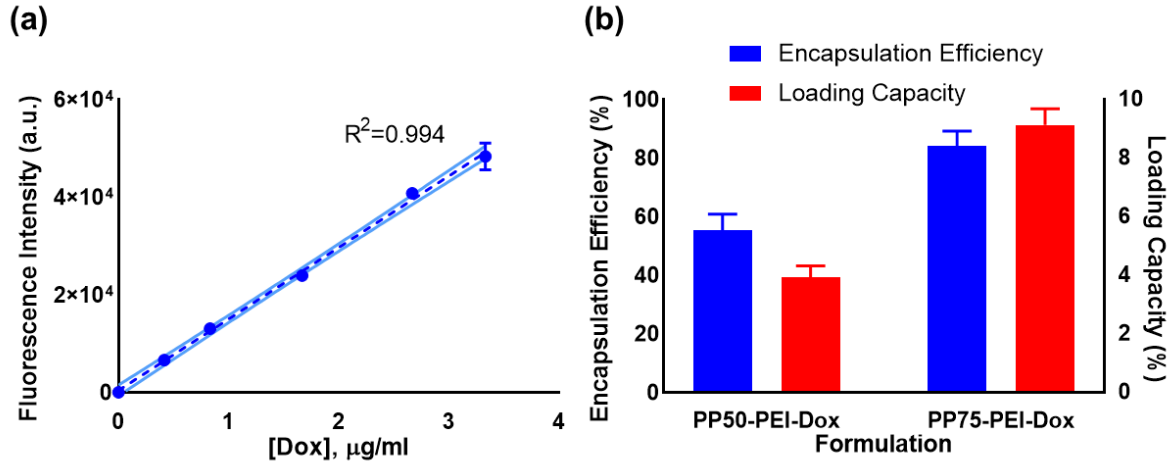

Figure 4-7. Encapsulation efficiency and loading capacity measurements. (a) A standard curve showing the correlation between fluorescence intensity and concentration. The blue lines represent the 95% confidence interval band. (b) Encapsulation efficiencies and loading capacities PP50-PEI-Dox and PP75-PEI-Dox at 4:1 PP to PEI assembly ratio. Error bars represent standard deviations.

At mixing ratios larger than 0.25 by weight, PP75 can load Dox at a higher rate than PP50 (Figure 4-8b). The loading capacity of PP75 decreases slightly from a mixing ratio of 0.8 to 1, while the decline in loading capacity of PP50 starts at the mixing ratio of 0.5. From the loading capacity data, it can be inferred that PP75 has reached full loading capacity at a mixing ratio of 0.8, and maximum encapsulation efficiency was achieved between mixing ratios of 0.25 and 0.5. PP50 also reached maximum loading capacity at 0.5 and the highest encapsulation efficiency is accomplished with a similar mixing ratio as PP75. The PP75 was able to reach higher encapsulation and loading capacity than PP50. This is likely due to the higher content of aromatic rings and higher hydrophobicity of PP75, therefore having more capacity to form hydrophobic association through π-π stacking with Dox.

The stability of PP-Dox coacervates was studied both in PBS solution and in presence of BSA (Figure 4-8c & d). BSA was also added to the system to better mimic the physiological condition, as protein adsorption can greatly affect the stability of NPs.[229] Some of the samples showed bulk phase separation right after mixing, while others remained turbid for longer periods of time. The longer the sample can remain turbid (emulsion form), the more stable the sample is. Therefore, the relative stability was defined as Abs_{0hr}/Abs_{24hr}, where Abs_{0hr} is the absorbance intensity at 480 nm right after the coacervates were made and Abs_{24hr} is the absorbance after the samples free stood for 24 hours. In PBS, PP75-Dox coacervate showed better stability than PP50-Dox in both PBS and BSA solutions at low mixing ratios. In both PBS and BSA solutions, PP75-Dox was more stable than PP50-Dox at mixing ratios of 0.125 and 0.25. While the biggest difference in PBS was observed at a mixing ratio of 0.2, in BSA solution it was at a mixing ratio of 0.125. Based on both the encapsulation efficiency and stability measurements, PP75 was recognized as the better polymer to form the nanocoacervate system with PEI and Dox.

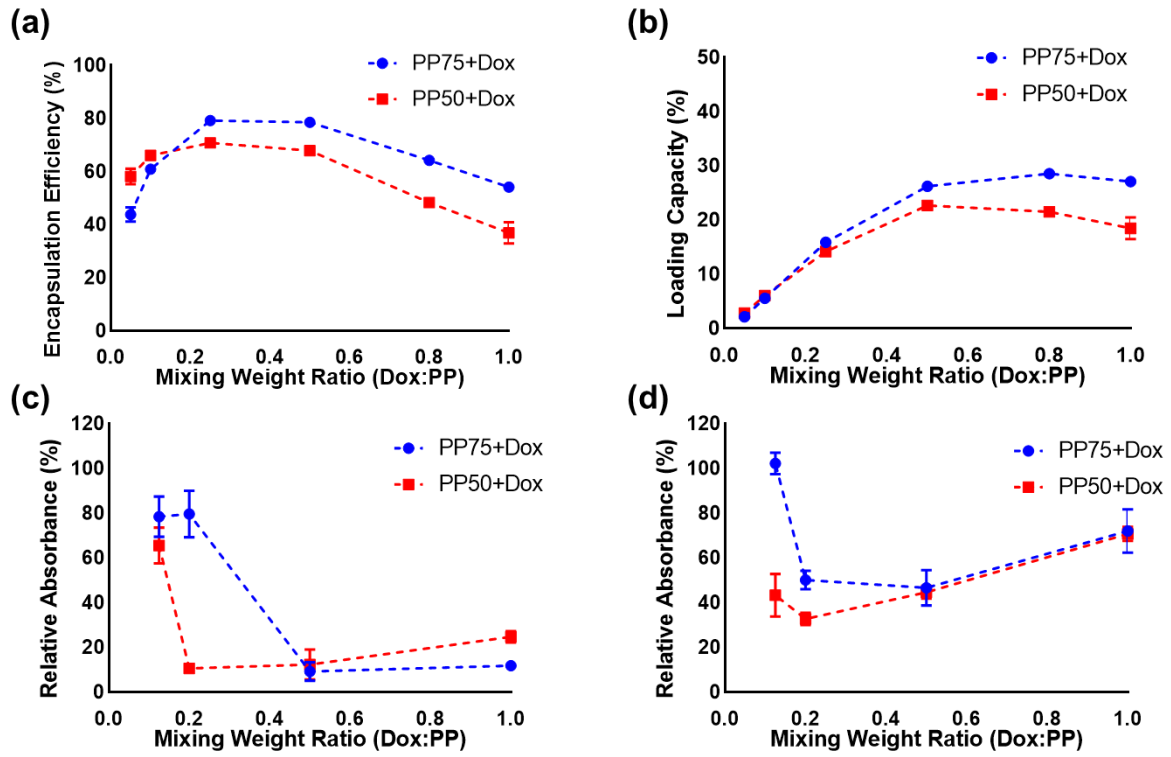

Figure 4-8. (a) Encapsulation efficiency and (b) Loading capacity of coacervate/complex made with various ratios of PP75+Dox and PP50+Dox, without PEI. Stability of coacervate made with various ratios of PP75+Dox and PP50+Dox in (c) PBS and (d)10 mg/mL BSA. Stability is evaluated by the change in UV-VIS absorbance intensity of the supernatant at 480 nm after allowing samples to stand for 24h. Error bars represent standard deviations.

The results of PP50 and PP75 complexing directly with Dox provide new insights into PP polymers as drug delivery agents. PP75 covalently conjugated to Dox through a disulfate bond (PP75-ss-Dox) was synthesized by Dr. Sun, an alumnus of the group (unpublished data). It was found that the PP75-ss-Dox had less cytotoxicity against the Hela cell line than free Dox at same treating concentrations, even though the uptake of Dox was comparable based on fluorescence intensity measured by flow cytometry. The weaker toxicity was attributed to insufficient disulfate bond clearage within the cells. The discovery that PP75 spontaneously forms complex/coacervate through physical interactions with Dox further explains the insufficient release of Dox from the conjugates. For one, released free Dox can quickly get trapped with PP75 via electrostatic and hydrophobic associations. For another, the PP75-ss-Dox might self-assemble into a coiled chain conformation through intramolecular interactions between Dox and phenylalanine moieties, making the disulfate bond difficult to be accessed by glutathione.

4.3.4 Influence of mixing sequence and different components on encapsulation

The mixing sequence of PP75-PEI-Dox coacervate on encapsulation efficiency was studied and summarized in Figure 4-9. The highest encapsulation is reached when PP75 is first mixed with Dox then followed by the addition of PEI. By allowing PP75 and Dox to complex first and then adding PEI to the system, more Dox can be included in the system. However, the difference is very small, indicating the process is largely thermodynamically controlled. Mixing PP75 first with PEI and then Dox achieved an encapsulation efficiency of 79.7 ± 3.9% and mixing PEI first with Dox and then PP75 realized an encapsulation efficiency of 82.0 ± 3.3%. The effects of different components on encapsulation efficiency were also studied. PP75-PEI-Dox, PP75-Dox, and PEI alone were compared for their encapsulation efficiency. The PP75-PEI is capable of encapsulating 84.2 ± 5.0% of feeding Dox, about the same as the 84.5 ± 1.0% efficiency achieved by PP75 alone. In comparison, PEI and Dox did not form any complex, so no precipitate was observed after centrifugation.

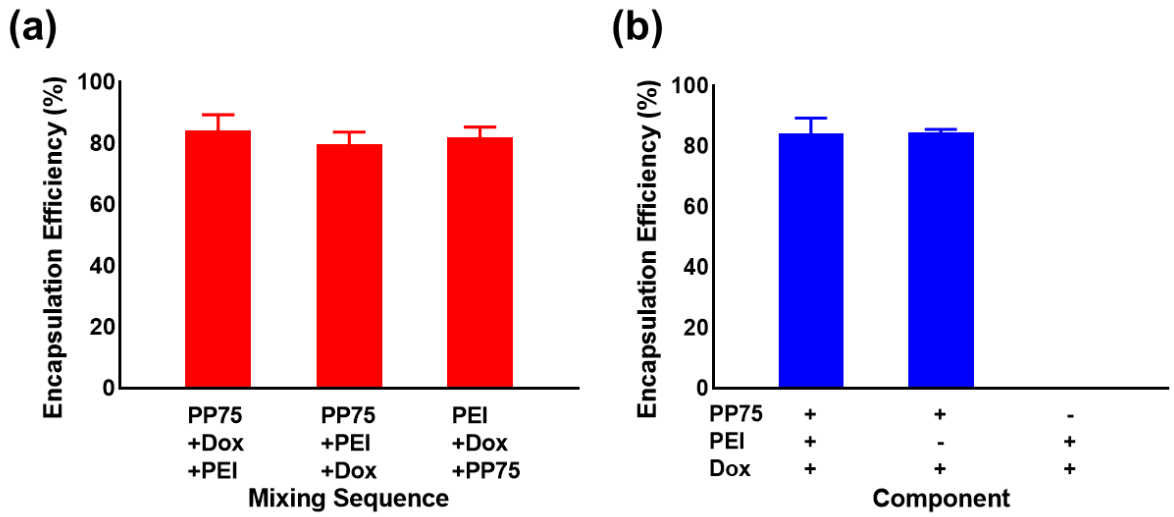

Figure 4-9. The encapsulation efficiency of Dox in PP75-PEI nanocoacervate made with (a) different mixing sequences and (b) different component combinations. Error bars represent standard deviations.

4.3.5 Morphology characterization of the nanocoacervate system

The morphology of the nanocoacervate was then investigated using SEM, TEM, and optical/fluorescence microscopy (Figure 4-10). SEM and TEM images revealed the formation of particulate structures of sizes ranging from 10 to 100 nm, consistent with the DLS measurement. Some particles were shown to be fused together, which could be caused by the drying process. Similar images were also observed in other reports in the literature.[230] It is

worth mentioning that both SEM and TEM were taken with dried samples, whose size and morphology might be slightly different than those of as-synthesized ones. Sub-micron spherical structures were also visualized using the optical microscopy and fluorescence microscopy, confirming the successful encapsulation of Dox.

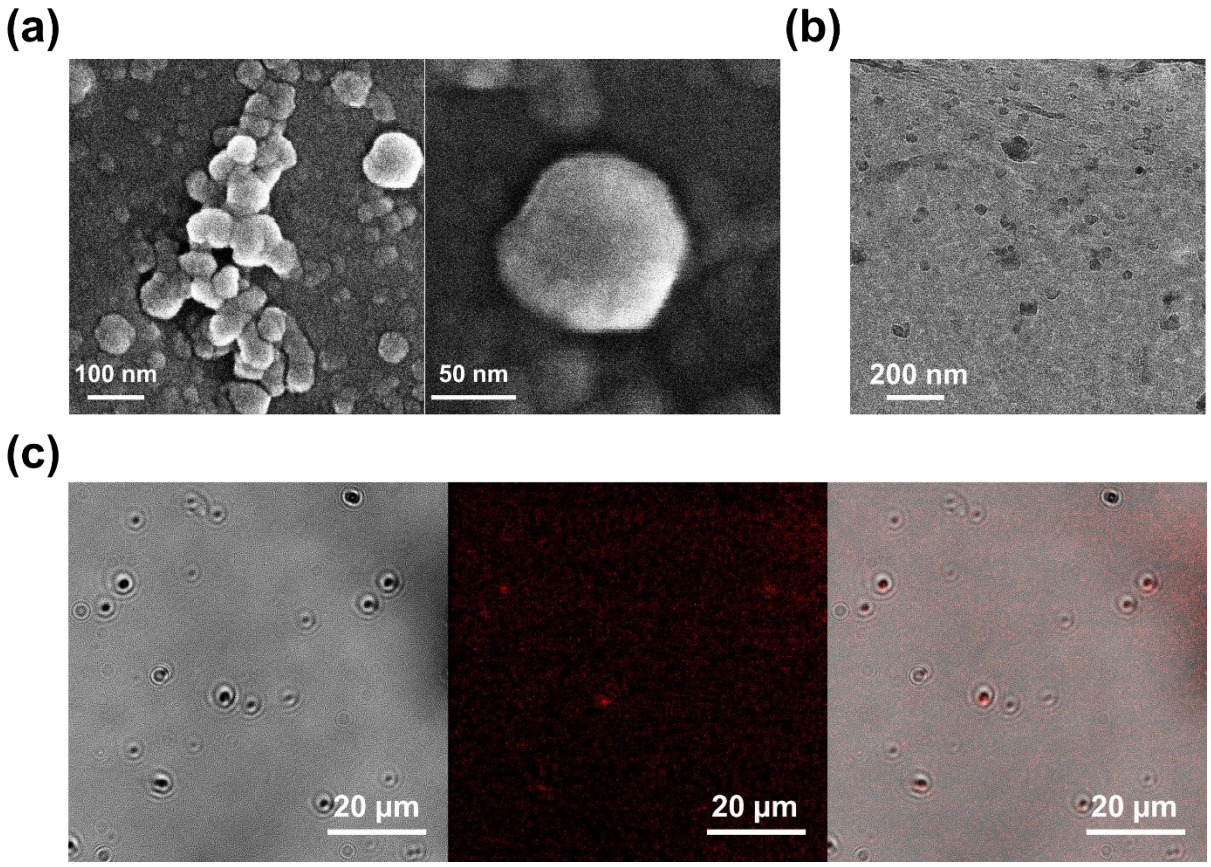

Figure 4-10. Characterization of the nanocoacervate morphology. (a) SEM images of PP75-PEI-Dox nanocoacervate made at a mixing ratio of 0.8. (b) TEM image of PP50-PEI-Dox nanocoacervate made at a mixing ratio of 0.8. (c) Bright field and fluorescence field (Dox) images of PP50-PEI-Dox nanocoacervate made at a mixing ratio of 0.8.

4.3.6 pH-responsive release of Dox from the nanocoacervate

The release profiles of Dox from PP75-PEI-Dox and PP75-Dox systems under various pH values were established (Figure 4-11). The blue curve shows the release of free Dox from the sample loading compartment of the dialysis device and serves as the benchmark. Compared with the neutral pH (red curve), the nanocoacervate system showed a much faster release rate under acidic conditions (pH = 5.5 & 6.5), which corresponds to late endosomes. The release rate was lowest at pH 4.5, even slower than at pH 7.4. One possible reason is that PP75 becomes insoluble below pH of 4.5 and Dox precipitated together with

the polymer and trapped within the solid. The result shows that releasing of Dox is slightly faster from PP75-PEI-Dox than from PP75-Dox under the same condition. This is likely due to the fact that when there are two polyelectrolytes in the system, as opposed to only one, more conformational change can be induced by the change of pH leading to faster release of the sequestered Dox. The overall results confirm the pH-responsive release properties of the nanocoacervate system and suggest that it can be used to target low pH physiological environments, such as within tumor and endo/lysosomes.

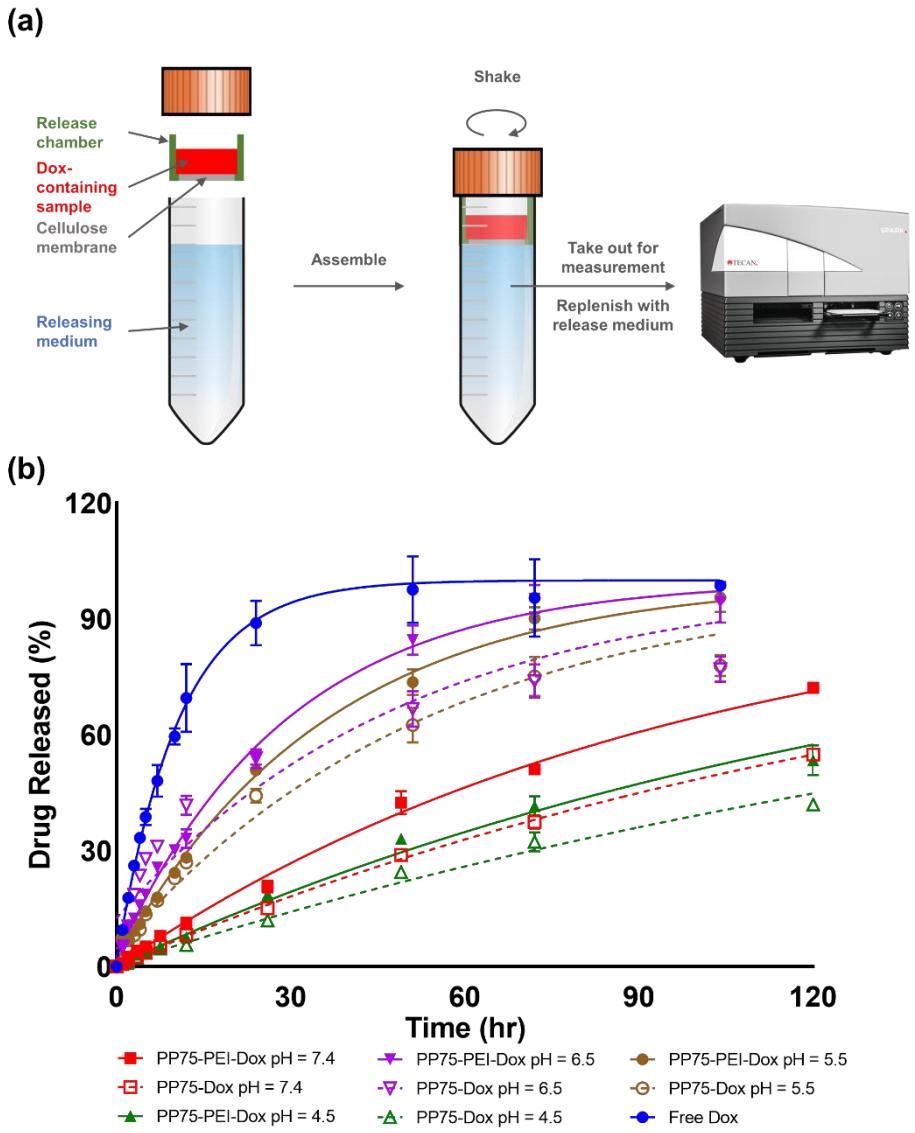

Figure 4-11. The pH-responsive drug release profile of the nanocoacervate system. (a) Schematic illustration of releasing experimental setup using a Slide-A-Lyzer™ MINI Dialysis Devices. (b) The release of Dox from PP75-PEI-Dox and PP75-Dox in PBS of various pH. The lines were obtained using exponential plateau fitting model with asymptote set at 100%. Error bars represent standard deviations.

4.4 Conclusions

Rapid nanocoacervate formulation of Dox was achieved through complex coacervation with a tertiary system consisting of PP polymer, PEI, and Dox. Two PP polymers with different degrees of L-phenylalanine substitution, PP50 and PP75 were investigated. The fabrication of the nanocoacervate system was accomplished by the simple mixing of the reagents by vortexing. ^{1}H-NMR spectroscopy and UV-Vis measurement revealed evidence of π-π stacking and hydrogen bonding formation during the assembly, suggesting that in addition to electrostatic interaction, the complex coacervation was driven by these two forces. The fabrication ratios of PP75 and PP50 were optimized based on turbidity, particle size, and ζ-potential measurements. The resulting colloidally stable nanocoacervate systems were turbidly red in color and exhibited large negative charge and bimodal particle size distribution with one close to 100 nm and the second close to 1 μm for both PP50 and PP75. PP75, due to its more hydrophobic nature with more phenylalanine groups, was capable of encapsulating more Dox and achieving higher stability than PP50. Therefore, PP75 was selected as the better polymer to form nanocoacervate.

The encapsulation efficiency and loading capacity of PP75 were evaluated to be 84.2 ± 5.0% and 9.14 ± 0.55%. The loading capacity can be an underestimation as it was calculated assuming all polymers end up in the coacervate system. It was found encapsulation of Dox was largely determined by PP polymer. The particle size and dry morphology of the PP75 nanocoacervate were further confirmed by SEM and TEM imaging, while the optical and fluorescence microscopy showed successful encapsulation of Dox into the nanocoacervate. The Dox release from PP75 nanocoacervate system was studied under various pH values. The release of Dox was accelerated with a slightly acid medium down to pH = 5.5. It was believed the pH responsiveness was due to the chain conformational change in both PP and PEI caused by the change in charge density as a result of protonation of both carboxylate and amine groups. The weak pH value also corresponds to the pH at which the PP polymers have strong membrane lytic and endosomal escape ability.

The results in the chapter demonstrated the feasibility of rapid nanoformulation in seconds through the coacervate system. The proof-of-concept system utilized both the electrostatic and hydrophobic interactions to effectively sequester Dox by simple mixing. The resulting nanocoacervate exhibited satisfactory particle size, colloidal stability, and pH-induced Dox release. By selecting the suitable functional polymer and payload pairs, this

method would become a platform technology for making bedside nanoformulations of a wide range of drugs. The biomedical application of the nanocoacervate as a drug delivery system will be covered in detail in the next chapter.

5 Delivery of doxorubicin as a model drug with coacervate system

5.1 Introduction

The development of multidrug resistance (MDR) in certain cancers to chemotherapy remains an unmet medical need in cancer treatment. Cancer cells can become resistant to any anticancer drug via various mechanisms which usually result in reduced accumulation within the cells. NP delivery systems have the potential to overcome MDR by facilitating drug intracellular trafficking and enhancing the retention of drugs within the cells. The nanocoacervate system contains dual intracellular trafficking polymers and is therefore a promising platform for delivering anticancer agents to MDR cancer cells. This chapter explores the ability of the nanocoacervate system developed in the previous chapter as a drug delivery system against cancer cell lines using various in vitro models.

The safety window of the nanocoacervate system was first established with two commercially available breast cancer cell lines. Next, the efficacies of nanocoacervate-Dox and pure Dox were compared in three breast cancer cell lines to make sure the nanosystem delivered Dox has at least comparable or superior efficacy to the pure Dox. Thirdly, the endocytosis pathway of the nanocoacervate system was confirmed using structured illumination microscopy in one of the breast cancer cell lines. Finally, to better assess the delivery effects of the nanocoacervate system, a pair of patient-derived head-and-neck cancer cell lines with distinct levels of drug resistance was used as the proximities. It was discovered that the nanocoacervate effectively enhanced the killing of cells by improving the Dox uptake and retention in the drug-resistant cell line in both 2D and 3D *in vitro* models. The results presented in the chapter demonstrated the great potential of the nanocoacervate to be utilized as a tool in multidrug-resistant cancer therapy.

5.1.1 Multidrug resistance in cancer cells via efflux pumps

MDR can appear via various mechanisms, including suppression of drug uptake, overexpression of efflux pump, activation of the detoxifying system, stimulation of DNA repair, etc.[231] Among different mechanisms, the efflux pump has been extensively studied. The most know p-glycoprotein 1 (P-gp) or multidrug-resistant protein 1 (MDR1), also known as ATP-binding cassette sub-family B member 1 (ABCB1), was first identified in the multidrug-resistant Chinese hamster ovary cells.[232] The other two types of ATP-binding

cassette (ABC) transporters, which can cause MDR in cancer cells, are multidrug resistance-associated protein 1 (MRP1 or ABCC1) and breast cancer resistance protein (BCRP or ABCG2).[233,234] Other members of the ABC transporter family, including ABCC2 – 5, ABCA2, and ABCB11, also exhibited certain levels of capability of transporting drugs; however, their ubiquity and correlation between MDR are yet to be established.[235]

P-gp can transport a variety of chemicals including but not limited to chemotherapeutic agents, with Dox being on the list.[236] The detailed discussion of transporting mechanism is beyond scope of this chapter. Briefly, substances can bind to P-gp from either within the inner leaflet of the cell membrane, if they partition in the double lipid layer, or directly from the cytoplasmic side.[237] P-gp then pumps out these substances in an ATP-dependent process.[238] There have been numerous clinical trials incorporating the use of P-gp inhibitors into chemotherapy; however, no clear clinical benefits were confirmed.[239] Part of the reason is that there lack clinically validated methods to identify the expression level of ABC transporters. As a result, clinical trials were performed without preselection of patients with high levels of ABC transporter expression.[240] Therefore, the development of reliable detection methods of efflux pump proteins is just as important as, if not more than, the discoveries of novel therapeutics.

5.1.2 Nanoparticle-mediated endocytosis

In addition to using inhibitors, NP-based drug delivery systems are viewed as promising tools to overcome efflux pumps in MDR cancer cells.[241] The fundamental mechanism for nanosystems to bypass the MDR conferred by efflux bumper is that they can enter the cells through endocytosis and release the anticancer drugs within the cytoplasm, therefore reducing the access of the drugs to the ABC transporters either from within the lipid bilayers or from the affinity of the inner leaflet. Kang et al. developed a Dox-loaded solid lipid NP system composed of curdlan and glycerol caprate which showed enhanced accumulation of Dox and a higher apoptotic cell death rate within the MCF7/ADR cell line.[242] Kievit et al. fabricated Dox conjugated iron oxide NPs using PEI and PEG as anchoring and stabilizing agents through the pH-cleavable hydrazone linkages. The delivery system increased the intracellular Dox accumulation for both drug-sensitive and drug-resistance C6 cell lines at 24 h, but only resulted in a higher cell apoptosis rate in resistant C6/ADR cell line.[243] Wang et al. demonstrated the effective delivery of Dox to MCF7/ADR using a GNP delivery system with Dox tethered via a hydrazone link and PEG spacers.[244] In

addition to the improvement in Dox retention and cytotoxic effects, this system also possesses an inherent fluorescence quenching property, which can help to monitor the Dox release from the nanosystem. Ye et al. created a polymeric NP system that co-delivers β-lapachone, a therapeutic generating ROS, and a ROS-responsive Dox prodrug.[245] The system is self-amplifying in cancer cells due to elevated catalytic activity as compared with normal cells. Enhanced cytotoxic effects were observed in MCF7/ADR but not in MCF7 and non-cancer cell line NIH/3T3. In addition, improved inhibition of tumor growth by the NPs was also achieved in MCF-7/ADR xenografted nude mice model.

5.1.3 Stimuli-responsive drug release from delivery systems

Smart NP-based drug delivery systems which release payloads upon designated stimuli can avoid premature release of loaded therapeutics and minimize systemic side effects. Stimuli can be categorized into internal and external in nature.[246] Internal stimuli, including pH, redox potential, and enzymes, are intrinsic physiological conditions that can be found in specific locations of the body. On the flip side, external stimuli, such as temperature, magnetic fields, ultrasound, and electromagnetic waves, refer to extrinsically applied conditions. From the delivery systems side, they can be specially engineered to respond to these stimuli by incorporating appropriate chemical and physical properties. For example, hydrazone and imine bonds can be cleaved under acidic pH, while disulfide bonds can be cleaved by the presence of glutathione.

Among all types of stimuli, pH value is of great research interest.[247] Acidic pH can be found in the gastrointestinal tract, lysosomes, and in some cancer cells (Warburg effect). In addition to cleavable covalent linkages as mentioned above, physical association in the drug delivery systems can also respond to changes in pH, leading to the release of payloads. Polyelectrolyte complexes, including coacervate systems, composed of weak polyelectrolytes are among this category.[248] Weak polyelectrolytes usually bear pH-dependent ionizable groups such as carboxylic acid or amine groups. The charge density and polymer chain conformation of weak polyelectrolytes vary as functions of pH and ionic strength. In a polyelectrolyte complex system, a change of charge density will disrupt the electrostatic attraction between opposite charges causing the dissembling of the structure. Therefore, such systems were exploited to fabricate pH-responsive delivery systems.[249]

5.1.4 PP polymer in delivery applications

One of the obstacles for the NP delivery systems is the partition and potential degradation, which can take place in the endosomes and lysosomes due to the acidic pH once the NPs enter the cells via endocytosis.[250] One strategy is to utilize ionizable weak polyelectrolytes which can switch their charge density and therefore hydrophobicity, leading to the fusing and disrupting the endosomal membrane.[250] As mentioned in the previous chapter, the PP polymer is one of such polymers, as it contains both the ionizable carboxylic acid group and the hydrophobic amino acid, L-phenylalanine, side chains. PP polymers have been shown to facilitate intracellular trafficking for delivering siRNA,[251] cryoprotectants,[252] and proteins,[253] fluorescence dye, and apoptotic peptide.[254]

Previous studies of PP polymer delivery systems focused on utilizing either covalent bonding or direct co-incubation to deliver payloads. The former has the advantage of well-defined loading architecture but can suffer from complicated chemical synthesis processes. The co-incubation method is only suitable for *in vitro* processes, such as *in vitro* gene transfection. In another report, PP75 and Dox were both incorporated in liposomes to mimic the spike proteins and viral genomes of a virus.[255] However, forming drug delivery systems via utilizing the anionic charge and hydrophobic side chains to form physical interactions with payloads has not been investigated with PP polymers before. The delivery efficacies of the nanocoacervate fabricated by complex coacervation among PP75, PEI, and Dox are discussed in this chapter.

5.2 Materials and methods

5.2.1 Materials

Doxorubicin Hydrochloride (Dox) was purchased from the Tokyo Chemical Industry and Sigma-Aldrich of Merk and used as received. Dulbecco's Modified Eagle Medium (DMEM), Dulbecco's Phosphate-Buffered Saline (DPBS), trypsin-EDTA, penicillin-streptomycin (Pen Strep), fetal bovine serum (FBS), 4',6-Diamidino-2-Phenylindole, Dihydrochloride (DAPI), and Lysotracker™ red were purchased from Thermo Fisher. CelTiter96® AQueous One Solution Cell Proliferation Assay was acquired from Promega. Paraformaldehyde was purchased from Sigma Aldrich. To prepare the samples for the experiments, Milli-Q water with a conductivity of less than 2 $\mu S\ cm^{-1}$ was used.

5.2.2 MTS assay with MCF7, MDA-MB-231, and T47D cell lines

MCF7, MDA-MB-231 (MDA231), and T47D cells were cultured in DMEM containing 10% FBS, 50 IU/mL penicillin and 50 g/mL streptomycin and maintained at 37°C in a humidified 5% CO2 incubator. The cells were seeded in 96-well plates at 10,000/well for 24 hours and then treated with the 100 µL culture medium containing PP75-PEI-Dox, PP75-Dox, PEI-Dox, and free Dox at various Dox treating concentrations. After respective treating time, the media was discarded. Each well was washed with 100µL DPBS followed by the addition of 120 µL MTS solution (100µL supplemented culture media + 20µL CelTiter 96® AQueous One Solution) and incubated at 37°C, 5% CO2 for 1 – 4 hours. A positive control of cells with DMEM only and a negative control of cells with DMEM/MTS assay reagent were also seeded. The absorbance of each well was measured at 490 nm (650 nm as the reference wavelength) using a Tecan Spark Multimode Microplate Reader. All experiments were conducted in at least triplicates. The percentage viability of cells was calculated according to the following equation: Cell viability (%) = (Absorbance of treated cells-blank)/(Absorbance of control cells-blank)×100. Blank= No cell, only media with MTS reagent.

5.2.3 Confocal fluorescent microscopy with MCF7 treated with nanocoacervate

Measurements were carried out using a Leica TCS SP5 confocal microscope. MCF7 cells are cultured on coverslips sitting at the bottom of wells in 24-well plates. Cells are seeded at 5×10^4 cells/well for 24 hours and then treated with 0.5 mL culture media containing PP75-Dox, PP50-Dox, or free Dox at Dox concentration at either 0.8 or 1.6 µg/mL. After 12 hours of treatment, the cells were fixed with 4% paraformaldehyde (Sigma-Aldrich) for 10 min. The coverslips were then mounted to microscope glass slides using Prolong Gold antifade moutant with DAPI.

5.2.4 Structured illumination microscopy (SIM) study of endocytosis of the naocoacervates

SIM imaging was performed using a customer three-color system build around an Olympus IX71 microscope stage, as we have previously described.[256] Laser wavelengths of 488 nm (iBEAMSMART- 488, Toptica), 561 nm (OBIS 561, Coherent), and 640 nm (MLD 640, Cobolt) were used to excite fluorescence in the samples. A 60Å~/1.2 numerical aperture (NA) water immersion lens (UPLSAPO 60XW, Olympus) focused the structured illumination pattern onto the sample. This lens captured the samples' fluorescent emission

light before imaging onto an sCMOS camera (C11440, Hamamatsu). Raw images were acquired with the HCImage software (Hamamatsu). MCF7 cells were treated with PP75 coacervate system and free Dox (both with 6.4 µg/ml Dox concentration) for various time periods and then stained with Lysotracker™ according to the protocol provided by Thermo Fisher before they were imaged by SIM. Reconstruction of the SIM images with LAG SIM Resolution-enhanced images was reconstructed from the raw SIM data with LAG SIM, a custom plugin for Fiji/ImageJ available in the Fiji Updater. SIM acquisition was performed with assistance from Dr. Meng Lu.

5.2.5 MTS assay with patient-derived head and neck cancer cell lines

The sensitive and resistant cell lines used for this study were established from two different Head and neck squamous cancer cell (HNSCC) patients as described previously[257]. For the generation of tumor spheroids sized 300–500 µm, 200 µL of sensitive and resistant, single-cell suspensions were seeded in ULA plates (Corning Life Sciences) at varying cell densities in the range of 0.25–0.75 × 10^5 cells/mL. The plates were incubated in a humidified 5% CO2 atmosphere at 37ºC (48-72 hours) for 3D tumor spheroids formation.

Monolayers of sensitive and resistant cell lines were seeded in 96-well flat-bottom plates at a cell density of 8000 cells/well in a 200 µL complete medium at 37ºC and 5% CO_2 atmosphere for 24 hours before coacervate treatment. After 24 hours, the culture medium was carefully aspirated, and monolayer cultures were treated with coacervates or free Dox at 42.5 to 1020 nM Dox concentration. Cells were treated for 72 hours. Sensitive and resistant spheroids were also treated with the same concentration used for the monolayer cell cultures, by replacing 50% of the culture medium with a freshly prepared drug-supplemented medium, followed by incubation at 37ºC and 5% CO_2 atmosphere for 72 hours. Cell cytotoxicity in the drug-treated monolayer cell cultures was assessed using the CellTiter96® AQueous One Solution Cell Proliferation Assay (Promega).

Briefly, at the end of 72 hours, the drug-supplemented medium was replaced with a 317 µg/mL MTS reagent-supplemented medium. For a total volume of 200 µL, 40 µL of the MTS reagent was added to each well and the plates were incubated at 37ºC and 5% CO2 atmosphere for 3 hours. At the end of the incubation period, absorbances at 490 and 650 nm were recorded using a microplate reader (VersaMax™, Molecular Devices). All experiments were performed in triplicates. The cytotoxicity experiment with the patient-derived cell lines

was carried out in collaboration with Dr. Mohammad Azharuddin from Linkoping University, Sweden.

5.2.6 Real-time live cell imaging of Dox uptake in 3D spheroids

The real-time calcein uptake and intracellular calcein accumulation were monitored in 3D sensitive and resistant tumor spheroids made with cells from pre-treated post diagnosed head and neck cancer cells.[257] After spheroid formation, the keratinocyte serum-free growth medium (KSFM, Gibco, Thermo Fisher Scientific) was carefully decanted without disturbing the spheroids. They were then incubated in serum-free KSFM medium containing non-fluorescent calcein acetoxymethyl ester (calcein-AM, 1 mM in Dimethyl sulfoxide (DMSO), Sigma AB) at a final concentration of 1 µM and verapamil (MDR1 inhibitor, 20 µM), for 72 hours at 37ºC and 5% CO_2 atmosphere. During the 72-hour incubation period, phase contrast and green fluorescence (CalceinEx/Em = 495/515 nm) images of the spheroids were acquired every 30 minutes using time-lapse fluorescent microscopy. A 10× objective was used for image acquisition (Incucyte Zoom™, Sartorius AG). The spheroids were also treated with free Dox and coacervate Dox ([Dox] = 50 – 800 nM), followed by live-cell imaging for red fluorescence as described above. Experiments were performed with at least triplicates for each individual study.

5.3 Result and Discussion

5.3.1 Cytotoxicity of empty nanocoacervate

Before using the nanocoacervate as a delivery agent, the cytotoxicities of the empty cargos, as well as the PP75 and PEI, were first investigated with MCF7 and MDA231 cell lines using MTS assay (Figure 5-1). As mentioned in the previous chapter, the MTS assay is a colorimetric proliferation assay, in which the MTS tetrazolium compound is bio-reduced by mitochondria into a colored formazan product that is soluble in cell culture media. The extent to which the tetrazolium compound is reduced is proportional to the number of viable cells, assuming mitochondria activity is directly related to cell viability. The absorbance of the final color is measured and converted to cellular viability. As shown in Figure 5-1, nanocoacervate, PP75, and PEI showed no obvious acute cytotoxicity against either MCF7 or MDA231 cell lines for 72 hours of treatment at treating concentrations up to 10 µg/ml or 17.2 µM equivalent Dox concentration.

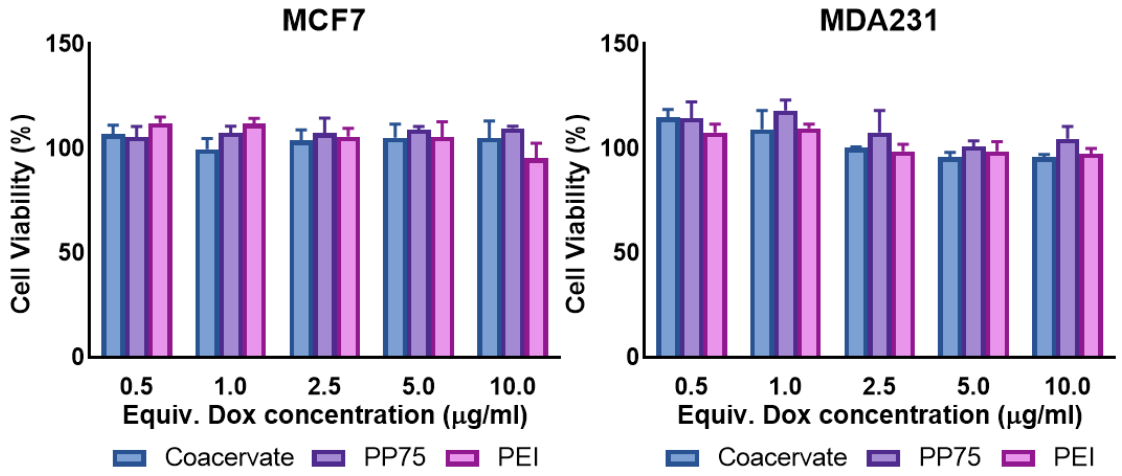

Figure 5-1. Cytotoxicity effects of delivering agents PP75-PEI, PP75, and PEI measured with MTS assay against (a) MCF7 and (b) MDA231 for 72 hours. Error bars represent standard deviations.

5.3.2 Delivery of Dox to commercial breast cell lines

To examine the delivery effectiveness of the nanocoacervate system, PP75-PEI-Dox, PP75-Dox, PEI-Dox, and free Dox were used to treat three distinct breast cancer cell lines, MCF7, MDA231, and T47D with 48- and 72-hour treatment.

5.3.2.1 Cytotoxicity of nanocoacervate delivered Dox in MCF7

In MCF7, nanocoacervate, PP75 alone, and PEI alone were all able to enhance the cytotoxicity of Dox at different treating concentrations at both 48 and 72 hours (Figure 5-2). Especially at the two highest doses, all three delivery systems lowered the cell viability by a considerable degree at both 48 and 72 hours. The respective dose-response curves and fitted IC_{50} values are also in agreement with this trend. Interestingly, PP75 and PEI alone were able to enhance the cytotoxicity of Dox to a higher extent than the nanocoacervate in MCF7.

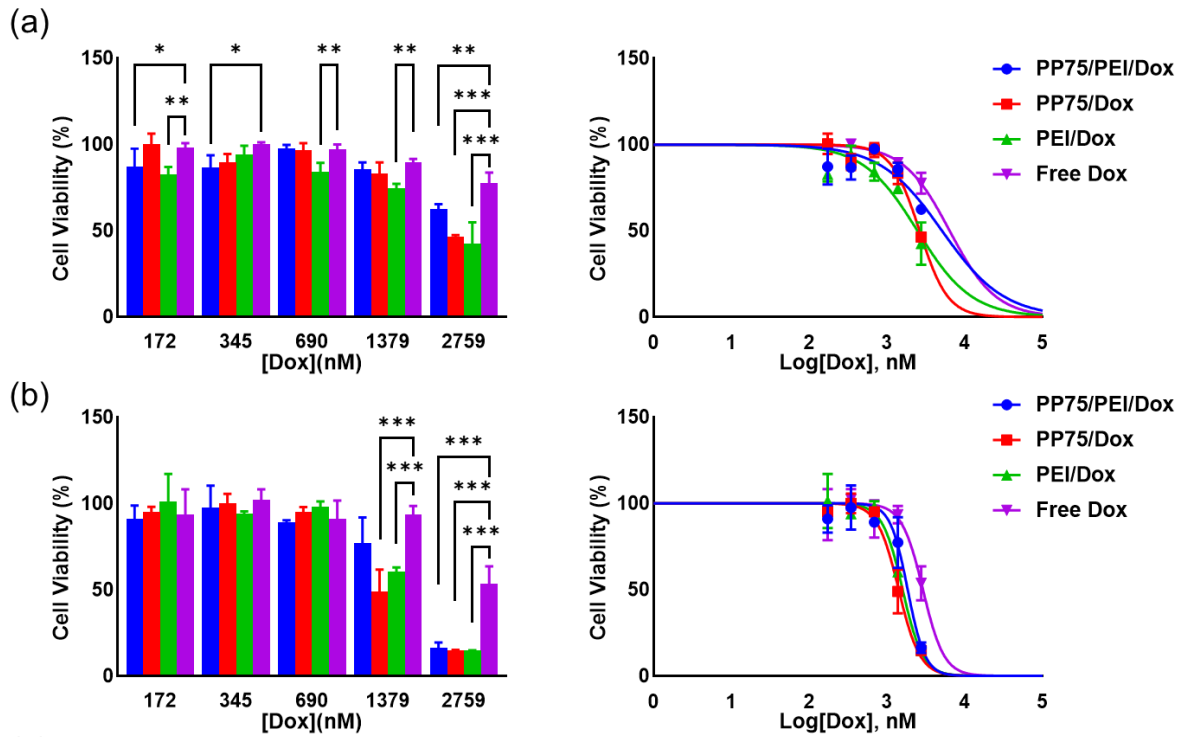

IC_{50} (nM)	PP75-PEI-Dox	PP75-Dox	PEI-Dox	Free Dox
48 hr	5.11×10^{3}	2.62×10^{3}*	2.46×10^{3}*	6.40×10^{3}
72 hr	1.85×10^{3}	1.42×10^{3}*	1.59×10^{3}*	2.90×10^{3}

Figure 5-2. Efficacies of nanocoacervate and individual components to MCF7 cell line. Cell viability as treated by different concentrations of PP75-PEI-Dox, PP75-Dox, PEI-Dox, and free Dox for (a) 48 and (b) 72 hours. Respective dose-response curves are plotted on the right-hand side ($p \leq 0.05$*, 0.01**, 0.001***). (c) Evaluated IC_{50} of the different drug delivery agent combinations in tabular format (*values differ from free Dox IC_{50} at 95% confidence interval). Error bars represent standard deviations.

5.3.2.2 Cytotoxicity of nanocoacervate delivered Dox in MDA-MB-231

The delivery effects of PP75, PEI, and PP75+PEI were also investigated in the MDA231 cell line (Figure 5-3). PP75-Dox is more efficacious than PP75-PEI-Dox which is more efficacious than PEI-Dox for the 48-hour treatment, whereas at the 72-hour time point there were no noticeable differences across different formulations. Like the result with MCF7, the PP75 alone exhibited better delivery efficacy than PP75-PEI nanocoacervate. However, the nanocoacervate was able to kill more cells than PEI alone, especially with the two highest doses at 48 hours, which contrasts with the result seen in MCF7.

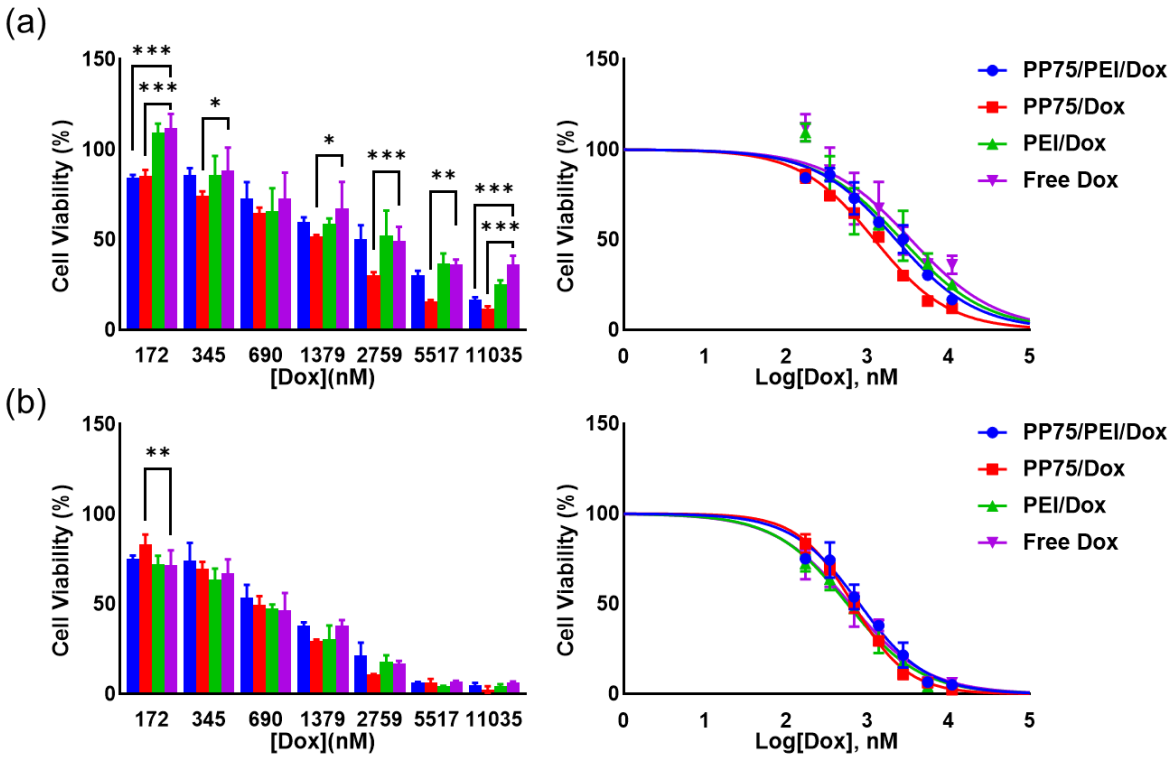

(c)

IC_{50} (nM)	PP75-PEI-Dox	PP75-Dox	PEI-Dox	Free Dox
48 hr	2.25×10^3	$1.22\times10^{3*}$	2.65×10^3	3.44×10^3
72 hr	798	664	565	616

Figure 5-3. Efficacies of nanocoacervate and individual components to MDA-MB-231 cell line. Cell viability as treated by different concentrations of PP75-PEI-Dox, PP75-Dox, PEI-Dox, and free Dox for (a) 48 and (b) 72 hours. Respective dose-response curves are plotted on the right-hand side ($p \leq 0.05$*, 0.01**, 0.001***). (c) Evaluated IC_{50} of the different drug delivery agent combinations in tabular format (*values differ from free Dox IC_{50} at 95% confidence interval). Error bars represent standard deviations.

5.3.2.3 Cytotoxicity of nanocoacervate delivered Dox in T47D

With the T47D cell line, the PP75-PEI-Dox nanocoacervate had the highest cytotoxicity, especially at the high dose range, and overall had the lowest IC_{50} values with both 48 and 72 hours of treatment. The PP75-Dox was able to substantially enhance the cytotoxicity of free Dox, although to a less degree than the nanocoacervate. The PEI-Dox exhibited similar performance as the free Dox at all treating concentrations with slightly lower overall IC_{50} values for both 48- and 72-hour treatments. This was not the case for MCF7 or MDA231 where PEI-Dox was able to achieve noticeably lower cell viability than free Dox in both cell lines.

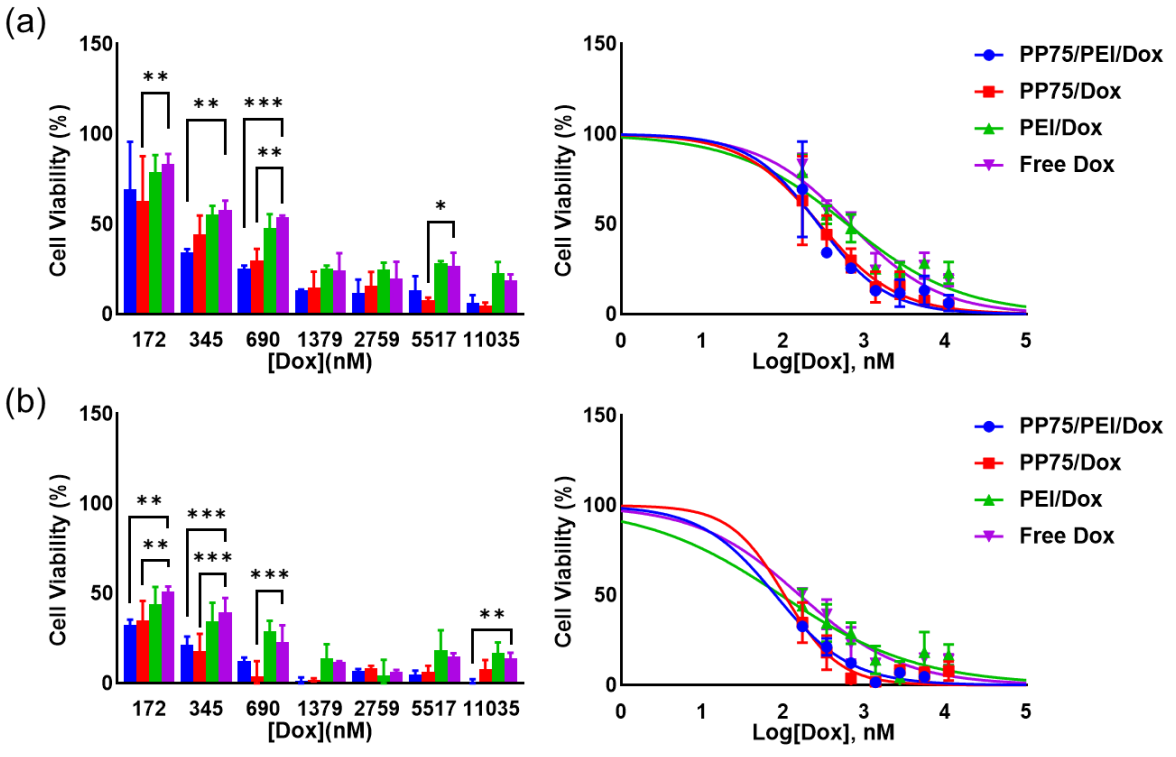

(c)

IC_{50} (nM)	PP75-PEI-Dox	PP75-Dox	PEI-Dox	Free Dox
48 hr	273*	281*	620	660
72 hr	80.7	104	94.6	161

Figure 5-4. Efficacies of nanocoacervate and individual components to T47D cell line. Cell viability as treated by different concentrations of PP75-PEI-Dox, PP75-Dox, PEI-Dox, and free Dox for (a) 48 and (b) 72 hours. Respective dose-response curves are plotted on the right-hand side ($p \leq 0.05$*, 0.01**, 0.001***). (c) Evaluated IC_{50} of the different drug delivery agent combinations in tabular format (*values differ from free Dox IC_{50} at 95% confidence interval). Error bars represent standard deviations.

To sum up, PP75-PEI and PP75 are both able to conjugate with Dox and improve the efficacy of Dox in killing three different types of breast cancer cells, even though the degree of improvement of the two systems differs in different cell lines. The PEI in the nanocoacervate also seems to promote the intracellular delivery of Dox as shown in MCF7 and MDA231, but not in the T47D cell line. The results called for more suitable *in vitro* models to demonstrate the delivery efficiency of the nanocoacervate.

5.3.3 Intracellular trafficking pathway of PP75 nanocoacervate

The intracellular trafficking pathway of the nanocoacervate was investigated using fluorescence microscopy. Previous reports have demonstrated the intracellular trafficking of PP polymer with covalently conjugated payloads through the endolysosomal endocytosis

pathway predominantly via the clathrin- and partially via the caveolin-mediated endocytosis mechanisms.[251] To confirm that the nanocoacervate system undergoes the endocytosis process, colocalization of Dox/nanocoacervate with lysosomes/late endosomes was investigated using structured illumination microscopy (SIM),[256] which enables the visualization of the structure of lysosomes and their contents at around 100 nm resolution. MCF7 cells were treated with either Dox-containing nanocoacervate or free Dox (negative control) for 1, 2, and 5 hours, and at the end of treatment, lysosomes and late endosomes were stained with lysotracker™. SIM was then used to image the colocalization of Dox and endo/lysosomes (Figure 5-5).

Free Dox has a low degree of colocalization with lysosomes (Figure 5-5b & d). The small amount of Dox residing within the lysosomes might be due to the sequestration of Dox in the organelles. Because of the basic and hydrophobic nature of the drug, Dox tends to accumulate in acidic organelles, such as lysosomes, where Dox can get protonated and lose membrane permeability.[258] This mechanism is considered to cause drug resistance and has been argued to be the main reason for the inefficiency of the well-known nanoformulation of Doxil®.[259,260] In comparison, Dox delivered by nanocoacervates can be seen closely colocalized with lysosomes at all treating times. In addition, there was considerable red fluorescence (free Dox) diffusing around the lysosomes in the coacervate group. With a longer treating time, more dispersed red fluorescence can be observed around lysosomes. This was likely the result of the Dox leaving the lysosomes via PP-mediated lysosomal escape. The result confirmed that PP75 nanocoacervate enters cells via the endolysomomal pathway and Dox was able to successfully escape from lysosomes via PP-mediated lysosomal escape.

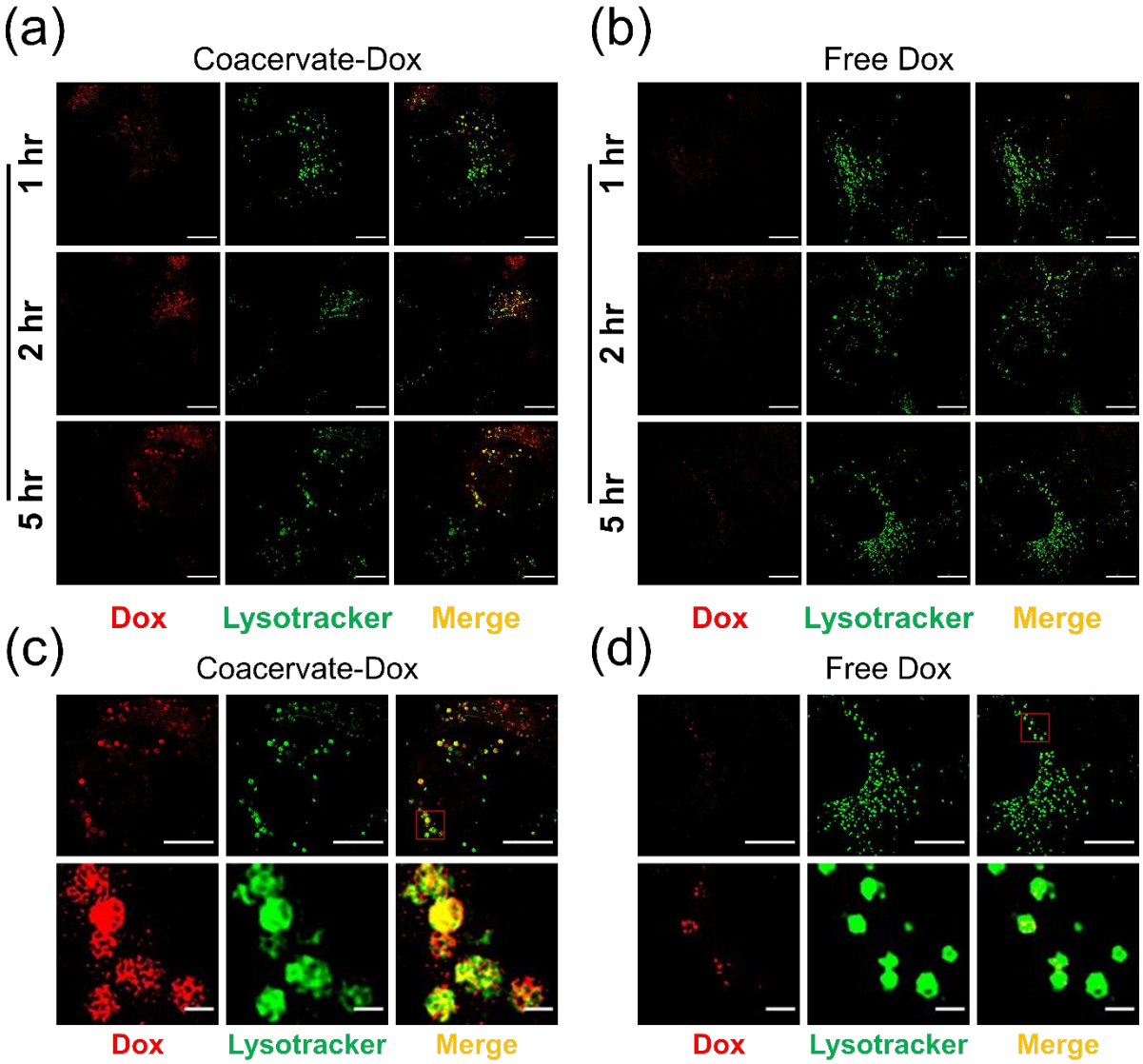

Figure 5-5. Colocalization of Dox and endolysosomes. Structured illumination microscopy (SIM) of MCF7 treated with either (a) nanocoacervate-Dox (red fluorescence) and (b) free Dox incubated with Lysotracker™ (green fluorescence) at 1, 2, and 5 hours, showing the subcellular distribution of free Dox and coacervate system. The scale bars represent 10μm. (c) & (d) Enlarged images of (a) & (b) at a 5-hour time point showing more details of the lysosome and Dox colocalization. Scale bars represent 10μm (top) and 1μm (bottom).

To confirm whether the Dox ultimately reached the nuclei, nanocoacervate and free Dox-treated MCF7 were imaged with confocal microscopy after 12 hours of treatment at two different dose levels (Figure 5-6). It can be observed that in both free Dox and nanocoacervate groups, red fluorescence (Dox) closely colocalize with blue fluorescence (DAPI), indicating that Dox successfully entered the nuclei within 12 hours. It is worth mentioning that both free Dox and nanocoacervate delivered Dox demonstrated dose-dependent distribution. It can be observed that at low the dose, the Dox (red fluorescence) appeared around the nuclei, whereas at the high dose the Dox colocalize with the nuclei more

closely. This trend held for both free drug and delivery system groups. The result indicates that a higher treating dose led to a faster accumulation of Dox in the nuclei. To combine the evidence from SIM and confocal images (Figure 5-5 & Figure 5-6), a clear delivery pathway of nanocoacervate can be outlined. The Dox, carried by nanocoacervate, enters the cells through the endocytosis pathway, then escapes from the endo/lysosomes via PP- and PEI-mediated lysosomal escape, and finally ends up in the nuclei, where it causes damages to the DNA via intercalation.

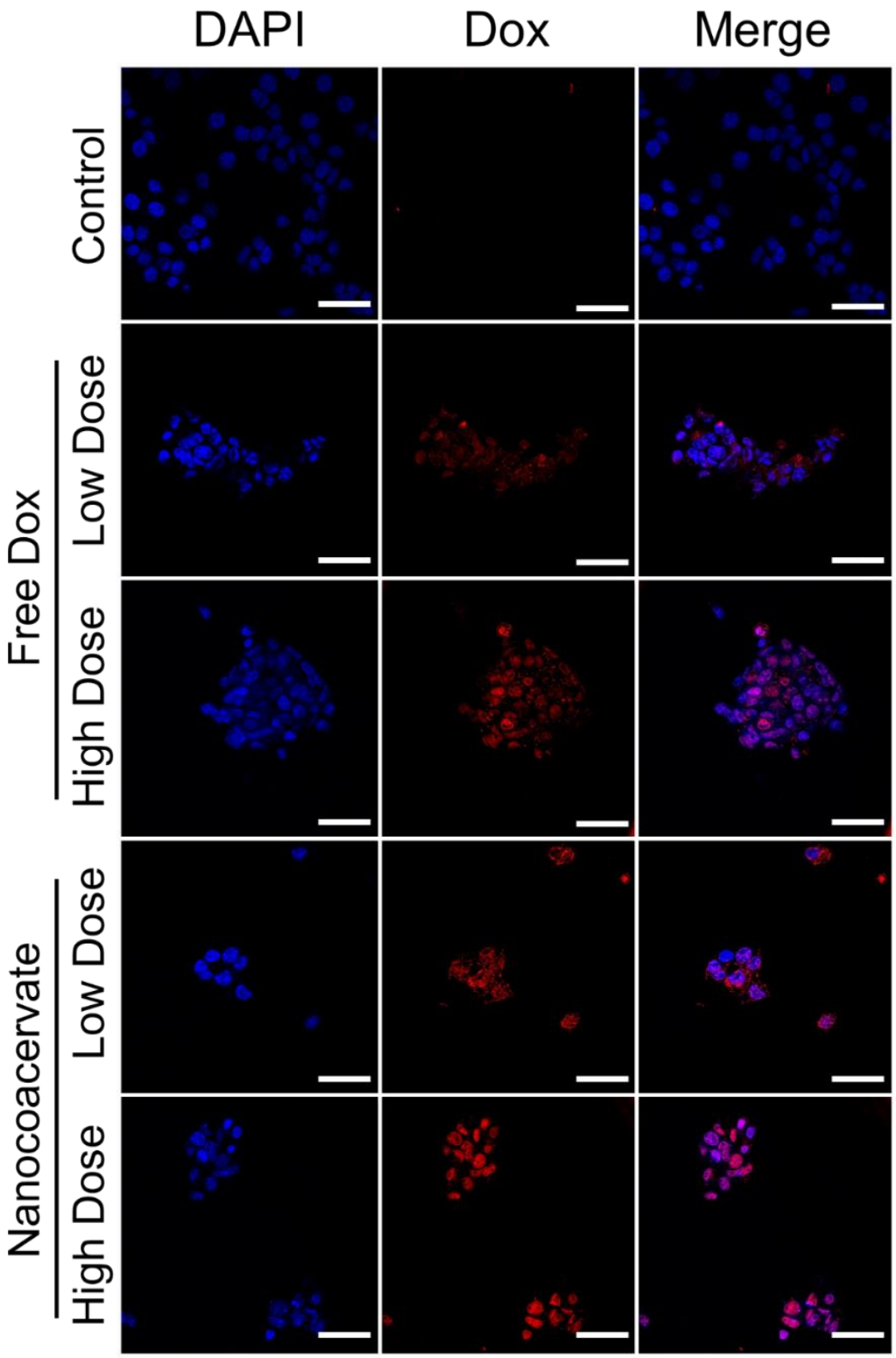

Figure 5-6. Localization and uptake of coacervate (fabricated at 80% [PP]/([PP]+[PEI])) delivered Dox by MCF breast cancer cells. Confocal microscopic imaging of MCF7 cells treated with coacervate and free Dox at low (0.8 µg/mL) and high (1.6 µg/mL) doses after 12 hours. The scale bar represents 50µm.

5.3.4 Enhanced cytotoxicity of Dox by nanocoacervate delivery system in 2D MDR monolayer model

The intracellular trafficking property of PP polymer makes the coacervate a suitable delivery vehicle in fighting against MDR exhibited in some cancer cells. These cells have overexpression of proteins, such as P-gp, which can pump out foreign substances, including chemotherapeutic agents. One way to bypass the reflux pump is to employ a delivery system that can enter cells through a mechanism other than simple diffusion (Figure 5-7).[244] The drug can enter cells together with the delivery system, and in this form, the drug will not be a substrate of P-gps. The drug can later be released from the delivery system inside cells, avoiding being pumped out easily.

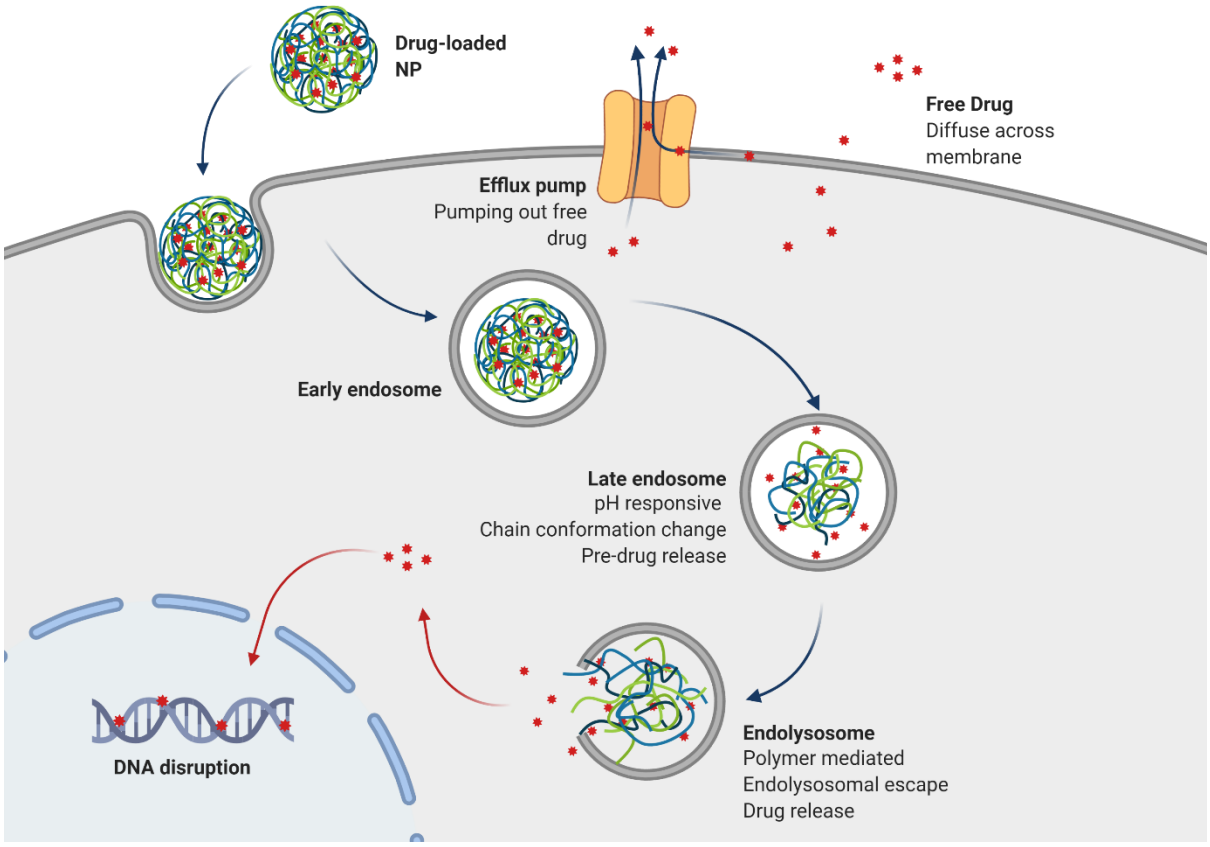

Figure 5-7. Schematic illustration of an MDR cell treated with nanocoacervate-Dox and free Dox. The free Dox enters the cell via simple diffusion and gets pumped out by the efflux pump easily. The nanocoacervate-delivered Dox enters the cell via endocytosis and Dox is released through pH-responsive disintegration of the nanocoacervate and polymer mediated endosome escape; thus, it has a greater chance of reaching the nucleus. Objects are not drawn to scale. Created with BioRender.com.

In vitro studies with previously established patient-derived head and neck cell lines exhibiting different levels of MDR were performed to confirm whether coacervate

nanoformulations retain the delivery properties of PP polymers and demonstrate potential for the treatment of MDR cancer.[257] A drug-sensitive (LK0917) and a drug-resistant (LK1108) cell lines were treated with the PP-containing nanocoacervate delivery system. The cytotoxicity of nanocoacervate delivered Dox to a 2D monolayer *in vitro* model was investigated by MTS assay (Figure 5-8).

Overall, the nanocoacervate delivered Dox showed comparable cell viability in both drug-sensitive and drug-resistant cell lines as the free Dox. The nanocoacervate even exhibited slightly higher IC_{50} (statistically insignificant) than the free Dox (Figure 5-8e). This result is similar to that observed with MDA231 cells treated with various Dox-containing formulations at 72 hours. It is understandable that the delivery system did not result in enhanced cytotoxicity in drug-sensitive cell lines, as the freely diffused Dox is sufficient to kill most of the sensitive cells. On the other hand, the improvement in Dox cytotoxicity by nanocoacervate in MCF7 and T47D (Figure 5-2 & Figure 5-4) suggests that there was a certain level of drug resistance in the two cell lines.

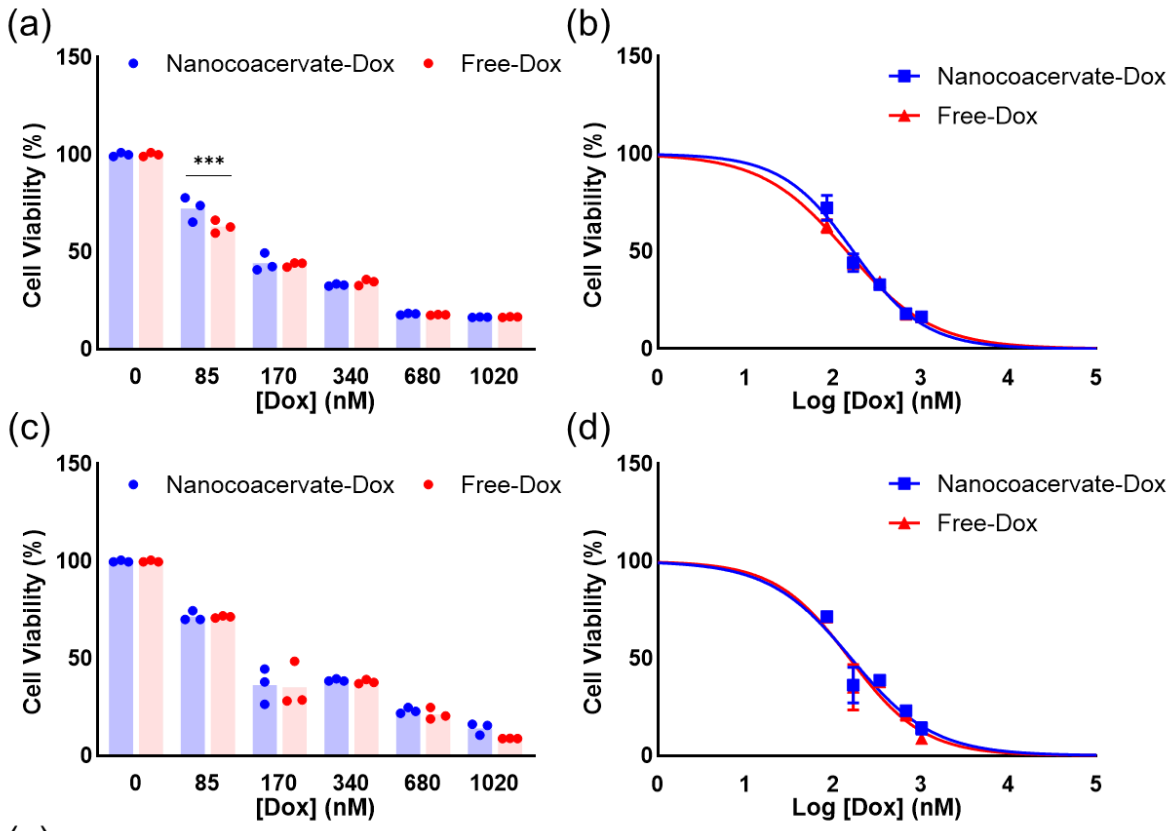

(e)

IC_{50} (nM)	Nanocoacervate	Free Dox
Sensitive	170	144
Resistant	161	155

Figure 5-8. Cytotoxicity of nanocoacervate delivered Dox in the 2D monolayer model as measured by MTS at 72 hours. Cell viability of (a) drug-sensitive (LK0917) and (c) drug-resistant (LK1108) cell line treated with PP75 nanocoacervate-Dox and free Dox at various concentrations. Dose-response curves of (b) drug-sensitive (LK0917) and (d) drug-resistant (LK1108) cell lines treated with PP75 nanocoacervate-Dox and free Dox at various concentrations ($p \leq 0.05$*, 0.01**, 0.001***). Fitted IC_{50} values are listed in tabular form in (e). Error bars represent standard deviations.

5.3.5 Enhanced cytotoxicity of Dox by nanocoacervate delivery system in 3D multicellular spheroid model

The results in Figure 5-8 contradict the hypothesis that the nanocoacervate delivery system can help bypass the drug resistance by carrying the drug into the cells and releasing the payloads once inside the cells. It was previously discovered that the difference in efflux pump of LK0917 and LK1108, which are patient-derived (non-standardized) cell lines, might not be reflected in simple 2D monolayer *in vitro* models. The 3D cellular spheroids were shown to better capture the drug-resistance of these cell lines.[257,261] Therefore, a previously

established 3D spheroid model was utilized to examine the delivery efficacy of the nanocoacervate system. The 3D spheroid model was first validated with a calcein probe (Figure 5-9). Calcein-AM is non-fluorescent and can be cleaved inside cells by intracellular esterase to render green fluorescence. In the MDR cell, the fluorescent calcein is quickly fluxed out of the cells. Therefore, calcein-AM serves as an indicator of MDR. It can be seen in Figure 5-9b, the accumulation of green fluorescence was much higher in the sensitive cellular spheroid than in the resistant ones.

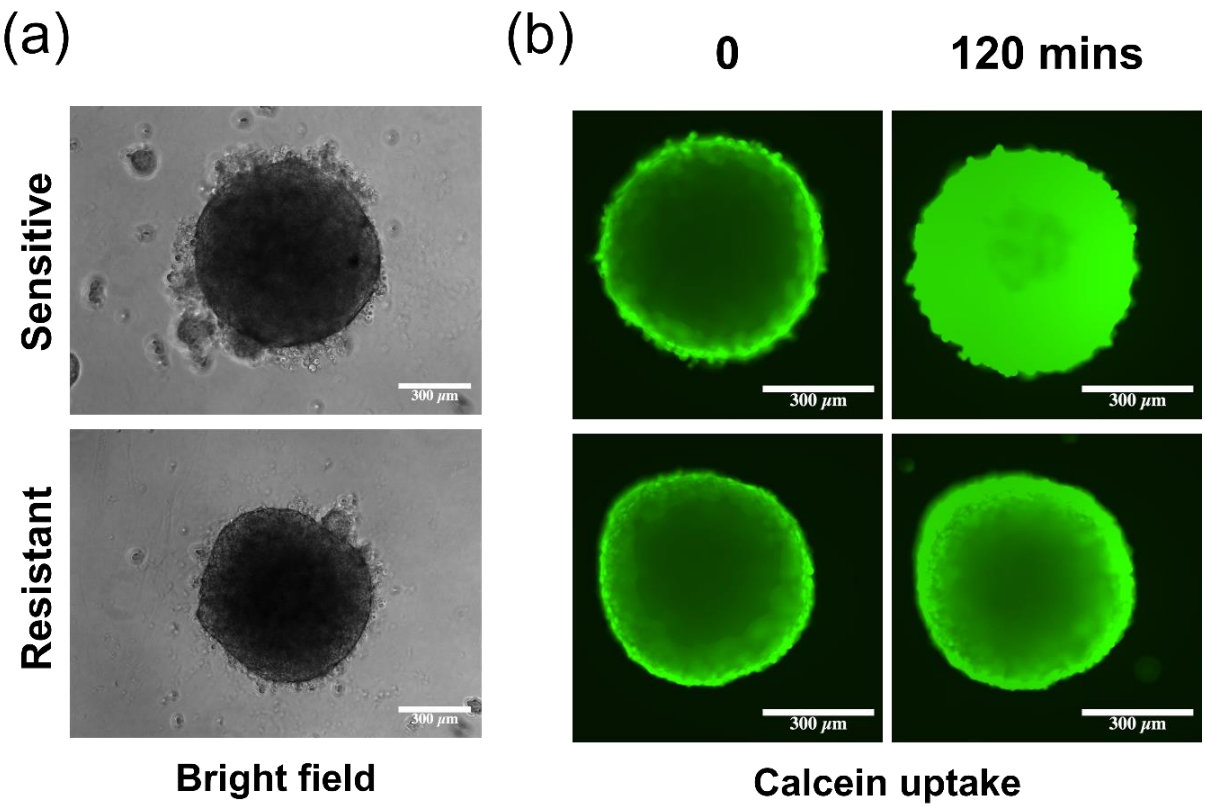

Figure 5-9. Validation of 3D tumor spheroid from pre-treated patient's cancer cell. (a) The corresponding bright field microscopic images of the spheroids. (b) Fluorescence microscopic images of 3D tumor spheroids made of drug-sensitive and drug-resistant cancer cells treated with calcein at 0 and 120 minutes.

Next, the efficacies of nanocoacervate delivered Dox and free Dox were compared in the 3D spheroid model using the MTS assay (Figure 5-10). In the sensitive spheroids, again there was no noticeable difference between nanocoacervate and free Dox. In fact, the free Dox had slightly lower IC_{50} than nanocoacervate. The resistant spheroid showed much higher cell viability than the sensitive spheroid for both nanocoacervate and free Dox at the same treating concentrations, which confirmed the validity of the resistant model. Between nanocoacervate and free Dox, the nanocoacervate resulted in lower IC_{50} than the free Dox

and exhibited higher cytotoxicity against the 3D tumor spheroid at 85, 340, and 1020 nM at 72 hours. In summary, a higher degree of difference in drug resistance between the sensitive and resistant cell lines was observed in the 3D spheroid model than in the 2D model, indicating that the drug resistance is better reflected in the 3D model than in the 2D model. Because the 3D spheroid better mimics the complex microenvironment of a tumor, it should be regarded as a more representative *in vitro* model than the 2D monolayer. The nanocoacervate showed improvement in Dox efficacy compared with the free drug, which was not observed in the 2D model. The results reveal that the nanocoacervate system improves the delivery of drugs to MDR cell lines and has the potential to be utilized to overcome MDR in tumor therapy.

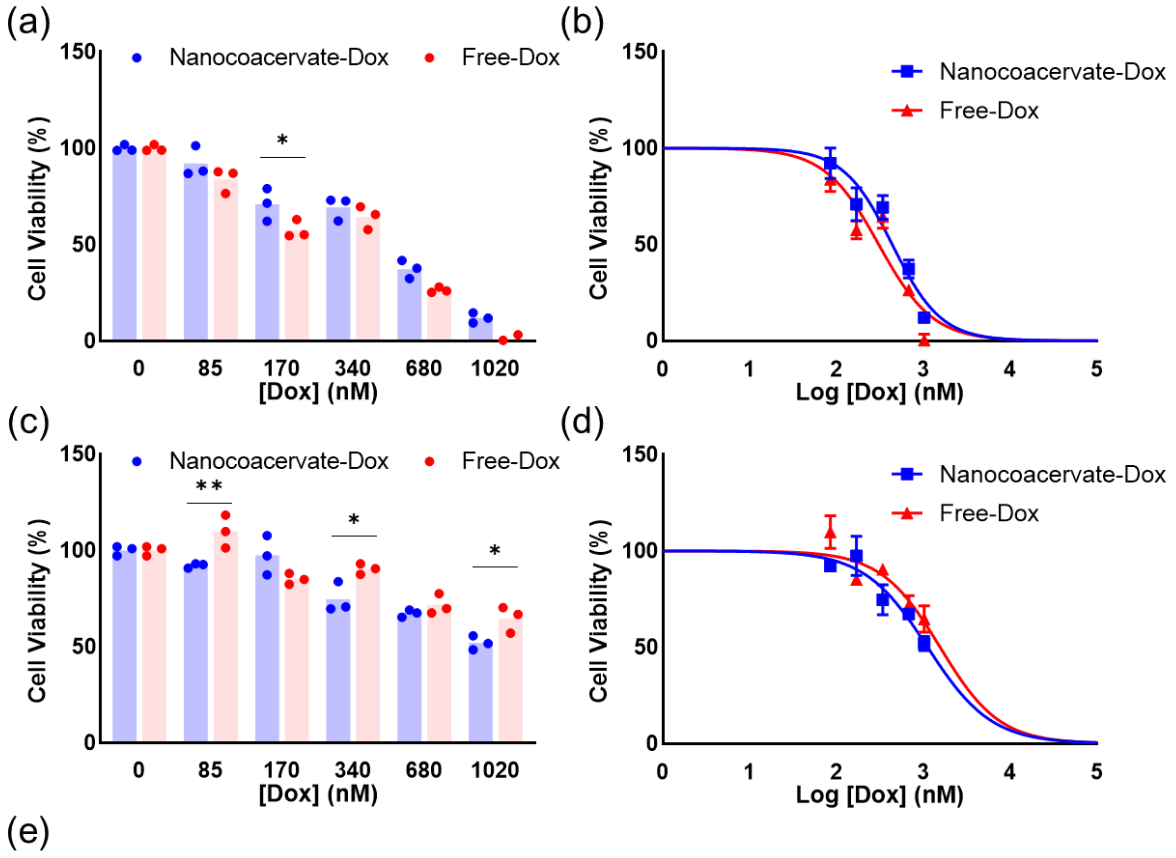

(e)

IC_{50} (nM)	Nanocoacervate	Free Dox
Sensitive	438	307
Resistant	1.12×10^3	1.56×10^3

Figure 5-10. Cytotoxicity of nanocoacervate delivered Dox in the 3D spheroid model as measured by MTS at 72 hours. Cell viability of (a) drug-sensitive (LK0917) and (c) drug-resistant (LK1108) cell lines treated with PP75 nanocoacervate-Dox and free Dox at various concentrations. Dose-response curves of (b) drug-sensitive (LK0917) and (d) drug-resistant (LK1108) cell lines treated with PP75 nanocoacervate-Dox and free Dox at various

concentrations ($p \leq 0.05$*, 0.01**, 0.001***). Fitted IC_{50} values are listed in tabular form in (e). Error bars represent standard deviations.

5.3.6 Enhanced delivery and accumulation of Dox by nanocoacervate delivery system in the 3D spheroid model

To cross-check the delivery efficiency of the nanocoacervate system in MDR cells, the Dox accumulation within the 3D multicellular spheroids was monitored using real-time fluorescence microscopic imaging (Figure 5-11). Overall, the resistant spheroids showed much less Dox uptake than the sensitive spheroids at the same treating times. The sensitive spheroids started to exhibit serious disintegration towards the end of treatment which might be caused by cell death. The resistant spheroids in contrast stayed intact in terms of shape due to the MDR and higher drug tolerance than the sensitive spheroids.

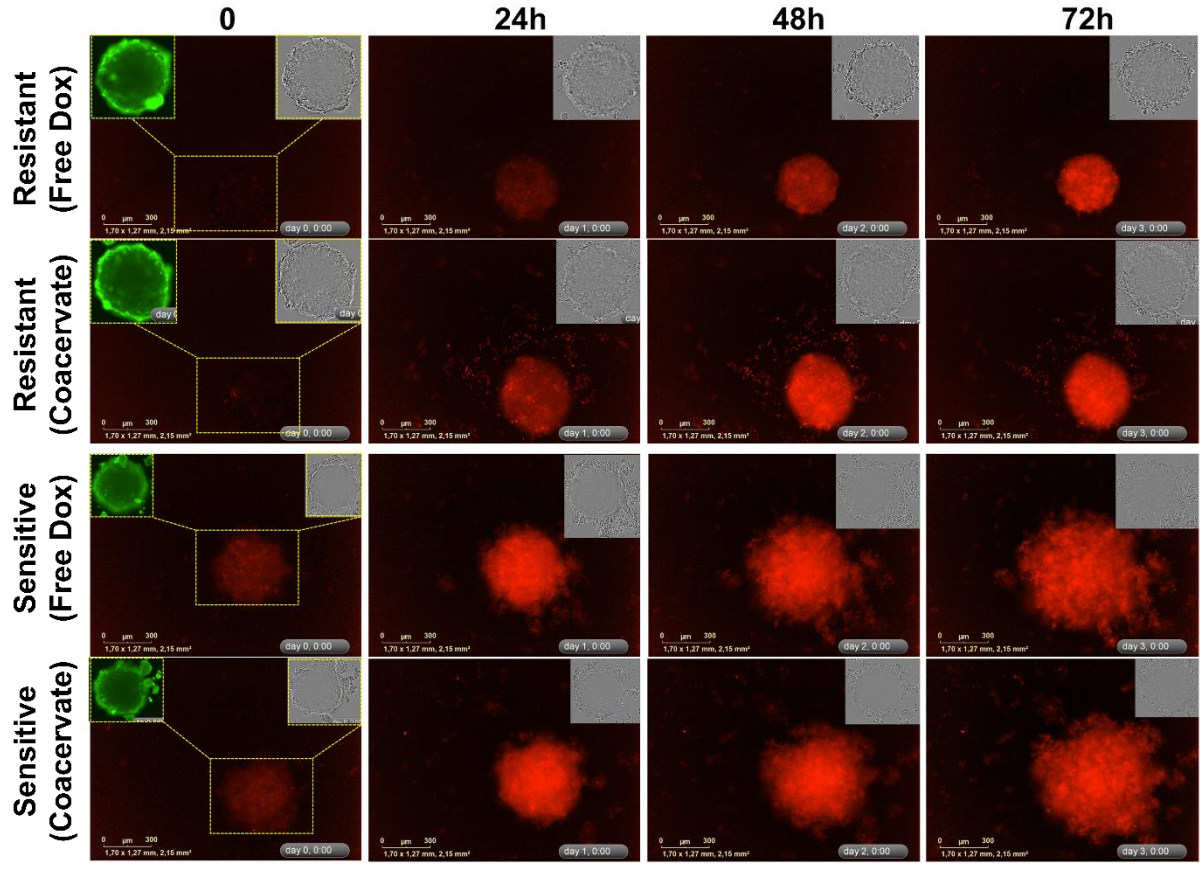

Figure 5-11. Real-time imaging of 3D tumor spheroids made with drug-sensitive (LK0917) and drug-resistant (LK1108) cancer cell lines over 72-hour treatment. Fluorescence images of resistant (top two rows) and sensitive (bottom two rows) spheroids treated with free Dox and nanocoacervate at [Dox] = 800 nM at various time points. The insets show the calcein intake and bright field of the spheroids. Scale bars represent 300 μm.

The quantitative analysis of fluorescence retention inside the spheroids was conducted. The raw fluorescence intensity (total fluorescence in the field of view) was recorded by the microscope (Figure 5-12). Figure 5-12a & b summarize the green fluorescence intensities by calcein in both sensitive and resistant spheroids. The control groups were treated only with calcein-AM and no drug, and the "+inhibitor" groups were treated with calcein and verapamil, which inhibits the activity of the efflux pump by blocking the calcium channel. The resistant spheroids showed a larger increase in green fluorescence with the addition of an inhibitor confirming the presence of MDR efflux pumps in the cell line. Interestingly, the sensitive spheroids also demonstrated some elevation in green fluorescence intensity, also indicating the existence of MDR proteins. The difference in the degree of enhancement, however, verified that there was a much higher level of overexpression of MDR proteins in the resistant (LK1108) cell lines than in the sensitive (LK0917) cell line.

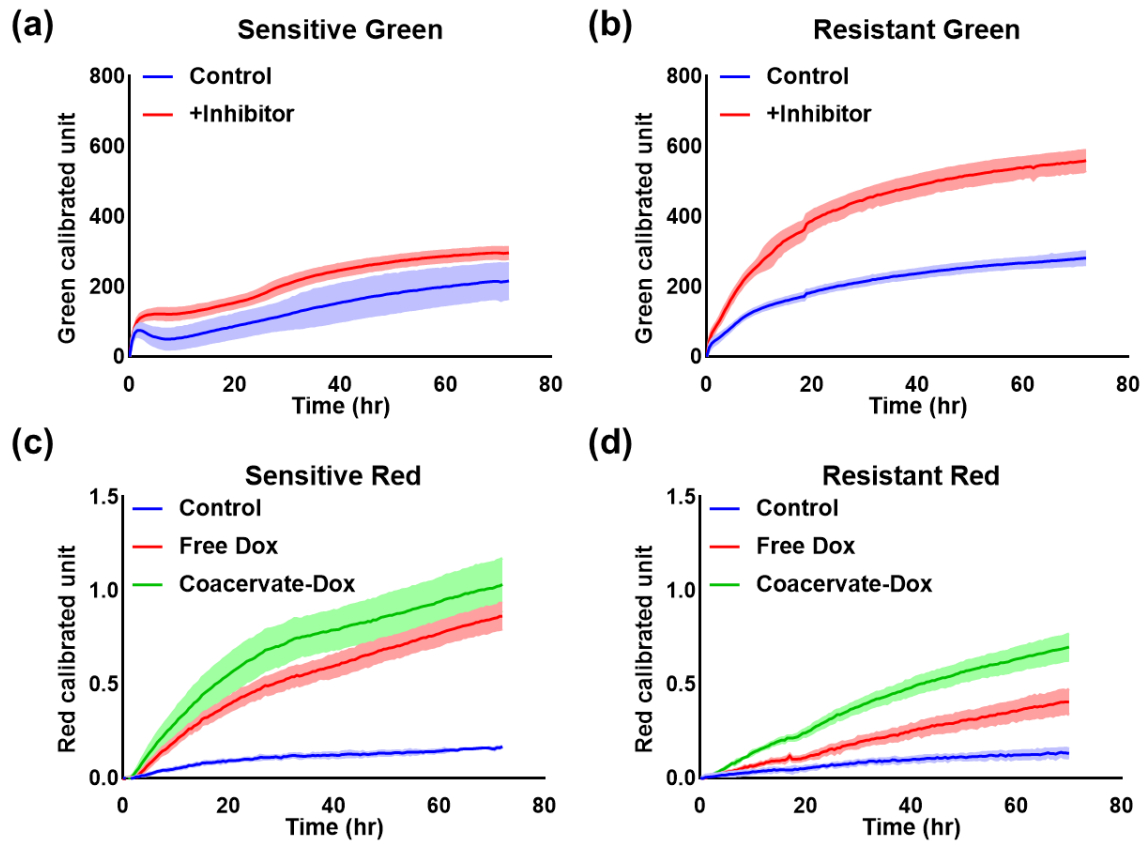

Figure 5-12. Raw total fluorescence intensity in the field of view as acquired by the microscope. Green channel fluorescence intensity of control groups (-/+ verapamil inhibitor) measured over 72 hours of calcein-AM treatment in (a) sensitive and (b) resistant spheroids. Red channel fluorescence intensity in (c) sensitive and (d) resistant spheroids treated with free Dox and nanocoacervate-Dox over 72-hour treatment. Error bands represent standard deviations of 3 independent replicates.

In terms of red fluorescence, the sensitive spheroids showed much higher Dox retention than the resistant spheroids as expected. In both cases, the nanocoacervate delivery system was able to improve the accumulation of Dox as displayed in red fluorescence intensity in the field of view. The degree of improvement was much more noticeable in the resistant spheroids than in the sensitive spheroids. The preliminary analysis of the raw data again confirmed that the nanocoacervate system can be a useful tool to deliver therapeutic agents to MDR cancer cells.

Next, to make a more accurate comparison of the Dox accumulation within the spheroids between different treatment groups, areas of interest for each image acquired during the real-time imaging were defined by manually creating masks to ensure that only the fluorescence signal within the spheroid area was considered (Figure 5-13). It was observed that nanocoacervate facilitated the penetration and accumulation of Dox in the resistant spheroids resulting in significantly higher red fluorescence intensity from 24 to 72 hours, although the difference was most prominent between 24 to 48 hours. On the contrary, no noticeable difference in Dox uptake between the free drug and the coacervate system was detected in sensitive spheroids except towards the end of the treatment (60 and 72 hours) which largely agrees with the cytotoxicity data. According to the cytotoxicity data (Figure 5-10a), the free Dox resulted in lower cell viability than the nanocoacervate at the high dose after 72 hours of treatment. Therefore, the lower red fluorescence accumulation in the sensitive spheroid by free Dox might be caused by more dead cells which allowed the leaking of Dox into media. The enhanced delivery of Dox into 3D resistant spheroids further validated the potential of the PP75-PEI nanocoacervate as a delivery system in MDR cancer therapy.

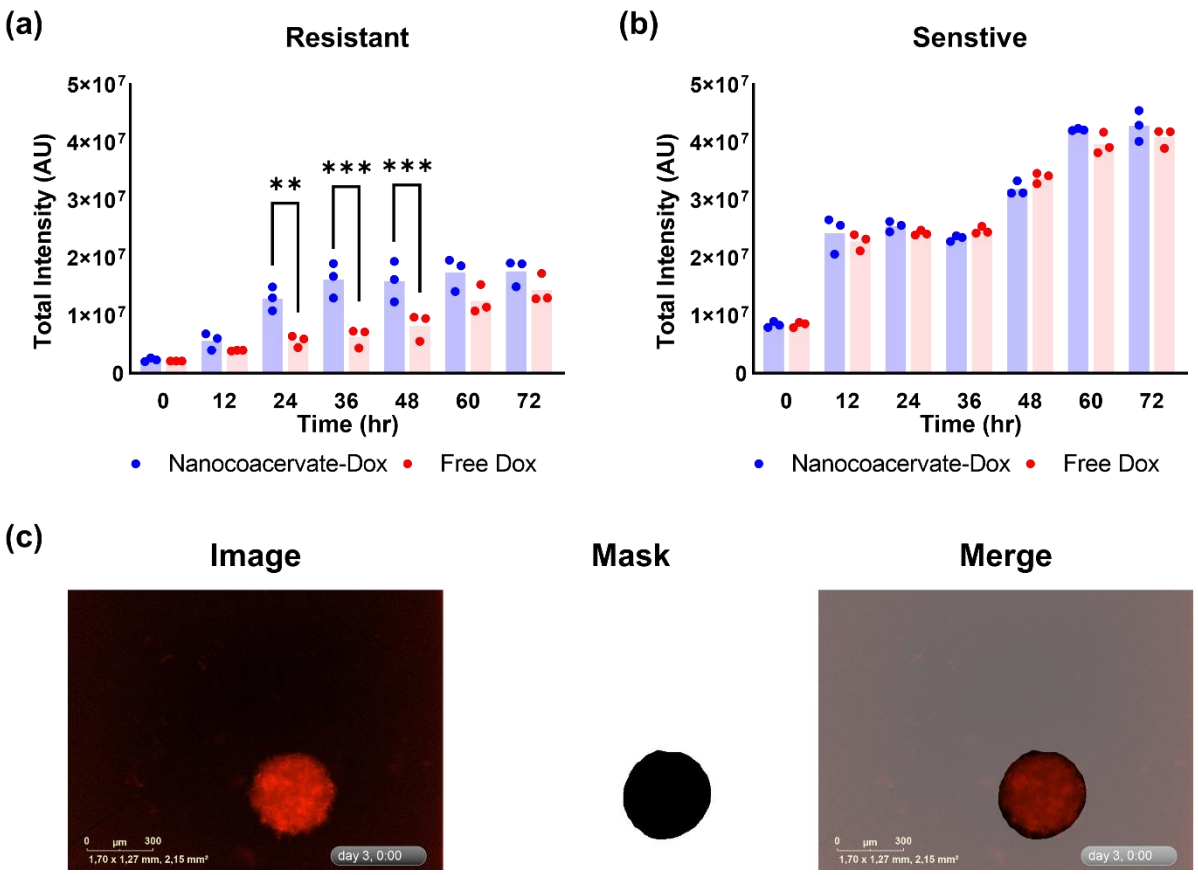

Figure 5-13. Quantitative analysis of red fluorescence accumulation and retention in 3D multicellular spheroids. Red fluorescence intensity at various time points in the (a) resistant and (b) sensitive cellular spheroids treated by nanocoacervate or free Dox (**$p \leq 0.01$, ***$p \leq 0.001$). (c) An example of a manually created mask defining the area of interest in fluorescence intensity analysis. Only the fluorescence intensity within the black area was analyzed. The mask in the merged figure was adjusted to be 60% transparent for a better display of the relative locations of the spheroid and the mask.

It is worth mentioning that the fluorescence accumulation and retention result did not completely translate into cytotoxicity effects. The discrepancy in the intra-spheroid fluorescence intensities between the nanocoacervate-treated group and free Dox-treated group is more prominent than the difference in the cell viabilities between the two groups. One possible reason behind the observation is the treating time selection. The MTS assay was performed as an endpoint test at 72 hours of treatment. From the fluorescence accumulation data (Figure 5-13), the biggest difference between nanocoacervate and free Dox occurred between 24 to 48 hours of treatment, while the gap narrowed after 48 hours. This could be caused by the death of outer cell layers with a long treating time of free Dox leading to more effective drug penetration as time passed by. Therefore, the MTS assay taken at a 72-hour

time point might not be the optimal endpoint to reflect the difference between the nanocoacervate and free Dox.

In addition, the disconnection between the fluorescence intensity and the cytotoxicity could be caused by the incomplete release of Dox from the coacervate system. As shown in the previous chapter, Dox can be effectively released from the nanocoacervate system at a slightly acidic pH (5.5 to 6.6) which corresponds to late endosome pH. However, based on the release data in Figure 4-11, it still took 5 days for Dox to reach close to 100% release from the nanocoacervate system, although in vivo release might be faster than that due to the presence of enzymes. The results suggested the interaction between PP75 and Dox might be too strong for efficient release of the Dox within the current treating time. This result calls for rethinking using PP polymer covalent conjugates to deliver payloads containing positive charge and π ring systems. For these systems to accomplish effective release of payloads, they have to undergo both efficient covalent bond cleavage and physical interaction dissociation, which in combination can easily offset the enhance intracellular trafficking effects of the PP polymer. Together with the data from the previous chapter, where PP50 exhibited low encapsulation efficiency, it can be inferred that a PP polymer with an intermediate L-phenylalanine substitution degree between 50 and 75 might be able to achieve both satisfactory encapsulation efficiency and faster release of Dox from the nanocoacervate system.

5.4 Conclusions

The nanocoacervate system composed of dual intracellular trafficking polymers, PP75 and PEI, and the chemotherapeutic drug Dox, was subject to various *in vitro* models for studying its delivery effects. Cytotoxicity assays were performed with various cell lines in both 2D and 3D fashions. Improved cell killing was observed with the nanocoacervate delivery system in 3 commercially available cell lines to various degrees. The mechanism of intracellular trafficking of the nanocoacervate system was proved to be the endolysosomal pathway using the SIM. The final destination of the Dox demonstrated dose-dependent distribution for both free and nanocoacervate delivered Dox as higher treating concentrations resulted in the faster localization in the nuclei according to the confocal imaging.

In contrast to the standard cell lines, the experiments with patient-derived head and neck cancer cell-line showing distinct levels of drug resistance revealed that the delivery effects of nanocoacervate system were more prominent in the resistant 3D spheroid model

whereas the drug-sensitive models (both 2D and 3D) and the resistant 2D model did not exhibit an obvious difference in cell viability between free Dox and nanocoacervate delivered Dox. This trend was also verified in real-time fluorescence imaging where the difference in Dox accumulation between free Dox and nanocoacervate delivered Dox was only seen in resistant 3D spheroids but not in the sensitive 3D spheroids. The results obtained from both standard and patient-derived cell lines not only confirmed the delivery effects of the nanocoacervate but also added new insights into the difference in 2D and 3D *in vitro* models. The different trends in the cytotoxicity data obtained between the resistant 2D and 3D models, where the latter showed lowered cell viability with nanocoacervate delivered Dox and the former did not, suggested that the 3D spheroid, resembling more of the complexity of a real tumor, was the better model to reflect the drug resistance than the 2D model.

The data presented in this chapter has proved the potential of the nanocoacervate as an effective delivery system to achieve efficient delivery of agents to MDR cells. The promoted intracellular delivery of PP75 and PEI was shown to be a promising platform, but further *in vivo* study is needed to verify their effectiveness. In addition, countless combinations of polymer-payload can be fabricated with well-designed intermolecular interactions. Polymers with other functions, such as active targeting or fluorescence tagging, can be incorporated to confer a wide range of functionalities to the delivery systems suitable for various biomedical applications.

6 Conclusions and future work

6.1 Conclusions

6.1.1 Process-engineered synthesis of uGNPs with fine tuning of size

In this project, a process-engineered synthesis was developed to fabricate uGNPs with precise size control at nanometric resolution. The process is based on the seed-templated growth strategy, which is composed of an initial seed formation reaction and a sequence of additions of gold precursor of predetermined amounts. The reaction conditions were set based on previous studies, so the formation of new particles only took place in the first seed formation step and further nucleation was suppressed in the later growth steps. Excess NaCit was present throughout while each aliquot of the gold precursor was added in a small amount, so that all gold precursor was consumed in each round. A controlled redox environment was maintained with a nitrogen purge during the entire synthesis process.

After each round of growth was finished, a portion of the reaction mixture was extracted, and the reaction mix was replenished with NaCit solution. This was then followed by the next addition of the gold precursor. The uGNPs series made with this method are capped with NaCit and are thus easily modifiable post-fabrication. On top of that, the synthesis requires only an aqueous environment, and the product contains only the uGNPs and non-toxic salts, so the uGNPs produced with this method are suitable for biomedical applications.

6.1.2 Mechanism study of the reduction of chloroauric acid by TA and NaCit

The seed formation step was accomplished using the Mühlpfordt method, namely the use of TA and NaCit as combinational reducing agents. This method allowed the formation of well-dispersed 3-nm uGNPs, upon which the rest of the uGNPs with increasing size were made. Despite the success of implementing this method in numerous studies, the exact reaction mechanism was not completely understood. To better understand the reaction mechanism, the TA-NaCit reaction was carried out with various amounts of TA and NaCit. It was found the reaction rate was dependent on both the concentrations of TA and NaCit. However, the amount of TA had much more influence on the rate, indicating that TA was the dominating reducing agent. The influence of the concentrations on the particle size was also investigated. The particle size was not noticeably affected by various TA and NaCit concentrations except when the concentration of TA was low, and the reaction essentially

turned into a Turkevich reaction. A seed-mediated growth reaction mechanism composed of an initial seed cluster formation exclusively controlled by TA and a subsequent growth process driven by both the remaining TA and NaCit was proposed.

6.1.3 Characterization of uGNPs

The uGNPs with increasing size from 3 to 15 nm were successfully fabricated using the process-engineered synthesis. The uGNPs were characterized by their dry and wet size using DLS and TEM. The size showed a single nanometer increment for each uGNP bath. The LSPR of each uGNP batch was also measured with UV-Vis spectroscopy. The peak position of the uGNPs shifted from just below 500 nm to around 520 nm with sizes ranging from 3 nm to 15 nm. The peak position increased rapidly from 497 nm to 519 nm corresponding to size being 3 nm to 7 nm while it only increased from 519 to 520 nm with sizes varying from 8 to 15 nm. The stability of the uGNPs was examined using a flocculation test in PBS solution, PBS + 10% FBS, and colorless cell culture media. The uGNPs lost colloidal stability in PBS solution as shown by the change of solution color and disappearance of the LSPR peak. In contrast, the uGNPs retained their colloidal stability in both FBS solution and cell culture medium. This is likely due to the protein and peptide that get adsorbed onto the uGNP surface helping to stabilize them in the high ionic strength environment. Lastly, the post-fabrication modification of uGNPs was verified with 8-arm thiol terminated PEG. PEGylated uGNPs exhibited an increase in hydrodynamic diameter, decrease in ζ-potential, and slight upshift in LSPR absorbance peak position. The PEGylation was further confirmed by a flocculation test using NaCl. All PEG-modified uGNPs showed no change in LSPR in ionic strength up to 100 mM, while the as-prepared uGNPs lost their colloidal stability around the same ionic strength (except the $uGNP_3$).

6.1.4 Acute cytotoxicity of uGNPs

The uGNPs were subject to a collection of biocompatibility tests to confirm their potential in biomedical applications. The acute cytotoxicity of the uGNPs was examined with 3 different cell lines, 293A, MCF7, and SW480. Smaller uGNPs exhibited enhanced proliferation in 293A and MCF7 at low and medium treating concentrations. The medium-sized uGNPs around 8 to 12 nm resulted in limited cytotoxic effects at specific time points and doses. Overall, the uGNPs fabricated using the seed-templated growth strategy showed no significant sign of acute cytotoxicity to the three cell lines. Cytotoxicity effects of uGNPs were also examined with THP-1 acute leukemia monocytes and their induced macrophages as

a part of an investigation of their immune compatibility. The uGNPs showed no acute cytotoxicity against both cell lines within 72 hours of treatment and promoted proliferation was observed with THP-1 monocytes treated with 8-nm and 12-nm uGNPs at medium concentrations. To sum up, the uGNPs demonstrated no acute cytotoxicity in different types of body and cancer cells as well as immune cells.

6.1.5 Complement activation induced by uGNPs

The ability of the uGNPs to activate the complement system was studied as well. As the complement activation is the first step to tag NPs for clearance *in vivo*, it dictates the clearance mechanism and targeting efficiency of NP administered *in vivo*. Activation markers C4, C3, and soluble C5b-9 were analyzed in the plasma samples incubated with uGNPs. All uGNPs of different sizes elicited comparable levels of activation of the three markers as the PBS treated negative control group and much lower levels of activation than the zymosan treated positive control. The results showed that the uGNPs, even without any antifouling coatings, do not cause complement activation *in vitro*.

6.1.6 uGNPs induced pro- and anti-inflammatory cytokines secretion

As another aspect of the immune compatibility test, the induced cytokines released by uGNPs in THP-1 monocyte and their induced macrophages was measured. With monocyte, secretion of 6 cytokines was elevated by $uGNP_3$ and $uGNP_6$, but not $uGNP_8$ or $uGNP_{12}$. Among the cytokines, TNF-α, IL-1β, and IL-8 are proinflammatory cytokines, IL-2 and IL-6 act as both pro- and anti-inflammatory cytokines, and IL-10 is an anti-inflammatory cytokine The results showed that smaller uGNPs could induce the secretion of more proinflammatory cytokines in monocytes indicating a probable proinflammatory effect. In macrophages, smaller $uGNP_3$ and $uGNP_6$ at low concentrations promoted the production of IL-10, IL-13, IL-1β, IL-2, TNF-α, and IL-8, while $uGNP_8$ and $uGNP_{12}$ had negligible effects on change in most cytokines release. In general, larger particles had fewer effects on cytokine release profile in both monocytes and macrophages and the smaller uGNPs seemed to direct cytokine release towards proinflammatory reactions.

6.1.7 Blood compatibility of uGNPs

The blood compatibility of uGNPs, specifically the thrombogenicity of the uGNPs, was evaluated as blood is the first biological component that encounters the uGNPs if they were to be intravenously injected. Both the intrinsic and extrinsic pathways in coagulation

were evaluated with APTT and PT. The APTT and PT of plasma samples treated by uGNPs of various sizes and at different concentrations all fall within the normal range. The results exhibited the high compatibility of uGNPs with blood and thus verified their fundamental safety profile as a potential platform for biomedical applications.

6.1.8 Fabrication of PP-PEI-Dox nanocoacervate system

In the effort to develop a facile and fast fabrication method to make instant nanoformulation of drugs, the complex coacervation system was employed. The instant nanoformulation is itself a cost-effective and simple fabrication method and is a promising way to bypass the requirement for long-term storage of nanomedicines in their NP form. The PP polymer, a class of bioinspired pseudopeptide which simulates the structure and pH-responsive endosomolytic activity of the viral peptide, was used together with PEI and Dox to form a tertiary coacervate system. The nanocoacervate system could be fabricated via simple mixing of the components in seconds. With an optimized mixing ratio, the colloidally stable and turbid mixture can be easily obtained in DPBS solution. The driving forces of the assembly of the nanocoacervate system were electrostatic interactions, π-π stacking, and hydrogen bonding. The nanocoacervate system verified the feasibility of making instant nanoformulation of drugs.

The self-assembly between PP polymer and Dox discovered in this study has provided valuable insights into the previously observed insufficient delivery of Dox using covalent PP75-Dox conjugates in our research group. Less cytotoxic effects were observed with Dox that was covalently attached to PP75 via disulfide bond than free Dox, even though the drug accumulation was comparable between the two groups. In addition to the insufficient cleavage of the disulfide bond as proposed in the previous report, the spontaneous assembly between Dox and PP75 could be an additional reason why Dox was not effectively released and allowed to intercalate the DNA. The results called for careful consideration of using PP polymer and other delivery cargos that contain similar structures for delivering hydrophobic and π-ring containing drugs. The self-assembly between the delivery system and the payloads through physical association might facilitate the loading of the drug and hinder the release of the drug at the same time. Therefore, specific attention should be directed to evaluating the potential physical associations when it comes to delivery system design.

6.1.9 Characterization of the nanocoacervate

The nanocoacervate was then characterized for its size distribution, ζ-potential, colloidal stability, drug encapsulation, and pH-responsive release of the drug. The nanocoacervate exhibited bimodal size distribution with one peak at 100 nm and another one around 1 μm. Spherical features with diameters around 100 nm were observed in both SEM and TEM images. The nanocoacervate possessed a large negative ζ-potential around -50 mV which provided strong interparticle repulsion for colloidal stability. The optimized mixing ratio resulted in 84.2 ± 5.0% encapsulation efficiency and 9.14 ± 0.55% (by weight) loading capacity, although the loading capacity might be an underestimation because it was calculated by assuming that all the polymers participated in the formation of the nanocoacervate system. In addition, the release of Dox from the coacervate delivery system was also studied. Both PP and PEI are weak polyelectrolytes, meaning their charge densities change with pH values. Therefore, the release profiles of Dox were established under various pH values. It was found that the release was expedited by an acid environment down to pH = 5.5, while more acidic pH actually slowed down the release. The stimulation pH corresponds to both the late endosome environment and the pH at which the PP polymer has membrane-lytic activity. Therefore, it has great potential to be used as a drug delivery system through the endosomal pathway.

6.1.10 Intracellular delivery pathway of nanocoacervate system

A previous report has concluded that PP-drug conjugate enters cells via the endocytosis pathway. The delivery pathway of the nanocoacervate system was investigated using SIM. Specifically, the colocalization of Dox (red fluorescence) and lysosome/late endosome (green fluorescence) was monitored. It was found that the nanocoacervate delivered Dox was mainly localized in the lysosomes as compared with the free Dox which did not show obvious preferential accumulation within the lysosome than in the cytosol. With a longer treating time, Dox was observed to escape from the lysosomes which was likely a result of PP75 and PEI mediated endosomal escape. The result verified the endosomal intracellular trafficking pathway and the successful escape of Dox from the lysosome into the cytosol. The Dox ultimately reached the cell nuclei at a dose-dependent rate as confirmed by confocal imaging.

6.1.11 Delivery of Dox by nanocoacervate in *in vitro* models

The delivery effects of nanocoacervate using Dox as a model drug were investigated with various *in vitro* models. Three different breast cancer cell lines. MCF7, MDA231, and T47D were treated with a nanocoacervate system containing Dox and the cytotoxic effects were compared with that of free Dox. Limited improvement of cytotoxic effects was observed with each cell line at a specific dose and treating time. The fitted IC50 of coacervate delivered Dox was significantly lower than free Dox only in T47D with 48-hour treatment. The delivery effect was then examined with a pair of patient-derived head and neck cancer cell lines with different levels of MDR. The cytotoxic effects were compared between nanocoacervate delivered and free Dox with both drug-sensitive and resistant cell lines in 2D monolayer and 3D multicellular spheroids models. The nanocoacervate delivered Dox exhibited similar and, in some cases, slightly weaker cytotoxicity than the free Dox in drug-sensitive cells both in 2D and 3D models. The similar killing effects between the delivery system and the free drug were expected in a drug-sensitive cell line. Interestingly, it was also the case for drug-resistant 2D model, where no improvement in the efficacy of Dox was detected when delivered by nanocoacervate. However, the nanocoacervate delivered Dox led to noticeably lower viability than the free Dox drug resistant 3D spheroid. The results suggested that i) the 3D cellular spheroid model, with a higher level of structural complexity and intercellular connectivity, better reflects the MDR nature of the cell line and ii) the nanocoacervate can help to bypass the efflux pumps in MDR cancer cell lines and deliver therapeutic agents such inside cells such as an anticancer drug.

To double-check the delivery effects of the nanocoacervate, real-time live cell imaging of the delivery process of Dox into the 3D spheroids was conducted. The red fluorescence intensity was recorded at various time points of treatment and taken as an estimation of the amount of Dox. It was found again that the accumulation of Dox was comparable in sensitive cellular spheroids regardless of whether the nanocoacervate system was applied. In contrast, the Dox accumulation in drug-resistant cellular spheroid was much more pronounced with the nanocoacervate than the free Dox by itself, especially between 24 to 48 hours of treatment. The difference in the accumulation of Dox in resistant spheroids by nanocoacervate and free Dox seemed more evident than the difference in the cell viability data between the two groups. The fact that the enhancement in Dox accumulation was not translated into cytotoxicity was likely a result of the possible inefficient release of Dox from the nanocoacervate and the sub-optimal time point at which the MTS assay was taken.

6.1.12 Addressing the bottlenecks in nanomedicine

The main goal of the studies is to tackle the bottlenecks in nanomedicine translation, specifically the size control and facile formulation. The process-engineered synthesis of uGNPs is a novel method to manufacture sub-10 nm NPs with nanometric size tuning. The uGNPs synthesis achieves precise size control by breaking the growth process into separate steps via process engineering. The multiple discrete growth steps allow extremely controlled growth, which ultimately produces NPs with narrow size distribution. This method has great potential to be translated into large-scale production. In addition, the method theoretically can be applied to other NP systems, especially metal NPs undergoing seed-mediated growth mechanism. The technique is particularly beneficial for synthesizing NPs for biomedical applications with strict size requirements, such as renal-clearable contrast agents.

The nanocoacervate system on the other hand provides a new concept for fabricating and formulating nanomedicine. The stability of nanomedicine during long-term storage is a crucial issue for clinical application. For example, the extremely low temperature requirement during storage, transportation, and distribution for LNP-mRNA vaccines (-80 °C for BioNTech and -20 °C for Moderna) has prevented the access to them by the wider global population in the less developed areas, such as Africa. The nanocoacervate demonstrates an instant nanoformulation that can be prepared in situ. With this method, components of a nanoformulation can be stored separately in dry powder form. Upon usage, they can then be reconstituted and mixed to form nanoformulation. Such a method has the potential to formulate a variety of therapeutic agents in a mix-and-go fashion and thus help bypass the special stability requirement in NP form during storage and transportation.

The results of both the studies are significant incremental advancements towards better translation of nanomedicine. The findings are by no means ideal solutions to completely address all the unmet needs in NP-based delivery systems. However, the outcomes can be further leveraged in further investigations to develop even more advanced systems for translation applications of nanomedicine.

6.2 Future work

This study has covered a collection of topics that the field of nanomedicine currently faces for more efficient translation. The results of the studies in this thesis have set the stage for many future opportunities in developing more powerful and effective nanosystems in

biomedical applications and beyond. A number of potential future directions that can be built upon the discoveries from this report are discussed in the following sections.

6.2.1 Development of continuous fabrication system for making uGNPs series

Continuous production of NPs with precisely controlled size and minimal manual intervention has many advantages over batch reaction for large-scale production. Continuous synthesis of NPs has been investigated intensively and systems such as microfluidics-based microreactors have been successfully developed to produce different kinds of NPs. The process-engineered seed-templated uGNP fabrication method was developed in a semi-batch style. To accommodate the seed-templated uGNPs synthesis method, the continuous synthesis system should comprise multiple microreactors (e.g., plug flow reactors) in series, with inlet and outlet streams in between allowing the removal of intermediate products and the replenishing of gold precursor for consequent particle growth. In addition, the unique advantages provided by microfluidic systems such as manipulation of picoliter level of liquid, and fine control of the mixing interface due to the laminar flow could allow further size control. Therefore, developing a microfluidics technology based continuous NP synthesis process would not only be a huge step towards translation of the uGNPs, but also potentially achieve size tuning at an even smaller resolution.

6.2.2 Investigation of uGNPs *in vivo* safety immunogenicity, biodistribution, and renal clearance

The biosafety and immune compatibility of the uGNPs were subject to an all-around framework of tests. Although the framework covers all important characteristics including cytotoxicity, immunogenicity, complement activation, and thrombogenicity for NP safety, the predictability of the results from these *in vitro* tests needs to be validified *in vivo,* such as in rodents and primates. As mentioned in Chapter 3, the physiological and clinical implications of the change in cytokine profile secreted by uGNP-treated monocytes and macrophages need to be investigated. Therefore, *in vivo* model could help to determine whether inflammatory effects are caused by the uGNPs. As found in the *in vitro* study that smaller uGNPs skew the cytokine secretion more than the larger ones, it is worth investigating the adjuvanticity of uGNPs in nanovaccines *in vivo,* especially focusing on the size effect.

Many other aspects of safety profiles of uGNPs can only be evaluated *in vivo*. Basic bodyweight and histopathological changes should be monitored for fundamental toxicity evaluation. The biodistribution and bioaccumulation of uGNPs can provide information on

potential organ-specific safety concerns which were not reflected in *in vitro* models. The pharmacokinetics and clearance pathway studies of uGNPs will help to evaluate the correlation between *in vitro* complement activation measurement and *in vivo* particle scavenging by the MPS. Additionally, the uGNPs series with finely turned size and facilely modifiable surface serves as a versatile platform to investigate the size and surface chemistry effects on the clearance pathway.

6.2.3 Exploration of biomedical applications of uGNPs

Due to the small size, uGNPs possess certain advantages over their larger counterparts in addition to the superior biocompatibility described above and therefore have great potential in many biomedical applications. For example, uGNPs of sizes below 10 nm are found to be paramagnetic and thus can be utilized as MRI contrast agents and magnetic hyperthermia therapeutic agents.[262] The seed-templated synthesis method can be used to generate uGNPs with finely tuned sizes falling in this size range. Therefore, it is a powerful tool for studying the size effects on magnetization and *in vivo* localization for potential clinical application in MRI scans. Similarly, GNPs can be used as PAI contrast agents due to their strong NIR absorption. In PAI, areas of interest are treated by non-ionizing laser pulses, which are absorbed by different molecules and converted to ultrasonic signals. Due to the difference in optical absorption, different molecules and tissue exhibit various conversion efficiencies. GNPs take the advantage of the low NIR range absorption of biological tissues, and can result in a great signal-to-noise ratio. Although NIR absorption is not unique for uGNPs as larger GNPs also absorb NIR irradiation readily, the small size of uGNPs makes them possible to be effectively cleared from the body via the renal pathway; thus, are more promising for clinical translation.

In addition to the bioimaging application, uGNPs are also a promising platform for making nanovaccines due to their potential adjuvanticity, especially for the smaller ones. The citrate-capped uGNPs can easily be modified with functionalized molecules through stronger linkages such as the gold-thiol chemistry. Antigens and targeting ligands can be easily anchored to the uGNPs. The uGNPs series would again be suitable for studying the size effects of specific immunization applications. Another research direction for utilizing the uGNPs is to build multivalent architectures. One type of such structure is the so-called “ultrasmall-in-nano” systems assembled from ultrasmall NP monomers. In such a system, the size of the overall nanoclusters can be up to micron level, while the building blocks of the

nanoclusters are smaller than the KFT. Such systems are designed to achieve long circulation time in the assembled form and efficient renal clearance once degraded.[263] The uGNPs series can be employed to construct such systems, and with the combination of different sized building blocks, special architectures and geometries can be obtained. On top of *in vivo* applications, uGNPs might also be found useful *in vitro* applications including biosensing and gene editing.

6.2.4 Structure optimization of PP polymers for making drug delivery system

As discussed in the chapter, the assembly of the nanocoacervate system was driven by a combination of electrostatic attraction, π-π stacking, and hydrogen bonding. Therefore, the number of aromatic rings borne by the polymer can influence the strength to complex with Dox. Indeed, it was found that PP50 had limited loading capacity while PP75 might suffer from the incomplete release of Dox. It would be beneficial to investigate the PP polymer with an intermediate degree of phenylalanine grafting which could lead to both satisfactory loading capacity and effective release.

Moreover, the solubility and size control over the nanocoacervate are also potential areas that can be improved through better molecular structural design. One such way would be to make a di-block-copolymer with PP and PEG. The resulting copolymer would have a much higher solubility in an aqueous environment due to the PEG segment, and likely still retain the endosomolytic properties. Furthermore, due to its amphiphilic nature, the PP-PEG copolymer can potentially form micelles for drug encapsulation under the right conditions, with the PP forming the interior hydrophobic environment. This would allow the formation of nanosystems with better defined particle size than the nanocoacervate, although micelle fabrication is unlikely to achieve the same instant nanoformulation as the nanocoacervate system.

6.2.5 Delivery of Dox to *in vivo* multidrug resistant tumor models

Given that the nanocoacervate delivery system has shown improved cytotoxicity against MDR cells in 3D *in vitro* cellular spheroid model, the next step would be to test the delivery efficacy in in vivo models, such as a xenograft mouse model. Before going to in vivo model, however, the biosafety and biocompatibility of the nanocoacervate system should be investigated following the same framework s established in Chapter 2. The *in vivo* study will help to take a step further in evaluating the clinical translation potential of the nanocoacervate. With the nanoscale size, the nanocoacervate is expected to have passive targeting properties.

Therefore, further improvement in antitumor activity is expected in in vivo model than in vitro model. In addition, it will also be interesting to investigate the in pharmacokinetics and biodistribution of the nanocoacervate system.

6.2.6 Development of more nanocoacervate-based drug delivery systems

As mentioned in Chapter 4, the PP-PEI coacervate has the potential to encapsulate other drugs that contain ionizable positive functional groups and aromatic rings, such as paclitaxel. In addition, other functional polymers can be incorporated to develop nanocoacervate systems with special applications. For example, folic acid conjugated polymers can be used in targeted delivery to cancer cells with overexpression of folate receptors. Nucleic acids and peptides, such as A10 RNA aptamer and DUP-1 peptide for targeting prostate-specific membrane antigen-positive ($PSMA^+$) and negative ($PSMA^-$) prostate cancer cells are also among the potential candidate for building coacervate systems. Other functional polymers such as inherently therapeutic polymer, biodegradable polymer, fluorescently tagged polymer, and stimuli-responsive polymer are suitable building blocks for making coacervates in delivery, imaging, and theranostics applications as well.

6.2.7 Combining the precise size control and facile fabrication

A final future research direction worth mentioning is to combine the precise size control in the uGNPs fabrication and the facile self-assembly in the nanocoacervate system into one nanoplatform. The method can be viewed as templated complex coacervation. Particularly, this can be accomplished by utilizing the uGNPs as core templates and decoraing the particle through physical association. Similar approaches have been reported in the literature (Figure 6-1a & b).[264,265] In a tentative design, a layer of cationic polyelectrolyte can be attached to the surface of uGNPs via thiol-gold linkage. Next, PP-PEG block copolymers and Dox can be complex to the system via electrostatic interaction and hydrophobic association (Figure 6-1c). Such a system would combine the advantages of nanometric size control, facile fabrication, and enhanced intracellular delivery into one platform.

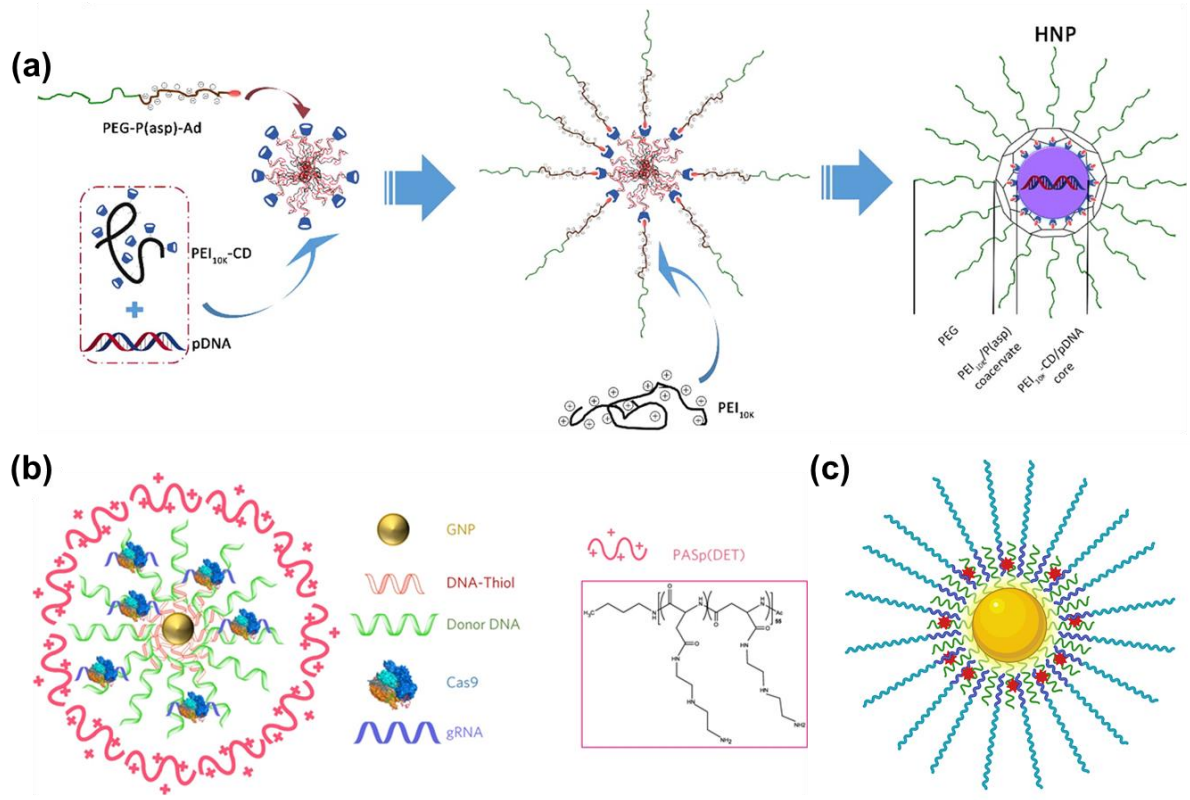

Figure 6-1. Schematic illustration of templated nanocoacervate systems. (a) Formation of hybrid NPs. PEI_{10K}-cyclodextrin (CD)/pDNA is first generated and Poly(ethylene glycol)-b-poly(aspartate)-adamantane (PEG-P(asp)-Ad) binds to the NP via Ad-CD interaction. More PEI_{10K} interacts with P(asp) through complex coacervation forming a cage around the NP core through the crosslinked network and confers PEG corona to the NPs. Reprinted with permission from reference.[264] Copyright 2016 American Chemical Society. (b) CRISPR–Gold is composed of 15 nm GNPs conjugated to thiol-modified oligonucleotides (DNA-Thiol), which are hybridized with single-stranded donor oligonucleotides and subsequently complexed with Cas9 ribonucleoprotein and the endosomal disruptive polymer poly(N-(N-(2-aminoethyl)- 2-aminoethyl) aspartamide) grafted diethylenetriamine (PAsp(DET)). Reprinted with permission from reference.[265] (c) A tentative design of templated nanocoacervate composed of uGNP core, a cationic polymer, Dox, and PP-PEG. Created with BioRender.com.

References

(1) Wagner, V.; Dullaart, A.; Bock, A.-K.; Zweck, A. *Nat. Biotechnol.* **2006**, *24*, 1211–1217.
(2) Bharathala, S.; Sharma, P. In *Nanotechnology in Modern Animal Biotechnology*; Elsevier, 2019; pp 113–132.
(3) Calzoni, E.; Cesaretti, A.; Polchi, A.; Di Michele, A.; Tancini, B.; Emiliani, C. *J. Funct. Biomater.* **2019**, *10*, 4.
(4) Vauthier, C.; Bouchemal, K. *Pharm. Res.* **2009**, *26*, 1025–1058.
(5) Allen, T. M.; Cullis, P. R. *Adv. Drug Deliv. Rev.* **2013**, *65*, 36–48.
(6) Miyata, K.; Christie, R. J.; Kataoka, K. *React. Funct. Polym.* **2011**, *71*, 227–234.
(7) Torchilin, V. *Adv. Drug Deliv. Rev.* **2011**, *63*, 131–135.*
(8) Huang, K.; Ma, H.; Liu, J.; Huo, S.; Kumar, A.; Wei, T.; Zhang, X.; Jin, S.; Gan, Y.; Wang, P. C.; He, S.; Zhang, X.; Liang, X. J. *ACS Nano* **2012**, *6*, 4483–4493.
(9) Moghimi, S. M.; Simberg, D. *Nano Today* **2017**, *15*, 8–10.*
(10) Knop, K.; Hoogenboom, R.; Fischer, D.; Schubert, U. S. *Angew. Chemie Int. Ed.* **2010**, *49*, 6288–6308.
(11) Kozma, G. T.; Mészáros, T.; Vashegyi, I.; Fülöp, T.; Örfi, E.; Dézsi, L.; Rosivall, L.; Bavli, Y.; Urbanics, R.; Mollnes, T. E.; Barenholz, Y.; Szebeni, J. *ACS Nano* **2019**, *13*, 9315–9324.
(12) Jiang, S.; Cao, Z. *Adv. Mater.* **2010**, *22*, 920–932.
(13) Gullotti, E.; Yeo, Y. *Mol. Pharm.* **2009**, *6*, 1041–1051.
(14) Naseri, N.; Ajorlou, E.; Asghari, F.; Pilehvar-Soltanahmadi, Y. *Artif. Cells, Nanomedicine, Biotechnol.* **2018**, *46*, 1111–1121.
(15) Kim, J.; Chhour, P.; Hsu, J.; Litt, H. I.; Ferrari, V. A.; Popovtzer, R.; Cormode, D. P. *Bioconjug. Chem.* **2017**, *28*, 1581–1597.
(16) Thakor, A. S.; Jokerst, J. V.; Ghanouni, P.; Campbell, J. L.; Mittra, E.; Gambhir, S. S. *J. Nucl. Med.* **2016**, *57*, 1833–1837.
(17) Chen, F.; Goel, S.; Hernandez, R.; Graves, S. A.; Shi, S.; Nickles, R. J.; Cai, W. *Small* **2016**, *12*, 2775–2782.
(18) Zhou, C.; Hao, G.; Thomas, P.; Liu, J.; Yu, M.; Sun, S.; Öz, O. K.; Sun, X.; Zheng, J. *Angew. Chemie - Int. Ed.* **2012**, *51*, 10118–10122.
(19) Bishop, C. J.; Kozielski, K. L.; Green, J. J. *J. Control. Release* **2015**, *219*, 488–499.*
(20) Moon, J. J.; Suh, H.; Polhemus, M. E.; Ockenhouse, C. F.; Yadava, A.; Irvine, D. J. *PLoS One* **2012**, *7*.
(21) Zhang, X. Q.; Dahle, C. E.; Baman, N. K.; Rich, N.; Weiner, G. J.; Salem, A. K. *J. Immunother.* **2007**, *30*, 469–478.
(22) Dubertret, B.; Calame, M.; Libchaber, A. J. *Nat. Biotechnol.* **2001**, *19*, 365–370.
(23) Zhou, W.; Gao, X.; Liu, D.; Chen, X. *Chem. Rev.* **2015**, *115*, 10575–10636.
(24) Yin, H.; Kanasty, R. L.; Eltoukhy, A. A.; Vegas, A. J.; Dorkin, J. R.; Anderson, D. G. *Nat. Rev. Genet.* **2014**, *15*, 541–555.
(25) Chen, F.; Ehlerding, E. B.; Cai, W. *J. Nucl. Med.* **2014**, *55*, 1919–1922.
(26) Bobo, D.; Robinson, K. J.; Islam, J.; Thurecht, K. J.; Corrie, S. R. *Pharm Res* **2016**, *33*, 2373–2387.*
(27) Germain, M.; Caputo, F.; Metcalfe, S.; Tosi, G.; Spring, K.; Åslund, A. K. O.; Pottier, A.; Schiffelers, R.; Ceccaldi, A.; Schmid, R. *J. Control. Release* **2020**, *326*, 164–171.*
(28) Banerjee, D.; Cieslar-Pobuda, A.; Zhu, G. H.; Wiechec, E.; Patra, H. K. *Trends Pharmacol. Sci.* **2019**, *40*, 403–418.
(29) Huang, H.; Feng, W.; Chen, Y.; Shi, J. *Nano Today* **2020**, *35*, 100972.*

(30) Martins, J. P.; das Neves, J.; de la Fuente, M.; Celia, C.; Florindo, H.; Günday-Türeli, N.; Popat, A.; Santos, J. L.; Sousa, F.; Schmid, R.; Wolfram, J.; Sarmento, B.; Santos, H. A. *Drug Deliv. Transl. Res.* **2020**, *10*, 726–729.*
(31) Richardson, J. J.; Caruso, F. *Nano Lett.* **2020**, *20*, 1481–1482.
(32) Wilhelm, S.; Tavares, A. J.; Dai, Q.; Ohta, S.; Audet, J.; Dvorak, H. F.; Chan, W. C. W. *Nat. Rev. Mater.* **2016**, *1*, 16014.**
(33) Sadauskas, E.; Danscher, G.; Stoltenberg, M.; Vogel, U.; Larsen, A.; Wallin, H. *Nanomedicine Nanotechnology, Biol. Med.* **2009**, *5*, 162–169.*
(34) Ye, L.; Yong, K.-T.; Liu, L.; Roy, I.; Hu, R.; Zhu, J.; Cai, H.; Law, W.-C.; Liu, J.; Wang, K.; Liu, J.; Liu, Y.; Hu, Y.; Zhang, X.; Swihart, M. T.; Prasad, P. N. *Nat. Nanotechnol.* **2012**, *7*, 453–458.
(35) Wu, P.; Yan, X.-P. *Chem. Soc. Rev.* **2013**, *42*, 5489.
(36) Gustafson, H. H.; Holt-Casper, D.; Grainger, D. W.; Ghandehari, H. *Nano Today* **2015**, *10*, 487–510.
(37) Mahmoudi, M.; Bertrand, N.; Zope, H.; Farokhzad, O. C. *Nano Today* **2016**, *11*, 817–832.*
(38) Alric, C.; Miladi, I.; Kryza, D.; Taleb, J.; Lux, F.; Bazzi, R.; Billotey, C.; Janier, M.; Perriat, P.; Roux, S.; Tillement, O. *Nanoscale* **2013**, *5*, 5930.*
(39) Kumar, N.; Kumar, R. In *Nanotechnology and Nanomaterials in the Treatment of Life-threatening Diseases*; Elsevier, 2014; pp 53–107.
(40) Longmire, M.; Choyke, P. L.; Kobayashi, H. *Nanomedicine* **2008**, *3*, 703–717.
(41) Tang, S.; Peng, C.; Xu, J.; Du, B.; Wang, Q.; Vinluan, R. D.; Yu, M.; Kim, M. J.; Zheng, J. *Angew. Chemie Int. Ed.* **2016**, *55*, 16039–16043.
(42) Soo Choi, H.; Liu, W.; Misra, P.; Tanaka, E.; Zimmer, J. P.; Itty Ipe, B.; Bawendi, M. G.; Frangioni, J. V. *Nat. Biotechnol.* **2007**, *25*, 1165–1170.
(43) Zhao, Y.; Sultan, D.; Detering, L.; Luehmann, H.; Liu, Y. *Nanoscale* **2014**, *6*, 13501–13509.
(44) Liu, J.; Yu, M.; Ning, X.; Zhou, C.; Yang, S.; Zheng, J. *Angew. Chemie Int. Ed.* **2013**, *52*, 12572–12576.
(45) Shen, S.; Jiang, D.; Cheng, L.; Chao, Y.; Nie, K.; Dong, Z.; Kutyreff, C. J.; Engle, J. W.; Huang, P.; Cai, W.; Liu, Z. *ACS Nano* **2017**, *11*, 9103–9111.
(46) Liang, G.; Jin, X.; Qin, H.; Xing, D. *J. Mater. Chem. B* **2017**, *5*, 6366–6375.
(47) Liu, T.; Chao, Y.; Gao, M.; Liang, C.; Chen, Q.; Song, G.; Cheng, L.; Liu, Z. *Nano Res.* **2016**, *9*, 3003–3017.
(48) Benezra, M.; Penate-Medina, O.; Zanzonico, P. B.; Schaer, D.; Ow, H.; Burns, A.; DeStanchina, E.; Longo, V.; Herz, E.; Iyer, S.; Wolchok, J.; Larson, S. M.; Wiesner, U.; Bradbury, M. S. *J. Clin. Invest.* **2011**, *121*, 2768–2780.
(49) Xu, J.; Yu, M.; Peng, C.; Carter, P.; Tian, J.; Ning, X.; Zhou, Q.; Tu, Q.; Zhang, G.; Dao, A.; Jiang, X.; Kapur, P.; Hsieh, J. T.; Zhao, X.; Liu, P.; Zheng, J. *Angew. Chemie - Int. Ed.* **2018**, *57*, 266–271.
(50) Choi, H. S.; Liu, W.; Liu, F.; Nasr, K.; Misra, P.; Bawendi, M. G.; Frangioni, J. V. *Nat. Nanotechnol.* **2010**, *5*, 42–47.
(51) Yang, S.; Sun, S.; Zhou, C.; Hao, G.; Liu, J.; Ramezani, S.; Yu, M.; Sun, X.; Zheng, J. *Bioconjug. Chem.* **2015**, *26*, 511–519.
(52) Zhou, C.; Long, M.; Qin, Y.; Sun, X.; Zheng, J. *Angew. Chemie - Int. Ed.* **2011**, *50*, 3168–3172.
(53) Burns, A. A.; Vider, J.; Ow, H.; Herz, E.; Penate-Medina, O.; Baumgart, M.; Larson, S. M.; Wiesner, U.; Bradbury, M. *Nano Lett.* **2009**, *9*, 442–448.
(54) Zhou, M.; Li, J.; Liang, S.; Sood, A. K.; Liang, D.; Li, C. *ACS Nano* **2015**, *9*, 7085–7096.

(55) Zhang, X.-D.; Wu, D.; Shen, X.; Liu, P.-X.; Fan, F.-Y.; Fan, S.-J. *Biomaterials* **2012**, *33*, 4628–4638.
(56) Yang, S.; Zhou, C.; Cai, X.-J. *Colloids Surfaces B Biointerfaces* **2015**, *135*, 751–755.
(57) Peng, C.; Gao, X.; Xu, J.; Du, B.; Ning, X.; Tang, S.; Bachoo, R. M.; Yu, M.; Ge, W. P.; Zheng, J. *Nano Res.* **2017**, *10*, 1366–1376.
(58) Peng, C.; Xu, J.; Yu, M.; Ning, X.; Huang, Y.; Du, B.; Hernandez, E.; Kapur, P.; Hsieh, J. T.; Zheng, J. *Angew. Chemie - Int. Ed.* **2019**, *58*, 8479–8483.
(59) Mahesh, K. V.; Singh, S. K.; Gulati, M. *Powder Technol.* **2014**, *256*, 436–449.*
(60) Wang, N.; Fuh, J. Y. H.; Dheen, S. T.; Senthil Kumar, A. *Bio-Design Manuf.* **2021**, *4*, 379–404.
(61) Esposito, S. *Materials (Basel).* **2019**, *12*, 668.
(62) Jenjob, R.; Phakkeeree, T.; Seidi, F.; Theerasilp, M.; Crespy, D. *Macromol. Biosci.* **2019**, *19*, 1900063.
(63) Deganello, F.; Tyagi, A. K. *Prog. Cryst. Growth Charact. Mater.* **2018**, *64*, 23–61.
(64) Li, X.; Xu, H.; Chen, Z.-S.; Chen, G. *J. Nanomater.* **2011**, *2011*, 1–16.
(65) Dykman, L.; Khlebtsov, N. *Chem. Soc. Rev.* **2012**, *41*, 2256–2282.
(66) Sau, T. K.; Rogach, A. L.; Jäckel, F.; Klar, T. A.; Feldmann, J. *Adv. Mater.* **2010**, *22*, 1805–1825.
(67) Ferrari, M. *Nat. Rev. Cancer* **2005**, *5*, 161–171.
(68) Choi, C. H. J. H. J.; Alabi, C. A. A.; Webster, P.; Davis, M. E. E. *Proc. Natl. Acad. Sci.* **2009**, *107*, 1235–1240.
(69) Hong, R.; Han, G.; Fernández, J. M.; Kim, B.; Forbes, N. S.; Rotello, V. M. *J. Am. Chem. Soc.* **2006**, *128*, 1078–1079.
(70) Kenney, M. E.; Basilion, J. P.; Burda, C.; Broome, A.-M.; Cheng, Y.; Meyers, J. D. *J. Am. Chem. Soc.* **2011**, *133*, 2583–2591.
(71) De Rosa, F. S.; Bentley, M. V. L. B. *Pharm. Res.* **2000**, *17*, 1447–1455.
(72) Weissleder, R. *Nat. Biotechnol.* **2001**, *19*, 316–317.
(73) Cao-Milán, R.; Liz-Marzán, L. M. *Expert Opin. Drug Deliv.* **2014**, *11*, 741–752.
(74) Lal, S.; Clare, S. E.; Halas, N. J. *Acc. Chem. Res.* **2008**, *41*, 1842–1851.
(75) Fairbairn, J. J.; Khan, M. W.; Ward, K. J.; Loveridge, B. W.; Fairbairn, D. W.; O'Neill, K. L. *Cancer Lett.* **1995**, *89*, 183–188.
(76) Huang, X.; Jain, P. K.; El-Sayed, I. H.; El-Sayed, M. A. *Photochem. Photobiol.* **2006**, *82*, 412.
(77) Raji, V.; Kumar, J.; Rejiya, C. S.; Vibin, M.; Shenoi, V. N.; Abraham, A. *Exp. Cell Res.* **2011**, *317*, 2052–2058.
(78) Cardinal, J.; Klune, J. R.; Chory, E.; Jeyabalan, G.; Kanzius, J. S.; Nalesnik, M.; Geller, D. A. *Surgery* **2008**, *144*, 125–132.
(79) Cho, S. H. *Phys. Med. Biol.* **2005**, *50*, N163–N173.
(80) Kong, T.; Zeng, J.; Wang, X.; Yang, X.; Yang, J.; McQuarrie, S.; McEwan, A.; Roa, W.; Chen, J.; Xing, J. Z. *Small* **2008**, *4*, 1537–1543.
(81) Kim, D.; Park, S.; Lee, J. H.; Jeong, Y. Y.; Jon, S. *J. Am. Chem. Soc.* **2007**, *129*, 7661–7665.
(82) Kah, J. C. Y.; Olivo, M.; Chow, T. H.; Song, K. S.; Koh, K. Z. Y.; Mhaisalkar, S.; Sheppard, C. J. R. *J. Biomed. Opt.* **2009**, *14*, 054015.
(83) He, X.; Gao, J.; Gambhir, S. S.; Cheng, Z. *Trends Mol. Med.* **2010**, *16*, 574–583.
(84) Shalaev, V. M.; Kawata, S. *Nanophotonics with Surface Plasmons*; Elsevier, 2007.
(85) Mirkin, C. A.; Letsinger, R. L.; Mucic, R. C.; Storhoff, J. J. *Nature* **1996**, *382*, 607–609.
(86) Wang, C. C.; Wu, S. M.; Li, H. W.; Chang, H. T. *ChemBioChem* **2016**, 1052–1062.
(87) Anselmo, A. C.; Mitragotri, S. *AAPS J.* **2015**, *17*, 1041–1054.

(88) Paithankar, D.; Hwang, B. H.; Munavalli, G.; Kauvar, A.; Lloyd, J.; Blomgren, R.; Faupel, L.; Meyer, T.; Mitragotri, S. *J. Control. Release* **2015**, *206*, 30–36.
(89) Arvizo, R. R.; Miranda, O. R.; Thompson, M. A.; Pabelick, C. M.; Bhattacharya, R.; Robertson, J. D.; Rotello, V. M.; Prakash, Y. S.; Mukherjee, P. *Nano Lett.* **2010**, *10*, 2543–2548.
(90) Chithrani, B. D.; Chan, W. C. W. *Nano Lett.* **2007**, *7*, 1542–1550.
(91) Pelka, J.; Gehrke, H.; Esselen, M.; Türk, M.; Crone, M.; Bräse, S.; Muller, T.; Blank, H.; Send, W.; Zibat, V.; Brenner, P.; Schneider, R.; Gerthsen, D.; Marko, D. *Chem. Res. Toxicol.* **2009**, *22*, 649–659.
(92) Fröhlich, E. *Int. J. Nanomedicine* **2012**, 5577.
(93) Verma, A.; Uzun, O.; Hu, Y. Y.; Hu, Y. Y.; Han, H.-S.; Watson, N.; Chen, S.; Irvine, D. J.; Stellacci, F. *Nat. Mater.* **2008**, *7*, 588–595.
(94) Albanese, A.; Chan, W. C. W. *ACS Nano* **2011**, *5*, 5478–5489.
(95) Alyautdin, R.; Khalin, I.; Nafeeza, M. I.; Haron, M. H.; Kuznetsov, D. *Int. J. Nanomedicine* **2014**, *9*, 795–811.
(96) Kulkarni, S. A.; Feng, S. S. *Pharm. Res.* **2013**, *30*, 2512–2522.
(97) Xue, W.; Liu, Y.; Zhang, N.; Yao, Y.; Ma, P.; Wen, H.; Huang, S.; Luo, Y.; Fan, H. *Int. J. Nanomedicine* **2018**, *13*, 5719–5731.
(98) Zarschler, K.; Rocks, L.; Licciardello, N.; Boselli, L.; Polo, E.; Garcia, K. P.; De Cola, L.; Stephan, H.; Dawson, K. A. *Nanomedicine Nanotechnology, Biol. Med.* **2016**, *12*, 1663–1701.
(99) Hoshyar, N.; Gray, S.; Han, H.; Bao, G. *Nanomedicine* **2016**, *11*, 673–692.
(100) Ohta, S.; Kikuchi, E.; Ishijima, A.; Azuma, T.; Sakuma, I.; Ito, T. *Sci. Rep.* **2020**, *10*, 18220.
(101) Mei, B. C.; Oh, E.; Susumu, K.; Farrell, D.; Mountziaris, T. J.; Mattoussi, H. *Langmuir* **2009**, *25*, 10604–10611.
(102) Berciaud, S.; Cognet, L.; Tamarat, P.; Lounis, B. *Nano Lett.* **2005**, *5*, 515–518.
(103) Faraday, M. *Philos. Trans. R. Soc. London* **1857**, *147*, 145–181.*
(104) Turkevich, J.; Stevenson, P. C.; Hillier, J. *Discuss. Faraday Soc.* **1951**, *11*, 55.**
(105) Campisi, S.; Schiavoni, M.; Chan-Thaw, C.; Villa, A. *Catalysts* **2016**, *6*, 185.
(106) Weare, W. W.; Reed, S. M.; Warner, M. G.; Hutchison, J. E. *J. Am. Chem. Soc.* **2000**, *122*, 12890–12891.
(107) Leff, D. V.; Brandt, L.; Heath, J. R. *Langmuir* **1996**, *12*, 4723–4730.
(108) Brust, M.; Walker, M.; Bethell, D.; Schiffrin, D. J.; Whyman, R. *J. Chem. Soc., Chem. Commun.* **1994**, 801–802.
(109) Hussain, I.; Graham, S.; Wang, Z.; Tan, B.; Sherrington, D. C.; Rannard, S. P.; Cooper, A. I.; Brust, M. *J. Am. Chem. Soc.* **2005**, *127*, 16398–16399.
(110) Male, K. B.; Li, J.; Bun, C. C.; Ng, S.-C.; Luong, J. H. T. *J. Phys. Chem. C* **2008**, *112*, 443–451.
(111) Schaaff, T. G.; Whetten, R. L. *J. Phys. Chem. B* **2000**, *104*, 2630–2641.
(112) Alkilany, A. M.; Murphy, C. J. *J. Nanoparticle Res.* **2010**, *12*, 2313–2333.
(113) Mühlpfordt, H. *Experientia* **1982**, *38*, 1127–1128.*
(114) Slot, J. W.; Geuze, H. J. *Eur. J. Cell Biol.* **1985**, *38*, 87–93.*
(115) Briñas, R. P.; Hu, M.; Qian, L.; Lymar, E. S.; Hainfeld, J. F. *J. Am. Chem. Soc.* **2008**, *130*, 975–982.
(116) Ohyama, J.; Hitomi, Y.; Higuchi, Y.; Tanaka, T. *Top. Catal.* **2009**, *52*, 852–859.
(117) Song, J.; Kim, D.; Lee, D. *Langmuir* **2011**, *27*, 13854–13860.
(118) Jun, H.; Fabienne, T.; Florent, M.; Coulon, P.-E.; Nicolas, M.; Olivier, S. *Langmuir* **2012**, *28*, 15966–15974.
(119) Bastús, N. G.; Comenge, J.; Puntes, V. *Langmuir* **2011**, *27*, 11098–11105.

(120) Ziegler, C.; Eychmüller, A. *J. Phys. Chem. C* **2011**, *115*, 4502–4506.
(121) Schulz, F.; Homolka, T.; Bastús, N. G.; Puntes, V.; Weller, H.; Vossmeyer, T. *Langmuir* **2014**, *30*, 10779–10784.
(122) Bastús, N. G.; Merkoçi, F.; Piella, J.; Puntes, V. *Chem. Mater.* **2014**, *26*, 2836–2846.
(123) Patra, H. K.; GuhaSarkar, D.; Dasgupta, A. K. *Anal. Chim. Acta* **2009**, *649*, 128–134.
(124) Agunloye, E.; Panariello, L.; Gavriilidis, A.; Mazzei, L. *Chem. Eng. Sci.* **2018**, *191*, 318–331.
(125) Piella, J.; Bastús, N. G.; Puntes, V. *Chem. Mater.* **2016**, *28*, 1066–1075.**
(126) Chakraborty, A.; Chakraborty, S.; Chaudhuri, B.; Bhattacharjee, S. *Gold Bull.* **2016**, *49*, 75–85.
(127) Ojea-Jiménez, I.; Bastús, N. G.; Puntes, V. *J. Phys. Chem. C* **2011**, *115*, 15752–15757.**
(128) Kettemann, F.; Birnbaum, A.; Witte, S.; Wuithschick, M.; Pinna, N.; Kraehnert, R.; Rademann, K.; Polte, J. *Chem. Mater.* **2016**, *28*, 4072–4081.
(129) LaMer, V. K.; Dinegar, R. H. *J. Am. Chem. Soc.* **1950**, *72*, 4847–4854.*
(130) Polte, J. *CrystEngComm* **2015**, *17*, 6809–6830.**
(131) Wuithschick, M.; Birnbaum, A.; Witte, S.; Sztucki, M.; Vainio, U.; Pinna, N.; Rademann, K.; Emmerling, F.; Kraehnert, R.; Polte, J. *ACS Nano* **2015**, *9*, 7052–7071.
(132) Pelaz, B.; del Pino, P.; Maffre, P.; Hartmann, R.; Gallego, M.; Rivera-Fernández, S.; de la Fuente, J. M.; Nienhaus, G. U.; Parak, W. J. *ACS Nano* **2015**, *9*, 6996–7008.
(133) Moyano, D. F.; Saha, K.; Prakash, G.; Yan, B.; Kong, H.; Yazdani, M.; Rotello, V. M. *ACS Nano* **2014**, *8*, 6748–6755.
(134) Azharuddin, M.; Zhu, G. H.; Das, D.; Ozgur, E.; Uzun, L.; Turner, A. P. F.; Patra, H. K. *Chem. Commun.* **2019**, *55*.
(135) Li, N.; Xia, T.; Nel, A. E. *Free Radic. Biol. Med.* **2008**, *44*, 1689–1699.
(136) Buzea, C.; Pacheco, I. I.; Robbie, K. *Biointerphases* **2007**, *2*, MR17–MR71.
(137) He, X.; Young, S.-H.; Schwegler-Berry, D.; Chisholm, W. P.; Fernback, J. E.; Ma, Q. *Chem. Res. Toxicol.* **2011**, *24*, 2237–2248.
(138) Mahmoudi, M.; Shokrgozar, M. A.; Sardari, S.; Moghadam, M. K.; Vali, H.; Laurent, S.; Stroeve, P. *Nanoscale* **2011**.
(139) Rocha, S.; Thünemann, A. F.; Pereira, M. do C.; Coelho, M.; Möhwald, H.; Brezesinski, G. *Biophys. Chem.* **2008**, *137*, 35–42.
(140) AshaRani, P. V.; Low Kah Mun, G.; Hande, M. P.; Valiyaveettil, S. *ACS Nano* **2009**, *3*, 279–290.
(141) Bhabra, G.; Sood, A.; Fisher, B.; Cartwright, L.; Saunders, M.; Evans, W. H.; Surprenant, A.; Lopez-Castejon, G.; Mann, S.; Davis, S. A.; Hails, L. A.; Ingham, E.; Verkade, P.; Lane, J.; Heesom, K.; Newson, R.; Case, C. P. *Nat. Nanotechnol.* **2009**, *4*, 876–883.
(142) Elsabahy, M.; Wooley, K. L. *Chem. Soc. Rev.* **2013**, *42*, 5552–5576.
(143) Duque, G. A.; Descoteaux, A. **2014**, *5*, 1–12.*
(144) Simón, C.; Gimeno, M. J.; Mercader, A.; Francés, A.; Garcia Velasco, J.; Remohí, J.; Polan, M. L.; Pellicer, A. *Mol. Hum. Reprod.* **1996**, *2*, 405–424.
(145) Kokkonen, H.; SÃ¶derstrÃ¶m, I.; RocklÃ¶v, J.; Hallmans, G.; Lejon, K.; Dahlqvist, S. R. *Arthritis Rheum.* **2010**, NA-NA.
(146) Szebeni, J.; Simberg, D.; González-Fernández, Á.; Barenholz, Y.; Dobrovolskaia, M. A. *Nat. Nanotechnol.* **2018**, *13*, 1100–1108.
(147) Chiu, S.; Bharat, A. *Curr. Opin. Organ Transplant.* **2016**, *21*, 239–245.
(148) Blandizzi, C.; Gionchetti, P.; Armuzzi, A.; Caporali, R.; Chimenti, S.; Cimaz, R.; Cimino, L.; Lapadula, G.; Lionetti, P.; Marchesoni, A.; Marcellusi, A.; Mennini, F. S.; Salvarani, C.; Girolomoni, G. *Int. J. Immunopathol. Pharmacol.* **2014**, *27*, 1–10.

(149) Hollenberg, S. M.; Cunnion, R. E.; Parrillo, J. E. *Chest* **1991**, *100*, 1133–1137.
(150) Kaneko, N.; Kurata, M.; Yamamoto, T.; Morikawa, S.; Masumoto, J. *Inflamm. Regen.* **2019**, *39*, 12.
(151) Hoffman, H. M.; Mueller, J. L.; Broide, D. H.; Wanderer, A. A.; Kolodner, R. D. *Nat. Genet.* **2001**, *29*, 301–305.
(152) Masters, S. L.; Dunne, A.; Subramanian, S. L.; Hull, R. L.; Tannahill, G. M.; Sharp, F. A.; Becker, C.; Franchi, L.; Yoshihara, E.; Chen, Z.; Mullooly, N.; Mielke, L. A.; Harris, J.; Coll, R. C.; Mills, K. H. G.; Mok, K. H.; Newsholme, P.; Nuñez, G.; Yodoi, J.; Kahn, S. E.; Lavelle, E. C.; O'Neill, L. A. J. *Nat. Immunol.* **2010**, *11*, 897–904.
(153) Bickel, M. *J. Periodontol.* **1993**, *64*, 456–460.
(154) Pease, J. E.; Sabroe, I. *Am. J. Respir. Med.* **2002**, *1*, 19–25.
(155) Apostolakis, S.; Vogiatzi, K.; Amanatidou, V.; Spandidos, D. A. *Cardiovasc. Res.* **2009**, *84*, 353–360.
(156) Tsai, S.-J. *Prog. Neuro-Psychopharmacology Biol. Psychiatry* **2021**, *106*, 110173.
(157) Gubler, U.; Chua, A. O.; Schoenhaut, D. S.; Dwyer, C. M.; McComas, W.; Motyka, R.; Nabavi, N.; Wolitzky, A. G.; Quinn, P. M.; Familletti, P. C. *Proc. Natl. Acad. Sci.* **1991**, *88*, 4143–4147.
(158) Watford, W. T.; Moriguchi, M.; Morinobu, A.; O'Shea, J. J. *Cytokine Growth Factor Rev.* **2003**, *14*, 361–368.
(159) Croxford, A. L.; Kulig, P.; Becher, B. *Cytokine Growth Factor Rev.* **2014**, *25*, 415–421.
(160) Wojdasiewicz, P.; Poniatowski, Ł. A.; Szukiewicz, D. *Mediators Inflamm.* **2014**, *2014*, 1–19.
(161) Bao, K.; Reinhardt, R. L. *Cytokine* **2015**, *75*, 25–37.
(162) Junttila, I. S. *Front. Immunol.* **2018**, *9*.
(163) Chomarat, P.; Banchereau, J. *Int. Rev. Immunol.* **1998**, *17*, 1–52.
(164) CHADBAN; TESCH; FOTI; LAN; ATKINS; NIKOLIC-PATERSON. *Immunology* **1998**, *94*, 72–78.
(165) Fiorentino, D. F.; Zlotnik, A.; Mosmann, T. R.; Howard, M.; O'Garra, A. *J. Immunol.* **1991**, *147*, 3815–3822.
(166) Oswald, I. P.; Wynn, T. A.; Sher, A.; James, S. L. *Proc. Natl. Acad. Sci.* **1992**, *89*, 8676–8680.
(167) Meng, D.; Liang, L.; Guo, X. *Eur. J. Inflamm.* **2019**, *17*, 205873921984340.
(168) Liao, W.; Lin, J.-X.; Leonard, W. J. *Immunity* **2013**, *38*, 13–25.
(169) Hoyer, K. K.; Dooms, H.; Barron, L.; Abbas, A. K. *Immunol. Rev.* **2008**, *226*, 19–28.
(170) Tanaka, T.; Narazaki, M.; Kishimoto, T. *Cold Spring Harb. Perspect. Biol.* **2014**, *6*, a016295–a016295.
(171) Pedersen, B. K.; Febbraio, M. A. *Physiol. Rev.* **2008**, *88*, 1379–1406.
(172) Vauthier, C.; Persson, B.; Lindner, P.; Cabane, B. *Biomaterials* **2011**, *32*, 1646–1656.*
(173) Green, R. J.; Davies, M. C.; Roberts, C. J.; Tendler, S. J. B. *Biomaterials* **1999**, *20*, 385–391.
(174) Suzuki, T.; Ichihara, M.; Hyodo, K.; Yamamoto, E.; Ishida, T.; Kiwada, H.; Ishihara, H.; Kikuchi, H. *Int. J. Pharm.* **2012**, *436*, 636–643.
(175) Neun, B. W.; Ilinskaya, A. N.; Dobrovolskaia, M. A. 2018; pp 149–160.
(176) Beltrame, M. H.; Catarino, S. J.; Goeldner, I.; Boldt, A. B. W.; de Messias-Reason, I. J. *Front. Pediatr.* **2015**, *2*.
(177) Vauthier, C.; Lindner, P.; Cabane, B. *Colloids Surfaces B Biointerfaces* **2009**, *69*, 207–215.
(178) Dobrovolskaia, M. A.; Aggarwal, P.; Hall, J. B.; McNeil, S. E. *Mol. Pharm.* **2008**, *5*, 487–495.

(179) Tanaka, K. A.; Key, N. S.; Levy, J. H. *Anesth. Analg.* **2009**, *108*, 1433–1446.
(180) Oslakovic, C.; Cedervall, T.; Linse, S.; Dahlbäck, B. *Nanomedicine Nanotechnology, Biol. Med.* **2012**, *8*, 981–986.
(181) Steuer, H.; Krastev, R.; Lembert, N. *J. Biomed. Mater. Res. Part B Appl. Biomater.* **2014**, *102*, 897–902.
(182) Sanfins, E.; Augustsson, C.; Dahlbäck, B.; Linse, S.; Cedervall, T. *Nano Lett.* **2014**, *14*, 4736–4744.
(183) Reardon, S. *Nature* **2015**, *523*, 266–266.
(184) Mollnes, T. E.; Brekke, O. L.; Fung, M.; Fure, H.; Christiansen, D.; Bergseth, G.; Videm, V.; Lappegard, K. T.; Kohl, J.; Lambris, J. D. *inflammation, Blood* **2002**, *100*, 1869–1877.
(185) Bergseth, G.; Ludviksen, J. K.; Kirschfink, M.; Giclas, P. C.; Nilsson, B.; Mollnes, T. E. *Mol. Immunol.* **2013**, *56*, 232–239.
(186) Lê, S.; Josse, J.; Husson, F. *J. Stat. Softw.* **2008**, *25*, 1–18.
(187) Kassambara, A. *Practical guide to principal component methods in R: PCA, M (CA), FAMD, MFA, HCPC, factoextra. Vol. 2.*; 2017.
(188) Patra, H. K.; Banerjee, S.; Chaudhuri, U.; Lahiri, P.; Dasgupta, A. K. *Nanomedicine Nanotechnology, Biol. Med.* **2007**, *3*, 111–119.
(189) Lu, S.; Xia, D.; Huang, G.; Jing, H.; Wang, Y.; Gu, H. *Colloids Surfaces B Biointerfaces* **2010**, *81*, 406–411.
(190) Li, C.; Li, Z.; Wang, Y.; Liu, H. *J. Nanomater.* **2016**, *2016*, 1–10.
(191) Connor, E. E.; Mwamuka, J.; Gole, A.; Murphy, C. J.; Wyatt, M. D. *Small* **2005**, *1*, 325–327.
(192) Pan, Y.; Neuss, S.; Leifert, A.; Fischler, M.; Wen, F.; Simon, U.; Schmid, G.; Brandau, W.; Jahnen-Dechent, W. *Small* **2007**, *3*, 1941–1949.
(193) Wang, S.; Lu, W.; Tovmachenko, O.; Rai, U. S.; Yu, H.; Ray, P. C. *Chem. Phys. Lett.* **2008**, *463*, 145–149.
(194) Sarma, J. V.; Ward, P. A. *Cell Tissue Res.* **2011**, *343*, 227–235.
(195) Kirschfink, M.; Mollnes, T. E. *Clin. Diagn. Lab. Immunol.* **2003**, *10*, 982–989.
(196) Lück, M.; Paulke, B. R.; Schröder, W.; Blunk, T.; Müller, R. H. *J. Biomed. Mater. Res.* **1998**, *39*, 478–485.
(197) Perevedentseva, E. V; F.Y., S.; T.H., S.; Y.C., L.; C.L., C.; Karmenyan, A. V; Priezzhev, A. V; Lugovtsov, A. E. *Quantum Electron.* **2011**, *40*, 1089–1093.
(198) De Paoli Lacerda, S. H.; Park, J. J.; Meuse, C.; Pristinski, D.; Becker, M. L.; Karim, A.; Douglas, J. F. *ACS Nano* **2010**, *4*, 365–379.
(199) Lin, Y.-C. *J. Biomed. Opt.* **2012**, *17*, 101512.
(200) Dobrovolskaia, M. A.; Patri, A. K.; Zheng, J.; Clogston, J. D.; Ayub, N.; Aggarwal, P.; Neun, B. W.; Hall, J. B.; McNeil, S. E. *Nanomedicine Nanotechnology, Biol. Med.* **2009**, *5*, 106–117.
(201) Salvador-Morales, C.; Zhang, L.; Langer, R.; Farokhzad, O. C. *Biomaterials* **2009**, *30*, 2231–2240.
(202) Khan, I.; Saeed, K.; Khan, I. *Arab. J. Chem.* **2019**, *12*, 908–931.
(203) Ohshima, H.; Miyagishima, A.; Kurita, T.; Makino, Y.; Iwao, Y.; Sonobe, T.; Itai, S. *Int. J. Pharm.* **2009**, *377*, 180–184.
(204) Wu, P.; Liu, Q.; Li, R.; Wang, J.; Zhen, X.; Yue, G.; Wang, H.; Cui, F.; Wu, F.; Yang, M.; Qian, X.; Yu, L.; Jiang, X.; Liu, B. *ACS Appl. Mater. Interfaces* **2013**, *5*, 12638–12645.
(205) Kapse, S. V.; Gaikwad, R. V.; Samad, A.; Devarajan, P. V. *Int. J. Pharm.* **2012**, *429*, 104–112.
(206) Tyrrell, Z. L.; Shen, Y.; Radosz, M. *Prog. Polym. Sci.* **2010**, *35*, 1128–1143.

(207) Chollakup, R.; Smitthipong, W.; Eisenbach, C. D.; Tirrell, M. *Macromolecules* **2010**, *43*, 2518–2528.**
(208) Donau, C.; Späth, F.; Sosson, M.; Kriebisch, B. A. K.; Schnitter, F.; Tena-Solsona, M.; Kang, H.-S.; Salibi, E.; Sattler, M.; Mutschler, H.; Boekhoven, J. *Nat. Commun.* **2020**, *11*, 5167.
(209) Oparin, A. I.; Synge, A. *The origin of life on the earth / Translated from the Russian by Ann Synge.*; Academic Press,: New York :, 1957.
(210) Blocher, W. C.; Perry, S. L. *Wiley Interdiscip. Rev. Nanomedicine Nanobiotechnology* **2017**, *9*, e1442.
(211) de Vasconcelos, C. L.; Bezerril, P. M.; dos Santos, D. E. S.; Dantas, T. N. C.; Pereira, M. R.; Fonseca, J. L. C. *Biomacromolecules* **2006**, *7*, 1245–1252.
(212) Battogtokh, G.; Ko, Y. T. *J. Control. Release* **2016**, *234*, 10–20.
(213) Lim, W. Q.; Phua, S. Z. F.; Zhao, Y. *ACS Appl. Mater. Interfaces* **2019**, *11*, 31638–31648.
(214) Ma, X.; Li, X.; Shi, J.; Yao, M.; Zhang, X.; Hou, R.; Shao, N.; Luo, Q.; Gao, Y.; Du, S.; Liang, X.; Wang, F. *Adv. Healthc. Mater.* **2019**, *8*, 1900661.
(215) Lungwitz, U.; Breunig, M.; Blunk, T.; Göpferich, A. *Eur. J. Pharm. Biopharm.* **2005**, *60*, 247–266.
(216) van der Aa, M. A. E. M.; Huth, U. S.; Häfele, S. Y.; Schubert, R.; Oosting, R. S.; Mastrobattista, E.; Hennink, W. E.; Peschka-Süss, R.; Koning, G. A.; Crommelin, D. J. A. *Pharm. Res.* **2007**, *24*, 1590–1598.
(217) Pack, D. W.; Hoffman, A. S.; Pun, S.; Stayton, P. S. *Nat. Rev. Drug Discov.* **2005**, *4*, 581–593.
(218) Fischer, D.; Li, Y.; Ahlemeyer, B.; Krieglstein, J.; Kissel, T. *Biomaterials* **2003**, *24*, 1121–1131.
(219) Eccleston, M. E.; Slater, N. K. H.; Tighe, B. J. *React. Funct. Polym.* **1999**, *42*, 147–161.
(220) Tonge, S. .; Tighe, B. . *Adv. Drug Deliv. Rev.* **2001**, *53*, 109–122.
(221) Chen, R.; Eccleston, M. E.; Yue, Z.; Slater, N. K. H. *J. Mater. Chem.* **2009**, *19*, 4217.**
(222) Chen, R.; Khormaee, S.; Eccleston, M. E.; Slater, N. K. H. *Biomaterials* **2009**, *30*, 1954–1961.**
(223) Zhao, M.; Zacharia, N. S. *Macromol. Rapid Commun.* **2016**, *37*, 1249–1255.**
(224) Pramanik, B.; Singha, N.; Das, D. *ACS Appl. Polym. Mater.* **2019**, *1*, 833–843.
(225) Singha, N.; Das, B. K.; Pramanik, B.; Das, S.; Das, D. *Chem. Sci.* **2019**, *10*, 10035–10039.
(226) Ren, D.; Dalmau, M.; Randall, A.; Shindel, M. M.; Baldi, P.; Wang, S.-W. *Adv. Funct. Mater.* **2012**, *22*, 3170–3180.
(227) Munnier, E.; Cohen-Jonathan, S.; Linassier, C.; Douziech-Eyrolles, L.; Marchais, H.; Soucé, M.; Hervé, K.; Dubois, P.; Chourpa, I. *Int. J. Pharm.* **2008**, *363*, 170–176.
(228) Ahn, B. K.; Das, S.; Linstadt, R.; Kaufman, Y.; Martinez-Rodriguez, N. R.; Mirshafian, R.; Kesselman, E.; Talmon, Y.; Lipshutz, B. H.; Israelachvili, J. N.; Waite, J. H. *Nat. Commun.* **2015**, *6*, 8663.
(229) Suvarna, M.; Dyawanapelly, S.; Kansara, B.; Dandekar, P.; Jain, R. *ACS Appl. Nano Mater.* **2018**, *1*, 5524–5535.
(230) Mohammadi, P.; Christopher, J.; Beaune, G.; Engelhardt, P.; Kamada, A.; Timonen, J. V. I.; Knowles, T. P. J.; Penttila, M.; Linder, M. B. *J. Colloid Interface Sci.* **2020**, *560*, 149–160.
(231) Gillet, J.-P.; Gottesman, M. M. 2010; pp 47–76.
(232) Juliano, R. L.; Ling, V. *Biochim. Biophys. Acta - Biomembr.* **1976**, *455*, 152–162.

(233) Cole, S.; Bhardwaj, G.; Gerlach, J.; Mackie, J.; Grant, C.; Almquist, K.; Stewart, A.; Kurz, E.; Duncan, A.; Deeley, R. *Science (80-.).* **1992**, *258*, 1650–1654.
(234) Doyle, L. A.; Yang, W.; Abruzzo, L. V.; Krogmann, T.; Gao, Y.; Rishi, A. K.; Ross, D. D. *Proc. Natl. Acad. Sci.* **1998**, *95*, 15665–15670.
(235) Gottesman, M. M.; Fojo, T.; Bates, S. E. *Nat. Rev. Cancer* **2002**, *2*, 48–58.
(236) Gros, P.; Neriah, Y. Ben; Croop, J. M.; Housman, D. E. *Nature* **1986**, *323*, 728–731.
(237) Safa, A. *Curr. Med. Chem. Agents* **2004**, *4*, 1–17.
(238) Gottesman, M. M.; Pastan, I. *Annu. Rev. Biochem.* **1993**, *62*, 385–427.
(239) Binkhathlan, Z.; Lavasanifar, A. *Curr. Cancer Drug Targets* **2013**, *13*, 326–346.
(240) Robey, R. W.; Pluchino, K. M.; Hall, M. D.; Fojo, A. T.; Bates, S. E.; Gottesman, M. M. *Nat. Rev. Cancer* **2018**, *18*, 452–464.
(241) Chen, Y.; Chen, H.; Shi, J. *Mol. Pharm.* **2014**, *11*, 2495–2510.
(242) Kang, K. W.; Chun, M.-K.; Kim, O.; Subedi, R. K.; Ahn, S.-G.; Yoon, J.-H.; Choi, H.-K. *Nanomedicine Nanotechnology, Biol. Med.* **2010**, *6*, 210–213.
(243) Kievit, F. M.; Wang, F. Y.; Fang, C.; Mok, H.; Wang, K.; Silber, J. R.; Ellenbogen, R. G.; Zhang, M. *J. Control. Release* **2011**, *152*, 76–83.
(244) Wang, F.; Wang, Y.-C.; Dou, S.; Xiong, M.; Sun, T.; Wang, J. *ACS Nano* **2011**, *5*, 3679–3692.
(245) Ye, M.; Han, Y.; Tang, J.; Piao, Y.; Liu, X.; Zhou, Z.; Gao, J.; Rao, J.; Shen, Y. *Adv. Mater.* **2017**, *29*, 1702342.
(246) Torchilin, V. P. pp 1–32.
(247) Zhu, Y.-J.; Chen, F. *Chem. - An Asian J.* **2015**, *10*, 284–305.
(248) Li, B.; Meng, Z.; Li, Q.; Huang, X.; Kang, Z.; Dong, H.; Chen, J.; Sun, J.; Dong, Y.; Li, J.; Jia, X.; Sessler, J. L.; Meng, Q.; Li, C. *Chem. Sci.* **2017**, *8*, 4458–4464.
(249) Lankalapalli, S.; Kolapalli, V. R. M. *Indian J. Pharm. Sci.* **2009**, *71*, 481.
(250) Eccleston, M. E.; Williams, S. L.; Yue, Z.; Chen, R.; Lee, C. K.; Anikina, E.; Pawlyn, C.; Barrand, M. A.; Slater, N. K. H. *Food Bioprod. Process.* **2005**, *83*, 141–146.
(251) Khormaee, S.; Choi, Y.; Shen, M. J.; Xu, B.; Wu, H.; Griffiths, G. L.; Chen, R.; Slater, N. K. H.; Park, J. K. *Adv. Funct. Mater.* **2013**, *23*, 565–574.
(252) Lynch, A. L.; Chen, R.; Dominowski, P. J.; Shalaev, E. Y.; Yancey, R. J.; Slater, N. K. H. *Biomaterials* **2010**, *31*, 6096–6103.
(253) Liechty, W. B.; Chen, R.; Farzaneh, F.; Tavassoli, M.; Slater, N. K. H. *Adv. Mater.* **2009**, *21*, 3910–3914.
(254) Kopytynski, M.; Chen, S.; Legg, S.; Minter, R.; Chen, R. *Adv. Ther.* **2020**, *3*, 1900169.
(255) Chen, S.; Chen, R. *ACS Appl. Mater. Interfaces* **2016**, *8*, 22457–22467.
(256) Young, L. J.; Ströhl, F.; Kaminski, C. F. *J. Vis. Exp.* **2016**.
(257) Azharuddin, M.; Roberg, K.; Dhara, A. K.; Jain, M. V.; Darcy, P.; Hinkula, J.; Slater, N. K. H.; Patra, H. K. *Sci. Rep.* **2019**, *9*, 20066.**
(258) Zhitomirsky, B.; Assaraf, Y. G. *Oncotarget* **2017**, *8*, 45117–45132.
(259) Guo, B.; Tam, A.; Santi, S. A.; Parissenti, A. M. *BMC Cancer* **2016**, *16*, 762.
(260) Seynhaeve, A. L. B.; Dicheva, B. M.; Hoving, S.; Koning, G. A.; ten Hagen, T. L. M. *J. Control. Release* **2013**, *172*, 330–340.
(261) Melissaridou, S.; Wiechec, E.; Magan, M.; Jain, M. V.; Chung, M. K.; Farnebo, L.; Roberg, K. *Cancer Cell Int.* **2019**, *19*, 16.
(262) Kwon, K. C.; Jo, E.; Kwon, Y.-W.; Lee, B.; Ryu, J. H.; Lee, E. J.; Kim, K.; Lee, J. *Adv. Mater.* **2017**, *29*, 1701146.
(263) Cassano, D.; Pocoví-Martínez, S.; Voliani, V. *Bioconjug. Chem.* **2018**, *29*, 4–16.
(264) Li, Y.; Humphries, B.; Wang, Z.; Lang, S.; Huang, X.; Xiao, H.; Jiang, Y.; Yang, C. *ACS Appl. Mater. Interfaces* **2016**, *8*, 30735–30746.
(265) Lee, K.; Conboy, M.; Park, H. M.; Jiang, F.; Kim, H. J.; Dewitt, M. A.; Mackley, V.

A.; Chang, K.; Rao, A.; Skinner, C.; Shobha, T.; Mehdipour, M.; Liu, H.; Huang, W. C.; Lan, F.; Bray, N. L.; Li, S.; Corn, J. E.; Kataoka, K.; Doudna, J. A.; Conboy, I.; Murthy, N. *Nat. Biomed. Eng.* **2017**, *1*, 889–901.

*** very important and * important references for further background information.*

Appendix I: Analytical techniques utilized in the report

APTT/PTT measurement

Activated partial thromboplastin time evaluates overall speed at which blood clots form by the intrinsic and the consequent common pathway (Figure 3-2). In a typical measurement, plasma is first separated from the blood sample, mixed with access calcium to counteract the anticoagulant effects, and then mixed with an activator. The clotting time can be measured optically by an automated instrument. In comparison, the prothrombin time (PT) measures the time it takes for blood to form clots via the extrinsic pathway and consequent common pathway. The procedure of PT test is similar to APTT test, with the activator being replaced by a tissue factor (e.g., thromboplastin). The APTT and PT tests were used to examine the blood compatibility and thrombogenicity of uGNPs.

Confocal Fluorescence Microscopy

The confocal microscopy, or confocal laser scanning microscopy, is an imaging technique to visualize fluorescence micrographs at high optical resolution. It uses a spatial pinhole to block out-of-focus light therefore forming depth-dependent images with increased resolution and contrast. It also allows reconstruction of 3D structure with multiple 2D images taken at different depths. Confocal fluorescence microscopy was utilized to investigate the colocalization of nanocoacervate and nuclei in Chapter 5.

Dynamic Light Scattering (DLS)

DLS is a size characterization technique of proteins, nanoparticles, polymers, and colloids dispersed in a liquid medium. In a typical measurement, a colloidal suspension is irradiated by a monochromatic light source. The light is then scattered by colloids and is collected by a photomultiplier. The diffracted light can experience either constructively interference resulting in bright spots or destructive interference resulting in dark regions on a speckle pattern. The intensity of the scattered light fluctuates over time because the particles undergo Brownian motion in the solution. The speckle pattern evolves over time due to the fluctuation of the scattering intensity, and the series of speckle patterns are analyzed by an autocorrelator. The exponential decay in autocorrelation function is correlated to the mobility of the colloids due to Brownian motion, which is influenced by particle size. For smaller particles, the decay rate is faster as they undergo faster Brownian motion producing more

fluctuation in the speckle pattern than larger particles. DLS was employed to characterize the particle size of uGNPs and nanocoacervate systems in this report.

Electrochemiluminescence Immunoassay (ECLIA)

The ECLIA is a quantitative measurement of antibodies based on the change in electrochemical luminescence. In ECLIA, the analyte of interest is immobilized by a capture antibody and tagged by an electrochemiluminescently labeled antibody through immune conjugation. The electrochemiluminescent label facilitates the generation of electronically excited species, which upon returning to the relaxed state can emit light signal. In an ECLIA, the analyte is first incubated with immobilized capture antibodies. Once the analyte is conjugated to the capture antibodies, the secondary or probing antibodies labeled with electrochemiluminescent agent (e.g., Ruthenium complexes) is added to tag captured analytes. After removal of non-specially bound probes, an intermediate-generating agent is added. The intermediate-generating agent turns into intermediate species (e.g., radicals) which transfers electrons via exergonic reactions to the electrochemiluminescence agent. The electrochemiluminescence agent goes into an excited state once receiving the electrons and emits light upon relaxation. The ECLIA was utilized to measure cytokines on the MSD multiplex assay platform.

Electrophoretic Light Scattering (EIS)

The EIS is based on the DLS technique, and it characterizes the ζ-potential of colloidal suspensions. While the motion of particle in DLS measurement is driven by Brownian's motion, the motion of particles is caused by an externally applied oscillating electric field in EIS. Therefore, the direction of the particle motion is determined by the charge sign and rate of the particle oscillation is correlated to the charge density borne by the particles. The motion of the charged particles under the external electric field produces the same series of speckle patterns as in the DLS and these are too analyzed by an autocorrelation function. EIS was used to measure the ζ-potential of uGNPs, nanocoacervate, and their derivative samples.

Enzyme-linked immunosorbent assay (ELISA)

The ELISA is a biochemical assay for analyzing the presence of a protein in liquid sample via antigen-antibody interaction. The protein to be measured is first immobilized onto the bottom of a plate well either non-specifically or specifically by a capture antibody. In the

latter case, the capture antibodies are already attached to the surface. After that, a enzyme-linked second antibody is added and conjugated to the immobilized protein at a different epitope than the capture antibody. Lastly, a substrate of the enzyme is added to produce a visible signal for quantification of the analyte. The plate is gently washed in between each step to remove excess and unattached molecules. ELISA was used to quantify the complement components in studying the complement activation of uGNPs.

Lactate dehydrogenase (LDH) Assay

The LDH assay is a cell viability assay based on membrane integrity. LDH is an enzyme that can be released from cells upon membrane damage or cell death. In a LDH assay, a water-soluble tetrazolium is added to the culture medium. If there were dead cells or disintegrated cell membrane, the released LDH is present in the medium and it can oxidize lactate and produce NADH. The tetrazolium can be reduced by the produced NADH to confer a colorimetric signal. The LDH assay is therefore used as a cytotoxicity assay. LDH assay was used to assess the cytotoxic effects of uGNPs on macrophages.

MTS Assay

MTS/MTT assay is one of the most widely utilized cytotoxicity assays. MTS [3-(4,5-dimethylthiazol-2-yl)-5-(3-carboxymethoxyphenyl)-2-(4-sulfophenyl)-2H tetrazolium] assay is regarded as a more convenient and water-soluble version of the MTT assay. It is based on the reduction of the MTS tetrazolium compound by viable cells to generate a colored formazan dye that is soluble in cell culture media. This conversion is carried out by NAD(P)H-dependent dehydrogenase enzymes in metabolically active cells. Therefore, the intensity of the final color is proportional to the number of viable cells. In an MTS assay, the cells are incubated with MTS agents for a specific amount of time so that the difference in number of viable cells can be captured. The reaction is often interrupted by a stop reagent. The intensity of color change is then characterized through the absorbance of the reaction solution. In the MTS assay, the positive control is usually the cells with no drug treatment and the negative control is the empty well with no seeded cells. MTS assay was employed to measure the cytotoxic effect of uGNPs and nanocoacervate delivery system.

Nuclear Magnetic Resonance (NMR) Spectroscopy

The NMR spectroscopy is an analytical technique to characterize the local magnetic fields around atomic nuclei. In the NMR spectroscopy, molecules are first subject to a

constant magnetic field leading to the alignment of the magnetic nuclear spins. The polarization of the nuclear spin is then disrupted by a weak oscillating magnetic field pulse usually in the transvers direction. As the perturbed nuclei return to the original aligned state, electromagnetic waves are emitted. A free induction decay nuclear magnetic resonance signal in the time domain can thus be obtained and transferred in the frequency using the Fourier Transform. Due to the different chemical environment, specifically the electron density, around each type of nuclei the local magnetic field is different. The chemical environment of nuclei can be inferred from the signal frequency (chemical shift) and signal peak shape (coupling) in the spectrum. ^{1}H-NMR spectroscopy was used to analyze the interaction between PP polymer and PEI in nanocoacervate assembly.

Scanning Electron Microscope (SEM)

SEM is an electron microscope technique for characterization of surface topography. In SEM, a sample is scanned by an electron beam, and the electrons interact with atoms in the sample, producing various signals that contain information about the surface topography and composition of the sample. Scanned sample produces secondary electrons, backscattered electrons, and characteristic X-rays, which are detected by respective detectors. The obtained signals are then converted to images revealing the surface topography. The samples must be electrically conductive to withstand the high energy electron beams. Therefore, for nonconductive materials, ultrathin conductive coatings (e.g., gold NPs, platinum NPs) may be applied to increase the conductivity. SEM was utilized to observe structural features of the nanocoacervate system.

Transmission Electron Microscopy (TEM)

The TEM is a microscope technique for observing the size, shape, and other structural features of the samples. The TEM operates on the same principles as the light microscope but uses electron beams rather than light. Due to the much shorter wavelength of electrons than that of light, the resolution of TEM images is a lot higher than that from a light microscope. During the TEM imaging, electrons are emitted from an electron gun at the top of a TEM. The electrons then travel through the microscope's vacuum tube and are focused by the electromagnetic lens into a very fine beam. The electron beam hits and passes through the very thin specimen. While traveling within the specimen, the electrons either scatter or pass right through to hit a fluorescent screen at the bottom of the microscope. Due to the different electron density hitting the screen, the image revealing fine internal structural traits, such as

crystal structures and grain boundaries, of the specimen can be obtained. Diffraction patterns can also be captured using TEM. Morphology characterization of uGNPs and nanocoacervate system was performed with TEM.

Ultraviolet-visible (UV-Vis) Spectroscopy

UV-Vis spectroscopy is an absorption or reflectance spectroscopy that covers the ultraviolet and the visible light wavelength range. The intensity of the electromagnetic wave at each wavelength is measure with respect to a blank sample. The absorption and reflectance of the sample in the visible light spectrum determines the color of the sample. In a UV-Vis spectroscopic measurement, the light source first emit light with broad range of wavelength. The light then passes through the wavelength selector (e.g., monochromator, absorption filter, interference filter, etc.) to contain only wavelengths of interest before reaching the sample. Next, the incident light shines upon the sample, which can be a liquid in a cuvette or a thin film on a transparent substrate. Once the light passes through the sample, a detector that can convert the intensity at each wavelength separately into readable electrical signals. UV-Vis spectroscopy was mainly used as a analytical tool for monitoring the LSPR of uGNPs in this report.